UNIVERSITAT POLITÈCNICA DE CATALUNYA BARCELONATECH

Preparation and characterization of nanocomposites based on polylactide manufactured by reactive extrusion-calendering : thermal, rheological, mechanical and fracture properties

Raja Nazrul Hakim bin Raja Nazri

Preparation and characterization of nanocomposites based on Polylactide manufactured by Reactive Extrusion-Calendering: Thermal, Rheological, Mechanical and Fracture Properties

Dissertation submitted to the

Technical University of Catalonia, Barcelona Tech

In Partial Fulfilment of the Requirements for the

Degree of Doctor of Philosophy

in **Materials Science and Engineering**

Author:

Raja Nazrul Hakim bin Raja Nazri

Main Director:

Dr. Maria Lluïsa Maspoch Rulduà

Thesis Director:

Dr. Orlando Onofre Santana Pérez

Department of Materials Science and Metallurgy

April 2018

Acknowledgement

First and foremost, I would like to offer my unreserved gratitude and praises to Almighty God for His generous blessing and grace bestowed upon me during the course of this research work.

I would like to express my deepest gratitude to my supervisor, Professor Dr. Maria Lluïsa Maspoch Rulduà for her invaluable advice, unwavering patience, guidance and encouragement throughout the period of this study. Likewise, the constant supervision, support and generous assistance offered by my thesis supervisor Professor Dr. Orlando Santana Onofre Perez during the duration of the study is also acknowledged. All the suggestions, constructive criticisms and careful review from both of you helped shape and improve this dissertation. Sincere thanks is also accorded to Dr. Jonathan Cailloux for contributing directly to this work with his assistance during experiments and providing data that were analyzed in this dissertation. I am grateful for your help and guidance.

My heartfelt thanks goes to Prof. Dr. Jordi Bou (Department of Chemical Engineering, Universitat Politècnica de Catalunya) for providing his time, effort and advice throughout the course of this study.

I wish to acknowledge Universiti Kuala Lumpur for providing the administrative and financial support for me to undertake this study. I would also like acknowledge the monetary funding received both under Erasmus Mundus Action 2 and Majlis Amanah Rakyat (MARA) programmes. I also like to convey my appreciation towards the Spanish Ministry of Science

and Innovation (MICINN) for the financial assistance that I have benefitted over the course of my study.

I would also like to put forward my gratitude to the all the present and past members of the Centre Català del Plàstic research group namely Profesor Dr. Antonio Martínez, Prof. Dr. Miguel Sánchez-Soto, Dr. Tobias Abt, Prof. Dr. Marcelo, Dr. Edgar, Dr. David, Prof. Dr. José Ignacio Velasco, Dr. Vera, Dr. Sylvia, Dr. Julio, Hooman, Noel, David, Javier and all the numerous people whose names have not been mentioned for their co-operation and help during my tenure in CCP research centre. Special thanks also goes to CCP administration members namely Anna, Susana and Alba for their kind assistance.

I wish to express my gratitude towards my wonderful parents and my family including my siblings and my in-laws for their understanding and support. Last but not least, my highest gratitude and appreciation towards my wife who has always been the love of my life and my pillar of strength throughout the course of this study.

Abstract

The aim of this Ph.D. thesis was to manufacture PLA nanocomposites sheets that has been reactively modified with predetermined concentrations of a multi-functional epoxide agent (Joncryl 4300F, BASF, Germany) through reactive extrusion on a pilot plant. A commercial extrusion grade of PLA (PLA 4032D, NatureWorks, Belgium) was individually reinforced with either a commercial grade of organomodified montmorillonite clay (o-MMT) (Cloisite 30B, Southern Clay Products, USA) or three commercial grade of fumed silica (nano-SiO_2){(CAB-O-SIL EH5,), (epoxy modified silica 6851HN and aminopropyl modified silica 6852HN, Skyspring Nanomaterials Inc., USA)}. Initial preliminary studies using an internal mixer were performed to monitor the effects of nanofillers and/or SAmfE addition on the PLA melt behaviour by monitoring the torque trace as a function of mixing time. Subsequently, using a masterbatch approach, PLA and reactively modified PLA nanocomposites sheets were prepared using co-rotating twin screw extruder with a screw diameter of 25 mm (L/D=36). An outcome of 15 meters of non-modified and reactively modified PLA composites reinforced with o-MMT (PLA/o-MMT composites) calendered sheets (nominal width: 100 mm; nominal thickness: 1 mm) and 15 meters of reactively modified PLA nanocomposites reinforced with nano-SiO_2 (PLA/nano-SiO_2 composites) calendered sheets (nominal width: 100 mm; nominal thickness: 0.6 mm) were manufactured using reactive extrusion-calendering process in pilot plant setup.

In the case of PLA/o-MMT composites, premature reactions between epoxy rings from multi-functional epoxide agent and -OH functionalities from o-MMT took place, reducing chain extension/branching reactions achieved in reactively modified PLA nanocomposites sheets (REX-PLA-C). Classical spectroscopic (FT-IR) and chromatographic (SEC-DRI) methods verifies these findings. In the case of PLA/nano-SiO_2 composites, SiO_2-polymer tethering reaction occurred in reactively modified PLA nanocomposites reinforced with either epoxy modified nano-SiO_2 (REX-PLA/SiO_2-E) and amino modified nano-SiO_2 (REX-PLA/SiO_2-A) sheets. In contrast, this reaction is absent in reactively modified PLA nanocomposites reinforced with non-modified nano-SiO_2 film (REX-PLA/SiO_2). However, both FT-IR and intrinsic viscosity measurements methods were unsuccessful to highlight the differences between unmodified and surface-modified nano-SiO_2.

Morphological analysis revealed PLA/o-MMT composites exhibited a homogenous and preferential distribution of clay particles in MD. However, the coexistence of mixed structures, involving tactoids of various sizes as well as intercalated clay layers were also observed. Nevertheless, a higher and finer dispersion of o-MMT particles was achieved through clay–polymer tethering via chain extender molecules. Likewise, PLA/nano-SiO_2 composites similarly exhibit a relatively homogeneous and sub-micron dispersion of nano-SiO_2. However, the improved chemical affinity of both surface modified nano-SiO_2 did not significantly improve the particle dispersion with presence aggregates were detectable. Probable layers of SiO_2-polymer tethering molecules may have surrounds these clusters of aggregates, encapsulating them within the matrix itself and are therefore not dispersible anymore since they are already chemically bonded.

Rheological analysis of REX-PLA-C revealed that both the melt elasticity and the melt response time increased with addition of o-MMT. On the other hand, PLA/nano-SiO_2 composites exhibit thermorheologically complex behaviour that can be principally attributed to formation of different non-uniform branched structures from addition of reactive agents. Cole-Cole plot revealed formation of filler inter-network in REX-PLA/SiO_2 which is absent in surface modified nano-SiO_2 reinforced PLA nanocomposites.

Presence of SiO_2 significantly modifies thermal behaviours of modified PLA. SiO_2 reduces cold crystallization temperature and increases the crystalline percentage of its respective modified PLA composites. Addition of non-modified nano-SiO_2 also influences the crystallization behaviour of the PLA nanocomposites. The isothermal crystallization kinetics of the PLA nanocomposites were studied using the Avrami analysis and the activation energy were determined using Arrhenius method. Addition of non-modified nano-SiO_2 enhances the crystallization rate and induces spherulitic growth mechanism with an athermal nucleation. Unfortunately, surface modified nano-SiO_2 did not seem to enhance PLA crystallization.

Mechanical parameters in tensile mode shows that the improved clay dispersion in REX-PLA-C enhanced multiple cavitation processes, notably improving PLA shear flow. However, the tensile behaviour of PLA/nano-SiO_2 composites remained unchanged whether silicas were added or not. A combined effect of physical ageing and nanofiller dispersion could be the reason for these trends.

The essential work of fracture analysis revealed that addition of o-MMT shows considerable improvements of specific essential work of fracture parameter and specific plastic work of dissipation of both PLA and modified PLA composites with o-MMT. This could be attributed to the combined effect of energy dissipation mechanisms such as de-cohesion and coalescence of micro-void. However, addition of nano-SiO_2 revealed no significant changes in the work required for the onset of crack propagation. However, a slight increase of work associated to the resistance of crack propagation accompanied with a decrease in volume of deformed material surrounding the ligament length were observed.

Resumen

El objetivo de esta tesis doctoral consistió en la fabricación de láminas de nanocompuestos de PLA que han sido modificados reactivamente a partir de un agente epóxido multifuncional (Joncryl 4300F, BASF, Alemania) con concentraciones predeterminadas de éste mediante extrusión reactiva en una planta piloto. El grado comercial de extrusión de PLA (PLA 4032D, NatureWorks, Bélgica) se reforzó individualmente con un grado comercial de arcilla de montmorillonita organomodificada (o-MMT) (Cloisite 30B, Southern Clay Products, EE. UU.) o bien con tres muestras de sílice ahumado de grado comercial (nano -SiO_2) {(CAB-O-SIL EH5,), (sílice modificada con epoxi 6851HN y sílice modificada con aminopropilo 6852HN, Skyspring Nanomaterials Inc., EE.UU.)}. Se realizaron estudios preliminares utilizando un mezclador interno para registrar los efectos de las nanocargas y / o la adición de SAmfE sobre el comportamiento de fusión del PLA al monitorear la evolución del torque en función del tiempo de mezclado. Posteriormente, utilizando un "masterbatch", se prepararon mezclas de PLA y láminas de nanocompuestos de PLA modificados reactivamente usando una extrusora de doble husillo co-rotatoria con un diámetro de husillo de 25 mm (L / D = 36). Se obtuvieron 15 metros de láminas calandradas (ancho nominal: 100 mm, espesor nominal: 1 mm) de compuestos de PLA modificados y no modificados reforzados con o-MMT (PLA / o-MMT) y 15 metros de láminas calandradas (ancho nominal: 100 mm, espesor nominal: 0,6 mm) de nanocompuestos de PLA modificados de forma reactiva reforzado con nano-SiO_2 (PLA / compuestos de nano-SiO_2) utilizando el proceso de calandrado por extrusión reactiva en la instalación de la planta piloto.

En el caso de los compuestos de PLA/o-MMT, las reacciones iniciales entre los anillos epoxi de agente epóxido multifuncional y funcionalidades -OH de o-MMT tuvieron lugar, reduciendo las reacciones de extensión / ramificación de cadena en hojas de nanocompuestos PLA modificados reactivamente (REX-PLA -DO). Los métodos espectroscópicos clásicos (FT-IR) y cromatográficos (SEC-DRI) verifican estos hallazgos. En el caso de compuestos de PLA/ nano-SiO_2, la reacción de anclaje del polímero-SiO_2 se produjo en nanocompuestos de PLA modificados de forma reactiva reforzados con nano-SiO_2 modificado con epoxi (REX-PLA/ SiO2-E) y nano-SiO_2 modificado con amino (REX-PLA/SiO_2-A) hojas. Por el contrario, esta reacción no tuvo lugar en los nanocompuestos PLA modificados reactivamente reforzados con una película de nano-SiO_2 no modificada (REX-PLA/SiO_2). Sin embargo, tanto los

métodos de medición FT-IR como de viscosidad intrínseca no tuvieron éxito para resaltar las diferencias entre nano-SiO2 sin modificar y con superficie modificada.

El análisis morfológico reveló que los compuestos de PLA/o-MMT exhibieron una distribución homogénea y preferencial de partículas de arcilla en MD. No obstante, también se observó la coexistencia de estructuras mixtas, que implican tactoides de diversos tamaños, así como capas de arcilla intercaladas. Sin embargo, se logró una dispersión más alta y más fina de las partículas de o-MMT a través del anclaje del polímero de arcilla a través de moléculas extensoras de cadena. Del mismo modo, los compuestos de PLA/nano-SiO_2 muestran de forma similar una dispersión relativamente homogénea y submicrométrica de nano-SiO2. Sin embargo, la afinidad química mejorada de los nano-SiO_2 modificados en la superficie no mejoró significativamente la dispersión de partículas con presencia de agregados detectables. Probablemente, capas de moléculas de anclaje de polímero de SiO_2 pueden haber rodeado estos grupos de agregados, encapsulándolos dentro de la propia matriz y, por lo tanto, ya no son dispersables ya que están químicamente unidos.

El análisis reológico de REX-PLA-C reveló que tanto la elasticidad de la masa fundida como el tiempo de respuesta de fusión aumentaban con la adición de o-MMT. Por otro lado, los compuestos de PLA/nano-SiO_2 exhiben un comportamiento termo-reológicamente complejo que puede atribuirse principalmente a la formación de diferentes estructuras ramificadas no uniformes a partir de la adición de agentes reactivos. La gráfica de "Cole-Cole" reveló la formación de una interfase de relleno en REX-PLA/SiO_2 que está ausente en los nanocompuestos PLA reforzados con nano-SiO_2 de superficie modificada.

La presencia de SiO_2 modifica significativamente los comportamientos térmicos del PLA modificado. Tanto el o-MMT como el SiO_2 reducen la temperatura fría de cristalización y aumentan el porcentaje cristalino de sus respectivos compuestos PLA modificados. La adición de nano-SiO_2 no modificado también influye en el comportamiento de cristalización de los nanocompuestos de PLA. La cinética de cristalización isotérmica de los nanocompuestos de PLA se estudió usando el análisis de Avrami y la energía de activación se determinó usando el método de Arrhenius. La adición nano-SiO_2 no modificado aumenta la velocidad de cristalización e induce el mecanismo de crecimiento esferulítico con nucleación atérmica.

Desafortunadamente, parece que la superficie de nano-SiO_2 modificado no mejora la cristalización de PLA.

Los parámetros mecánicos en modo de tracción muestran que la dispersión de arcilla mejorada en REX-PLA-C mejoró los procesos de cavitación múltiple, mejorando notablemente el flujo de cizalla de PLA. No obstante, el comportamiento a la tracción de los compuestos de PLA/nano-SiO_2 permaneció sin cambios independientemente de la presencia de sílices. Un efecto combinado del envejecimiento físico y la dispersión de las nanocargas podría ser la razón de estas tendencias.

El trabajo esencial del análisis de fracturas reveló que la adición de o-MMT muestra mejoras considerables en el trabajo esencial específico del parámetro de fractura y el trabajo plástico específico de disipación de los compuestos PLA y PLA modificados con o-MMT. Esto podría atribuirse al efecto combinado de los mecanismos de disipación de energía, como la descohesión y la coalescencia del micro-vacío. Sin embargo, la adición de nano-SiO_2 no reveló cambios significativos en el trabajo requerido para el inicio de la propagación de fisuras. No obstante, se observó un ligero aumento del trabajo asociado a la resistencia a la propagación de grietas acompañada de una disminución en el volumen de material deformado que rodea la longitud del ligamento.

Table of Contents

List of Figures

List of Tables

Abbreviations and Symbols

Abbreviations and symbols are presented in an alphabetical order.

Abbreviations

a.u.	Arbitrary unit
CCP	Centre Català del Plàstic
c.f.	compare
DDENT	Deeply-Double-Edge-Notched Tensile
DSC	Differential Scanning Calorimetry
e.g.	For example
EPFM	Elastic Plastic Fracture Mechanics
ESIS-TC4	European Structural Integrity Society-Technical Committee 4
EWF	Essential Work of Fracture
HMW	High Molecular Weight
i.e.	That is
IFPZ	Inner Fracture Process Zone
IR	Infrared spectroscopy
LA	Lactic Acid
LCB	Long chain branching
LVE	Linear viscoelastic region
MWD	Molecular weight distribution
n/a	Not available
OPDZ	Outer Process Deformation Zone
PLA	Poly(Lactic Acid)
SEC-DRI	Size Exclusion Chromatography with Differential Refractive Index detector
TEM	Transmission Electron Microscopy
THF	Tetrahydrofuran

Symbols

A_0	Transversal section of the tensile samples	m^2
E	Elastic or Young's Modulus	Pa
E', E''	Storage and loss modulus (DTMA analysis)	Pa
E_a	Activation energy	kJ/mol
G', G''	Storage and loss modulus	Pa
$\|G^*(\omega)\|$	Absolute value of the complex modulus as a function of the angular frequency	Pa
h	Height of the OPDZ zone (DDENT specimens)	mm
H	Enthalpy	$J.g^{-1}$
l	Ligament length	mm
L_0	Initial gauge length of the tensile specimens (50 mm)	mm

M_i	Molar mass of the component molecules of type *i*	-
M_n	Number-average molecular weight	$g.mol^{-1}$
M_v	Viscosity-average molecular weight	$g.mol^{-1}$
M_w	Weight-average molecular weight	$g.mol^{-1}$
M_z	Z-average molecular weight	$g.mol^{-1}$
n_i	Fraction of the component molecules type *i*	-
R	Gas constant	$J.K^{-1}.mol^{-1}$
t	Thickness	mm
t	Time	s or min
$Tan\ \delta$	Loss factor	-
T_c, T_{cc}	Crystallization and cold crystallization temperature	°C
T_g, T_{gm}	Glass transition and midpoint glass transition	°C
W	Width	mm
w_e	Specific essential work of fracture	$kJ.m^{-2}$
W_e	Essential work of fracture (per unit area)	kJ
w_f	Specific work of fracture	$kJ.m^{-2}$
W_f	Work required for the whole fracture process	kJ
w_i	Weight-fraction of the component molecules type *i*	-
w_p	Specific non-essential work of fracture	$MJ.m^{-3}$
W_p	Non-essential work of fracture (per unit volume)	$MJ.m^{-1}$
X_c	Degree of crystallinity	%
ZG	Distance between grips	mm
ΔH_m^0	Melting enthalpy of 100 % crystalline PLA	$J.g^{-1}$
ΔH_{cc}	Cold crystallization enthalpy	$J.g^{-1}$
ΔH_m	Melting enthalpy	$J.g^{-1}$
ΔL_x	Increase in specimen length between gauge marks during tensile experiments	mm
$\Gamma(t)$	Torque trace as a function of mixing time	Nm
β	Shape Factor of OPDZ Zone (DDENT specimens)	-
βw_p	Non-essential work of fracture or plastic term	$MJ.m^{-3}$
δ	Phase angle	°
ε_b	Strain at break	%
ε_y	Yield strain	%
η_0	Zero-shear rate viscosity	Pa.s
$\lvert\eta^*(\omega)\rvert$	Absolute value of the complex viscosity as a function of angular frequency	Pa.s
v	Wavenumber (FT-IR experiments)	cm^{-1}
v_e	Entanglement density	$mmol.m^{-3}$
σ_y	Yield strength	Pa
ω	Angular frequency	$rad.s^{-1}$

Chapter 1. Introduction

1.1 Introduction

Over 49 million tons of plastics is consumed Europe alone in 2015 of which 39.9 % was used to manufacture packaging (Associations of Plastic Manufacturers, 2017). A majority of these plastics were produced from petroleum, which is a finite, non-renewable resource. The price of oil per barrel fluctuates considerably and currently the price hovers around €60 euros per barrel. Unfortunately, usually plastic manufactured goods were intended for short service life (typically less than one year from manufacturing) before it rapidly succumbs to becoming part of the solid waste stream.

In Europe, 25.8 million tonnes of post-consumer plastics waste ended up in the official waste streams in 2014. Out of that number, 69.2% was recovered through recycling and energy recovery processes (Associations of Plastic Manufacturers, 2017). Consequently, 30.8% still went to landfill, together with its low rate of decomposition, leading to its progressive accumulation in the various environmental compartments, as not only for their incautious abandoning in the environment, but also as for the lack of an efficient capillary-organized collection of industrial and domestic waste accumulation. This problem is becoming increasingly acute as the global plastics production estimated a sustained growth trend of 1.5 % year-on year increase (Associations of Plastic Manufacturers, 2017).

Environmental harm deriving from the disposal of petroleum-based non-degradable plastics has been a major problem all over the world for a very long time. One of the strategies to solve these problems is by recycling waste plastics, but the plastics pollution cannot be solved by waste plastics recycling alone since it is not always possible to recover all of the used plastics. Another strategy is to replace petroleum based products with the use of biodegradable plastics *i.e.* bioplastics which can be defined as materials whose physical and chemical properties undergo deterioration and completely degrade when exposed to microorganisms, carbon dioxide (aerobic) processes, methane (anaerobic processes), and water (aerobic and anaerobic processes) without the consumption of thermal energy (Babu et al., 2013; Prieto, 2016).

Bioplastics are not just one single material. They comprise of a whole family of materials with different properties and applications. According to European Bioplastics, a plastic material is defined as a bioplastic if it is either biobased, biodegradable, or features both properties (European Bioplastics e.V., 2017). Generally, biodegradable bioplastic undergoes biodegradation (composting), which is a natural and complex process of decomposition facilitated by biochemical mechanisms by microorganisms, macromolecules the material is totally degraded by microorganisms with production of carbon dioxide (under aerobic conditions) or methane (under anaerobic environment), water, mineral salts and new microbial cellular constituents (biomass) (Calmon-Decriaud et al., 1998). The products of the biodegradation can be re-absorbed by nature, which closes the bioplastic lifecycle. Thus, it is clear that the greatest benefits will be achieved with those that are biobased bioplastics and biodegradable.

Biobased bioplastics from renewable and biodegradable materials can be produced from natural materials either starch, cellulose and protein. Biobased bioplastics can also be made from oils, such as palm seed, linseed, soy bean, etc. or fermentation products, like polylactic acid (PLA), polyhydroxyalkanoate (PHA), and polyhydroxybutyrate (PHB) (Shimao, 2001).

Among these, PLA is the material that has piqued the most amount of interest because:

i. the lactic acid monomer can be obtained from renewable agricultural sources of low cost (sucrose and starch),
ii. can be easily processed in the standard thermoplastics processing techniques
iii. be recycled or composted may decompose without being separated from the organic matter and
iv. possess a range of mechanical properties that is comparable to those of atactic polystyrene, when in an amorphous state and comparable to polyethylene terephthalate (PET) when in the semi-crystalline state.

Somewhere in the late 1980s and throughout the beginning of 1990s, the “first generation of biopolymers” were introduced to the mass market for the first time. These pioneering biopolymers which are biologically degradable are mostly based on starch and polyhydroxyalkanoates that is chiefly produced by microbial fermentation processes. However, these biopolymers failed to gain commercial success in spite of its favourable assessment and promising growth forecasts. This comes down in particular to its yet untried material properties as well as a lack of incentives and policies implemented by governments to expand and encourage the public and industries for replacement of single-use plastic products with biopolymers (Babu et al., 2013; Endres and Siebert-Raths, 2011).

In recent years, what is now a much improved "second generation biopolymers" have emerged in the market. The various research, development and optimization of various biopolymers have translated into successful commercialization of the "second generation biopolymers". These degradable and compostable biopolymers are comparable with petrochemical-based polymers in terms of processing and use properties.

However, it still suffers with slight economies of scale disadvantages due largely to their still low production volume. Unfortunately, the most common applications of second generation of biopolymers are still mainly focused on single or short-term use applications such as in agricultural, horticultural sectors and compostable packaging especially in Europe and America (Endres and Siebert-Raths, 2011; European Bioplastics e.V., 2017; La Rosa, 2016).

However, primary criterion for the development of "third generation biopolymer" is concentrated on developing bio-based but yet durable materials for multi-use moderate- to long-term applications. For this generation of biopolymer, the composability factor no longer becomes the principal consideration instead it is to create a more sustainable production of polymers from renewable resources henceforth reducing the dependency on dwindling supplies of petrochemical resources. The third generation biopolymer are mostly targeted for applications used in automotive, electronics and other industries outside the field of packaging. (Endres and Siebert-Raths, 2011).

For PLA to be utilized in multiple use moderate- to long-term appplications, it is a necessary requirement for them to be both tough and strong, yet the two attributes are often mutually exclusive. Does having relatively high strength but low toughness exclude PLA from being used for durable applications ?. This is where the concept of tailoring the properties of PLA to attain the ideal stiffness−toughness balance comes into play. Reinforcement by montmorillonite clay (o-MMT) and fumed silica (nano-SiO_2) addition could aid in achieving this objective. The improvements in properties such as the increase of the elongation at break and modulus, increased maximum service temperature and decreased permeability to gas have been reported by various authors (Giannelis, 1998; LeBaron et al., 1999; Lv et al., 2016; Maspoch et al., 2009; Sinha Ray and Okamoto, 2003b; Xiong et al., 2015; Zhen and Wang, 2016). However, to fully realize these advantages it is necessary to achieve excellent dispersion for both of the filler within the polymeric matrix (Alexandre and Dubois, 2000; Khankrua et al., 2013; Pavlidou and Papaspyrides, 2008).

Addition of o-MMT and nano-SiO_2 also impart double benefits in which it can help to address PLA's main shortcoming in terms of its slow rate of crystallization from melt when compared with many other thermoplastics. Due to this, PLA is commonly found in amorphous state after processing. In its amorphous state, the maximum temperature at which the PLA retains its mechanical properties is determined by its glass transition temperature (T_g) which is approximately 56 °C. An alternative for solving such problems is by enhancing its ability to crystallize and thus increasing the crystallinity of PLA, which can be achieved by adding nanofillers such as o-MMT and nano-SiO_2 which can act as nucleating agent (Murariu et al., 2015; Xu et al., 2015; Zou et al., 2012). At temperatures above T_g, these crystallites act as anchor points that restrict deformation of the amorphous phase, leading to an increased stiffness

of the PLA. For its part, the addition of nanofillers decreases the surface free energy barrier required for nucleation to occur and increase the density of crystal nuclei, allowing crystallization takes place at higher temperatures and require less time.

While interesting mechanical properties and oxygen permeability were achieved for PLA nanocomposites, several extrusion steps were necessary to reach sufficient clay dispersion. This resulted in severe degradation of the polymeric matrix due to combined effect of multiple processing steps and the presence of the clay organo-modifier (bearing hydroxyl groups). Consequently, the MW significantly decreased; thus affecting the final properties (Carrasco et al., 2011a; Gamez-Perez et al., 2011a).

Numerous authors have reported that this degradation reactions can be addressed by addition of multi-functional reactive agents using reactive extrusion process (Al-Itry et al., 2014; Cailloux, 2015; Japon et al., 2000; Raquez et al., 2008). Using continuous reactive extrusion process, a relatively efficient chemical reactions can be obtained with relatively short reaction times. Due to its high chemical efficiency and absence of solvents used, this process is considered to be fairly economical and environmentally friendly. This processing method is easily scalable and implemented within the context of an industrial scale production (Gaspar-Cunha et al., 2011; Xanthos, 1992). Consequently, interesting results have been achieved with this approach. One of the more important ones are the increased melt elasticity of PLA have been reported which is especially imperative to resolve or minimize numerous issues such as sagging of melts and necking during film/sheet casting, film blowing and/or foaming (Cailloux, 2015; Cailloux et al., 2013; Cailloux et al., 2014; Cailloux et al., 2015). Despite of the structural modifications (*i.e.* chain extension and branching) achieved using multi-functional epoxide

agent (SAmfE), these modifications does not translate into significant enhancements in mechanical properties and fracture behaviour.

Along with modifications on the chain topology achieved with presence of multi-functional epoxide agent, remnant reactivity due to the unreacted epoxy groups were also reported by Cailloux et al. (2015). The combination of these factors could provide some support for the conceptual premise that an increase of shear viscosity due to chain topology modifications with the remaining reactivity could improve nanofiller dispersion due to better interaction between matrix and filler. The increase on viscosity can increase the local shear field, favouring either clay delamination or de-agglomeration of fumed silica, thus improving the degree of dispersion of the nanofillers. The remaining reactivity and depending on the surface treatment of the filler can improve the interaction between these phases, improving the stress transfer which can then translate into improvement of mechanical performance.

1.2 PhD Framework and objectives

In light of the above informations, Centre Català del Plastic (CCP) have developed two research projects entitled: "Architectural modifications of a PLA matrix through a one-step reactive extrusion-calendering process to enhance the processability, the fracture behaviour and the preparation of biodegradable nanocomposites" (*Ref*: MAT2010-19721-C02-01) and “REXBIOBLEND: PLA bioblends prepared by reactive extrusion” (ref: MAT2013-40730-P). Both projects undertaken were intended to extend the application windows of PLA from being single use short-term applications to multiple use moderate- to long-term applications while biodegradability becomes second importance. Both of these projects are funded by the Ministry

of Science and Innovation and a majority of its research activities were carried out in laboratories in Centre Català del Plàstic (CCP) in Terrassa (Spain).

This thesis is part of the research projects of MAT2010-19721-C02-01 and MAT2013-40730-P and complements studies in the CCP on processing, degradation and recyclability of PLA nanocomposites.

In this work, an extrusion grades PLA resin with a trade name of PLA 4032D® is utilized as matrix, manufactured by Natureworks®. A multi-functional epoxide agent oligomeric agent with a trade name of Joncryl ADR-4300F® was selected as reactive agents produced by BASF®. As potential nano reinforcement, four types reinforcing filler were chosen. An organically modified montmorillonite clay with a trade name of Cloisite 30B®, manufactured by Southern Clay Products® was first chosen. Subsequently, three types of fumed silica will be exploited namely CAB-O-SIL® EH5 supplied by Cabot Corporation®, epoxy modified silica 6851HN® and aminopropyl modified silica 6852HN® manufactured by Skyspring Nanomaterials Inc.®. Detailed description of these materials are given *Chapter 3*.

In view of the above considerations, the main objectives of this PhD are listed below:

a) *Evaluation of the reactions of organically modified montmorillonite clay in a commercial grade poly(lactic acid) modified through reactive extrusion using a multi-functional epoxide agent.*
b) *Evaluation of the reactions of non-modified / surface-modified fumed silica in a commercial grade poly(lactic acid) modified through reactive extrusion using a multi-functional epoxide agent.*

c) *Manufacturing of organically modified montmorillonite clay reinforced PLA nanocomposites sheet using "reactive extrusion-calendering process" at pilot plant-scale (maximum production capacity of 5 kg.h^{-1}).*

d) *Manufacturing of non-modified / surface-modified fumed silica reinforced PLA nanocomposites films using "reactive extrusion-calendering process" at pilot plant-scale (maximum production capacity of 5 kg.h^{-1}).*

e) *Investigation of the reaction, rheological, morphological, thermal, mechanical and fracture properties relationships in manufactured organically modified montmorillonite clay reinforced PLA nanocomposites sheets obtained at pre-industrial scale.*

f) *Investigation of the reaction, rheological, morphological, thermal, mechanical and fracture properties relationships in manufactured non-modified / surface-modified fumed silica reinforced PLA nanocomposites films obtained at pre-industrial scale.*

1.3 Specific objectives

In this work, the following specific objectives are listed below:

Step 1. Reactive processing at laboratory-scale (internal mixer, 50 g/batch) of PLA/o-MMT nanocomposites

- Evaluation of the effect of multi-functional epoxide agent and/or organically modified montmorillonite clay on the reaction profile of PLA nanocomposites.

Step 2. Reactive processing at pilot plant-scale (up to 5 kg.h^{-1}) of PLA/o-MMT nanocomposites

2.1) Modified PLA sheets reinforced with organically modified montmorillonite clay manufacturing via a "reactive extrusion calendering process"

- Preparation of PLA and modified PLA sheets reinforced with organically modified montmorillonite clay.

2.2) Physical-chemical characterization

- Determination of the molecular weight distribution (MWD)
- Characterization of reactivity between SAmfE and organically modified montmorillonite clay.

2.3) Rheological characterization

- Determination of the rheological master curves.
- Validation of the reaction between multi-functional epoxide agent and organically modified montmorillonite clay.
- Validation of dispersion of organically modified montmorillonite clay.

2.4) Morphological characterization

- Evaluation of dispersion of organically modified montmorillonite clay in PLA and modified PLA matrix.

2.5) Thermal characterization

- Standard calorimetric and thermo-mechanical evaluations (thermal transitions and degree of crystallinity).
- Influence of the organically modified montmorillonite clay on crystallization kinetics in non-isothermal and isothermal conditions.

2.6) Mechanical characterization

- Evaluation of the organically modified montmorillonite clay addition on the mechanical parameters under uniaxial tensile loading.

2.7) Fracture characterization

- Assessment of the fracture behaviour using essential work of fracture (EWF) of PLA and modified PLA reinforced with organically modified montmorillonite clay.
- Investigation of possible changes in the micromechanisms of deformation

Step 3. Reactive processing at laboratory-scale (internal mixer, 50 g/batch) of PLA/nano-SiO_2 composites

Evaluation of the effect of multi-functional epoxide agent and non-modified / surface-modified fumed silica on the reaction profile of PLA nanocomposites.

Step 4. Reactive processing at pilot plant-scale (up to 5 $kg.h^{-1}$) of PLA/nano-SiO_2 composites

4.1) Modified PLA films reinforced with non-modified / surface-modified fumed silica manufacturing via a "reactive extrusion calendering process"

- Preparation of modified PLA films reinforced with nano-SiO_2.

4.2) Physical-chemical characterization

- Characterization of reactivity between multi-functional epoxide agent and non-modified / surface-modified fumed silica.
- Determination of the intrinsic viscosities and estimation of molecular weight averages of PLA/nano-SiO2 composites.

4.3) Rheological characterization

- Determination of the rheological master curves.
- Validation of the reaction between multi-functional epoxide agent and non-modified / surface-modified fumed silica.

- Validation of dispersion of non-modified / surface-modified fumed silica.

4.4) Morphological characterization

- Evaluation of dispersion of non-modified / surface-modified fumed silica in modified PLA matrix.

4.5) Thermal characterization

- Standard calorimetric and thermo-mechanical evaluations (thermal transitions and degree of crystallinity)
- Influence of the non-modified / surface-modified fumed silica on crystallization kinetics in non-isothermal and isothermal conditions

4.6) Mechanical characterization

- Evaluation of the non-modified / surface-modified fumed silica addition on the mechanical parameters under uniaxial tensile loading.

4.7) Fracture characterization

- Assessment of the fracture behaviour using essential work of fracture (EWF) of modified PLA reinforced with non-modified / surface-modified fumed silica.
- Investigation of possible changes in the micromechanisms of deformation

Chapter 2. General State of Art

2.1 Overview on Polymer Nanocomposites

The significance of polymer nanocomposite technology is not based exclusively on the mechanical reinforcement of the neat resin or just merely a direct replacement of current micro-sized filler or blend technology. Rather, its appeal can be derived from imparting value-added properties that is unobtainable in the neat resin, without sacrificing the resin's inherent favourable processability, physical, mechanical properties and not at the expense of adding excessive weight (Zhang et al., 2006). Conventionally, producing "multifunctional" materials in terms of blend or composite impose compromises between desired performance, mechanical properties, cost, and processability. Nevertheless, repetitively, improved properties as compared to those of the pure polymers or conventional particulate composites have been reported for polymer nanocomposites containing substantially less filler (typically 1 – 5 vol. %) and thus enabling greater retention of the inherent processability of the neat resin (Ray and Easteal, 2007; Zhang et al., 2013).

2.2. Nanocomposites

Polymer nanocomposites is characteristically defined as two-phase systems that is made up of polymers and fillers of which at least one dimension is in the nano-range (1 - 100 nm) (Paul and Robeson, 2008; Ray and Easteal, 2007; Vaia and Giannelis, 2001). The nanofillers can be made up several geometries such one-dimensional nanotubes or nanofibers, two-dimensional clay platelets, or three-dimensional spherical particles (Kumar et al., 2009; Murariu et al., 2015). The advantages of nanoparticles are derived from its phenomenally high specific surface area, in which even at low concentrations, major effects on the macroscopic properties can be attained.

Over the past several years, polymer nanocomposites have attracted considerable interest in both academia and industry. However, one of the outstanding problems are to control the state of dispersion of the nanoparticles, which is highly determined by the preparation method. Therefore, different preparation methods for polymer nanocomposites will be discussed, followed by how this influences the state of dispersion. It is well established that particle dispersion critically affects nanocomposite properties, however, it is not apparent that a single state of particle spatial distribution should optimize any given macro scale properties. Depending on the system thermodynamics and preparation protocol, nanoparticles can aggregate, uniformly disperse or cluster (Jancar et al., 2010).

2.2.1. Dispersion degree

As stated above, the advantages of nanocomposites (or the nano-effect) can only be fully exploited if the degree of dispersion of the particles can be precisely controlled. For most properties (i.e. thermal, physical, mechanical etc.), a perfectly homogeneous dispersion usually yields positive improvements. However for improvements in electric conductivity properties, Halperin et al. (1985) and Sokolowska et al. (2013) suggested a percolating network of nanofillers is preferred which is achieved by controlled aggregation of the particles. Several factors linking to the mediocre performance of nanocomposites could have been attributed to the aggregation of particles including poor dispersion, ineffective inter-phase load transfer, process-related shortcomings, poor alignment (especially in the case of one-dimensional and two-dimensional nanofillers) and the fractal nature of filler clusters (Blaker et al., 2011).

The surface area of different filler geometry is also another key factor that predominantly influences the state of dispersion of nanoparticles (Schaefer and Justice, 2007). *Figure 1.1* shows idealized one-, two- and three-dimensional nanoparticles. Examples include one-dimensional montmorillonte clays, two-dimensional halloysite nanotubes and three-dimensional fumed silica spheres. Conventionally low-dimensional fillers (i.e. of one-dimensional and two-dimensional nanofillers) are more difficult to disperse than three-dimensional fillers. The specific surface area of nanofillers are also vastly diverse, going from the highest specific surface for single dimensional filler *e.g.* (about 725 $m^2.g^{-1}$ for exfoliated montmorillonite), the intermediate one for three dimensional filler (about 380 $m^2.g^{-1}$ for fumed silica), to the lowest one for two dimensional filler (above 60 $m^2.g^{-1}$ for halloysite nanotubes) (Murariu et al., 2015). Theoretically, higher surface area will likely augment the particle contact area making it ideal for an improved particle-matrix interactions. Given the aforementioned considerations, therefore one-dimensional sheets (*i.e.* o-MMT) and spherical particles (*i.e.* fumed silica) were chosen for this study.

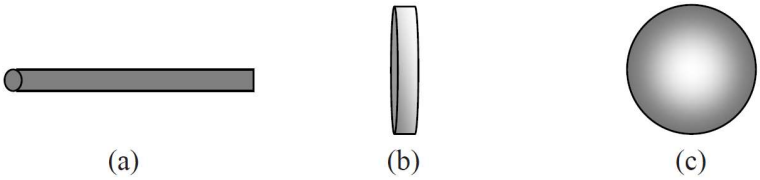

Figure 2.1. *Scheme of (a) one-dimensional, (b) two-dimensional and (c) three-dimensional nanoparticles (adapted from (Murariu et al., 2015)).*

In addition to the geometry of the nano filler, factors such as relative size of the nanoparticles to the polymer also affects the final state of dispersion of the nano filler. Mackay

et al. (2006) have state that if the radius of gyration, R_g of the linear polymer is greater than the radius of the nano-filler, the thermodynamic stability of the nanocomposite will be enhanced.

While Shen et al. (2008) added that if the radius of nano filler size is similar to the R_g of polymer, the nano filler will experience fast diffusion, and it will disperse through the polymer melts without necessarily waiting for chains to relax their conformations. However, if R_g of the polymer is smaller than the radius of the nano filler, the surface energy mismatch between the polymer chains and the nano filler would be higher, hence leading to aggregation of the nano filler (Mackay et al., 2006; Shen et al., 2008).

The polymer- nano filler interaction is another parameter that influences the final state of dispersion of nano filler within the polymer matrix. Another solution to suppress aggregation is by modifying the surface the nano particles (Bansal et al., 2005; Green and Mewis, 2006) . Even though this approach has been proven to be relatively successful in some cases, the nano particles can also self-assemble into highly anisotropic structures (Akcora et al., 2009). Although it is possible to decrease the probability of aggregation to a certain extent, it is extremely difficult to attain complete homogeneity. Various methods have been used for the determination of the heterogeneity of nanocomposites. The most frequently used and successful technique is electron microscopy. Other approaches include the analysis of particle characteristics, X-ray diffraction, and the measurement of composite properties.

2.3. Biodegradable Polymer Nanocomposites

The term biodegradable polymers can be defined as polymers that are able degrade and can be gradually be absorbed or eliminated by human body. This degradation can be induced

by either hydrolysis or chain scission caused by metabolic processes (Drumright et al., 2000; Sinha Ray, 2013a). Nevertheless, specific conditions in term of pH, humidity, oxygenation and the presence of some metals could also contribute to accelerate the rate of biodegradation of such polymers (Cheaburu-Yilmaz et al., 2015; Endres and Siebert-Raths, 2011). From the perspective of sustainability and environmental concerns, polymers derived from renewable biomass sources and also agricultural by-products that are completely degradable at the end of their useful life are considered as ideal for the development of bionanocomposites.

Lately, a several types of biobased polymers, such as thermoplastic starch, polylactide or poly(lactic acid) (PLA), chitosan, and poly(hydroxyl butyrate), have become commercially available. However, the most promising and extensively studied polymer in this field is PLA (Maiti et al., 2002; Rasal et al., 2010; Saeidlou et al., 2012). PLA is a thermoplastic polyester derived from renewable resources and is completely biodegradable and bioabsorbable (Endres and Siebert-Raths, 2011). Lactic acid (LA) is the most extensively produced carboxylic acid in nature, and the current industrial production of LA is based on the microbial fermentation of carbohydrates (Ghaffar et al., 2014).

In the last few years, massive research and development effort have been dedicated towards the hybrid organic-inorganic systems, especially given to those in which nanofillers are dispersed in a polymer matrix (Balazs et al., 1999; Mark, 2006; Sinha Ray and Okamoto, 2003b). This class of materials is called polymer nanocomposites and shows unique value-added properties that are completely absent in neat matrices and conventional composites. Researchers believe that the interaction between filler and matrix at a nanoscale level is the basis for new and novel properties of the nanocomposites as opposed to conventional composites (Bergaya et al., 2012; Giannelis, 1996; Winey and Vaia, 2007).

In recent years, special attention has been given to the benefits of polymer nanocomposite technology to improve the inherent properties of biopolymers (Hule and Pochan, 2007; Singh and Ray, 2007; Sinha Ray and Bousmina, 2005). The potential in the field of bionanocomposites is immense when considering the variety of biopolymers and potential nanoparticles available with the vast possibility of end-user applications. Recent opportunities to improve food quality and shelf life while reducing plastic waste have stimulated the exploration of new bionanocomposite-based packaging materials (Ahmed and Varshney, 2011; Sinha Ray et al., 2003a). The balanced mechanical properties, functionalities, and biocompatibility of bionanocomposites also provide an exciting platform for the design and fabrication of new materials for biomedical applications (Hule and Pochan, 2007; Pawar et al., 2014). In this regard, a number of exciting application concepts are currently under development, such as sutures, tissue engineering, drug delivery systems, and surgical implants, including architecturally fabricated stents that could replace conventional metallic ones.

2.4. Polylactide based Nanocomposites

There are numerous publications utilizing polylactide based nanocomposites with organically modified montmorillonite clay as reinforcement that has been extensively studied by numerous research group (Ahmed et al., 2010; Bocchini et al., 2010; Carrasco et al., 2011a; Carrasco et al., 2014; Castiello et al., 2012; Chow et al., 2014; Chow and Lok, 2009; Coiai et al., 2017; Duan et al., 2013; Gamez-Perez et al., 2011a; Jalalvandi et al., 2015; Kramschuster et al., 2007; Li et al., 2009; Liu et al., 2015; Liu et al., 2013; Maiti et al., 2002; Maspoch et al., 2015; Meng et al., 2012; Nam et al., 2003; Neppalli et al., 2014; Nieddu et al., 2009; Ogata et al., 1997; Olewnik and Richert, 2014; Ortenzi et al., 2015; Papageorgiou et al., 2010; Picard et

al., 2011; Sabatini et al., 2015; Saiter et al., 2016; Sinha Ray and Okamoto, 2003a; Vasanthan et al., 2011; Wu et al., 2009; Zou et al., 2012).

However, Ogata et al. (1997) reported the first PLA-clay nanocomposite in 1997 prepared using chloroform as a solvent. The montmorillonite clay was modified with distearyl-dimethylammonium chloride (DSAC). The paper reported that inadequate dispersion of clay in the PLA matrix by this method, which was evidenced by presence of clay tactoids, which comprise of several stacks monolayer of clay platelets per tactoid. It was also reported that a slight improvement in the Young's modulus of PLA-clay nanocomposites were observed. This result was chiefly attributed to an absence of intercalation geometry in PLA-clay nanocomposites.

The first successful preparation of intercalated PLA-layered silicate nanocomposites was reported by Sinha Ray et al.(2003b). The paper reported the melt extrusion of PLA and dimethyl dioctadecyl ammonium ions modified montmorillonite clay (C_{18}-MMT) to prepare the nanocomposite. The nanocomposites had clay loadings of 2, 3 and 4.8 wt.% of C_{18}-MMT clay while the role of oligo-(ε-caprolactone) (o-PCL) as a compatibilizer in a PLA/clay nanocomposite was also investigated. The presence of a compatibilizer (0.2 to 3 wt. %) improved the mechanical properties of nanocomposite to a great extent. The hydroxyl functional compatibilizers helped in generation of a flocculated clay structure by enhancing hydroxylated edge-edge interaction of the silicate layers. The PLA/layered silicate nanocomposites exhibited improved material properties in both solid and melt states as compared to the PLA matrix without clay.

Subsequently, Sinha Ray et al. (2003a) also studied the melt rheology of the PLA-clay nanocomposites prepared. The master curves of storage moduli (*G'(ω))* and loss modului *(G"(ω))* for nanocomposites displayed considerably lower terminal region slope values of *G'(ω)* and *G"(ω)* as compared to neat PLA. The nanocomposite with high C_{18}-MMT content also exhibited near shear independency of *G'(ω)* and *G"(ω)* values in lower temperature dependence angular frequency ($a_T\omega$) regime. This observation was defined by the author as having characteristics of material exhibiting a pseudo-solid-like behavior. This is mainly attributed to the formation of a spatially-linked structure of clay platelets in PLA matrix which caused the preventive relaxation of PLA chain occurring due to the high geometric constraints or physical jamming of PLA polymer chains. The flow activation energy and complex viscosity of PLA also increased in the presence of C_{18}-MMT clay. An important observation from this work was the tendency of PLA-clay nanocomposites to show strain-induced hardening behavior under uniaxial elongation flow.

Maspoch et al. (2015) analyzed the ductile-brittle transition behaviour of organo-modified montmorillonite-based Poly(lactic acid) films (PLA/o-MMT) using the essential work of fracture (EWF) methodology and enthalpy relaxation analysis. It was reported that presence of organo-modified montmorillonite improved the fracture parameters of PLA nanocomposites. Increasing the o-MMT amount commensurately increased the fracture parameters especially for the non-essential term (βw_p) which is commonly associated to the crack propagation resistance. The rate of enthalpy relaxation (β_H), associated to the physical aging kinetics shows that physical aging at 30°C of PLA/o-MMT samples exhibited slower enthalpy relaxation kinetics as compared to the pristine polymer.

Additionally, there are several papers that worked with PLA/organically modified montmorillonite clay nanocomposites and utilizes multifunctional epoxy compounds with a trade name of Joncryl® as chain extender (Al-Itry et al., 2012; Meng et al., 2012; Najafi et al., 2012a; Najafi et al., 2013). Joncryl® (BASF Corporation) is a glycidyl methacrylate-based copolymer generally obtained by free-radical copolymerization known for its efficiency to create branched structures. Meng et al. (2012) prepared PLA nanocomposites reinforced with two types of organically modified montmorillonite clay (*i.e.* Cloisite® 30B and Nanomer® I.34TCN) and Joncryl® ADR-4368 as chain extender. A substantial increase of PLA matrix's molecular weight was observed with the addition of 0.5 wt.% Joncryl®. Using H^1-NMR analysis, Meng and co-workers have confirmed that the molecular structure of PLA and PLA-based nanocomposites were also changed from linear to a branched or cross-linked structure depending on Joncryl® loading and processing temperature. It was also stated that incorporation of Joncryl® does not impair the clay dispersion in the PLA nanocomposites. However, due to the possible reaction of Joncryl® epoxy groups with the hydroxyl groups in the organo-modifier of montmorillonite clay and the more severe thermal degradation resulting from the addition of organically modified montmorillonite clay, the increase of molecular weight for the PLA-based nanocomposites is less spectacular than PLA modified Joncryl® with alone.

Najafi et al. (2013) have investigated the effect of organically modified montmorillonite clay (*i.e.* Cloisite® 30B) and Joncryl® ADR-4368 as chain extender on the non-isothermal, isothermal crystallization kinetics, and morphology of PLA-based nanocomposites. It was reported that the organically modified montmorillonite clay particles were found to act as nucleating agents and yield a faster overall rate of crystallization. Joncryl incorporation, however, confined the crystallization process due to the formation of a long-chain branching

(LCB) structure, resulting in the disruption of chain packing. Therefore, the degree of crystallinity and the rate of crystallization decreased, while the cold-crystallization temperature was dramatically increased in non-isothermal crystallization.

Likewise, a lot of publications have been widely reported on PLA/silica nanocomposites preparation and properties (Basilissi et al., 2013a; Chang et al., 2015; Dorigato et al., 2012; Fukushima et al., 2011; Gong et al., 2014; Lai and Hsieh, 2016; Murariu et al., 2015; Pilić et al., 2015; Wang et al., 2006; Wang et al., 2008a; Wen et al., 2009; Wen et al., 2011; Yan et al., 2007b; Zhang et al., 2008a; Zhu et al., 2010). For instance, Yan et al. (2007b) initially prepared nanosilica grafted with lactic acid prior to the modified silica being melt blended with PLA matrix to enhance the interfacial interactions. It was observed that the elongation at break of the nanocomposites were increased up to 8 times. Subsequently, Yan et al. (2007a) also studied the structural characteristics and thermal properties of plasticized poly(L-lactide)-silica nanocomposites synthesized by a sol-gel method and pointed out a great extent of improvement in tensile strength with a small amount of silica.

Zhu et al. (2010) reported that 1 wt.% of oleic acid-modified silica could enhance the flexibility of PLA up to 3.2 times in their prepared PLA/modified SiO_2 nanocomposites. The steady-state viscosity was successfully utilized to probe the aggregation of PLA nanocomposites up to 5 wt.% modified silica content. As expected, the presence nanosilica increases the viscosity of the melt. It was reported that concentration of nanosilica up to 3 wt.% modified silica content will perturbed the normal flow of the PLA and hindered the mobility of the chain segments in the direction of flow. However, increasing the amount of nanosilica does not further increase viscosity. Basilissi et al. (2013a; 2013b) prepared PLA nanocomposites using self-synthesized PLA by bulk ring opening polymerization.

It was reported the highest complex viscosity value of PLA nanocomposites were using an unmodified nanosilica compared to silane-modified nanosilica. Presence of hydrogen bonds between -Si-OH groups of silica and -C=O groups of PLA have been pointed out as fundamental factor to this trend. Dorigato et al. (2012) investigated thermo-mechanical and optical properties of PLA-based nanocomposites reinforced with non-treated and surface treated nanosilica. Results from this work suggested that the higher surface area of untreated nanosilica at resulted to be effective at increasing elastic modulus due to the extended filler–matrix interaction, while the finer dispersion of silica aggregates at the nanoscale obtained with surface treated nanoparticles led to noticeable improvements of the tensile properties at yield and at break, both under quasi-static and impact conditions. It was also observed that the fracture toughness and the creep stability were substantially enhanced by nanosilica addition.

Murariu et al. (2015) have investigated the effect of organically modified montmorillonite clay (*i.e.* Cloisite® 25A), high surface fumed silica (*i.e.* CAB-O-SIL H5) as reinforcing nanofillers and ethylene bis-stearamide (EBS) as plasticizer on the thermal properties under heating, isothermal and non-isothermal conditions of PLA-based nanocomposites. It was reported that both montmorillonite clay and fumed silica especially EBS treated ones behave as remarkable nucleating agents and could promote the PLA crystallization. It was especially evident in the half-time crystallization of PLA/fumed silica nanocomposites under isothermal conditions was reduced to 1.5 minutes only compared to 52 minutes for PLA neat. Crystallinity percentage of PLA neat were also significantly increased from 6 to 28% and 35% with the addition of montmorillonite clay and fumed silica respectively.

The preparation methods, nanofiller concentration and type of surface modification are three important factors in order to optimize the properties of PLA nanocomposites. A literature survey of the main processing conditions and results of PLA nanocomposites reinforced with either montmorillonite clay or fumed silica are listed in *table 2.1.*

Table 2.1. *Summary of preparation methods of either montmorillonite clay or fumed silica reinforced PLA-based nanocomposites with the corresponding results.*

Authors (Year)	Main objective	PLA Grades and Type of fumed silica *[supplier]*	Preparation Summary	Summary of Observations
Zhang et al. (2008)	Thermal Properties of poly(lactic acid) fumed silica nanocomposites: Experiments and molecular dynamics simulations	PLA 4060D *[NatureWorks]* Fumed silica (Cab-O-Sil TS530) *[Cabot Corp]*	Brabender twin screw extruder mixer -All nanofillers and PLA were melt compounded by Brabender twin screw extruder at 2 wt. % of filler loading. (L/D ratio: 20) -temperature: 170 °C (feeding zone to die) -screw rotation speed:20 rpm.	-An increase of 2°C in the T_g and 12°C improvement of thermal stability were observed for PLA–silica nanocomposites as compared to the neat PLA. -Molecular dynamics simulation revealed that the radii of gyration of PLA chains around the nanoparticle decreased because the polymers were bended and compressed when they attach to the smaller nanoparticle. The shear viscosity also increased when PLA chains approached the surface of the nanoparticle.
Zhu et al. (2010)	Preparation and Properties of Polylactide–Silica Nanocomposites	PLA Biomer L9000 *[Biomer Inc.]* Unmodified fumed silica *[Nanjing University of Technology]*	Fumed Silica Modification - Modified fumed silica ($OA–SiO_2$) were prepared by grafting oleic acid on the surface of unmodified fumed silica. Haake melt mixer - Modified fumed silica, unmodified fumed silica and polylactide were mixed in a HAAKE Rheocord 90 at 0.5, 1 and 3.0 wt. % of filler loading. -screw rotation speed :60 rpm -temperature:165°C -blending time: 10 min.	-Thermal characterization shows that a decrease in T_g was observed attributed to the plastication of $OA–SiO_2$ nanoparticles on the PLA chains. Crystallization of PLA nanocomposites also was enhanced with addition of $OA–SiO_2$ nanoparticles especially at filler loading higher than 0.5 wt. %. -Rheological analysis shows that the viscosity of the PLA nanocomposites increased with increasing silica content especially at 5 wt. % silica loading. It was concluded that higher order structure (a filler–network structure) was present in the PLA nanocomposite. -Mechanical characterization reveal that the elongation at break increased significantly at the expense of tensile strength with addition of $OA–SiO_2$ nanoparticles.

Authors (Year)	**Main objective**	**PLA Grades and Nanofiller type *[supplier]***	**Preparation Summary**	**Summary of Observations**
Papageorgiou et al. (2010)	PLA nanocomposites: Effect of filler type on non-isothermal crystallization	PLA Resorbaid® *[Cousin Biotech]* Fumed silica (Aerosil 200) *[Degussa AG]* Montmorillonite (Cloisite 20) *[Southern Clay Products Inc.]*	<u>Solution Film Casting</u> -PLA was dissolved using a mixture of dichloromethane /tetrahydrofuran 50/50 (w/w). Different nanofillers were dispersed in the solution at 2.5 wt. % of filler loading -temperature: room temperature - stirring: 1 hour. -sonication: 1 hour. -drying time: 3 days (vacuum)	-Morphological examination shows homogeneous dispersion of fumed silica was achieved with aggregates with sizes of less than 100 nm. -Dynamic mechanical analysis revealed highest storage modulus of PLA/fumed silica nanocomposites due to probable hydrogen bonding interaction. -Non-isothermal crystallizations study revealed changes in crystallization mechanism of PLA nanocomposites due to heterogeneous nucleation caused by fumed silica particles. Effective activation energy computed was also lowest for PLA/fumed silica nanocomposites.
Bocchini et al. (2010)	Polylactic Acid and Polylactic Acid-Based Nanocomposite Photooxidation	PLA 2002D *[NatureWorks]* Montmorillonite (Cloisite 20) *[Southern Clay Products Inc.]* Hydrophilic fumed silica, HDKN20 *[Wacker S.A.]*	<u>Microextruder Melt mixer</u> -All fillers and PLA were melt blended using Microextruder DSM Micro 15CC Twin Screw Compounder at wt. 5% filler loading -screw rotation speed :100 rpm -temperature:180°C -blending time: 5 min. -N_2 atmosphere	-Morphological examination shows homogeneous dispersion of fumed silica was achieved despite some residual aggregates by about 3-10 μm were observed on the sample surface. -Photo oxidation analysis shows PLA/fumed silica nanocomposites low photooxidation rate, having a low absorbance in the UV and visible range and no metal impurities compared to PLA/MMT nanocomposites. This makes PLA/fumed silica nanocomposites an excellent material for outdoor applications.

Authors (Year)	Main objective	PLA Grades and Type of fumed silica *[supplier]*	Preparation Summary	Summary of Observations
Wen et al. (2011)	Study of the thermal stabilization mechanism of biodegradable poly(L-lactide)/silica nanocomposites	PLA 4032D *[NatureWorks]* Fumed silica (Aerosil 200) *[Degussa AG]*	Haake melt mixer - Fumed silica and polylactide were mixed in a HAAKE Rheomix 600 at 1, 3, 5, 7 and 10 wt. % of filler loading. -screw rotation speed :60 rpm -temperature:175°C -blending time: 5 min.	- The incorporation of fumed silica in a polymer matrix has been found to enhance thermal stability. Thermal decomposition for the PLA nanocomposites shifts to a higher temperature range than that for neat PLA and the decomposition temperature increase commensurate with the silica content. -Rheological test shows neat PLA displays a pseudo-newtonian behaviour in the low-frequency range while PLA nanocomposites show a higher complex viscosity and a more pronounced shear thinning behaviour with increasing silica loading. The solid-like viscoelastic response results of PLA nanocomposites is attributed to the formation of a percolation network at higher silica loading (i.e. 7 and 10 wt. %) due to the confinement effect of nanofillers on the motion of polymer chains. -SEM micrographs shows that all silica nanoparticles are uniformly distributed in the PLA matrix except for a few aggregates at below 5 wt %. filler loading. However, silica agglomeration was evident at silica filler loading greater than 7 wt. %.
Fukushima et al. (2011)	Preparation, characterization and biodegradation of biopolymer nanocomposites based on fumed silica	PLA 4042D *[NatureWorks]* 3 types of fumed silica (HDK D05, HDK C10 and HDK N20) *[Wacker S.A.]*	Brabender melt mixer -All fumed silica nanofillers and PLA were melt compounded using Rheomix Brabender OHG 47055 at 5 wt. % of filler loading. -screw rotation speed :60 rpm -temperature:165°C -blending time: 5 min.	-Morphological examination shows homogeneous dispersion of fumed silica was achieved with aggregates with sizes of less than 100 nm for PLA/HDK N20 nanocomposites. -DSC revealed decrease of ΔH_{cc}, ΔH_m and T_{cc} for all PLA/silica nanocomposites while T_g were slightly increased. It is mainly attributed to the restricted polymer chain movements after addition of nanosilica. -Biodegradation studies indicate that presence of silica slows the nanocomposites degradation rate compared to neat PLA.

Authors (Year)	**Main objective**	**PLA Grades and Nanofiller type *[supplier]***	**Preparation Summary**	**Summary of Observations**
Dorigato et al. (2012)	Effect of Silica Nanoparticle on the Mechanical Performance of Poly(Lactic Acid)	PLA PLE 005 *[NaturePlast]* Aerosil 90, Aerosil 200 and Aerosil 380 are unmodified fumed silica *[Evonik]* while Aerosil R805 and Aerosil R816 are modified with octylsilane and hexadecylsilane respectively *[Evonik]*	<u>Haake melt mixer</u> -All fumed silica nanofillers and PLA were melt compounded in PolyLab Rheomix R600 at 2 wt. % of filler loading -screw rotation speed :90 rpm -temperature:160 ˚C -blending time: 10 min.	-The addition of unmodified and surface-modified fumed silica nanoparticles does not significantly affect thermal properties PLA nanocomposites. It also does not show any appreciable nucleating effect on the polymeric matrix. - Unmodified fumed silica induces a slight decrease of strain at break while surface modified silica slightly enhances the elongation at break of PLA nanocomposites. -Modified fumed silica leads to formation of silica aggregates with lower dimensions and improvement of dispersibility compared to unmodified ones. Presence of organosilane on the surface of the modified fumed silica was attributed to a lowering of the inter-particle attractive forces.
Khankrua et al. (2013)	Thermal and Mechanical Properties of Biodegradable polyester/silica Nanocomposites	PLA2003D *[NatureWorks]* Fumed silica (Aerosil A200) *[Degussa AG]*	<u>Extrusion</u> PLA were dry-mixed with silica at content from 0.1, 0.2, 0.5, 1.0, 2.5 and 5.0 wt.%. Then, it was extruded using twin screw extruder (SHJ-25) -temperature: 150 to 170 °C (feeding zone to die) -screw rotation speed:60 rpm.	- SEM micrographs revealed that homogeneous dispersion of fumed silica was achieved up to 0.1-0.5 wt. %. At higher than 0.5 wt. %. silica loading, 100 to 200 nm sized agglomerates can be observed. - Improvement of mechanical properties of PLA/fumed silica nanocomposites were observed up to 0.5 wt. % silica loading. Modulus and elongation at break commensurately decrease at silica loading greater than 0.5 wt. %. - No significant improvement on the heat deflection temperature value of PLA/fumed silica nanocomposites were observed.

Authors (Year)	Main objective	PLA Grades and Nanofiller type *[supplier]*	Preparation Summary	Summary of Observations
Lai et al. (2013)	Preparation and Properties of Melt-Blended Polylactic Acid/ Polyethylene Glycol-Modified Silica Nanocomposite	PLA 4060D *[NatureWorks]* Unmodified fumed silica (Aerosil A200) *[Evonik]*	<u>Fumed silica modification</u> - GPS-Silica was prepared by grafting γ-glycidoxypropyl-trimethoxy silane (GPS) on the surface of fumed silica. -temperature: 70°C - stirring: 1 hour. -sonication: 30 minutes. -drying time: 1 day (vacuum) - mPEG-Silica was prepared by grafting Methoxy Poly-ethylene glycol (mPEG) on the surface of fumed silica. -temperature: -10°C - stirring: 45 minutes. -sonication: 30 minutes. -drying time: 1 day (vacuum) <u>Brabender melt mixer</u> -All nanofillers and PLA were melt compounded in Brabender 815605 at 1, 4 and 10 wt. % of filler loading. -screw rotation speed :80 rpm -temperature:160°C -blending time: 10 min.	- ^{13}C NMR and FTIR characterizations shows that both GPS and mPEG were successfully grafted onto surface of nanosilica. -TEM images revealed dispersion degree of modified silica appeared to be slightly improved over non-modified ones. However the difference was very limited. -DSC revealed slight shift of T_g to lower temperature for PLA/mPEG-silica nanocomposites. It is mainly attributed to the enhanced segmental mobility of PLA chains due to mPEG plasticizer. No noticeable difference in thermal properties observed for other PLA nanocomposites prepared. -Mechanical properties were most improved with PLA/unmodified silica nanocomposites at 10 wt. % loading. Mechanical properties of PLA nanocomposites with modified silica were lower than neat PLA to the plasticizing effect of surface modifier.

Authors (Year)	**Main objective**	**PLA Grades and Nanofiller type *[supplier]***	**Preparation Summary**	**Summary of Observations**
Qian et al. (2013)	Aluminated mesoporous silica as novel high-effective flame retardant in polylactide	PLA 3251D *[NatureWorks]* Unmodified fumed silica, SBA-15 without surface organo-modification *[Anhui Jingye Nanotechnology Co.]*	Fumed Silica Modification - Modified flame retardant fumed silica (Al-SBA-15) of aluminumisopropoxide on the surface of unmodified fumed silica (SBA-15). Haake melt mixer - Al-SBA-15, SBA-15 and polylactide were mixed in a HAAKE Rheocord 90 at 0, 0.2, 0.5 and 1.0 wt. % of filler loading. -screw rotation speed :60 rpm -temperature:165°C -blending time: 10 min.	-Flame retardancy properties of polylactide were significantly improved by Al-SBA-15. - Fumed silica presence increased T_g of PLA composites, showing they hindered the molecule movement. -Unmodifed fumed silica accelerated hydrolytic degradation process of PLA. Modifed fumed silica retarded the hydrolysis degradation of PLA due to hydrophobicity of additives improved the hydrolysis resistance of PLA and the terminal groups of PLA might be trapped in the mesoporous structure of Al-SBA-15, reducing the self-catalysis hydrolytic degradation process of PLA.
Gong et al. (2014)	Synergistic effect of fumed silica with Ni_2O_3 on improving flame retardancy of poly(lactic acid)	PLA 4032D *[NatureWorks]* Fumed silica (Aerosil 200) *[Degussa AG]*	Haake melt mixer -All fumed silica nanofillers, nickel peroxide (Ni_2O_3) and PLA were melt compounded in PolyLab Rheomix R600 at 1, 3 and 5 wt. % of filler loading while Ni_2O_3 loading was fixed at 5 wt. %. -screw rotation speed :100 rpm -temperature:180 °C -blending time: 10 min.	-Morphological examination shows homogeneous dispersion of fumed silica was achieved with agglomerates between 200 – 300 nm for PLA/fumed silica nanocomposites. -Cone calorimeter analysis reveals that the presence of silica improve the flame retardancy of PLA. It acted as an insulating barrier to prohibit the oxygen and feedback of heat from reaching the underlying substrate. -Rheological study revealed that neat PLA displays a pseudo-newtonian behaviour in the low-frequency range while PLA nanocomposites show a higher complex viscosity and a more pronounced shear thinning behaviour with 5 wt. % silica loading. The solid-like viscoelastic response results of PLA nanocomposites is attributed to the probable percolation network at 5 wt. % silica loading.

Authors (Year)	Main objective	PLA Grades and Nanofiller type *[supplier]*	Preparation Summary	Summary of Observations
Murariu et al. (2015)	Recent advances in production of poly(lactic acid) (PLA) nanocomposite: a versatile-method to tune crystallization properties of PLA	PLA 4032D *[NatureWorks]* Fumed Silica (Cab-O-Sil H5) *[Cabot Corp]* Cloisite 25A *[Southern Clay Products Inc.]*	<u>Nanofiller modification</u> - Modified nanofillers was prepared by "dry-coating" nanofillers with N,N'- Ethylene bis(stearamide) using a laboratory Rondol turbo-mixer. -mixing volume: n.s. -screw rotation speed :100 rpm -temperature:160°C -blending time: 10 min. <u>Brabender melt mixer</u> -All nanofillers and PLA were melt compounded by Brabender bench scale kneader (model 50 EHT) at 3 wt. % of filler loading. -screw rotation speed :70 rpm -temperature:165°C -blending time: 10 min.	-Morphological examination shows homogeneous dispersion of fumed silica was achieved with aggregates lower than 100 nm for PLA/fumed silica nanocomposites. The presence of strong particle-particle interactions due to high concentration of silanol groups show strong self-networking ability and therefore it is more difficult to break the big aggregates during the melt-blending process. -DSC revealed no significant modifications of T_g for PLA nanocomposites. However, isothermal crystallization analysis revealed increased degree of crystallinity achieved especially in PLA/silica nanocomposites compared to neat PLA. -Mechanical test of PLA nanocomposites with modified nanofillers shows slight improvements of rigidity and impact resistance compared to neat PLA.

2.5. Crystallization in Polymer

Crystallization of polymers is a process associated with alignment of their molecular chains. These chains fold together and form ordered regions called lamellae, which composes of larger spheroidal structures named spherulites. It is very well known that most polymer crystallization happened under conditions that is far removed from equilibrium. This could be generally credited to the considerably long chain length of the polymer, that could have constrained these chains from disentangling from one another in melt state. Ultimately, these will impede these chains from achieving regular conformation and aligning itself parallel to each other and forming an ordered crystal structure. Due to this, only a fraction of the polymer chains are transformed into crystals under such conditions of restraint.

Further introduction of polymer structural irregularities such as branch points, copolymerized units, cross-links, end-groups, or atactic segments etc. could reduce the ability of chains to re-order for formation of stable crystals and thereby suppressing crystallization. Thus, it is implied that the presence of such polymer structural irregularities influenced the mechanism of crystallization and subsequently the nature of crystals formed. There are several different types of crystal morphologies and several theories have been developed with the aim of understanding the crystallization mechanism of the polymers.

2.5.1. Semi-crystalline Polymer Models

2.5.1.1. Fringed micelle Model

The earliest concept of morphological models of semi-crystalline polymers structure was the concept of the fringed micelle model (Flory, 1954). This model is based on inter-related long molecules, small crystals which constitutes the crystalline region interspersed in a sea of

amorphous materials (Bower, 2002). The model suggests the occurrence of fibrillar crystallites, which can grow both parallel and perpendicular to the chain axes in the crystalline regions while the amorphous regions are made up of disordered chain conformations. Each chain typically passes through several crystallites and small crystallites can thus be reconciled with long chains as shown in *figure 2.2.*

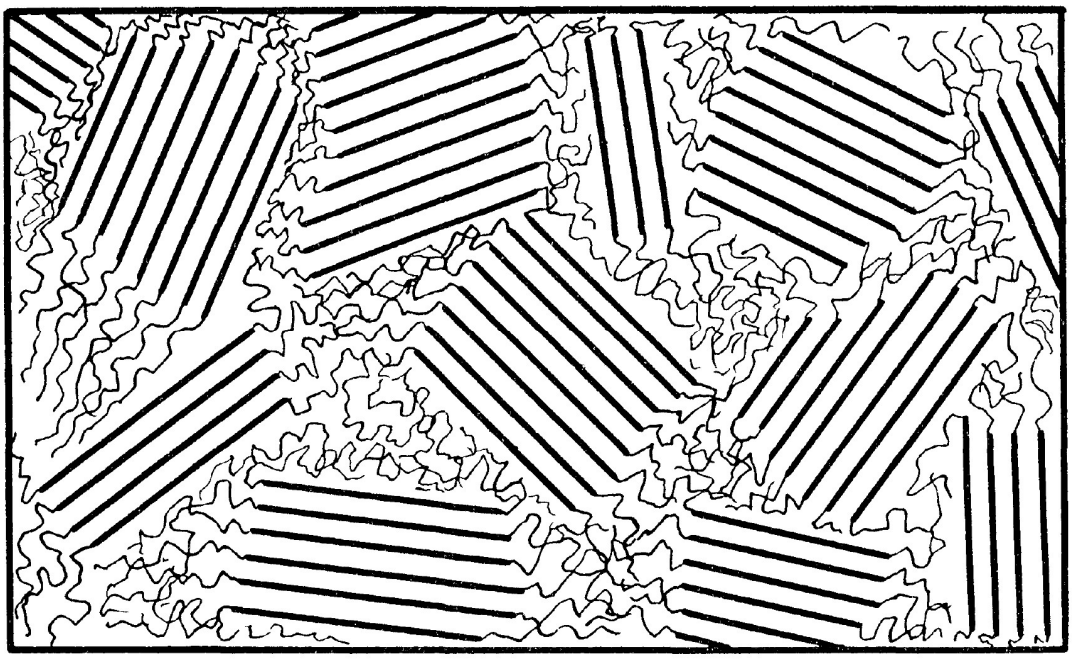

Figure 2.2. *The fringed-micelle model for semi-crystalline polymers (adopted from (Flory, 1954)).*

The fringed micelle model helps elucidate the dissipation of molecular order from the crystalline to the amorphous regions. It also clarifies the mechanical properties of the samples based on the physical linkages (fringes) between the two regions. However, it is incapable of providing an insight on the morphological features such as spherulites and its association with melt crystallized polymers.

2.5.1.2. Chain Folding Model

The idea of chain-folding in polymer crystals was first discussed by Storks (1938) in his analysis of electron diffraction data on gutta percha films (a natural rubber trans-polyisoprene).It was proposed that the chains of semi-crystalline trans(polyisoprene) had to fold back and forth. However, it was inconceivable at that time because the lamellar crystals have not yet been recognized as a native structure. This idea lay dormant until the early 1950s. Subsequently, Keller (1957), Till (1957) and Fischer (1957) had reported that polyethylene single crystals grown from dilute solution were in the form of intertwining fibrils or lamellae that were regularly shaped when viewed under an electron microscope. These lamellae observed were reported to have thicknesses of approximately 10 nm and lateral dimensions of several microns. The chain axes were parallel to the thickness direction of these lamellar crystals and given the extended length of a polymer chain, it was proposed that a chain must traverse a given crystallite many times to conform. This led to the concept of chain folding in semi-crystalline polymers. Keller (1968) further suggested that that the chains traversing a crystallite re-entered the crystallite at adjacent positions by means of hairpin-like bends. This findings is further reinforced by Patil and Reneker (1994) findings using atomic force microscopy in which adjacent re-entry or regularly chain-folded structure has been predominant in crystallizations from dilute solutions and is schematically depicted in *figure 2.3 (a)*.

However, Flory (1962) has disputed the adjacent re-entry model proposed by Keller. It was proposed that due to the spatial requirements for the growing crystals, only less than half of the chains emanating from the lamellar crystal surface can be accommodated by the neighbouring disordered amorphous phase. Consequently, more than half of these chain sequences will return to the crystal face from which it originated. This re-entry transpires via

chain loops of varying lengths present in between the crystallite and the amorphous regions. However, chains that do not re-enter a vicinal crystallite will abandon the basal plane of the crystal to be converted into disordered amorphous region. Alternatively, these chains could eventually enter an adjacent crystallite. Such a possibility of chain folding often referred to as the "switchboard model" is schematically illustrated in *figure 2.3 (b)*. The proportions between disordered amorphous and ordered crystalline regions in a semi-crystalline polymer are contingent upon crystallization conditions, molecular weight and presence of chain defects and/or irregularities.

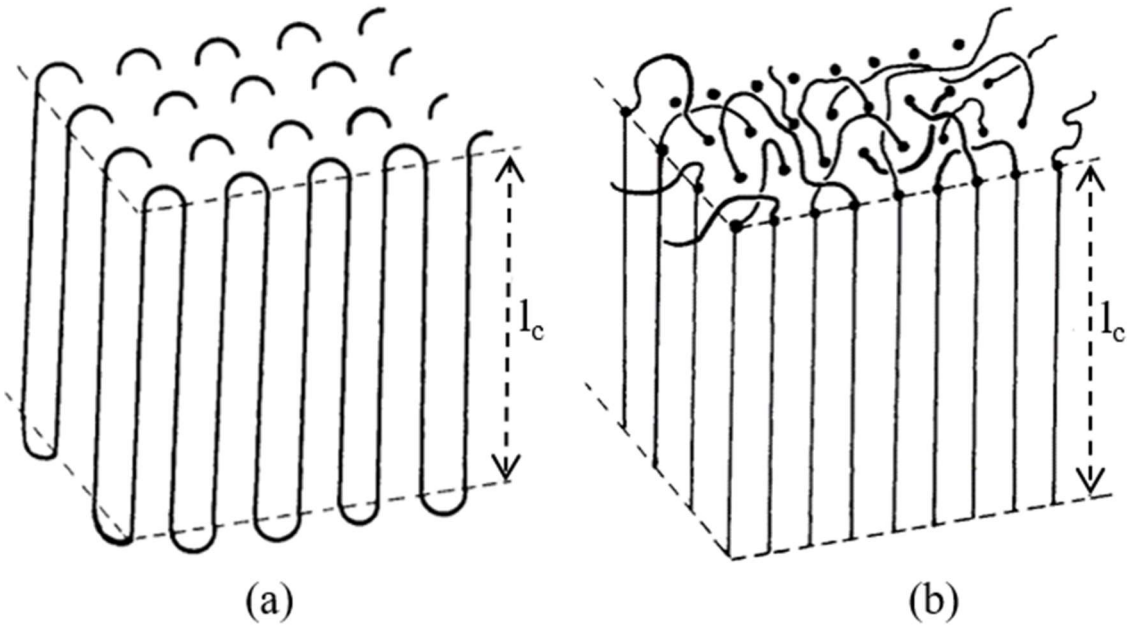

Figure 2.3. *Lamellar crystallite with (a) regularly folded lamellar crystal with thickness (l_c) model versus (b) irregular "switchboard" lamellar crystal with thickness (l_c) model (adapted from (Flory, 1962)).*

However, Flory (1962) does concede that due to the scarcity of polymer in a dilute solution, and the greater mobility of chain rearrangement, orderly development of successive folded array is the most stable state for a crystallite in solution as opposed to deposition of

sequences at the kink in a given outer layer anticipated for melt crystallization. Thus, there is no ambiguity that chain folding in the crystallization of polymers from dilute solutions is highly regular, conforming closely to Keller's model. However, chain folding in melt crystallization may be between the extremes of a regularly folded arrangement and a random "switchboard" arrangement. However, the precise ratio is highly governed by factors such as molecular weight, crystallization conditions and the flexibility of polymer chains.

2.5.2. Morphology of Semi-Crystalline Polymer

It was aforementioned that the principal crystalline unit in a melt-crystallized linear polymer is ordinarily a thin chain-folded lamella similar in general character to a single crystal when crystallized using very dilute solutions. These crystals will possess thicknesses of approximately 100 Å and lateral dimensions of several microns (Keller, 1957; Keller, 1968; Till, 1957). Nonetheless, the formation of these crystals are heavily influenced by the type and concentration of solvent used as well as crystallization conditions (Flory, 1962). However, if the polymer concentration is increased to more than 0.1% w/v, multi-lamellar structures such as lamellar stacks, sheaves etc. may emerged (Abe et al., 2000).

Predominantly, highly crystallizable, flexible linear polymers that crystallize from melt often leads to lamellae aggregating together in the form of a complex spherical structures called spherulites. Spherulites may be viewed as spherical aggregates of lamellae that originate from a common center and radiate outwards as shown in *figure 2.4*.

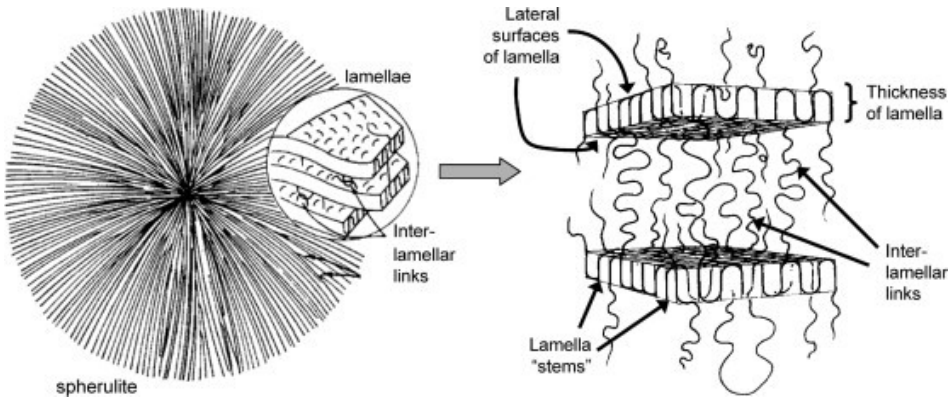

Figure 2.4. *Schematic illustration of spherulite, lamella, and amorphous phase structures. Adopted from (Cheng et al., 2011; Hoffman et al., 1976)*

Spherulite comprises of chain-folded lamellae radiating from solitary central point. Polymer chain axes in lamallae are more or less perpendicular to radius of spherulite. Branching causes spherulite to become spherical in shape after sufficient growth. Spherulites dimensions are typically of the order of microns and sometimes, even millimeters. The spherulites will continue to grow radially until it has fully impinged on each other. Measurement of the growth rate until the time of impingement will impart valuable information regarding the mechanism of crystallization in the polymer, and has been the focus of several research groups.

2.6 Polymer Rheology

2.6.1. Introduction

The term "Rheology" was introduced by Professor Eugene Cook Bingham was a professor and head of the department of chemistry at Lafayette College, Indiana. He defined it as study of deformation and flow of matter, especially in the non-Newtonian flow of liquids and the plastic flow of solids. Eventually, the term was widely accepted in 1929 and subsequently the American Society of Rheology was established. Polymeric materials are made of very long chain-like macromolecules which made it dissimilar from other conventional materials such as metals or ceramics. This causes complexity in the rheological behaviour in the molten state.

Polymeric materials are subjected myriad forms of stress and undergoes flow and other deformations during processing and during performance. However, polymer rheology also are highly dependent on the nature of the polymer since each polymeric materials possess its own rheological attributes. There are numerous different grades of commercial polymers that are on the market and possess an assortment of process characterizations, even if it belongs from the same base polymer. Hence, polymer rheology study is important for understanding and determining melt processability of polymers as well as the physical properties of the end products (Barnes, 1989; Han, 2007) .

Generally, there are two physical laws that can be used to describe the relationship between shear stress and deformation or rate of deformation. The first is Hooke's Law, which defines the rheological behaviour of the elastic solid. It states that the applied elastic shear stress, τ is proportional to the strain, γ and the proportionality constant is the shear modulus, G.

When the shear stress-shear strain is plotted in a diagram, an ideal elastic behaviour is represented by a straight line with a constant slope of magnitude G which is represented in *equation 2.1*.

$$\tau = G\gamma \tag{2.1}$$

The elastic behaviour is represented by this spring diagram. When a constant load is applied to the spring it deforms, and after releasing the load, the spring instantaneously returns to its initial position as illustrated in *figure 2.5.*

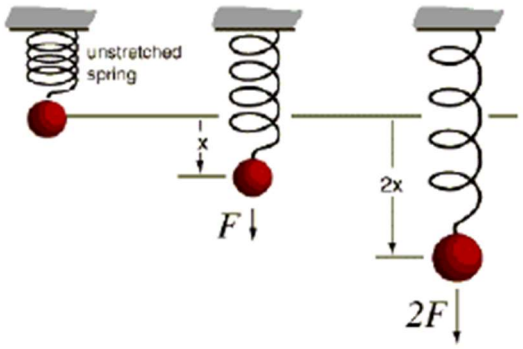

Figure 2.5. *Spring model for ideal elastic behaviour*

On the other hand, Newton's law applies to a viscous fluid such as low molecular weight liquids and solutions, e.g. water, solvents, silicon oils and blood plasma, where the shear stress, τ is directly proportional to the strain rate, $\dot{\gamma}$ which is represented in *equation 2.2*.

$$\tau = \eta\dot{\gamma} \tag{2.2}$$

The fluid viscosity, η is a material constant and are independent from the deformation rate. Th This viscous behaviour could explained using a diagram depicting a dashpot piston that is immersed in oil inside a cylinder. When a constant load is applied, the piston moves

continuously, and after releasing the load, the piston position remains constant and no recovery takes place as illustrated in *figure 2.6*.

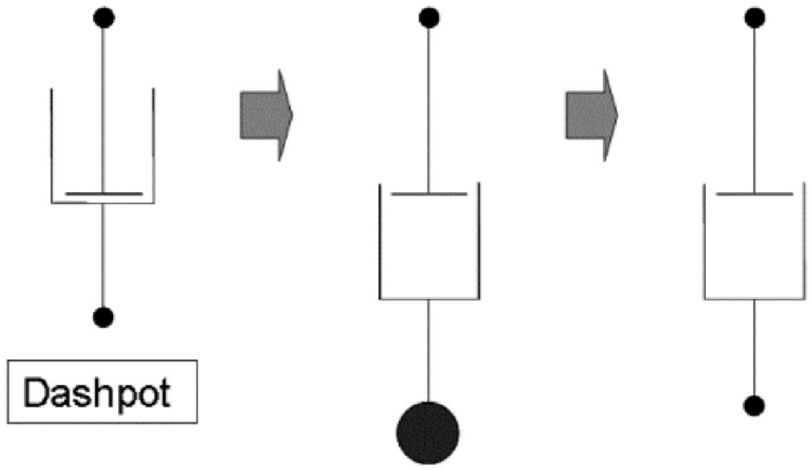

Figure 2.6. *The dashpot model for ideal viscous behaviour.*

In case of Newtonian fluids, the viscosity depends primarily upon temperature and hydrostatic. This means that in a plot of τ as function of $\dot{\gamma}$ at any given temperature, straight line with a constant slope will be observed that is independent of $\dot{\gamma}$.

In the case of materials such as the high molecular weight liquids, which include polymer melts and solutions of polymers, as well as liquids, in which fine particles are suspended (slurries and pastes), are considered as non-Newtonian fluids. These materials do not obey the Newtonian relationship between τ and $\dot{\gamma}$. In this case, the slope of τ versus $\dot{\gamma}$ curve will not be constant as $\dot{\gamma}$ changes. For non-Newtonian fluids such as the polymer melts, when η decreases with increasing shear rate, this behaviour is called shear thinning (pseudoplastic behaviour). This behaviour stems from the orientation and disentanglement of the entangled polymer chains when the applied $\dot{\gamma}$ is higher than critical value.

Ostensibly, when the viscosity increases as the fluid is subjected to a higher $\dot{\gamma}$., this behaviour is called shear-thickening behaviour. However, shear-thinning behaviour is more common than shear-thickening. The shear thinning behaviour is expressed by the power-law model. This equation was formulated by Ostwald de Waele in *equation 2.3*.

$$\tau = K\dot{\gamma}^{n} \tag{2.2}$$

where n is the slope and *K* is the intercept of log τ versus log $\dot{\gamma}$.

2.6.2. Oscillatory shear rheology

Oscillatory shear rheological experiments can be carried out either in small amplitude (SAOS) or large amplitude oscillatory shear (LAOS) conditions. In this section, a brief overview will on the SAOS conditions used throughout the dissertation is presented. The main focus is to characterize and quantify the linear viscoelastic behaviour of melted polymer nanocomposites.

Small/large amplitude oscillatory shear response.

The small amplitude oscillatory shear (SAOS) response of complex fluids can impart valuable data on the slow relaxation process related with structures formed by nanoparticles. Initially, small amplitude sinusoidal strain (γ) will be applied and subsequently within a few cycles upon start-up, the shear stress response (τ) will exhibit sinusoidal oscillations at the same frequency (ω) with a phase lag (δ) with respect to the applied strain wave. The aforementioned descriptions can be formulated mathematically as:

$$\gamma = \gamma_0 sin\omega t \tag{2.3}$$

$$\tau = \tau_0 \sin(\omega t + \delta) \tag{2.4}$$

This expression of stress wave can be decomposed into two waves of the same frequency, one term in-phase with the strain wave ($sin\omega t$) and the other term is at 90° out-of-phase with the strain wave ($cos\omega t$) as illustrated in *figure 2.7.*

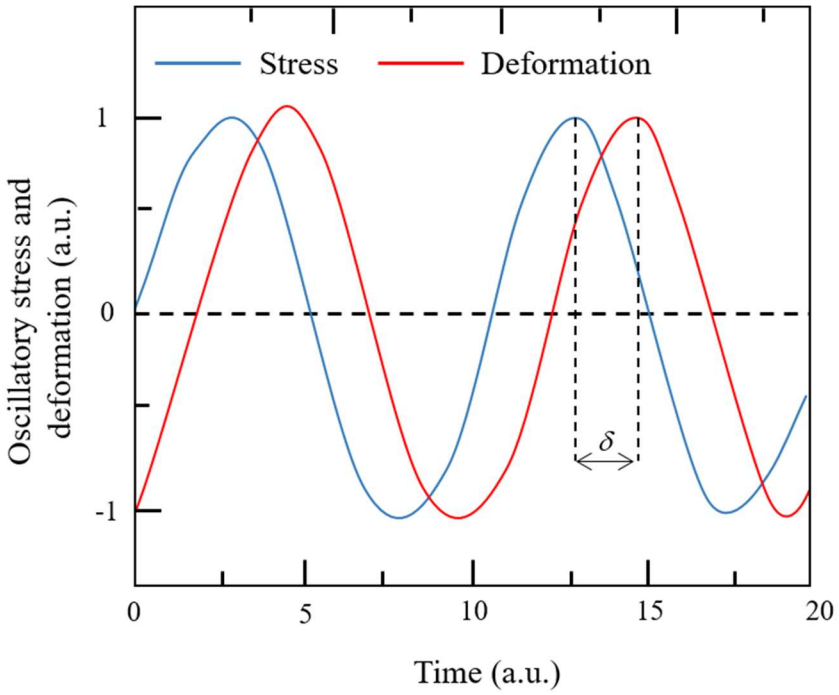

Figure 2.7. *Oscillatory stress (τ) wave and the resulting strain (γ) response wave.*

Subsequently, it is possible to demonstrate mathematically that:

$$\tau = G'\gamma_0 sin\omega t + G"y_0 cos\omega t \tag{2.5}$$

From the ratio of the applied stress to that of the resulting deformation, the magnitude of the complex shear modulus |*G*(ω)*|, which is the overall response of the system, is calculated as follows:

$$|G^*(\omega)| = \frac{\tau_0}{\gamma_0} \tag{2.6}$$

in which complex shear modulus $|G^*(\omega)|$ can be separated into two components: in-phase or elastic modulus (G') and out-of-phase or loss modulus are dynamic moduli defined based on the decomposition procedure.

$$G^* = G' + G"i \tag{2.7}$$

In-phase or elastic modulus (G') is defined as an elastic component, namely the dynamic storage modulus ($G'(\omega)$) which is in phase with the strain. Or on another term, it is when a material behaves like an elastic solid and stores energy

$$|G'(\omega)| = |G^*(\omega)|.cos\delta(\omega) \tag{2.8}$$

On the other hand, the out-of-phase or loss modulus $G"$ (*i.e.* imaginary part) is a measure of energy dissipated per cycle of deformation per unit of sample volume. Or this when a material behaves like an ideal liquid and dissipates energy.

$$|G''(\omega)| = |G^*(\omega)|.sin\delta(\omega) \tag{2.9}$$

$$Energy\ dissipated\ = \int_0^t \tau : Ddt = \int_0^{2\pi/\omega} \tau\gamma_0\omega cos\omega t dt = \pi G"\gamma_0^2 \tag{2.10}$$

Based on *equation 2.6*, the magnitude of the complex viscosity, $|\eta^*(\omega)|$ is given by:

$$|\eta^*(\omega)| = |G^*(\omega)|/\omega \tag{2.11}$$

In a typical experimental conditions, an isothermal frequency sweep will restrict the measurement of the viscoelastic properties to a frequency range of 4 decades only (0.0628 - 628 rad.s^{-1}). This will cause the terminal regime of polymers with long relaxation times such as polyolefins to remain experimentally unreached. Infinitely low ω using oscillatory shear experiments will be very hard to reach due to the considerably lengthy measurement times. A typical frequency sweep experiment with 10 points per decades and up to a minimum measurement frequency of 0.0628 rad.s^{-1} will take approximately 24 minutes. Consequently,

this renders frequency sweep at very low ω inaccessible because the data sets may be inaccurate due to potential sample ageing effect.

These experimental limitations can be circumvent using the Time-Temperature Superposition (TTS) principle. The measurement of standard isothermal frequency sweeps at several different temperatures will then be superposed, thus enabling expansion of frequency range over the estimation of the linear viscoelastic data (LVE) data. This superposition principle can be used to determine temperature-dependent mechanical properties of linear viscoelastic materials from known properties at a reference temperature.

2.6.3. Time -temperature superposition principle

The TTS general principle is based on the effect of an increase in temperature is nearly equivalent to an increase in time dependence of molecular motions and of relaxation times or a decrease in frequency. When properly applied, TTS yields plots in terms of reduced variables that can be used with considerable confidence to deduce the effect of molecular parameters, and also to predict viscoelastic behaviour in regions of the time or frequency scale not experimentally readily accessible.

Based from the above, experimental determination of frequency-dependent curves of isothermal viscoelastic mechanical properties at several temperatures and for a small range of frequencies can be shifted horizontally on the logarithmic frequency axis onto each other using a horizontal shift factor (a_T) as illustrated in *figure 2.8*. By applying the a_T factor onto the whole range of frequencies allows for the generation of master curves which would augment the frequency range.

The computation of a_T is dependent upon on either Williams, Landel, Ferry (WLF) (*c.f. equation 2.12*) or Arrhenius equation (*c.f. equation 2.13*) functions which is conditional upon the temperature range under study and how close it is to T_g of the material analyzed.

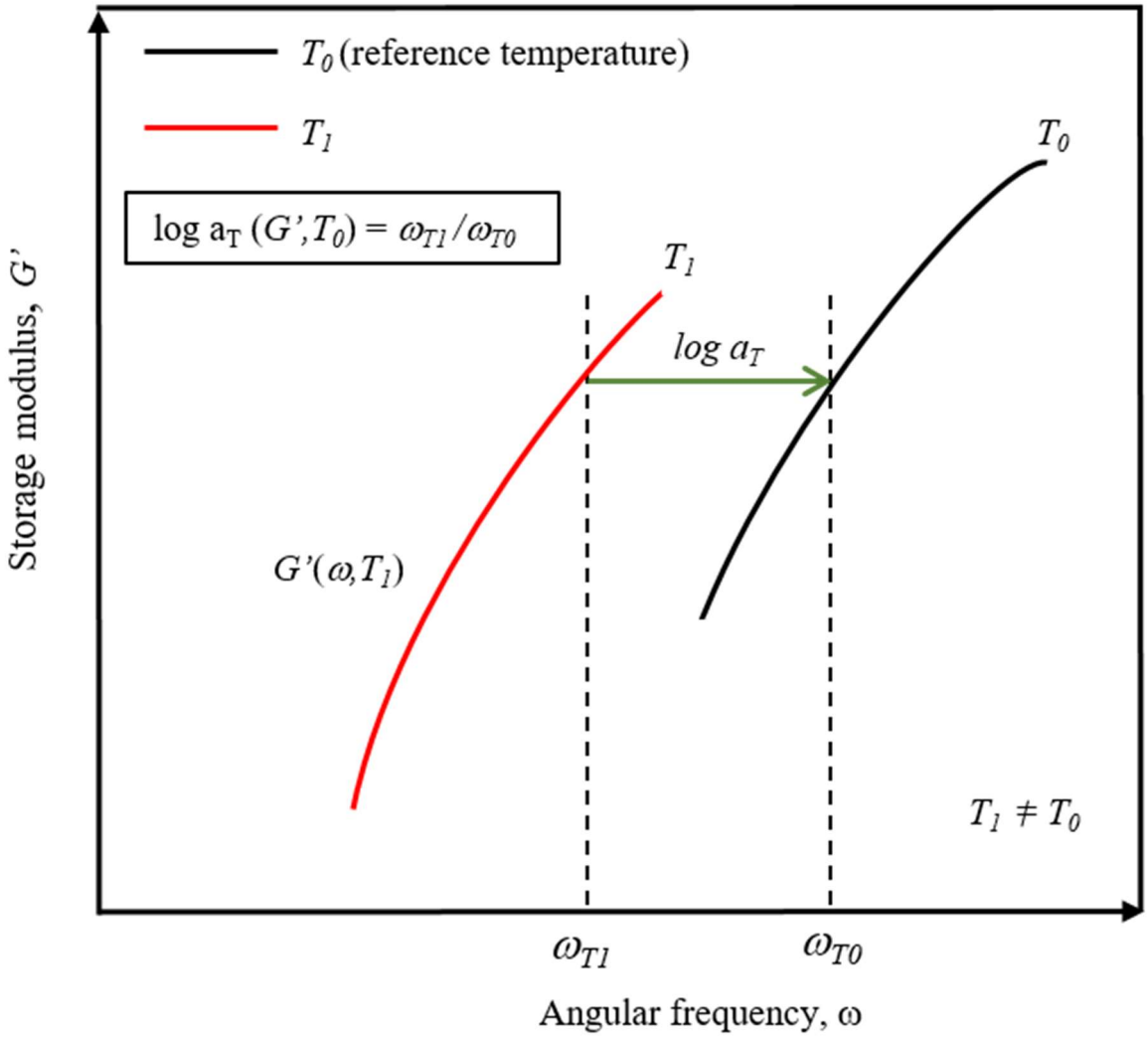

Figure 2.8. *Schematic TTS principle representation of temperature dependence of dynamic storage modulus of a viscoelastic material under periodic excitation. T_o defines the reference temperature (adapted from Cailloux (2015)).*

According to Dealy and Larson (2006), the temperature dependence of the rheological data within 100 ºC of their T_g can be suitably modelled by the Williams-Landel-Ferry or WLF

model for polymers that possess extremely slow crystallization kinetics or non-crystallizable polymers. However, the Arrhenius equation is favoured to describe the a_T relation with temperature if the temperature range is either narrow and/or superior to 100 ºC above T_g.

The Williams-Landel-Ferry or WLF equation is expressed as :

$$\log(a_T(T)) = \frac{-C_1(T - T_0)}{[C_2 + (T - T_0)} \tag{2.12}$$

While the Arrhenius equation is expressed as :

$$\ln(a_T(T)) = \frac{E_a}{R}(\frac{1}{T} - \frac{1}{T_0}) \tag{2.13}$$

Given that E_a is the activation energy for flow and R the gas constant. C_1 and C_2 are empirical constants obtained from curve fitting. T_0 is the reference temperature and T the temperature of measurement.

The main motivations behind the development of the TTS principle lies in the fact that this allows for augmentation of the range of frequencies or time over which the linear behaviour is determined. Additionally, applying TTS will also impart informations about the molecular structure of the investigated samples.However, careful consideration should be adopted while utilizing TTS. The TTS principle will not hold when relaxation times and molecular motions of the investigated samples are not temperature-independent and constituent components does not lie on a single correlation. This due to the fact that shift factor is both temperature and time-dependence (*i.e.* thermorheologically complex polymers). Due to this, mere shifting of the rheological response curves horizontally and vertically at different temperatures would it be inadequate to produce a valid TTS master curve.

Chapter 3. Materials

3.1. Poly(lactic acid)

Initially, Lactic acid was discovered in 1780 by Swedish chemist, Carl Wilhelm Scheele, who isolated the lactic acid from sour milk as an impure brown syrup and literally named it based from its origins: “Mjölksyra”. Later in 1841, a French scientist named Edmond Frémy reported a process for large-scale production of lactic acid from fermentation of milk. In 1881, Charles E. Avery successfully filed a United States patent on an improved process for the manufacture of lactates by fermentation using a lactic ferment that led to lactic acid being first produced commercially at Littleton, Massachusetts, USA. Lactic acid is produced by the fermentation of sugar and water or by chemical process and is commercially usually sold as a liquid. (Groot et al., 2010; Ren, 2010a; Sin et al., 2013a).

Lactic acid (chemically, 2-hydroxypropanoic acid, LA), also known as milk acid, is the most widely occurring carboxylic acid in nature. Lactic acid is derived from converting sugar or starch obtained from vegetable sources (e.g., corn, wheat, or rice) using either bacterial fermentation or from a petrochemical route. Since producing lactic acid using fermentation is the more ecologically friendly approach, it has been the widely adopted by manufacturers since 1990 (Gupta and Kumar, 2007; Rasal et al., 2010; Södergård and Stolt, 2002).

Fundamentally, PLA will degrade to form lactic acid, which is normally present in body tissues and some foods. Subsequently, the lactic acid enters the tricarboxylic acid cycle and will decomposes into carbon dioxide and water. PLA can degrade by hydrolysis and also microbial attack. At higher temperatures and humidity, high molecular weight PLA are

generally insusceptible to microbes contamination. This distinctive attribute of PLA is excellent for applications where the polymer would be in direct contact with the human body or foods and for this reason amongst others it has been approved by FDA. PLA can also be degraded by enzymes which accelerate hydrolysis of PLA as well as other biodegradable plastics and can be incorporated into the natural cycle of organic materials (Masaki et al., 2005). In an ideal composting environement, PLA will only take 3-4 weeks for complete degradation. The first stage of degradation is hydrolysis to water-soluble oligomers and lactic acid.

Currently, at least twelve companies are producing commercial PLA resin around the world namely Archer Daniels Midland Company (ADM) (United States of America), Cargill Dow Polymers LLC (United States of America), Toray Industries (Japan), DuPont-Plantic Technologies Limited JV(Australia), Mitsui Chemicals, Inc. (Japan), Tong-Jie-Lang (China), Zhejiang Hisun Biomaterials Limited (China), P.T. Toyota Bio Indonesia (Indonesia), Solanyl Biopolymers Inc. (Holland), Corbion Purac Biomaterials (The Netherlands), Shimadzu Corp. (Japan) and Total Petrochemicals-Galactic Escanaffles JV (Belgium) (Bioplastics Information, 2017).

In November 1997, Cargill Dow LLC which is the biggest PLA manufacturer was founded as a 50/50 joint venture between Cargill Inc and The Dow Chemical Company to pursue the commercialization of PLA polymers under the trade name NatureWorks® (Vink et al., 2003). However in 2011, “PTT Chemical PCL” have acquired 50 percent stake in NatureWorks® LLC. Its main manufacturing facility in Blair, Nebraska produces nearly 150,000 tonnes/year of PLA in 2014. It is has been projected to produce 450,000 tonnes/year by 2020 (Shen and Haufe, 2009).

3.1.1. Physical and chemical properties of PLA

Lactic acid (2-hydroxy propionic acid), the single monomer of PLA, is produced via fermentation or chemical synthesis. The two optically active isomers configurations of lactic acid, *i.e. L*-lactic acid and *D*-lactic acid are shown in *figure* 3.1. Pure *L*-lactic acid or *D*-lactic acid, or mixtures of both components are needed for the synthesis of PLA.

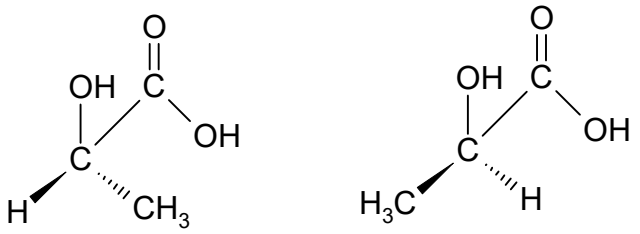

L-lactic acid *D*-lactic acid

Figure 3.1. *The stereoisomers of lactic acid.*

At ambient temperature, homopolymer of lactic acid is physically in the form of white powder with a measured T_g and T_m values of approximately 55°C and 175°C, respectively. High molecular weight (HMW) PLA on the other hand, is described as colourless, glossy, rigid thermoplastic material with properties mimicking polystyrene. By utilizing these two lactic acid isomers, four distinct materials can be manufactured:

i. Poly(*D*-lactic acid) (PDLA), which is a crystalline material with a regular chain structure;
ii. poly(*L*-lactic acid) (PLLA), which is hemi-crystalline, and likewise with a regular chain structure;
iii. poly(*D,L*-lactic acid) (PDLLA) which is amorphous and
iv. meso-PLA, obtained by the polymerization of *D,L*-lactide (meso-lactide).

The stereochemical purity of the lactide monomers is one of the key components that governs a majority of the material properties of the obtained PLA. However, meso-Lactide (i.e. which contains an *L*- and a *D*-isomer) is an unavoidable side product of lactide production and must be separated from *L*- and *D*-lactides to attain high stereochemical purity. Kolstad (1996) investigated the crystallization behaviour of copolymers of L-lactide and meso-lactide. He found that every 1% of meso-lactide co-monomer—or *D*-isomer— causes a 3 °C reduction in the melting point of the PLA copolymer. This underlines the need for a low meso-lactide content in the monomer mixture for semi-crystalline PLA, because meso-lactide formation by racemization that lowers the stereochemical purity of the PLA are inevitable during melt polymerization of lactides.

According to Mehta et al. (2005), racemization or conversion of one optical enantiomer to another are heavily influenced by factors such as temperature, pressure, time at a given temperature or pressure, the presence of catalysts or impurities, and relative concentrations of the two enantiomers at any given time during the polymerization process. The higher the content of the *L*-lactides, the higher the melting point, crystallinity, crystallization rate and mechanical strength observed. On the other hand, high proportions of the *D*-lactic and meso-Lactide enantiomers will reduce the rate of crystallization making it amorphous and having a brittle behaviours (Grijpma et al., 1994; Groot et al., 2010; Santana et al., 2010). However, presence of *D*-isomer content would help in tailoring the properties of polymer produced. Controlled copolymerization mixtures of *L*- and *D*-lactides for example would offers the advantage of manipulation over a variety of PLA properties.

Similarly, Tsuji (2005) suggested stereo-complexation of PLLA and PDLA would imparts PLA-based materials with higher mechanical performance, thermal resistance and hydrolysis resistance for more demanding applications. However, this is only achievable with PLA grades of high stereochemical purity. In order to prepare high-quality PLA, it is necessary to start with lactide monomers with the lowest meso-lactide content that is technically achievable by purification (Groot et al., 2010).

In terms of its optical characteristics, PLA is naturally transparent and can be coloured to various degrees of translucency and opacity. Unfortunately, having less than 10% elongation at break, PLA is considered to be very brittle and thermally unstable (Rasal and Hirt, 2009). This is mainly due to the T_g of PLA being close to room temperature that could lead to accelerated ageing process. This ageing process leads to a reduction in free volume as well as an increase in the density of molecular entanglement and tie molecules. (Aou et al., 2007; Santana et al., 2010). Eventually, this results in reduced molecular mobility and low energy dissipation when subjected to mechanical stimuli which could lead to ductile–brittle transition behaviours (Hutchinson, 1995; Hutchinson, 1997; Santana et al., 2010). In addition, the lack of reactive side-chain groups and the hydrophobic character of PLA due to its static water contact angle of approximately 80° could also limit the successful implementation of PLA without modifications in most practical applications (Rasal et al., 2010).

In terms of solubility, PDLA, PLLA and PDLLA dissolve in organic solvents namely benzene, chloroform, dioxane, etc. and can be hydrolysed by simple hydrolysis of ester bonds even in the absence of a hydrolase. PLA has a degradation half-life in the environment in the order of 6 months to 2 years, reliant upon on the size and shape of the article, its isomer ratio

and the temperature. The mechanical properties of PLA will also vary widely depending on its degree of crystallinity and whether it is annealed or oriented (Garlotta, 2001). Some of the physical and chemical properties of PLA are summarized in *table 3.1*.

Table 3.1. *Selected physical and chemical properties of PLA (Adopted from (Xiao et al., 2012)).*

Properties	**PDLA**	**PLLA**	**PDLLA**
Solubility	All are soluble in benzene, chloroform, acetonitrile, tetrahydrofuran (THF), dioxane etc., but insoluble in ethanol, methanol, and aliphatic hydrocarbons		
Crystalline structure	Crystalline	Hemicrystalline	Amorphous
Glass transition temperature, T_g (°C)	50 - 60	55 - 60	Variable
Melting Temperature, T_m (°C)	≈180	≈180	Variable
Decomposition temperature (°C)	≈200	≈200	185 - 200
Elongation at break (%)	20 - 30	20 - 30	Variable
Breaking strength (g/d)	4.0 - 5.0	5.0 - 6.0	Variable
Half-life in 37°C normal saline	4 - 6 months	4 - 6 months	2 - 3 months

3.1.2. Synthesis of PLA

Three main synthetic methods can be used to obtain HMW PLA (higher than 100 000 Daltons) from lactic acid:

- The direct condensation process which is a solvent-based process has been researched for many years by many science fraternities. Unfortunately, nobody have succeeded in synthesizing poly(lactic acid) with a high enough molecular weight and useful properties using this method. This is mainly due to the difficulties of finding the ideal equilibrium between free acids, water, and

polyesters and the viscous polyester melt in combination with the difficulty in removing by-produced water (Ajioka et al., 1995; Auras et al., 2004; Garlotta, 2001; Ren, 2010b).

- The azeotropic dehydrative condensation polymerization process developed by Mitsui Chemicals Co. brought a breakthrough in increasing the molecular weight of the polycondensation of LA. This method successfully yield PLA with a high molecular weight without the use of chain extenders or adjuvants albeit with a relatively long reaction time. Solvents with high boiling point were used for the removal of the dissociated water by means of azeotropic distillation technique. This polymerization process seems promising for obtaining a high molecular weight PLA with improved cost performance. However, it seems that this polymerization route is not being favoured anymore due to the utilization of organic solvents which makes this process environmentally unappealing (Davachi and Kaffashi, 2015; Drumright et al., 2000; Ren, 2010b).
- The ring opening polymerization (ROP) process of the cyclic lactide dimer is the method most commonly used commercially. Though the ROP of lactide was first studied long back (1932), only low molecular weight polymer was produced until lactide purification techniques were devised by DuPont in 1954. Nature Works LLC has developed a solvent-free, low-cost continuous process for the production of PLA from coRN-derived dextrose. The resulting PLA, commercially branded as Ingeo™ biopolymer, is the first synthetic polymer to be produced from annually renewable resources. *Figure 3.2* illustrates the three synthesis methods for obtaining for obtaining HMW PLA.

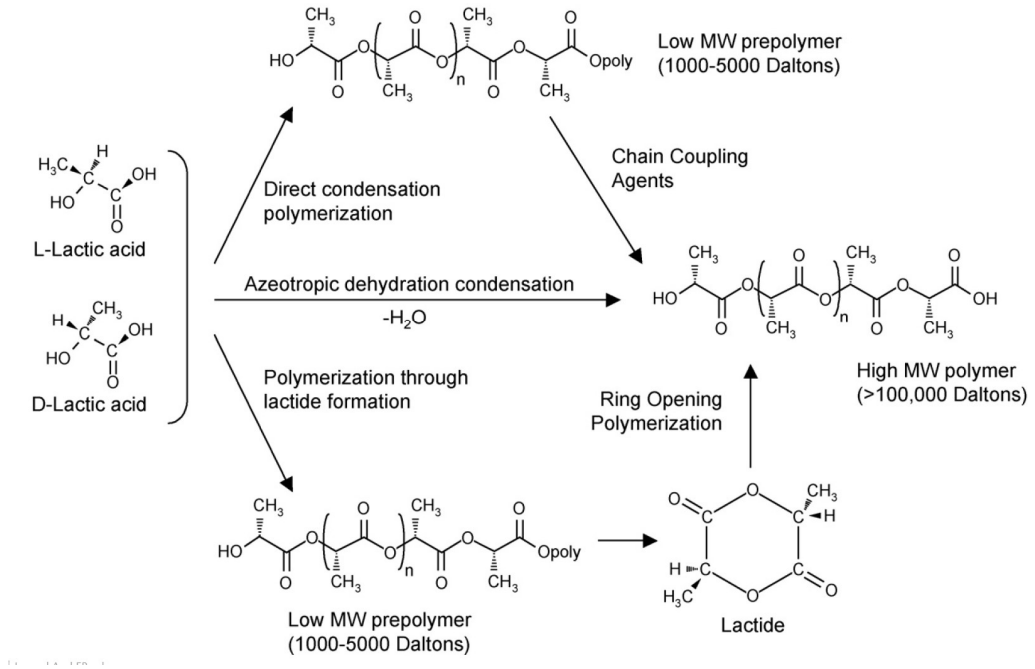

Figure 3.2. *Three synthesis methods for obtaining for obtaining HMW PLA. Adapted from (Auras et al., 2004; Farah et al., 2016; Lim et al., 2010).*

3.1.3. Degradation mechanisms of PLA

The poor thermal stability of PLA resins at high temperature encountered in the range of conventional processing temperatures has been broadly investigated and the degradation mechanisms are well established (Gupta and Deshmukh, 1982; Henton et al., 2005; Kopinke et al., 1996; Sin et al., 2013b). Studies have indicated that the most important parameters in melt processing of PLA involve temperature, residence time, moisture content of the polymer, and atmosphere which could also affect thermal stability of PLA (Johansson, 2016) .

The main degradation mechanisms include hydrolysis of the ester linkages by trace amounts of water, which occurs more or less randomly along the backbone of the polymer (Elsawy et al., 2017; Tsuji, 2010), zipper-like depolymerization catalysed by the remaining polymerization catalyst (Jamshidi et al., 1988; Sin et al., 2013b), oxidative, random main-chain scission (Gupta and Deshmukh, 1982; Johansson, 2016), intra and intermolecular transesterification reactions (Kopinke et al., 1996; Zhang et al., 1992). Last but not least, pyrolysis might also be considered as a depolymerization mechanism at elevated temperatures (>300 ºC) (Nishida et al., 2003). The degradation side-products will be water, cyclic oligomers, lactic monomers, lactides, and residual catalysts (Inkinen et al., 2011).

Hydrolitic degradation

Hydrolytic degradation is defined as random hydrolysis of ester linkages on the polymer backbone in the presence of water which leads to a substantial MW reduction of the initial polymer during melt processing (Södergård and Inkinen, 2011). When temperatures exceed T_g of PLA, hydrolytic degradation typically occurs at a much faster and the polymer chain would undergo hydrolysis both in solid and melt state. The reaction is dependent on the molecular weight and the degree of crystallinity (Johansson, 2016). Authors have stated that hydrolytic degradation can be autocatalytic through the action of carboxylic acid end groups (Henton et al., 2005; Taubner and Shishoo, 2001). The rate of hydrolytic degradation is highly dependent commensurate with the amount residual moisture, water concentration and processing temperatures (Södergård and Inkinen, 2011). The general mechanism of the hydrolytic degradation is illustrated in *figure 3.3* below.

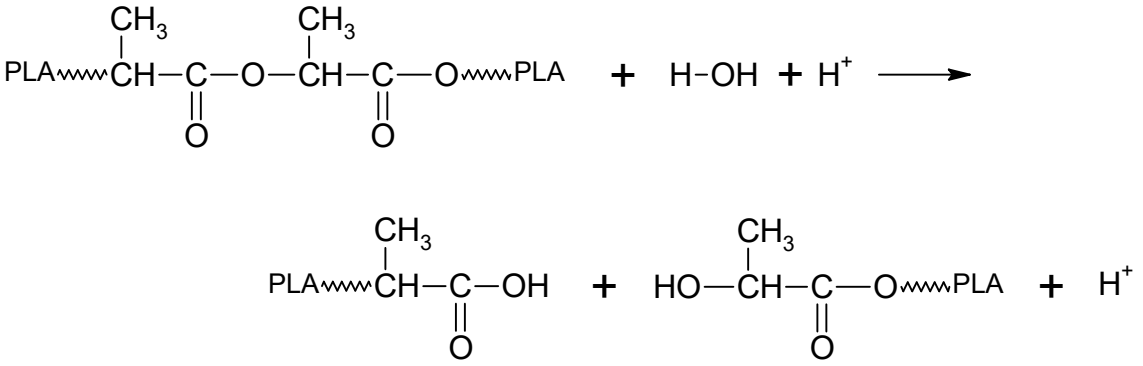

Figure 3.3. *Autocatalytic hydrolytic degradation mechanism of PLA (adapted from (Mohanty et al., 2005)*

Transesterification mechanism.

Generally, there are two types of transesterification mechanisms *i.e.* intramolecular and intermolecular. With regards to intramolecular transesterification, it is a thermal-based degradation mechanism which is an unattractable occurrence as it increases the polydispersity index and reduces the molecular weight of PLA which affects the mechanical properties of the material as illustrated in *figure 3.4.*

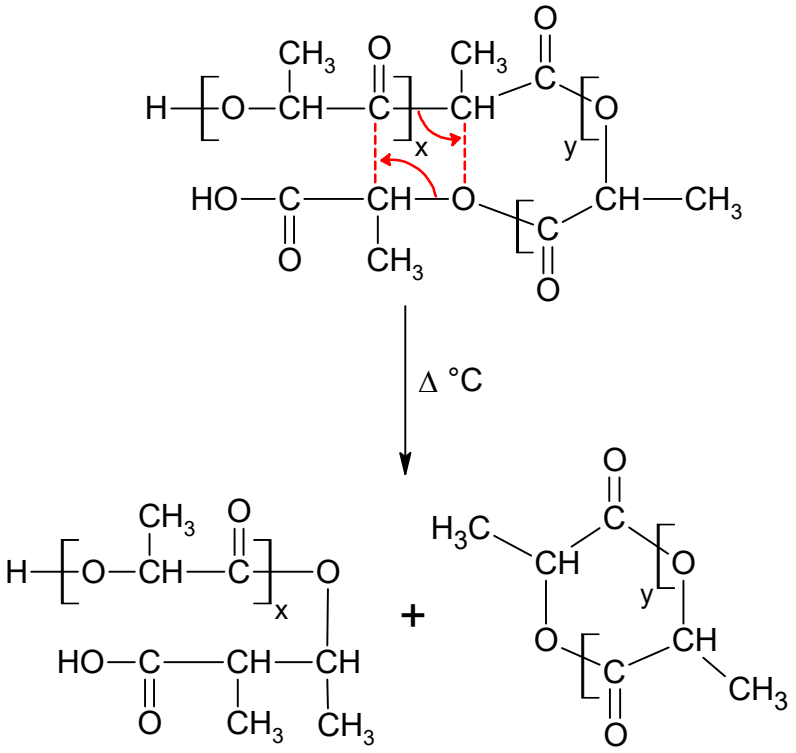

Figure 3.4. *Intramolecular transesterification of PLA that leads to depolymerization during processing (Cailloux, 2015; Kopinke et al., 1996; Murray et al., 2015).*

Referring to *figure 3.4*, the formation of either a lower molecular weight sub-linear chain together with a lactide if $x = 1$ (referred to as backbiting) or formation of cyclic oligomer if $x \geq 2$ could occur by intramolecular transesterification during melt processing. Kopinke et al. (1996) and Wachsen et al. (1997) have reported that intramolecular transesterification for PLA is found to be dominant at high temperatures (>200 °C) during melt processing and results in the formation and degradation of cyclic polylactide oligomers. Zhang et al. (1992) added that intramolecular transesterification degradation reaction would be accelerated by existence of monomer, oligomer and hydroxyl groups.

Meanwhile, intermolecular transesterification degradation modifies the arrangement of different polymeric segments (Najafi et al., 2012b). It can be defined as radicals exchange

reaction of two ester linkages between two different chains during melt processing. As an outcome of this degradation, polydispersity could be augmented, crystallinity could be reduced, inferior mechanical properties and decrease solubility in solvents could be observed. However in some cases, effects of transesterification reactions can be used to obtain new distinct polymer properties (Lipik et al., 2010; MacDonald et al., 1991). The intermolecular transesterification mechanism is illustrated in *figure 3.5.*

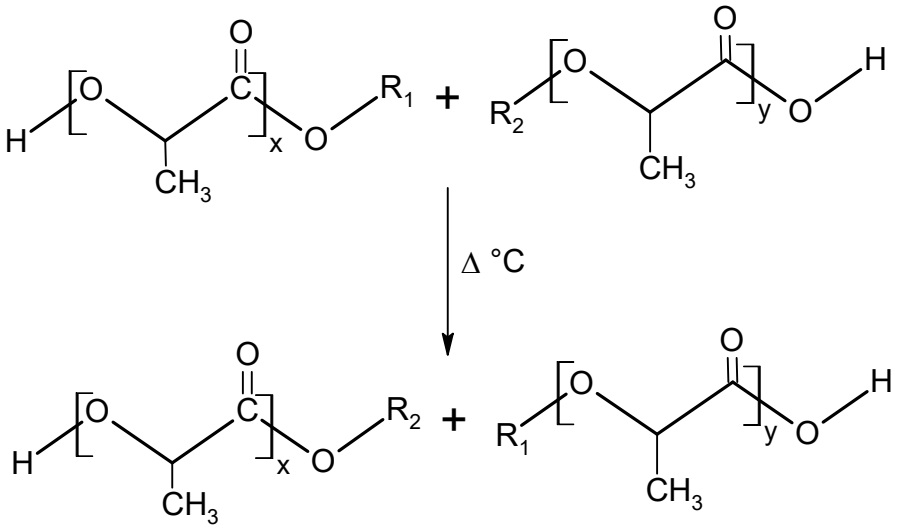

Figure 3.5. *Intermolecular transesterification degradation of PLA at elevated temperatures. Adopted from (Cailloux, 2015; Najafi, 2011).*

Pyrolytic Cis eliminations

Cis-elimination reaction only happened at very high temperatures (>300ºC) and are rarely encountered during typical melt processing. The pyrolitic elimination of an ester linkage generates two new sub-chains, one containing carboxylic acid end group while the other contains an acyclic group. Both of these sub-chains have lower molecular weight compared to its initial polymeric chain (Rizzarelli and Carroccio, 2015; Wang et al., 2008b). *Figure 3.6* displays the general mechanism of this pyrolysis reaction.

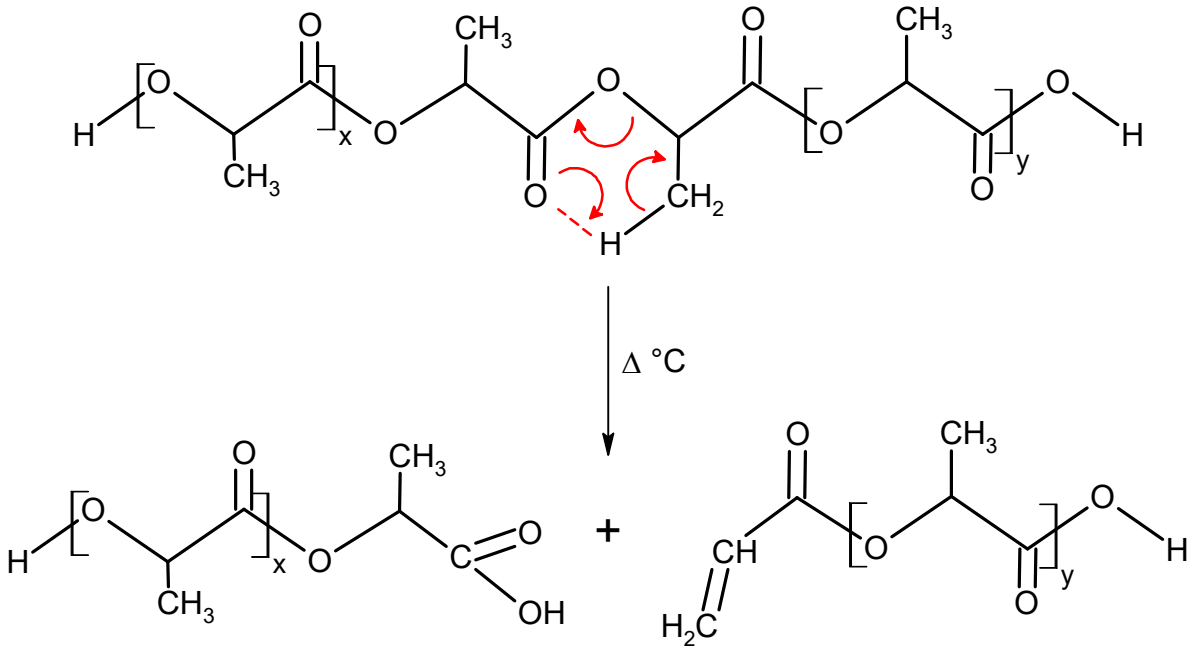

Figure 3.6. *Pyrolitic Cis elimination degradation mechanism of PLA. Adopted from (Cailloux, 2015; Wang et al., 2008b)*

3.2. Styrene-acrylic multi-functional-epoxide oligomeric agent (SAmfE)

Chain extension with diisocyanates is undoubtedly the most commonly applied chain-extension approach for PLA. Although diisocyanate compound is the most popular reactive agent used to achieve chain extension with PLA, unfortunately it has a narrow processing window. However, owing to its severe acute toxicity and volatility, the interest previously garnered in using this reactive agent is diminishing. Alternatively, dianhydride and isocyanurate-based compounds possess exceedingly long reaction times with PLA that causes the matrix to degrade. On the other hand, peroxide compounds in liquid form are volatile and creates unnecessary difficultly during extrusion.

Based on these arguments, styrene-acrylic multi-functional-epoxide oligomeric agent (referred to as SAmfE) were selected to overcome the above drawbacks. It allows for enhancement of molecular weight at a broad range of processing temperatures (Meng et al., 2012). The improvement of shear and elongational properties of modified PLA with SAmfE have been already highlighted in deep-draw thermoforming and orientation processes.

SAmfE has also been known to impart compatibilization effect on polymer blends. Ojijo and Ray (2015) used SAmfE for in-situ reactive compatibilization of PLA and poly(butylene succinate-co-adipate), PBSA, resulted in the modification of the PLA/PBSA blend structure from linear to long branched chains. This enhances the impact strength of PLA/PBSA (60/40) blend from 4.6 to 38.4 $kJ.m^{-2}$. It was also observed that the particle size of PBSA of dispersed phase shrunk by 74 % with the addition of 0.6 % SAmfE and further reduction was noticed with increase in SAmfE content owing to effective compatibilization. Dong et al. (2013) have also reported SAmfE was successful at increasing the ductility and percentage elongation of PLA/PBAT blends, to a maximum of 500 %.

3.3. Nanofillers

3.3.1 Montmorillonite (MMT) nanoclay

a) Structure and properties of MMT

Clay minerals are essentially made up of hydrous aluminium silicates, and are generally classified as phyllosilicates, or layer silicates. It is made up of a combination of tetrahedral and octahedral sheets. The tetrahedral sheet comprises mainly from silica whilst the octahedral sheet comprises diverse elements such as Al, Mg and Fe. Ultimately, the arrangement and composition of the octahedral and tetrahedral sheets account for most of the

differences in their physical and chemical properties. A natural stacking of tetrahedral and octahedral sheet occurs in the specific ratios and modes, leading to the formation of the 1:1 and 2:1 layer silicates. Typical example of 1:1 layer silicate is kaolinite clay which consists of metal-hydroxide and silicon-oxygen network of sheets fused together by hydrogen bonding (Murray, 2006; Tjong, 2006; Zaarei et al., 2008).

However, the most commonly used layered silicates for the preparation of polymer nanocomposites belong to 2:1 layered silicates. Its crystal structure consists of layers made up of two tetrahedrally coordinated silicon atoms fused to an edge-shared octahedral sheet of either aluminum or magnesium hydroxide. The stacking of the layers leads to a regular van der Waals gap between the layers called the interlayer or gallery. Typically, the silicates gallery or layer thickness is nominally 1 nm, and the lateral dimensions of these layers can vary from 30 nm to several microns or larger, depending on the particular layered silicate. Main 2:1 layer silicates classifications include mica, smectite, vermiculite, and chlorite. Additionally, the smectite group is further divided into montmorillonite (MMT), nontronite, saponite and hectorite species (Bharadwaj et al., 2002; Sheng et al., 2004; Thellen et al., 2005).

MMT is one of the widely used nanoclay filler materials for nanocomposites. The typical composition of MMT is $Na_{1/3}(Al_{5/3}Mg_{1/3})Si_4O_{10}(OH)_2$ (Beall and Powell, 2011; Zanetti et al., 2000). The crystal structure of MMT is illustrated as *figure 3.7 (Sinha Ray, 2013c)*. A single aluminum hydroxide octahedral sheet is sandwiched between two layers of silicon oxide tetrahedral sheets (Beall and Powell, 2011). The space between the layers, which is referred to as the interlayer or gallery spacing, is approximately 1 nm and its lateral dimension is approximately 200 nm. The galleries of MMT are occupied by hydrated Na^+ or K^+ cations (Beall and Powell, 2011; Sinha Ray, 2013c).

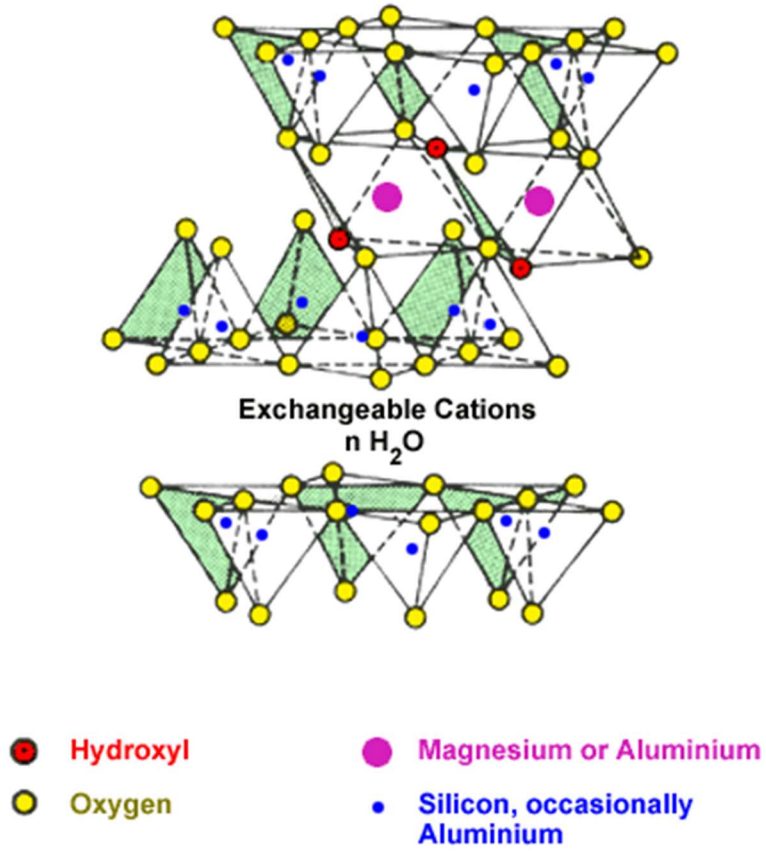

Figure 3.7. *Basic structure of a 2:1 phyllosilicate (Adapted from (Sinha Ray, 2013c)).*

Due to the physical dimensions of MMT, it possess an attractive trait as a filler material in which it has high aspect surface to volume ratio in 2-dimensional sheets form and

consequently large surface areas. The tremendous surface area available for polymer-clay interaction allows polymer chains to effectively transfer stress into filler particles (Shi et al., 1996).

b) Organically Modified MMT

The layered silicates of montmorillonite in its pristine state which is coincidently hydrophilic are only miscible with hydrophilic polymers such as poly(ethylene oxide) (PEO) (Aranda and Ruiz-Hitzky, 1992). This is due to the fact that naturally occuring layered silicates usually contain hydrated Na^+ or K^+ cations (Sinha Ray and Okamoto, 2003b). It is proven that high dispersion degree of the stacks of MMT or nanoplatelets, into individual layers is vital for preparing nanocomposites (Giannelis, 1996). This requires the ability to fine-tune the surface chemistry to be compatible with a chosen polymer matrix (Pavlidou and Papaspyrides, 2008).

The interlayers or intergallery regions of pristine MMT are balanced by Van der Waals forces. Attributable to the existence of the cations on the interlayers, the layered silicates are greatly hydrophilic and thus naturally incompatible with most polymers. However, the cations in the galleries can be easily substituted with other cations to render the clay becoming more compatible with non-polar polymers. In an organically modified montmorillonite clay (o-MMT), the surfactants are cationic and will migrate in between the galleries where it will substitute in place of hydrated cations. The most common cationic surfactants used are alkylammonium and alkylphosphonium salts. The role of alkylammonium cations in the organo silicates is to lower the surface energy within the galleries and improve the interlayer distance (Krishnamoorti et al., 1996). A list of commercial available organic modified MMT and its counter ions is shown in *table 3.2*.

Table 3.2. *Common counter ions of organically modified clay (Wool, 2005).*

o-MMT **Trade name**	**Counter Ion**	**Modifier Concentration** **(mEq/100g of clay)**
Cloisite® 10A	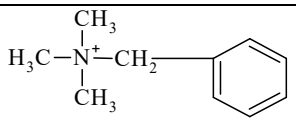	125
Cloisite® 15A	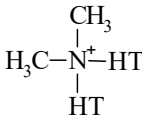	125
Cloisite® 20A	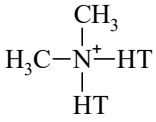	95
Cloisite® 25A	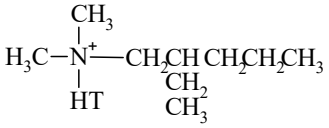	95
Cloisite® 30B	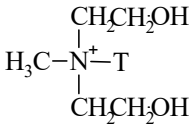	90

Where HT is hydrogenated tallow : ≈65 % C_{18}, ≈30 % C_{16} and ≈5 % C_{14} and T is a tallow fatty chain having the following composition : ≈65 % C_{18}, ≈30 % C_{16} and ≈5 % C_{14}.

These cationic surfactants modify interlayer interactions by lowering the surface energy of the inorganic component and improve the wetting characteristics with the polymer (Wu et al., 2009). It can also provide functional groups that can react with the polymer or initiate polymerizations of monomers and thereby improve the strength of the interface between the polymer and inorganic (Sinha Ray, 2013b). Furthermore, cation exchange using long chain surfactant molecules will directly expands the gallery spacing between MMT intergalleries (Haldorai and Shim, 2016). The enlarged gallery spacing helps facilitate the diffusion of

polymer chains in between the individual layers, thus its importance for the enhancement of the degree of dispersion for final composite morphology after processing.

Ultimately, the properties of the final nanocomposites are still contingent on amalgam of factors such as the type of clay, clay modifier, types of polymers, and the intercalation methods. These factors will directly affect the degree of exfoliation of the layered silicates in the polymer matrix. An effective exfoliation and dispersion of the layered silicate is imperative to achieve the optimum potential of the nanocomposites prepared.

3.3.2 Fumed Silica

a) Synthesis and properties of fumed silica

Fumed silica is an insoluble white powder; composed of Silicon (Si) and Oxygen (O) atoms in their structure with a chemical formula (SiO_2) occurring in both crystalline and amorphous form. Alternatively, it is also known as pyrogenic silica because oxidation of the SiO_2 particles is conducted in a flame. In its structure, Si and O are linked by covalent bond, the Si with tetrahedral coordination bonded with 4 atoms of O leads to a high melting temperature of silica, due to a strong covalence bond (Flörke et al., 2000; Vansant et al., 1995). It consists of microscopic droplets of amorphous silica which are fused into branched, chainlike and three-dimensional secondary particles which then agglomerate into the tertiary particles (Bergna and Roberts, 2005b). It has extremely low bulk density and high surface area. It has the tendency to undergo sintering with reactive alumina and form mullite and this phase is highly advantageous for refractory applications (Vansant et al., 1995).

There are many different synthesis methods to prepare fumed silica, mainly divided into two categories:

- "Wet" chemical route to prepare the fumed silica in the liquid phase and
- "Dry"/Thermal chemical route to form silica at high temperature (Bergna and Roberts, 2005b; Flörke et al., 2000).

"Wet" process synthesis of fumed silica

It is commonly used process to synthesize fumed silica is by acidulation of aqueous solution of sodium silicate from sand. As the name suggest, this process takes place in liquid state and it is a relatively low cost. However, silicas produced according to the wet process usually contain sulphate and alkali or alkaline earth ions (≈ 1000 ppm) and relatively wide distribution of particle sizes.

A system of chemical reactions has been developed by Stöber et al. (1968) which permits the controlled growth of spherical silica particles of uniform size by means of hydrolysis of alkylsilicates and subsequent condensation of silicie acid in alcoholic solutions. Till this day, this is the most commonly method used for preparing silica nano-particles in studied literature, which deals with preparation and characterization of fine silica at laboratory scale. By employing Stöber methods, Bogush et al. (1988) successfully precipitate monodisperse silica particles from ethanol solutions containing ammonia, water, and tetraethyl orthosilica (TEOS). The monodisperse particles The maximum particle size achievable are approximately 800 nm. Two equations which describe the hydrolysis and condensation are:

$$Si(OR)_4 + 4H_2O \rightarrow Si(OH)_4 + 4R - OH \quad (3.1)$$

$$Si(OH)_4 \rightarrow SiO_2 + 2H_2O \quad (3.2)$$

It was found that five factors influencing the size of final particles, namely concentration of TEOS, ammonia and water, type of alcohol used as the solvent and reaction temperature. Suspension of silica prepared by "wet" processes can be finally centrifuged and then desiccated or additionally treated before drying.

"Dry"/Thermal process synthesis of fumed silica

The largest part of silica nano-particles production is produced by thermal processes, in spite of the extensive research efforts expended on the controlled growth of silica by suspensions. Industrially, the most commercially successful method of manufacturing fine silica particles was developed by researchers from Degussa AG led by Henry Kloepfer-Geschicte (Bergna and Roberts, 2005b).

This process uses silicon tetrachloride ($SiCl_4$) in liquid form with boiling point 57.6°C as the precursor. This mixture is combusted with hydrogen by special burners prior to being mixed chloride vapour. Adiabatic flames used were meticulously controlled to yield a high-velocity particle-laden product stream. Reagents used are silicon tetrachloride, a hydrocarbon fuel, and air. It is produced by action of gaseous chlorine in fused metallic silicon. A representative combustion reaction under which the fumed silica is created could be characterized by these equations (Flörke et al., 2000):

$$2H_2O + O_2 \rightarrow 2H_2O \quad (3.3)$$

$$SiCl_4 + 2H_2O \rightarrow 2SiO_2 + HCl \quad (3.4)$$

So in summary

$$2H_2O + O_2 + SiCl_4 \rightarrow SiO_2 + 4HCl \quad (3.5)$$

The process layout diagram of fumed silica production is illustrated in *figure 3.8.*

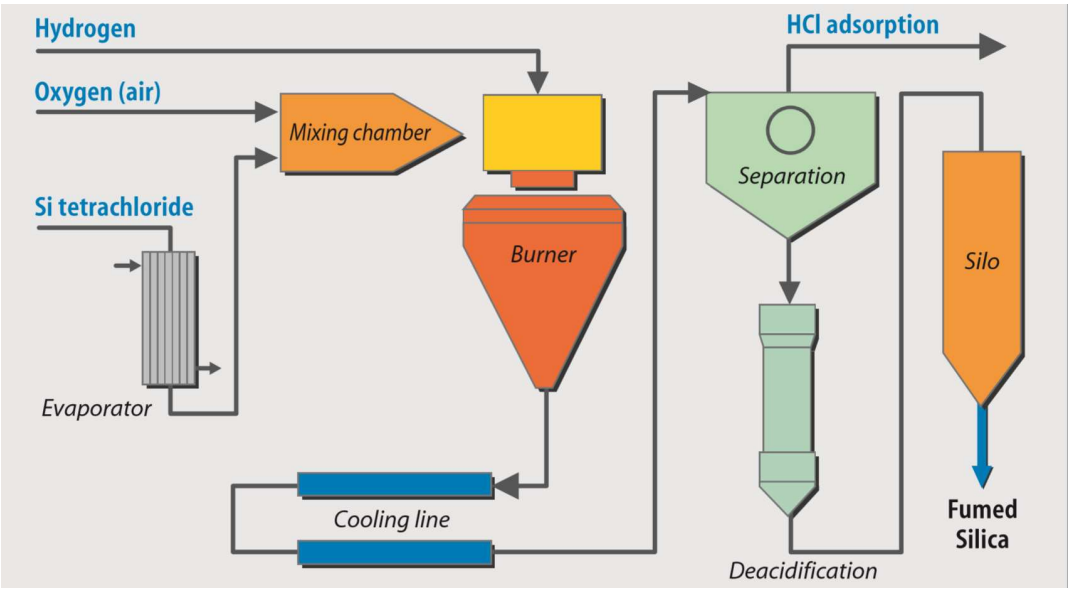

Figure 3.8. *The process layout diagram of fumed silica production. Adopted from (Kloepfer-Geschichte, 2006).*

This process carries several advantages. It far easier to control the size of forming primary particle and aggregate by varying the concentration of reactants, temperature of combustion and also dwell time of generated dust in burner chamber (Ulrich and Rieh, 1982). Additionally, this process allows the formation of mono-disperse particles with easily removable by-product (hydrochloric acid) and practically no contamination by reagents (Bergna and Roberts, 2005a; Flörke et al., 2000).

The fumed silica synthesized by this method has a random network structure formed by SiO_4 tetrahedrons, which are highly disordered. Even with heated up to 1000 °C, the fumed silica does not change its morphology and will not crystallize neither (Evonik Industries GmbH, 2015; Flörke et al., 2000; Vansant et al., 1995). Visually, fumed silica is identified as a loose, bluish-white powder with about 98 % by volume of air. The tapping density of fumed silica is around 0.05-0.12 g/cm^3, which is very less than the silica density (2.2 g/cm^3). The primary particles of fumed silica are extremely small, around 7-40 nm. They contact with each other by hydrogen bonds or van deer Waals force and build up a loose, non-isolated network (Flörke et al., 2000; Majesté, 2016). *Figure 3.9* presents the TEM micrograph of a typical commercial fumed silica.

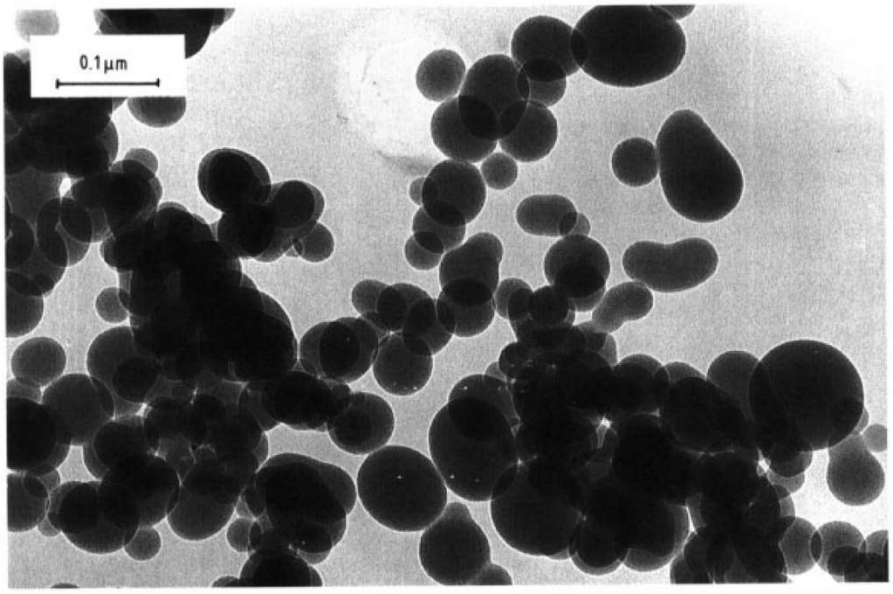

Figure 3.9. *TEM photograph of fumed silica with an average primary particle size of ca. 40 nm and a specific surface area of ca. 50 m^2/g (adapted from (Flörke et al., 2000)).*

The biggest fumed silica producer in the world currently is Evonik (who sells it under the trade name Aerosil®). Other major global producers of fumed silica includes Cabot Corporation (trade name Cab-O-Sil®), Wacker Chemie (trade name HDK®), Dow Corning, Tokuyama Corporation (trade name Reolosil®), OCI (trade name Konasil®), Orisil (trade name Orisil®) and Xunyuchem (trade name XYSIL®). A list of several commercially available fumed silicas from Evonik Industries and its physicochemical properties are listed in *table 3.3*

Table 3.3. *Commercially available fumed silicas grades from Evonik Industries and its physicochemical properties (Kloepfer-Geschichte, 2006).*

Properties	**AEROSIL® 90**	**AEROSIL® 130**	**AEROSIL® 150**	**AEROSIL® 200**	**AEROSIL® 300**	**AEROSIL® 380**
Behavior with respect to water	Hydrophilic					
Appearance	Fluffy white powder					
BET-Surface Area ($m^2.g^{-1}$)	90 ±15	130 ±25	150 ±15	200 ±25	300 ±30	380 ±30
Average Primary Particle Size (nm)	20	16	14	12	7	7
Moisture (2 hours at 105 °C) (wt. %)	≤ 1.0	≤ 1.5	≤ 0.5	≤ 1.5	≤ 1.5	≤ 2.0
Ignition loss (wt. %)	≤ 1	≤ 1	≤ 1	≤ 1	≤ 2	≤ 2.5
pH value	3.7 - 4.7	3.7 - 4.7	3.7 - 4.7	3.7 - 4.7	3.7 - 4.7	3.7 - 4.7
Sieve residue (according to Mocker, 45 µm) (wt. %)	≤0.05	≤0.05	≤0.05	≤0.05	≤0.05	≤0.05

Some of the more important applications of fumed silica are for improving the rheological properties of paints, for reinforcing elastomers and as surface modifiers which when dispersed into resin or other organic system increases viscosity, imparts thixotropic behaviour. When fumed silica is incorporated in either melt or liquid state in a polymeric system, strong attractive forces between silica particles can arise during the steady state. These particle surface forces would entice aggregates that coalesce to clump together into large agglomerates, until a three-dimensional network is formed. As this three-dimensional network grows in dimension, the viscosity of the melt or liquid rises significantly. This phenomenon means that a high viscosity can be built up by only small amounts of nanofillers.

In the case of hydrophilic nanoparticles, Wen et al. (2011) and Gong et al. (2014) reported that these interactions are typically caused by hydrogen bonds between silanol groups on the surfaces of adjacent particles. With hydrophobic silica, additional hydrophobic interactions and forces of attraction occur between the silica particle surfaces that has been substituted with silyl group (Si-R_3). Under shearing, breakdown of hydrogen bonds occurs. The particle-particle interactions are broken down and the nanoparticles can move with respect to one another. This breaks down the particle network, and the agglomerates become smaller. The viscosity of the liquid decreases. The greater the applied shear force, the more fluid the substance becomes (Cassagnau, 2008).

Additionally, due to the primary size of fumed silica is small, it could be used as added filler for reinforcement in polymer matrix because of its very high surface to volume ratio. Silica have been widely used in various applications such as ingredients in food, pesticides, and personal care products; as fillers in plastics, rubbers, and coatings; and as starting materials

for semiconductors, silicates, and ceramics (Uhrlandt, 2006). It wasn't until the start of the 21st century that silica has also been explored for biomedical applications (Argyo et al., 2014; Slowing et al., 2007; Vivero-Escoto et al., 2012). Amorphous silica with high surface area is important to many key chemical applications, including absorbents, thermal insulators, and catalyst supports (Bergna and Roberts, 2005b). However, ultimately its application and value of silica are also highly dependent upon its crystallinity and micro-structure (Vansant et al., 1995).

b) Functionalization of fumed silica

Fumed silica particles prepared by thermal or "wet" process always carries hydroxyl groups bonded on silicon atom called silanol group. Silanol groups are formed on the silica surface in the course of its synthesis during the condensation polymerization of $Si(OH)_4$ or by rehydroxylation of thermally dehydroxylated silica with water or aqueous solutions. At a sufficient concentration, these silanol groups turns fumed silica particle surface into hydrophilic. The OH groups behaves as the centre of molecular adsorption during interaction with adsorbates capable of forming a hydrogen bond with the OH groups, or, more generally, of undergoing donor–acceptor interaction (Bergna and Roberts, 2005a; Zhuravlev, 2000).

Listed are possible types of silanol groups and siloxane bridges that have been identified occurring on the surface or in the internal structure of amorphous silica:

1. Single silanol groups, also called isolated or free silanol groups.
2. Silanediol groups, also called germinal silanols.
3. Silanetriols groups.
4. Hydrogen-bonded vicinal silanols (single or geminal), including terminal groups.

5. Internal silanol groups involving OH groups, sometimes classified as structurally bound water.
6. Strained and stable siloxane bridges.
7. Physically adsorbed H_2O, hydrogen-bonded to all types of surface silanol.

These silanol groups structures are illustrated in *figure 3.10*.

Fumed silicas are hydrophilic; however, a hydrophobic character is more favorable for some applications. In order to impart water resistant properties towards fumed silica particles, replacing of -OH in silanol group with another water-repellent functional groups would render it hydrophobic. In most cases, “organic silicon” which consist of an inorganic silicon-oxygen backbone chain with organic side groups (usually chlorine) or other functional group attached to the silicon atoms are preferred. Other terms that are used for these molecules are silane coupling agents. Some of the most common silane coupling agents include chloroalkylsilanes, hexamethyldisilazane, alkoxyalkylsilanes, and polydimethylsiloxanes. These coupling agents are widely used for both hydrophobization of fumed silica.

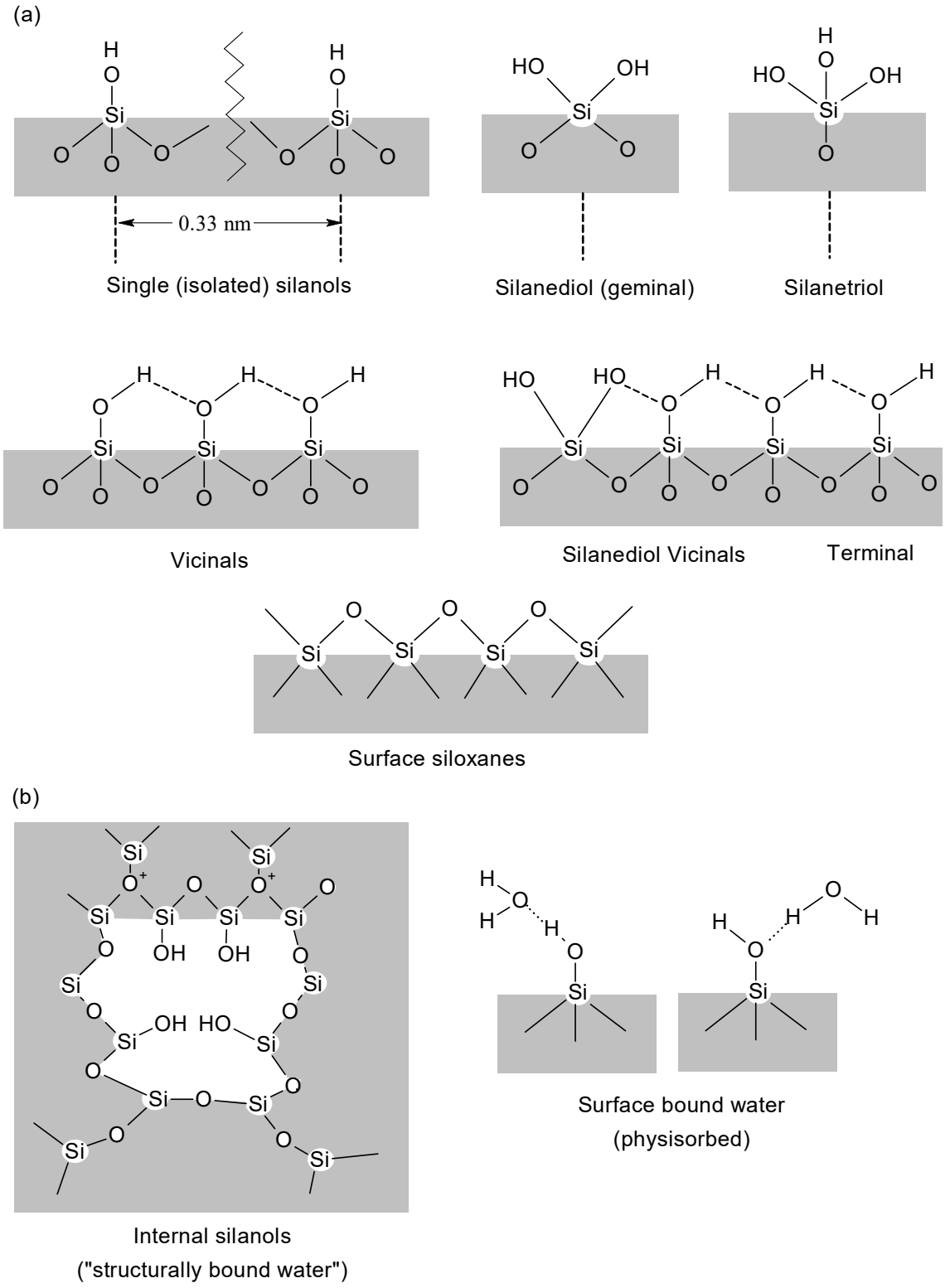

Figure 3.10. *a) Possible types of silanol groups and siloxane bridges occurring on the surface of colloidal silica particles; b) Surface bound water and internal silanols. (Adapted from (Flörke et al., 2000)).*

One of the most common modification in order to manufacture hydrophobic fumed silica are by substituting surface silanol groups with chlorotrimethylsilane. The resulting silica thus is no longer wettable by water and was introduced on the market under the trade name Aerosil® R972. The general reaction of hydrophobization of fumed silica using chlorotrimethylsilane substitution is illustrated in *figure 3.11.*

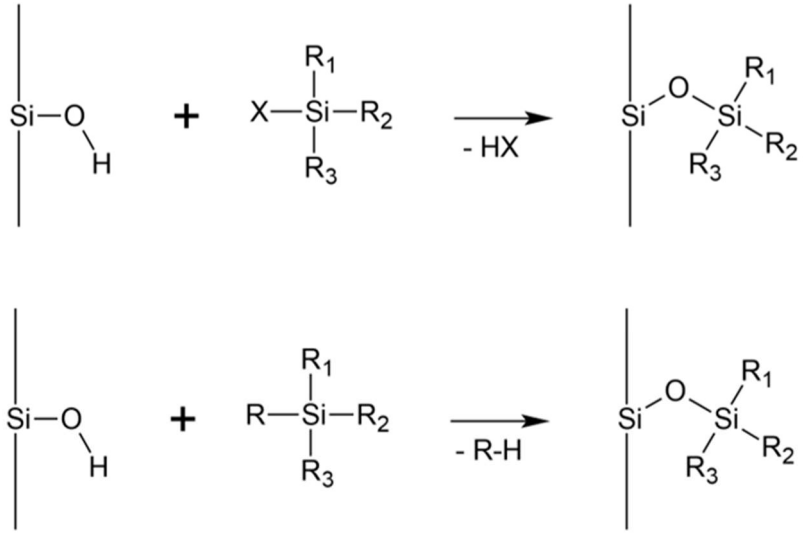

*where R_1, R_2 and R_3 are methyl groups and X is chlorine.

Figure 3.11. *Hydrophobization of fumed silica by chlorotrimethylsilane substitution. (Adapted from (Kloepfer-Geschichte, 2006))*

Not only hydrophobization, functionalizing silica particle surface could also allow for specific and unique applications of silica nanoparticles to be explored, something that would otherwise be inaccessible. For instance in biomedical application, Knežević et al. (2011) have successfully surface modified silica nanoparticles with pH or light sensitive triggers to release doxorubicin by capping aminopropyl trimethoxysilane (APTS) functionalized particles with nitroveratryl carbamate, which breaks away from the amino propyl group in the presence of UV radiation or in acidic environments.

In the fabrication of polymer nanocomposites, the incorporation of silica nanoparticles with an extremely large surface area would result in poor dispersion of fumed silica particles in the polymer matrix due to its incompatibility with the polymers and its large surface to volume ratio. For example, physical blending of hydrophobic polymers (*e.g*., polypropylene or poly(lactic acid)) with hydrophilic inorganic particles (e.g., fumed silica particles) could lead to phase separation or agglomeration of particles, resulting in poor mechanical, optical, and electrical properties. Functionalization of silica particles could produce a better interaction and dispersion of the silica particles in the polymeric matrix hence a significant improvement in the mechanical performance.

3.5 Selection of materials for the study

3.5.1. Poly(lactic acid)

An extrusion grades PLA resin with a trade name of PLA 4032D® purchased from NatureWorks LLC. (Arendonk, Belgium) in pellets form were selected for the study. Its technical characteristics are listed in *table 3.4.*

Table 3.4. *Technical specifications for PLA grades used.*

Properties	ASTM method	Ingeo 4032D®
Sample nomenclature	-	PLA/PLA neat
Tacticity	-	Random optical copolymers
D-lactide content (%)	-	2
Density, ρ (g.cm^{-3})	D1505-03	1.24
Number-average molecular weight, M_n (kg.mol^{-1}) [a]	D5296-97	77 ±1
Weight-average molecular weight, M_w (kg.mol^{-1}) [a]	D5296-97	165 ±4
z-Average molecular weight, M_z (kg.mol^{-1})[a]	D5296-97	298 ±34
Polydispersity index, *PDI* [a]	D5296-97	2.1 ±0.1
Melt Flow Index (g/10 min) (210ºC/2.16kg)[b]	D5296-97	6.4 ± 0.3

[a]Relative values determined for raw materials using SEC-DRI experiments (*c.f. chapter 6, section 6.2.1*).
[b] Value taken from Cailloux (2015).

Due to its hygroscopic nature, the presence of even small amounts of moisture will hydrolyze the biopolymer in the melt phase, reducing the molecular weight. It was recommended that the PLA resins must be thoroughly dried just prior to melt processing. It is absolutely essential that the resins is dried to less than 250 parts per million (ppm) (<0.025 wt.%) of moisture and maintained at this moisture level throughout the whole melt processing. However for melt processes with long residence times or using melt temperatures greater than 240 °C, a significantly reduced moisture content less than 50 ppm is recommended for melt processes for maximum retention of molecular weight and physical properties (NatureWorks LLC, 2005; NatureWorks LLC, 2007).

3.5.2. Styrene-acrylic multi-functional-epoxide oligomeric agent (SAmfE)

A styrene-acrylic multi-functional-epoxide oligomeric agent with a trade name of Joncryl ADR-4300F® has been selected for the present study. It was supplied by BASF® (Ludwigshafen, Germany). SAmfE is basically a resin specifically designed for reaction with polyesters, and has been shown to significantly increase the molecular weight of PLA and PET. Addition of SAmfE allows for MW enhancement at a much broader range of processing temperatures than neat polymer. The improvement of thermal stability, rheological and mechanical properties of modified PLA with SAmfE have been published by Alexy et al. (2011) and Cailloux et al. (2013). Its technical specifications are listed in *table 3.5.*

Table 3.5. *Technical specifications for the SAmfE agent used in this work (BASF Corporation, 2006; Cailloux, 2015).*

Properties	**Joncryl ADR-4300F®**
Material nomenclature	SAmfE/ reactive agent
Particle size (mm)	2.5 - 4.0
Specific gravity	1.08
Weight-average molecular weight, M_w (g.mol^{-1})	5500
Epoxy equivalent weight (g.mol^{-1})	433
Functionality	≈12
Glass transition, T_g (ºC)	56
Typical dosage (%)	0.1-1.0
Processing temperature range (ºC)	170-330
Glassy state	amorphous

Each SAmfE molecule has approximately 12 epoxide functional groups, which are reasonably stable under normal conditions but will react quickly and irreversibly with carboxylates. Ultimately, several polymer chains could be bonded to each SAmfE molecule. Its mid epoxy functionality formula is shown in *figure 3.12*.

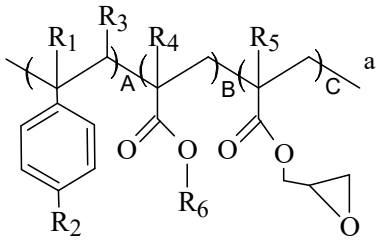

Figure 3.12. *Chemical formula of SAmfE agent (based on (BASF Corporation, 2006)).*

In which R_1–R_5 denotes H, CH_3, a higher alkyl group, or combination of them and R_6 is an alkyl group. Meanwhile SAmfE molecular chain are composed of three classes of solid or liquid monomers *i.e.* styrenics (referred to as repeat unit A) and methacrylates (referred to as repeat unit B) and its repeating units are in between 1 and 20. On the other hand, glycidyl acrylates (an epoxy-functional acrylate) (referred to as repeat unit C) in which the repeating units are in between 1 and 12.

3.5.3. Organically modified montmorillonite

Organically modified montmorillonite that is commecially known as Cloisite® 30B (referred to as o-MMT) in powder form was selected. o-MMT was surface modified with alkyl quaternary ammonium ions (MW ≥ 404.8 g.mol^{-1}) where T represents an alkyl group with approximately 65 % $C_{18}H_{37}$, 30 % $C_{16}H_{33}$, 5 % $C_{14}H_{29}$, were supplied by Southern Clay Products, Inc. According to the manufacturer's technical data sheet, the concentration of organomodifying agent in MMT is 90 meq/100g, which weight loss on ignition is about 30 %, the average particle size range ranged between 2-13 nm and the moisture content is below 2 % (Southern Clay Products, 2005). Its technical specifications are listed in *table 3.6.*

Table 3.6. *Technical characteristics of Cloisite 30B® (Alamri and Low, 2013).*

Properties	**Cloisite 30B®**
Material nomenclature	o-MMT/ reinforcing filler
Colour	Off-white
Density (g.com^{-3})	1.98
d-spacing (001) (nm)	1.85
Aspect ratio	200 - 1000
Surface area (m^2.g^{-1})	750
Mean particle size (μm)	6

3.5.3. Fumed silica and surface modified silica

Three high surface area fumed silica nanofillers which henceforth will be named as nano-SiO_2 (purity > 99.8% SiO_2) supplied in powder form were used as reinforcing filler. Their principal characteristics are reported in *table 3.7*. Introduction of epoxy and amino functional groups are used to induce chemical interactions between nano-SiO_2 filler surface functionalities and reactive agents.

Table 3.7. *Technical specifications for all fumed silicates.*

Trade name	**CAB-O-SIL® EH5**	**6851HN ®**	**6852HN ®**
Supplier	Cabot	Skyspring Nanomaterials Inc.	
Functional group of the surface modifier	-	Aminopropyl	Epoxy
Sample nomenclature	SiO_2	SiO_2-A	SiO_2-E
Surface area ($m^2.g^{-1}$)	380	90-130	90-130
Average particle diameter (nm)	7	10-20	10-20

Chapter 4. Processing Methods

The organization this chapter are divided into two main parts namely preparation of REX-PLA/o-MMT nanocomposites and REX-PLA/nano-SiO_2 composites preparation. Listed below are the specific details of how each type of nanocomposites were prepared at a laboratory scale to pilot plant scale using internal mixer and twin-screw extruder-calender respectively. Finally, the nomenclature used in conjunction with de-aging thermal treatment subjected on all the manufactured nanocomposites sheets are also explained in this chapter.

4.1 Preparation of REX-PLA/o-MMT Nanocomposites preparation

4.1.1. Preparation of Masterbatch

Initially, pristine PLA resin was dried at 80 ºC for 3h in a Piovan hopper-dryer (DSN506HE, Venice, Italy) (dew point = -40 ºC). SAmfE flakes on the other hand were vacuum-dried overnight at room temperature using silica gel as dessicant. Due to hydrophilic nature of o-MMT, it was dried at 130 ºC for 22 hours using a convection oven (J.P. Selecta, S.A., Barcelona, Spain) prior to processing. The utilization of powders is unappealing at an industrial scale due to the tendency of powders to generate respirable airborne dust during handling and becoming an inhalation hazard capable of causing severe irritation. In order to circumvent these issues, two different PLA-based masterbatches were initially prepared.

Firstly, SAmfE flakes was powdered using mortar and pestle and vacuum-dried overnight at room temperature over silica gel prior to extrusion. Next, PLA and SAmfE were melt compounded using a single screw extruder IQAP-LAP E30-25D (IQAP Group, Barcelona, Spain), with a screw diameter of 30 mm with an L/D ratio of 25 to manufacture a

masterbatch of PLA with reactive agent (referred to as MB_{SAmfE}). The extruder featured four heating zones which is set at 130, 132, 135 and 135 °C from the feeding zone to the die, respectively. The screw speed was set to 60 rpm and the measured t_{res} was 1 min. Prior to processing, PLA and 5 wt.% SAmfE were first dry-mixed by shaking them in a plastic ziplock bag and then groove fed into the extruder. The extrudate was water-cooled and pelletized (cut length ≈ 5 mm). The above processing conditions were selected in order to prevent premature chain extension/branching reactions.

On the other hand, PLA and o-MMT were melt compounded using an intermeshing co-rotating twin screw extruder COLLIN Kneter 25X24D with a screw diameter of 25 mm with an L/D ratio of 36, (COLLIN GmbH, Ebersberg, Germany) in order to manufacture a masterbatch of PLA with clay (referred to as MB_{clay}). The intermeshing co-rotating twin screws used comprises of three 100 mm kneading block segments that were equally distributed along screw length. The extruder contains seven heating zones set which is set at 140, 150, 155, 160, 165, 165 and 165 °C from the feeding zone to the die, respectively. The extruder was starve-fed while the screw speed was set to 120 rpm in order to enhance o-MMT dispersion leading to a nominal residence time (t_{res}) of 1.5 min. Once the extrusion line started and stabilized with pristine PLA resin, PLA and o-MMT were introduced simultaneously in the hopper of the feeding zone under a N_2 blanket. The feeding rate of o-MMT was adjusted to PLA resin in order to obtain a nominal dosage of 10 wt.% of o-MMT using a miniaturized prototype volumetric feeder. Vacuum was applied in the metering zone to remove any volatiles resulting from the extrusion stage. The extrudate was water-cooled and pelletized (cut length ≈ 5 mm). The masterbatch preparation conditions are summarized in *table 4.1.*

Table 4.1. *The masterbatch preparation conditions.*

Processing parameters	Conditions	Additional notes
Materials drying condition		
PLA		
Temperature (ºC)	80	dew point (-40 ºC)
Time (h)	3	-
SAmfE		
Temperature (ºC)	25 ±2	at room temperature with vacuum applied
Time (h)	overnight	over silica gel
o-MMT		
Temperature (ºC)	130 ºC	-
Time (h)	22	-
MB_{SAmfE} extrusion condition		
Screw speed (rpm)	60	-
Residence time (min)	1	-
Temperature profile		
Zone 1 (ºC) (Feeding zone)	130	SAmfE addition
Zone 2 (ºC) (melting and	132	-
Zone 3 (ºC) compression zones)	135	-
Zone 4 (ºC) (Die)	135	-
SAmfE nominal concentration (wt.%)	5	
MB_{clay} extrusion condition		
Screw speed (rpm)	120	-
Residence time (min)	1.5	-
Temperature profile		
Zone 1 (ºC) (Feeding zone)	140	Nitrogen blanket o-MMT addition
Zone 2 (ºC)	150	-
Zone 3 (ºC) (melting and	155	-
Zone 4 (ºC) compression zones)	160	-
Zone 5 (ºC)	165	-
Zone 6 (ºC) (metering zone)	165	Vacuum applied
Zone 7 (ºC) (die)	165	-
o-MMT nominal concentration (wt.%)	10	-
Masterbatches drying condition		
Temperature (ºC)	90	-
Time (h)	4	-

Subsequently, the respective PLA, SAmfE and o-MMT contents in the masterbatches prepared using the above processing methods were measured. *Table 4.2* list the actual composition of PLA, SAmfE and o-MMT content within each masterbatch prepared.

Table 4.2. *Type of masterbatch and the measured SAmfE and o-MMT composition in the respective masterbatches.*

Sample nomenclature	PLA content (wt.%)	Nominal SAmfE amount (wt.%)	Nominal o-MMT amount (wt.%)
MB_{SAmfE}[a]	95.9	4.1	0
MB_{clay}[b]	91.4	0	8.6

[a]Measured using Fourier Transform Infrared Spectroscopy (FTIR) measurements based on the Beer-Lambert law (Bellamy, 2010).
[b]Measured using calcination method according to ASTM D5630-01 standard.

In order to increase the degree of crystallinity, both masterbatches manufactured were subjected to a recrystallization process in a convection oven at 90 °C for 4 hours. This will enable the newly prepared masterbatches to be dried at higher temperatures for further processing.

4.1.2. Laboratory-scale: Internal Mixer

Pristine PLA resins, MB_{SAmfE} and MB_{clay} pellets were blended to reach nominal reactive agent concentration of 0.5 wt.% and nominal filler loading of 2.5 wt.% using laboratory scale internal mixer (Brabender Plastic-Corder W50EHT, Brabender GmbH & Co., Duisburg, Germany), equipped with a torque measuring system. Torque data acquisition was performed using a commercial WinMix Brabender Mixer software version 3.2.31. The mixing chamber had a nominal volume of 55 cm^3 and was equipped with two counter-rotating mixing screws (roller blade type "W"). Three different electrical heating elements and a compressed air cooling system allowed temperature conditioning in the mixing chamber. The bulk temperature of the processed material was measured using a separate thermocouple situated in the mixing chamber.

In order to prepare a predetermined concentration of o-MMT and SAmfE in PLA blend as previously stated, dilution of both filler and reactive agent concentration from the prepared masterbatch must be performed. Initially mixture ratio (MR) of each masterbatch is computed. The formula used to determine MR is shown in *equation 4.1.*

$$MR = \frac{Component\ percentage\ in\ masterbatch\ (\%)}{Predetermined\ dilution\ percentage\ of\ component\ in\ blend\ (\%)} \quad (4.1)$$

Next, the actual masterbatch weight required for dilution were calculated by the division of the total weight of blend with MR as shown in *equation 4.2.*

$$Masterbatch\ weight\ \ required\ for\ dilution\ (grams) = \frac{Total\ weight\ of\ blends\ (grams)}{MR} \quad (4.2)$$

Using the equations above, the actual weight of PLA pellets, MB_{SAmfE} and MB_{clay} blended to reach a nominal of 0.5 wt.% SAmfE concentration and 2.5 wt.% of o-MMT loading to prepare all the investigated blends were calculated and listed in *table 4.3*.

Table 4.3. *Actual weight PLA pellets, MB_{SAmfE} and MB_{clay} and composition of all investigated blends.*

Blends nomenclature	Actual weight PLA pellets (grams)	Actual weight MB_{SAmfE} amount (grams)	Actual weight MB_{clay} amount (grams)	Neat PLA content (wt.%)	Nominal SAmfE amount (wt.%)	Nominal o-MMT amount (wt.%)
PLA	50	0	0	100.0	0	0
REX-PLA	43.90	6.10	0	99.5	0.5	0
PLA-C	35.46	0	14.54	97.5	0	2.5
REX-PLA-C	29.36	6.10	14.54	97.0	0.5	2.5

Prior to processing, pristine PLA resin, MB_{SAmfE} and MB_{clay} pellets were vacuum-dried overnight at 55 °C using silica gel as dessicant to remove any excess moisture. The mixing chamber was preheated at a nominal temperature of 180 ºC and the screw rotation speed was set to 50 rpm. Initially, the mixing chamber was purged with nitrogen (N_2, 3 bars) for 2 minutes in order to remove the ambient atmosphere. Once all the setting conditions were optimized, predetermined amount of pre-dried PLA resin was introduced into the mixing chamber and the N_2 blanket was established depending on the blends formulation. Due to the solid state of PLA resin, the initial torque value increased exponentially. Subsequently once the resin melts, the high torque peak rapidly decreased. A completely melted state was observed within 4 minutes. This was considered as the starting point of all the experiments. Next, the corresponding amount of MB_{SAmfE} and MB_{clay} was added into the mixing chamber. Torque (Γ) vs. mixing time (t) traces was observed for 35 minutes to monitor the progression of the reaction. An

optimum reaction time of 13 min was deduced from these mixing experiments. Successive new blends were mixed using this optimum reaction time of 13 min. The internal mixer was stopped and the material was removed and cooled to room temperature. The laboratory scale processing conditions are summarized in *table 4.4.*

Table 4.4. *The laboratory scale processing conditions of PLA and REX-PLA/o-MMT nanocomposite blends.*

Processing parameters	Conditions	Additional notes
Materials drying condition		
PLA, MB_{SAmfE} and MB_{clay}		
Temperature (ºC)	55	Vacuum were applied
Time (h)	overnight	silica gel as dessicant
Melt-blending processing condition		
Screw speed (rpm)	50	-
Residence time (min)	35	Nitrogen blanket
Set point temperature (ºC)	180	-
SAmfE nominal concentration (wt.%)	0.5	-
o-MMT nominal concentration (wt.%)	2.5	-

4.1.3. Pilot-plan scale: Reactive extrusion-calendering

An identical COLLIN twin screw extruder as described for the preparation of MB_{clay} coupled to a COLLIN Teachline CR72T vertical three-polished chrome roller stack (COLLIN GmbH, Ebersberg, Germany) was used to manufacture 15 m of calendered sheets (nominal width: 100 mm; nominal thickness : 1 mm) of each formulation. The pilot plant scale of PLA and REX-PLA/o-MMT nanocomposites sheets preparation conditions are summarized in *table 4.3.*

Table 4.5. *The pilot plant scale of PLA and REX-PLA/o-MMT nanocomposites sheets preparation conditions.*

Processing parameters	Conditions	Additional notes
Materials drying condition		
PLA, MB_{SAmfE} and MB_{clay}		
Temperature (ºC)	80	dew point (-40ºC)
Time (h)	3	-
Reactive extrusion condition		
Screw speed (rpm)	40	-
Residence time (min)	4.5	-
Temperature profile		
Zone 1 (ºC) (Feeding zone)	150	Nitrogen blanket PLA and masterbatches addition
Zone 2 (ºC)	160	-
Zone 3 (ºC) (melting and	160	-
Zone 4 (ºC) compression zones)	160	-
Zone 5 (ºC)	170	-
Zone 6 (ºC) (metering zone)	175	Vacuum applied
Zone 7 (ºC) (die)	175	-
SAmfE nominal concentration (wt.%)	0.5	Diluted from 4.1 wt. % Joncryl content in MB_{SAmfE}
o-MMT nominal concentration (wt.%)	2.5	Diluted from 8.6 wt. % o-MMT content in MB_{Clay}
Calendering condition		
Chill roll temperature (ºC)	50	-
Chill roll speed (rpm)	1.25	-

Prior to processing, pristine PLA resins and both masterbatches were dry-mixed and subsequently dried at 80 °C for 3h in a Piovan hopper-dryer (DSN506Hel, Venice, Italy) in order to prevent hydrolysis degradations. Since the main emphasis of this work was a reactive extrusion-calendering process in a pilot plant, t_{res} was maximized using a screw speed of 40 rpm; thus leading to a maximum t_{res} of 4.43 min. The seven heating zones were set to 150, 160, 160, 160, 170, 175 and 175 °C from the feeding zone to the die, respectively. The extrusion line was started and stabilized with pristine PLA resins before introducing the corresponding dry blends in the hopper of the feeding zone under a N_2 blanket. Vacuum was applied in the metering zone to remove volatiles resulting from the different reactions. The chill roll temperature was set to 50 °C with a rotation speed of 1.25 rpm. A schematic representation of the cumulative compounding steps to prepare PLA and REX-PLA/o-MMT nanocomposites sheets is illustrated in *figure 4.1*.

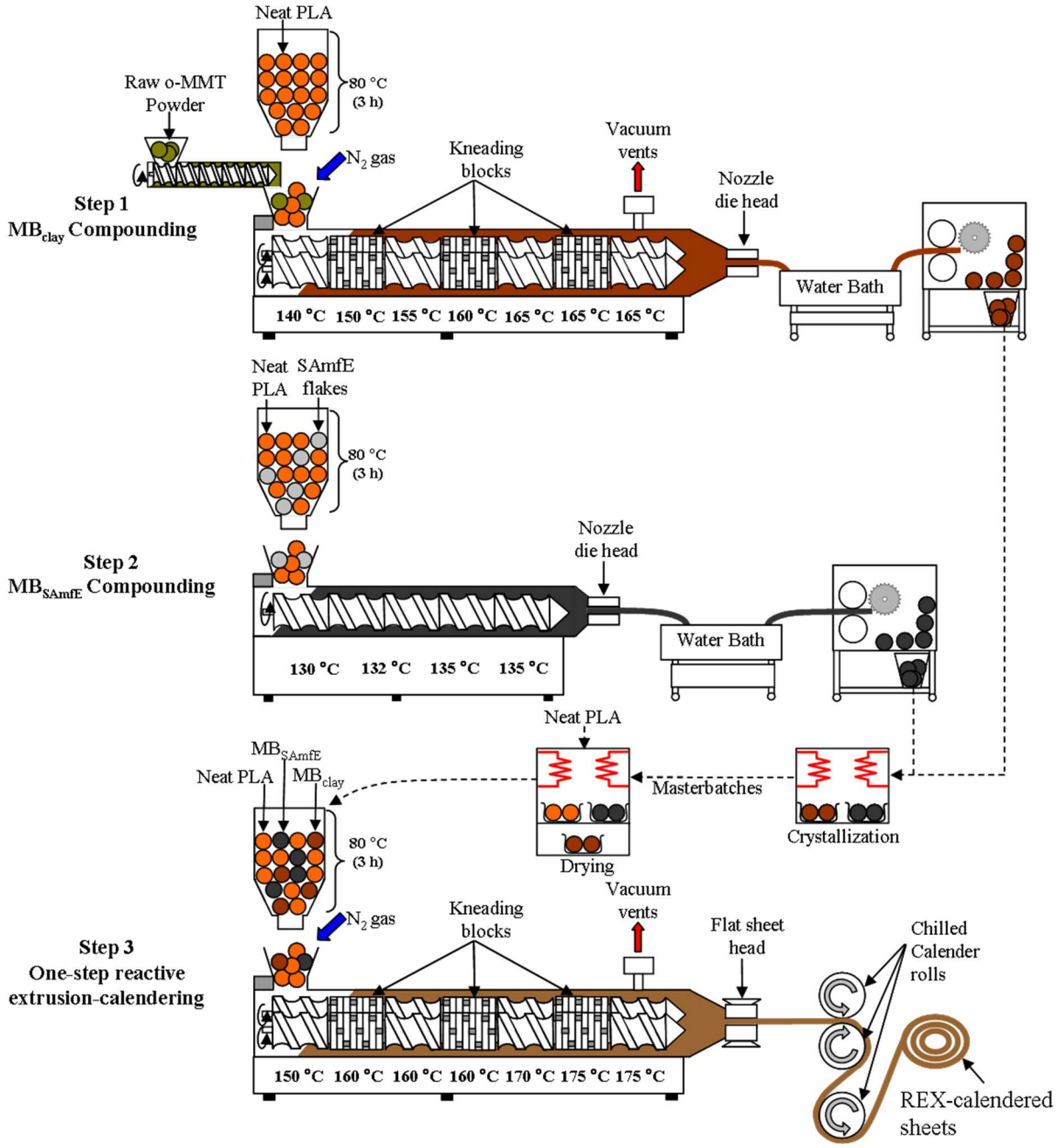

Figure 4.1. *Schematic representation of masterbatch manufacturing with successive reactive-extrusion processing.*

Regarding material formulation including SAmfE, the melt pressure at the die, which can be related to a basic rheological response of the processed material, was monitored throughout extrusion time. The die pressure increased with extrusion time up to a constant value. At this point, the die pressure remained relatively stable with the extrusion time; suggesting a stabilization of the rheological response of PLA to chain extension and/or branching reactions. Accordingly, sample prior to SAmfE addition (referred to as PLA) and from the stabilized die pressure regime (referred to as REX-PLA and REX-PLA-C, respectively) were analyzed. PLA-C samples were obtained from the part of sheet exhibiting a roughly constant clay content.

4.1.4. Sample nomenclature and de-aging thermal treatment

All the manufactured sheets are specified in *table 4.6* where the sheets were distinguished by the composition of SAmfE and o-MMT that was diluted from both MB_{SAmfE} and MB_{clay} pellets to reach nominal reactive agent concentration of 0.5 wt.% and nominal filler loading of 2.5 wt.%. However, it was found that the inherent brittleness of PLA will not affect the end use behaviour but also the handling and processing, leading to important limitations in large-scale production. The resulting brittleness usually leads to unfavorable outcomes especially during sample preparation. Cailloux (2015) have reported that these issues may be lessened by applying a thermal treatment at T_g or slightly above T_g to PLA. Based on this recommendation, a thermal treatment was applied to the extruded sheets following the procedures as depicted in *figure 4.2.* This is to minimize the occurrence of excessive defects during preparation of test specimens especially for mechanical and fracture characterizations.

During the thermal treatments, the manufactured sheets were subjected to heating at 60 ± 1 ºC for 40 minutes in a convection oven (J.P. Selecta, S.A., Barcelona, Spain) and immediately quenched in an ice water bath (2 ± 2 ºC) for 15 minutes after heating. The quenched sheets were immediately dried before different test specimens for mechanical and fracture test were extracted from the centre of the sheet parallel to the machine direction (MD) and stored at room temperature (26 ±2°C, 50 % RH) for one week prior to performing the test. This is done to equilibrate the thermodynamical state due to the high effect that aging process has on PLA which coincidently also simulate industrial storage conditions.

Table 4.6. *Notations and compositions of all investigated samples.*

Sample nomenclature	Neat PLA content (wt.%)	Nominal MB_{clay} amount (wt.%)	Nominal MB_{SAmfE} amount (wt.%)	Measured [a] o-MMT content (wt.%)	Measured [b] SAmfE content (wt.%)
PLA	100.0	0	0	-	-
REX-PLA	99.5	0	0.5	-	0.5 ±0.1
PLA-C	97.5	2.5	0	2.5 ±0.2	-
REX-PLA-C	97.0	2.5	0.5	2.5 ±0.1	0.5 ±0.1

[a] Measured using calcination method according to ASTM D5630-01 standard.
[b] Measured using Fourier Transform Infrared Spectroscopy (FTIR) measurements based on the Beer-Lambert law (Bellamy, 2010).

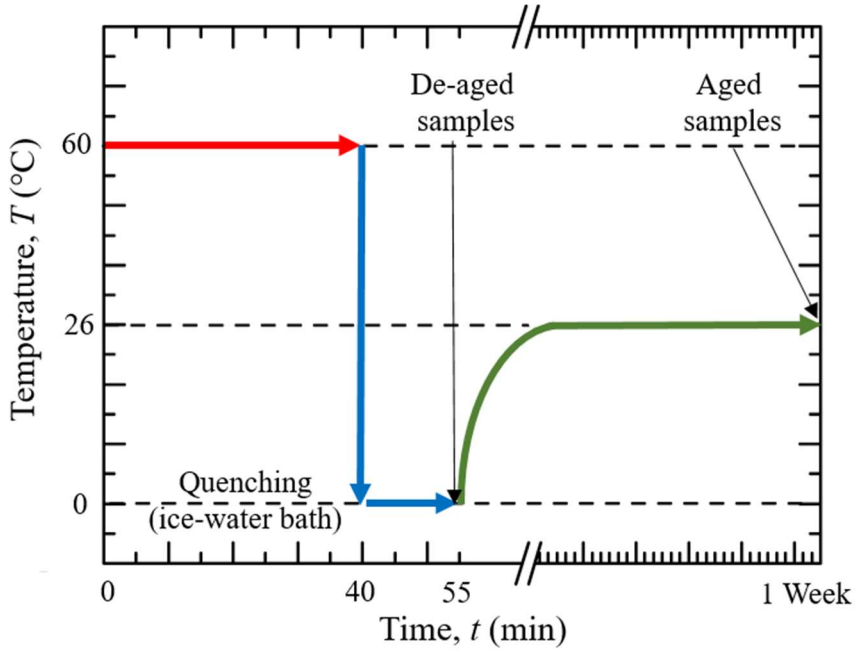

Figure 4.2. *Illustration of thermal treatment conditions subjected to the extruded sheets.*

4.2 REX-PLA/nano-SiO_2 composites preparation

4.2.1. Preparation of Masterbatch

For the production of REX-PLA/nano-SiO_2 composites sheets, preparation of masterbatch using solution casting technique has been exploited. It involves the use of a solvent that are able to dissolve PLA solely by mechanical stirring at room temperature and SiO_2 being able to be disperse in the solvent. Additionally, the solvent should also be volatile enough that it can be removed by evaporation at room temperature. In regards of these criteria, chloroform ($CHCl_3$) with 99% purity were chosen as the default solvent.

Three different PLA-based masterbatches using fumed silica (SiO_2), epoxy-surface modified silica (SiO_2-E) and amino-surface modified silica (SiO_2-A) (referred to as MB_{SiO2}, $MB_{SiO2\text{-}E}$ and $MB_{SiO2\text{-}A}$, respectively) were prepared. In a typical procedure, a 750 mL beaker equipped with a magnetic stirrer was charged with 500 mL of chloroform. At a stirring speed

of 300 rpm, 25 gram of PLA was dissolved for 3 hours at room temperature. After complete dissolution of PLA resin, 11 gram of the corresponding nano-SiO_2 fillers were added to the PLA solution and were subsequently stirred for an additional 3 hours. Next, the PLA-nano-SiO_2 solution was sonicated using a high-intensity ultrasonic bath (J.P. Selecta, S.A., Barcelona, Spain) for 30 minutes to achieve better homogenization. Then, the sonicated solution were casted on a glass plate and were dried for 12 hours at room temperature. Later, the dried films were collected and subsequently dried at 100 ºC for 2 hours in a convection oven. A domestic mixer were used to grind the dried films to obtain powder form. The powder was then sifted and homogenized using a 60 mesh woven metal wire filter.

On the other hand, the preparation of MB_{SAmfE} were performed using the intermeshing corotating twin screw extruder as previously described in *section 4.1.3*. Similar drying conditions were used for both PLA resin and SAmfE powder. However the extruder temperatures were set at 150, 160, 160, 160, 170, 175 and 175 °C from the feeding zone to the die, respectively. The extruder was starve-fed while the screw speed was set to 35 rpm. The extrudate was then water-cooled and pelletized (cut length ≈ 5 mm). Lastly, all prepared masterbatches were recrystallized in a convection oven at 90 °C for 4 hours. The masterbatch preparation conditions are summarized in *table 4.7*.

Table 4.7. *PLA-nano-SiO_2 and REX-PLA masterbatch preparation conditions.*

Processing parameters	Conditions	Additional notes
Solution casting conditions		
PLA resin dissolution in chloroform		
Temperature (ºC)	26 ±2	at room temperature
Time (h)	3	-
nano-SiO_2 dissolution in PLA solution		
Temperature (ºC)	26 ±2	at room temperature
Time (h)	3	-
PLA- nano-SiO_2 solution sonication conditions		
Temperature (ºC)	26 ±2	at room temperature
Time (h)	0.5	-
PLA- nano-SiO_2 solution film casting		
Temperature (ºC)	26 ±2	at room temperature
Time (h)	12	-
PLA- nano-SiO_2 film drying conditions		
Temperature (ºC)	100	-
Time (h)	2	-
Film grinding and homogenization	-	
Nominal powder size (μm)	≈ 250	Using 60 mesh domestic filter
SiO_2, SiO_2-E and SiO_2-A nominal concentration (wt.%)	30	-
MB_{SAmfE} extrusion condition		
Screw speed (rpm)	35	-
Residence time (min)	4.1	-
Temperature profile		
Zone 1 (ºC) (Feeding zone)	45	Nitrogen blanket SAmfE addition
Zone 2 (ºC)	165	-
Zone 3 (ºC) (melting and	165	-
Zone 4 (ºC) compression zones)	170	-
Zone 5 (ºC)	180	-
Zone 6 (ºC) (metering zone)	190	Vacuum applied
Zone 7 (ºC) (die)	190	-
SAmfE nominal concentration (wt.%)	0.6	-
Masterbatches drying condition		
Temperature (ºC)	90	-
Time (h)	4	-

Subsequently, the respective PLA, SAmfE and o-MMT contents in the masterbatches prepared using the above processing methods were measured. *Table 4.8* list the actual composition of PLA, SiO_2, SiO_2-E and SiO_2-A content within each masterbatch prepared.

Table 4.8. *Type of masterbatch and the measured SAmfE and nanosilica composition in the respective masterbatches.*

Sample nomenclature	PLA content (wt.%)	Nominal SAmfE amount[a] (wt.%)	Nominal Nanosilica amount[b] (wt.%)
MB_{SAmfE}[a]	95.9	4.1	0
MB_{SiO2}[b]	71.3	0	28.7
$MB_{SiO2\text{-}E}$[b]	71.1	0	28.9
$MB_{SiO2\text{-}A}$[b]	71.9	0	28.1

[a]Measured using Fourier Transform Infrared Spectroscopy (FTIR) measurements based on the Beer-Lambert law (Bellamy, 2010).
[b]Measured using Thermogravimetric Analysis (TGA) according to ASTM E1131-08 standard.

4.2.2. Laboratory-scale: Internal Mixer

Similar to REX-PLA/o-MMT nanocomposites, the effects of nano-SiO_2 and SAmfE on the PLA melt behaviour were monitored using an internal mixer as previously detailed in *section 4.1.2*. The torque, which can be related to the apparent viscosity, was used to follow the evolution of the different reactions (*i.e.* degradation as well as chain extension/branching reactions).

Prior to melt mixing, the actual weight of PLA, MB_{SAmfE}, MB_{SiO2}, $MB_{SiO2\text{-}E}$ and $MB_{SiO2\text{-}A}$ pellets required for dilution for preparation of all the investigated blends were calculated using *equations 4.1* and *4.2*. Generally the blends investigated composed of

nominal nanosilica filler loading of 2.5 wt.% and nominal reactive agent concentration of 0.5 wt.%. The actual weight of PLA, MB_{SAmfE}, MB_{SiO2}, $MB_{SiO2\text{-}E}$ and $MB_{SiO2\text{-}A}$ pellets used and composition of blends are listed in *table 4.9.*

Table 4.9. *Actual weight PLA pellets and masterbatches and the composition of all investigated blends.*

Blends nomenclature	Actual weight PLA pellets (grams)	Actual weight MB_{SAmfE} amount (grams)	Actual weight MB_{SiO2} amount (grams)	Actual weight $MB_{SiO2\text{-}E}$ amount (grams)	Actual weight $MB_{SiO2\text{-}A}$ amount (grams)	Neat PLA content (wt.%)	Nominal SAmfE amount (wt.%)	Nominal nano-SiO_2 amount (wt.%)
REX-PLA	43.90	6.10	0	0	0	99.5	0.5	0
REX-PLA/ SiO_2	39.54	6.10	4.36	0	0	97.0	0.5	2.5
REX-PLA/ SiO_2-E	39.57	6.10	0	4.33	0	97.0	0.5	2.5
REX-PLA/ SiO_2-A	39.45	6.10	0	0	4.45	97.0	0.5	2.5

Prior to melt mixing, PLA resin, MB_{SAmfE}, MB_{SiO2}, $MB_{SiO2\text{-}E}$ and $MB_{SiO2\text{-}A}$ pellets were vacuum-dried overnight at 55 °C using silica gel as a dessicant. Initially, a predetermined amount of PLA pellets was introduced into the mixing chamber depending on the blends formulation. A continuous flow of N_2 gas blanket was introduced in the mixing chamber throughout the mixing process in order to minimize thermo-oxidative degradations. Due to the solid state of PLA pellets, the initial torque value increased exponentially. Subsequently once the resin melts, the high torque peak rapidly decreased. A completely molten state was observed within 4 min. This was considered as the starting point of the experiments. Next, the corresponding amount of MB_{SAmfE}, MB_{SiO2}, $MB_{SiO2\text{-}E}$ and $MB_{SiO2\text{-}A}$ pellets was added depending on the blends formulation into the mixing chamber at this time. Melt blending were performed using identical set point temperature and screw speed as previously described (refer to *section 4.1.2.*). For each blend, torque (Γ) vs. mixing time (t) was monitored for 30 min.

The laboratory scale processing conditions of REX-PLA and REX-PLA/nano-SiO_2 composites blends are summarized in *table 4.10.*

Table 4.10. *The laboratory scale processing conditions of REX-PLA and REX-PLA/SiO_2 nanocomposite blends.*

Processing parameters	Conditions	Additional notes
Materials drying condition		
PLA, MB_{SAmfE}, MB_{SiO2}, MB_{SiO2-E} and MB_{SiO2-A}		
Temperature (ºC)	55	Vacuum were applied
Time (h)	overnight	silica gel as dessicant
Melt-blending processing condition		
Screw speed (rpm)	50	-
Residence time (min)	30	Nitrogen blanket
Set point temperature (ºC)	180	-
SAmfE nominal concentration (wt.%)	0.5	Diluted from 4.1 wt. % Joncryl content in MB_{SAmfE}
SiO_2, SiO_2-E and SiO_2-A nominal concentration (wt.%)	2.5	Diluted from ≈ 28 wt. % nanosilica content in respective masterbatch

4.2.3. Pilot-plan scale: Reactive extrusion-calendering

In order to avoid moisture absorption, PLA and MB_{SAmfE} pellets were dried at 80 ºC for 3h in a Piovan hopper-dryer as described in *section 4.1.3* before processing. On the other hand, all the previously prepared PLA-based masterbatches with SiO_2, SiO_2-A and SiO_2-E (referred to as MB_{SiO2}) nanofillers were vacuum-dried at 90 ºC for 4 hours over silica-gel.

Next, MB_{SiO2} was melt blended with PLA and MB_{SAmfE} pellets using the twin screw extruder as previously described in *section 4.1.3* for homogenization. The seven heating zone of the extruder were set at 150, 170, 180, 190, 195, 200 and 200 °C from the feeding zone to the die, respectively. The screw speed was 45 rpm and t_{res} of 4.5 min. The feeding rate of MB_{SiO2} was adjusted to PLA and MB_{SAmfE} in order to obtain a nominal dosage of 2.5 wt. % of SiO_2 using a Collin twin screw volumetric feeder (COLLIN GmbH, Ebersberg, Germany). N_2 blanket were supplied in the feeding zone while vacuum was applied in the metering zone. The extrudates (referred to as REX-PLA/SiO_2, REX-PLA/SiO_2-A and REX-PLA/SiO_2-E, respectively) were water-cooled and pelletized (cut length ≈ 5 mm). Next, all the pellets were subjected to recrystallization process by placing it in a convection oven at 90 °C for 4h prior to nanocomposites sheet fabrication. *Table 4.11* summarized the processing conditions used for preparation of REX-PLA/nano-SiO_2 composites pellets at a pilot plant scale.

Table 4.11. *The pilot plant scale of REX-PLA/nano-SiO_2 composites pellets preparation conditions.*

Processing parameters	Conditions	Additional notes
Materials drying condition		
PLA and MB_{SAmfE},		
Temperature (ºC)	80	dew point (-40ºC)
Time (h)	3	-
MB_{SiO2}, MB_{SiO2-E} and MB_{SiO2-A}		
Temperature (ºC)	90	vacuum were applied
Time (h)	4	silica gel as dessicant
Extrusion for production of pellets condition		
Screw speed (rpm)	45	-
Residence time (min)	4.5	-
Temperature profile		
Zone 1 (ºC) (Feeding zone)	150	nitrogen blanket PLA and masterbatches addition
Zone 2 (ºC)	170	-
Zone 3 (ºC) (melting and	180	-
Zone 4 (ºC) compression zones)	190	-
Zone 5 (ºC)	195	-
Zone 6 (ºC) (metering zone)	200	vacuum were applied
Zone 7 (ºC) (die)	200	-
SAmfE nominal concentration (wt.%)	0.5	
o-MMT nominal concentration (wt.%)	2.5	-
Masterbatches drying condition		
Temperature (ºC)	90	-
Time (h)	4	-

Finally, an identical twin screw extruder as described above coupled to a COLLIN Teachline CR72T vertical three-polished chrome roller stack (COLLIN GmbH, Ebersberg, Germany) with similar processing conditions as described above was used in order to manufacture 15 meters of calendered sheets (nominal width: 100 mm; nominal thickness: 0.6 mm) of each formulation. The pilot plant scale of REX-PLA and REX-PLA/nano-SiO_2 composites sheets preparation conditions are summarized in *table 4.12.*

Table 4.12. *The pilot plant scale of REX-PLA/nano-SiO_2 composites sheets preparation conditions.*

Processing parameters	Conditions	Additional notes
Materials drying condition		
PLA and MB_{SAmfE}		
Temperature (ºC)	80	dew point (-40ºC)
Time (h)	3	-
MB_{SiO2}, $MB_{SiO2\text{-}E}$ and $MB_{SiO2\text{-}A}$		
Temperature (ºC)	90	vacuum were applied
Time (h)	4	silica gel as dessicant
Extrusion for production of sheet condition		
Screw speed (rpm)	45	-
Residence time (min)	4.5	-
Temperature profile		
Zone 1 (ºC) (Feeding zone)	150	Nitrogen blanket PLA and masterbatches addition
Zone 2 (ºC)	170	-
Zone 3 (ºC) (melting and	180	-
Zone 4 (ºC) compression zones)	190	-
Zone 5 (ºC)	195	-
Zone 6 (ºC) (metering zone)	200	Vacuum applied
Zone 7 (ºC) (die)	200	-
SAmfE nominal concentration (wt.%)	0.6	
o-MMT nominal concentration (wt.%)	3	-
Calendering condition		
Chill roll temperature (ºC)	50	-
Chill roll speed (rpm)	1.25	-

4.2.4. Sample nomenclature and de-aging thermal treatment

All the nanocomposites sheets manufactured are specified in *table 4.13* where the sheets were distinguished by the type of nano-SiO_2 incorporated. Similarly, it was observed that all the manufactured REX-PLA and REX-PLA/nano-SiO_2 composites sheets were brittle. A thermal treatment was applied to the extruded sheets following the procedures as depicted in *figure 4.2.* The thermal treatment procedure has been described in *section 4.1.4.*

Table 4.13. *Notations and compositions of all investigated samples.*

Sample nomenclature	Neat PLA amount (wt.%)	Nominal nanosilica amount (wt.%)	Nominal SAmfE amount (wt.%)	Measured [a] nanosilica content (wt.%)	Measured [b] SAmfE content (wt.%)
REX-PLA	100.0	0	0.5	-	-
REX-PLA/SiO_2	97.0	2.5	0.5	1.9 ±0.3	0.5 ±0.1
REX-PLA/SiO_2-E	97.0	2.5	0.5	2.5 ±0.4	0.5 ±0.1
REX-PLA/SiO_2-A	97.0	2.5	0.5	2.2 ±0.2	0.5 ±0.1

[a]Measured using Thermogravimetric Analysis (TGA) according to ASTM E1131 - 08 standard.
[b]Measured using Fourier Transform Infrared Spectroscopy (FTIR) measurements based on the Beer-Lambert law (Bellamy, 2010)

Chapter 5. Experimental methods

5.1. Physico-chemical characterization

5.1.1. Fourier Transform-Infrared Spectroscopy (FT-IR)

FT-IR Absorption spectra of REX-PLA masterbatch for the determination of SAmfE content were recorded using Nicolet 6700 FT-IR spectrometer (Thermo Fisher Scientific, Waltham, MA, USA) using transmission sampling technique. The FT-IR spectra of the specimen were obtained at a total of 32 scans using wavenumber interval ranging from 400 to 4000 cm^{-1} at 4 cm^{-1} resolution. Data were acquired and analyzed using a commercial OMNIC software version 7.3 Service Pack 1.

In order to quantify of the SAmfE content in REX-PLA extruded sheets, an internal standard FT-IR method based on Beer-Lambert law (*c.f. equation 5.1*) was created.

$$A = \varepsilon . C . l. \tag{5.1}$$

Where A is the is the measured absorbance, ε is the wavelength-dependent absorptivity coefficient, *C* is the molar concentration of the attenuating species and *l* the path length.

Initially, 20 different PLA/SAmfE solutions were prepared ranging from 0 to 80 wt.% by dissolving a total amount of one gram of PLA together with several concentrations of SAmfE using reagent grade chloroform ($CHCl_3$) as the solvent (with purity ≥ 99.8%). Next, all the solution prepared was cast onto glass plates and moved along the glass plate to distribute the solution as evenly as possible. All the casted solutions were then allowed to air-dry for 15 minutes prior to FT-IR measurements. The integrated areas of peak at 1600 and 1490 cm^{-1} which corresponds to SAmfE aromatic ring were normalized to the integrated peak area that

represents the vibrations stretching C-OO groups of PLA (870 cm^{-1}) which was chosen as the internal standard according to *equation 5.2*.

$$\frac{A_{SAmfE}}{A_{PLA}} = k\frac{C_{SAmfE}}{C_{PLA}} \tag{5.2}$$

Where A_{SAmfE} is the integrated absorbance peak area of SAmfE group and C_{SAmfE} the percentage of SAmfE added in the solution. A_{PLA} is the integrated absorbance peak area of a characteristic PLA group and C_{PLA} the percentage of PLA dissolved in the solution. k is the relative response factor.

These experimental points were then plotted and a regression line is fitted using the method of least-squares. The resultant calibration curves are shown in *figure 5.1*. k was determined from the slope as indicated in the respective curve. Looking at *figure 5.1* revealed that generally both calibration curve revealed good linear proportionality between the relative peak areas and relative concentrations of C_{SAmfE}/C_{PLA} to a "critical" C_{SAmfE}/C_{PLA} ratios. However above this ratio, a vertical linearity deviation was observed which has been similarly reported by Cailloux (2015).

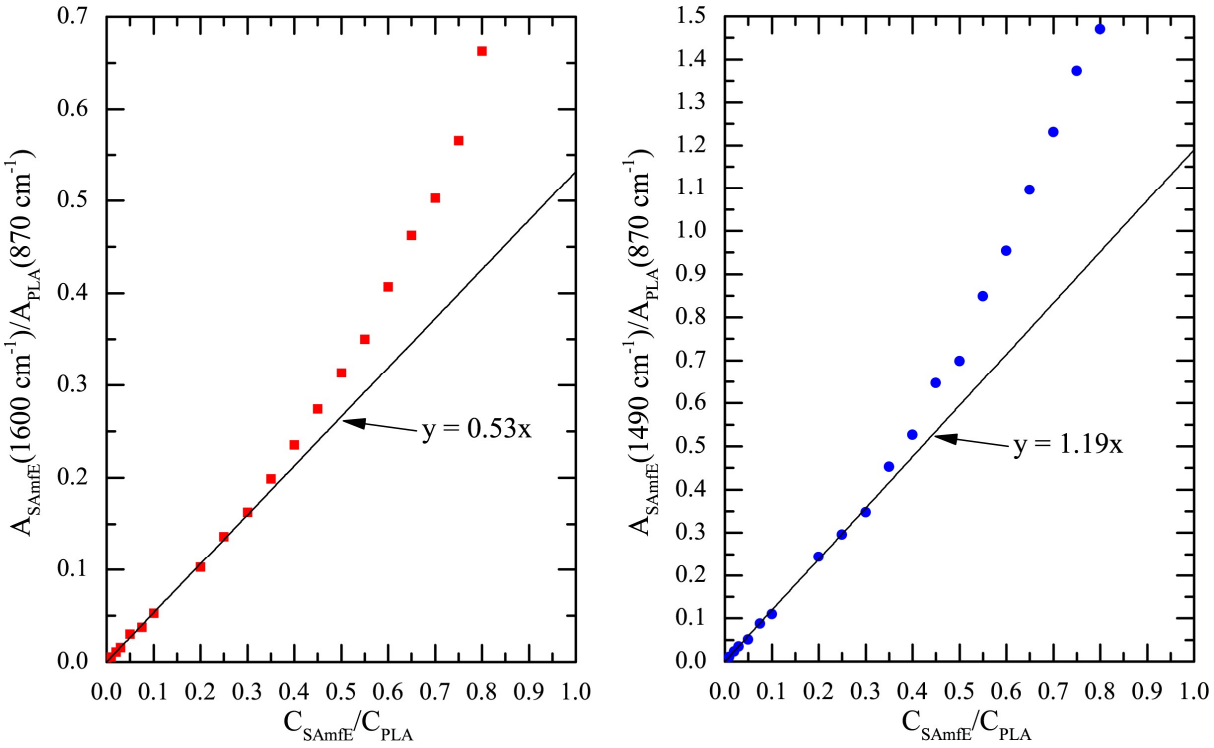

Figure 5.1. FT-IR calibration curves generated using different concentration of SAmfE. The relative response *k* is indicated for each curve.

On the other hand, for verification of the surface functionalization of the nanosilica used, its respective IR spectra were investigated using FT-IR Absorption spectra of REX-PLA nanocomposites sheets/films were recorded using Jasco 4100 spectrometer (Jasco International, Tokyo, Japan) in attenuated total reflectance (ATR) mode. Spectra were obtained in the wavenumber interval ranging from 600 to 4000 cm^{-1} with a total of 16 scans and a resolution of 4 cm^{-1}. Data were acquired and analyzed using a Jasco Spectra Manager^{TM} CFR Part II Version 2.04.

In order to validate nano-SiO_2 grafting onto REX-PLA, its respective IR absorption spectra were investigated using Jasco 4100 spectrometer (Jasco International, Tokyo, Japan) in attenuated total reflectance (ATR) mode which has been similarly described in the preceding paragraphs. Spectra were obtained in the wavenumber interval ranging from 600 to 4000 cm^{-1} with a total of 16 scans and a resolution of 4 cm^{-1}. Similarly, all the data were analyzed using a Jasco Spectra Manager^{TM} CFR Part II Version 2.04.

5.1.2. Wide-Angle X-ray Diffraction (WAXD)

The effect of SAmfE grafting on the *d*-interlayer spacing of clay platelets was investigated using Wide-Angle X-ray Diffraction (WAXD). WAXD experiments were performed using a Bruker D8 Advance Diffractometer (Bruker AXS GmbH, Karlsruhe, Germany), with line collimation equipped with Cu-K_α radiation at a wavelength of 0.1542 nm, tube voltage of 40 kV and tube current of 40 mA was used to obtain XRD patterns. The interlayer distance was determined from the position of the diffraction peak, according to the Bragg's diffraction equation, *equation 5.3* (Kumar et al., 2010).

$$2d\ sin\theta = n\lambda \tag{5.3}$$

Where *d* is the interlamellar spacing, θ the angle of reflection, *n* the order of reflection and λ the wavelength of radiation.

5.1.3. Size Exclusion Chromatography (SEC)

Molecular weight distributions (MWD) were determined from size exclusion chromatography (SEC) analysis, using an Agilent HPLC model Infinity 1260 SEC system (Agilent Technologies, Santa Clara, CA, USA) equipped with a differential refractive detector (SEC-DRI) at room temperature. An Agilent PL hexafluoroisopropanol (HFIP) gel specialist

column (300 x 7.5 mm) with a separation range from 200 to 800 kg.mol^{-1} was used at a flow rate of 2 mL.min^{-1}. Hexafluoroisopropanol (1,1,1,3,3,3-hexafluoro-2-propanol, HFIP) containing 0.02 mol.L^{-1} of sodium trifluoroisopropanol was used as the mobile phase to achieve isocratic elution and prevent the "polyelectrolyte effect". The calibration were performed by injecting a mixture of 7 narrow poly(methyl methacrylate) standards with MWs covering the entire MW range of the investigated samples (from 2 to 900 kg.mol^{-1}) to perform the logarithm of molecular weight vs. retention time calibration using the peak position calibration method (Eksteen and Pardue, 2003).

Several prerequisites would have to be fulfilled to perform a reliable analysis. Initially, a full dissolution of the sample was achieved by dissolving a predetermined amount of each material for 20 minutes at room temperature. However, clay must be removed by centrifugation prior to proceeding with SEC analysis. Next, polystyrene-divinylbenzene (PS-DVB) packings were selected as the stationary phase due to its chemical inertness to prevent absorption issues. In order to avoid shear degradation in the injector and to extensive band broadening due to viscous fingering, a suitable injection concentration was determined using *equation 5.4* (Gaborieau and Castignolles, 2011).

$$[\eta] \times C \times 0.1 \times V_{inj} < 0.5 \; to \; 0.1 \qquad (5.4)$$

where $[\eta]$ is the intrinsic viscosity in dL.g^{-1}, C is the injection concentration in g.L^{-1}, and V_{inj} is the injection volume in mL. Plot of distribution of characteristic molecular weight averages in a polymer with a Schultz–Flory distribution is depicted in *figure 5.2.* The calculations for number-average molecular weight (M_n), the weight average molecular weight (M_w) and z-average molecular weight (M_z) for all the investigated samples were computed using the equations below (Fried, 2003; Van Krevelen and Te Nijenhuis, 2009)

$$M_n = \frac{\int_0^\infty w(M)dM}{\int_0^\infty w(M)/Mdm} \tag{5.5}$$

$$M_w = \frac{\int_0^\infty M.w(M)dM}{\int_0^\infty w(M)dm} \tag{5.6}$$

$$M_z = \frac{\int_0^\infty M^2.w(M)dM}{\int_0^\infty M.w(M)dm} \tag{5.7}$$

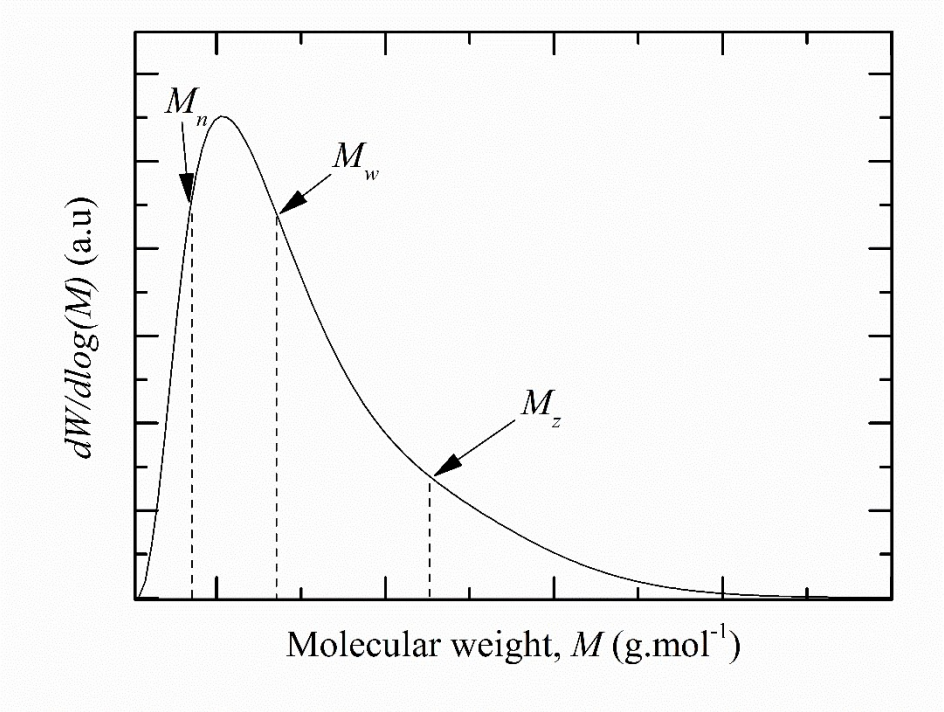

Figure 5.2. *Plot of distribution of molar mass in a polymer with a Schultz–Flory distribution. Dashed lines indicate the position of M_n, M_w and M_z values (Adapted from (Van Krevelen and Te Nijenhuis, 2009))*

The polydispersity index (PDI) is a measure of the distribution of molecular mass in a given polymer sample. PDI of a polymer is calculated using *equation (5.8)*:

$$PDI = \frac{M_w}{M_n} \tag{5.8}$$

5.1.4. Intrinsic Viscosity

The intrinsic viscosity of the polymer is an experimental quantity derived from the measured viscosity of the polymer in solution or calculated using Mark-Houwink constants (Poole and Schuette, 1984). The dilution–extrapolation procedures is a simple method to determine the molecular weight a solute of well-known structure and solution behavior by measurement of viscosity, in which viscosity of liquid is measured by comparing the viscosity of an unknown liquid with that of liquid whose viscosity is known. In this method, viscosity of liquid is measured by comparing the flow times of two liquids of equal volumes using similar viscometer (Tesoro, 1984).

Ubbelohde-type viscometer was used for measuring intrinsic viscosity of a polymer sample as depicted in *figure 5.3*. The viscometer was statically installed vertically in a precision constant-temperature water bath to allow the flow times of the various solutions between the gauge lines to be measured. The solution of highest concentration was always prepared first. The first solution is introduced into the reservoir then sucked through the capillary and measuring bulb. The solution is then allowed to travel back through the measuring bulb and the time it takes for the liquid to pass through the two calibrated marks is a measure for viscosity.

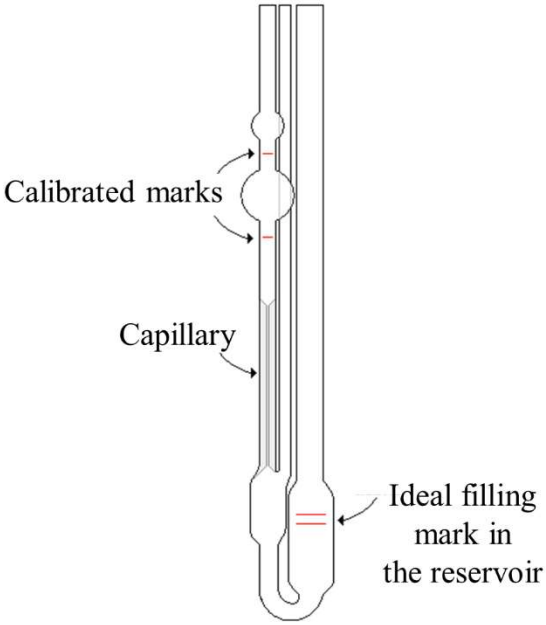

Figure 5.3. *Ubbelohde-type viscometer used for intrinsic viscosity measurement.*

For the highest precision, the following precautions are observed. The viscosity measurement is made in a constant-temperature bath regulated to at least 30 ±0.2 °C with chloroform ($CHCl_3$) as the solvent. The measurement for each concentration were repeated until five consecutive values differ from their mean value by no more than 0.5 seconds. The efflux time is kept preferably more than 100 seconds to minimize the need for applying corrections to the observed data. Next, flow times of four different concentrations (concentration range 0 - 1.5 wt. %) of the investigated sample solution were recorded, each repeated at least five times.

Initially, inherent/reduced viscosity (η_r) and specific/inherent viscosity (η_{sp}) were calculated from time of flow recorded at various concentrations using the equations below.

$$\eta_r = t/t_0 \tag{5.9}$$

Where η_r is relative viscosity, t is time taken for solution (REX-PLA/nanofillers) to pass through the calibration marks, t_0 is is time taken for solvent ($CHCl_3$) to pass through the calibration mark.

$$\eta_{sp} = t - t_0/t_0 \tag{5.10}$$

Where η_{sp} is specific viscosity, t is time taken for solution (REX-PLA/nanofillers) to pass through the calibration marks, t_0 is is time taken for solvent ($CHCl_3$) to pass through the calibration mark. Subsequently, intrinsic viscosities were obtained by extrapolating plots of η_{sp}/c and η_r/c versus c plots to zero concentrations as depicted in *figure 5.4.* The intrinsic viscosity is given by the common ordinate intercept of these graphs as indicated by the arrow.

The intrinsic viscosity, η as function of average molecular weight, M is represented by Mark-Houwink-Sakurada equations:

$$[\eta] = KM_v{}^{\alpha} \tag{5.9}$$

where K and α are constants for a given polymer–solvent–temperature system. Schindler and Harper (1979) presented K = 2.21 x 10^{-4}; α = 0.77 as Mark-Houwink constants for PLA in chloroform at 30 °C. Subsequently M_n and M_w can be determined using *equation 5.12* and *5.13,* respectively (Fried, 2003; Hiemenz and Lodge, 2007).

$$\bar{M}_n : \bar{M}_v : \bar{M}_w = 1 : (1 + \alpha) : 2 \tag{5.12}$$

$$\overline{M_n} = \left[\frac{\sum N_i M_i}{\sum N_i}\right] = \overline{M_v} = \left[\frac{\sum N_i M_i^{(1+a)}}{\sum N_i M_i}\right] = \overline{M_w} = \left[\frac{\sum N_i M_i^{(2)}}{\sum N_i M_i}\right] \tag{5.13}$$

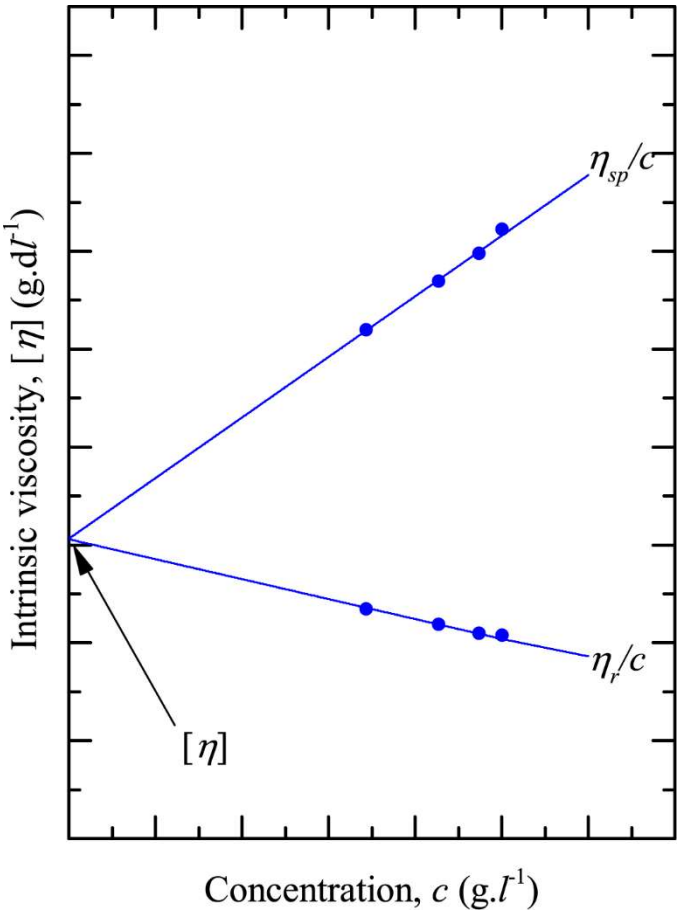

Figure 5.4.*Typical reduced and inherent viscosity concentration curves observed for all of the investigated samples. Arrow indicates the intrinsic viscosity value determined by the intercept between reduced and inherent viscosity plot.*

5.1.5. Differential Scanning Calorimetry (DSC)

a) Standard thermal analysis

DSC analysis was conducted in a DSC 2000 equipment (TA Instruments, New Castle, DE, USA) that is cooled using an Intracooler TA Instruments TC100 Chiller system (TA Instruments, New Castle, DE, USA) under dried N_2 atmosphere. 3 to 4 mg of each sample were encapsulated in aluminium T_{zero} pan. Initially, experiments were conducted at a heating/cooling rate of 10 ºC.min^{-1} using the following protocol:

- **First heating scan (H1)** from 30 °C to 200 °C and isothermally held at 200 °C for t_{eq} = 2 min in order to reveal the thermal transitions and to erase the previous thermal history, respectively.
- **Cooling scan (C)** from 200 °C to 30 °C in order to induce a controlled or "standard" thermal history and isothermally held at 30 °C for t_{eq} = 1 min.
- **Second heating scan (H2)** from 30 °C to 200 °C in order to determine the thermal properties.

In order to improve accuracy and to minimize the errors brought by baseline fluctuations and calibrations, this procedure were repeated three times using fresh samples taken from different zones of the manufactured sheets.

The following calorimetric parameters were determined from the above steps:

- **The midpoint glass transition temperature** ($\boldsymbol{T_{g,m}}$). It is defined as the temperature at half-height of the heat capacity surge ($1/2\Delta C_p$) or alternatively called as the "temperature of half-unfreezing". T_g can also be taken as the "inflection" point, which is slightly different and corresponds to the peak in the derivative of the heat flow or heat capacity versus temperature. However, the mid-point method T_g has been generally considered to be more reliable than the method using the "inflection" temperature (Menczel et al., 2008).
- The cold crystallization transition was described using two parameters: The **cold crystallization temperature** ($\boldsymbol{T_{cc}}$) which is determined at the point when the exotherm peak was reached and the **cold crystallization enthalpy** ($\boldsymbol{\Delta H_{cc}}$) by integration of corresponding area of the exothermic peak of cold crystallization.

- The melting transition was described using three parameters: The **melting peak temperature** (***T_{mp}***) was determined as the point when the endotherm peak was reached and the **end melting temperature** (***T_{me}***) as the temperature at the end peak of the melting endotherm (*i.e.* the temperature when melting is complete). The **melting enthalpy** (***ΔH_m***) was determined by integration of corresponding area underneath the dominant endothermic melting peak.
- The crystallization transition during the cooling run was described using two parameters: The **crystallization temperature** (***T_c***) was determined as the point when the exotherm peak was reached and the **crystallization enthalpy** (***ΔH_c***) by integration of corresponding area underneath the cold crystallization peak.
- The **degree of crystallinity** (***X_c***) was calculated from the first and second heating scans according to *equation 5.14*:

$$\chi_c(\%\ crystallinity) = \frac{\Delta H_m - \Delta H_{cc}}{\Delta H_m^0}.100 \quad (5.14)$$

Where ΔH_m is the melting enthalpy and ΔH_{cc} the cold-crystallization enthalpy. ΔH_m^0 is the melting enthalpy for a 100 % crystalline PLA specimen (*i.e.* $\Delta H_m^0 = 93.6\ J.g^{-1}$) (Perego and Cella, 2010).

b) Non-isothermal crystallization analysis

Regarding non-isothermal crystallization kinetics, the experiments were carried out using the following thermal protocol (see *figure 5.5* for a schematic representation of the procedure):

- **(a)** Erasing the thermal history of each sample by heating and equilibrating at 200 ºC for t_{eq} = 2 min.

- **(b)** Cooling scan from 200 ºC to 30 °C at cooling rates of 1.5 ºC.min^{-1} to investigate the non-isothermal crystallization behaviour.
- **(c)** Subsequently, sample are isothermally held at 30 °C for t_{eq} = 2 min.
- **(d)** Heating up to 200 ºC cooling rates of 10 ºC.min^{-1}.
- **(e)** Equilibrate at to 200 ºC for t_{eq} = 2 min to erase thermal history.
- **(f)** Cooling scan from 200 ºC to 30 °C repeated at different cooling rates (*i.e.* 2.5, 5, 7.5, 10, and 20 ºC.min^{-1}).

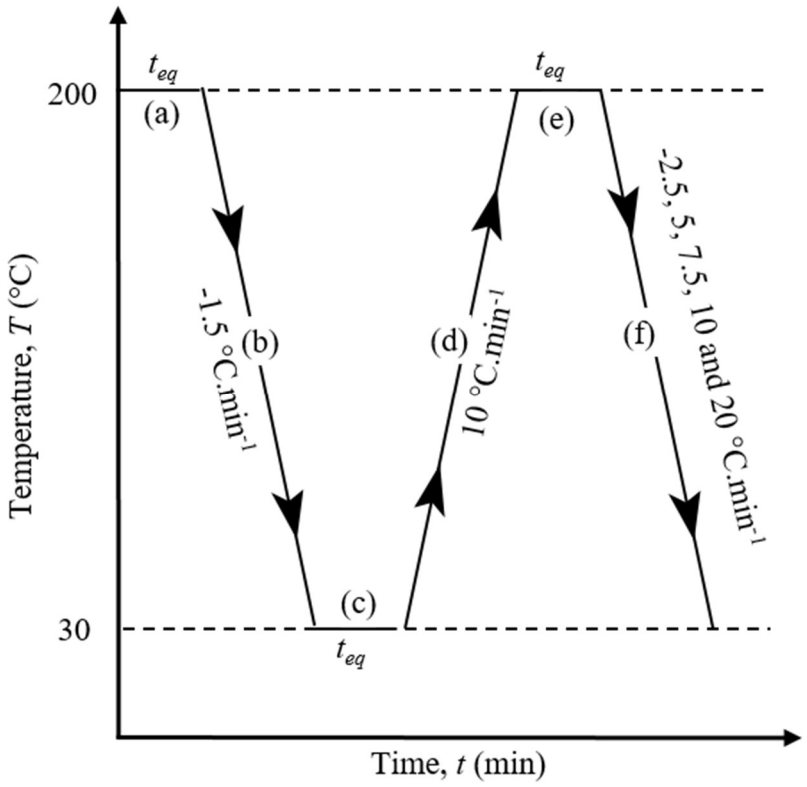

Figure 5.5. *Schematic representation of the non-isothermal crystallization procedure. The alphabets specify the thermal protocol involved.*

c) Isothermal crystallization analysis

Regarding isothermal crystallization kinetics, the experiments were carried out using the following thermal protocol (see *figure 5.6* for a schematic representation of the procedure):

- **(a)** Erasing the thermal history of each sample by heating and equilibrating at 200 ºC for t_{eq} = 2 min.
- **(b)** Cooling scan from 200 ºC to desired crystallization temperature, T_c1 (130 ºC) at cooling rates of 40 ºC.min^{-1} to investigate the isothermal crystallization behaviour.
- **(c)** Subsequently, sample are isothermally held at T_c1 for 30 min.
- **(d)** Heating up to 200 ºC cooling rates of 10 ºC.min^{-1}.
- **(e)** Equilibrate at to 200 ºC for t_{eq} = 2 min to erase thermal history.
- **(f)** Cooling scan from 200 ºC to different crystallization temperature, T_c2 (128 ºC) at cooling rates of 40 ºC.min^{-1}. This step is repeated at different T_c (namely 126, 124, 122, 120, 118, 116, 114, 112 and 110 ºC.min^{-1}).

The crystallization temperatures were selected in order to ensure a proper thermal protocol including a straight base line, as recommended by Lorenzo et al. (2007). Since it is important that DSC be able to cool and equilibrate as fast as possible in order to detect the complete crystallization exothermic peak, calcium oxide was introduced in the reference pan and the PID values of the cooler control were optimized.

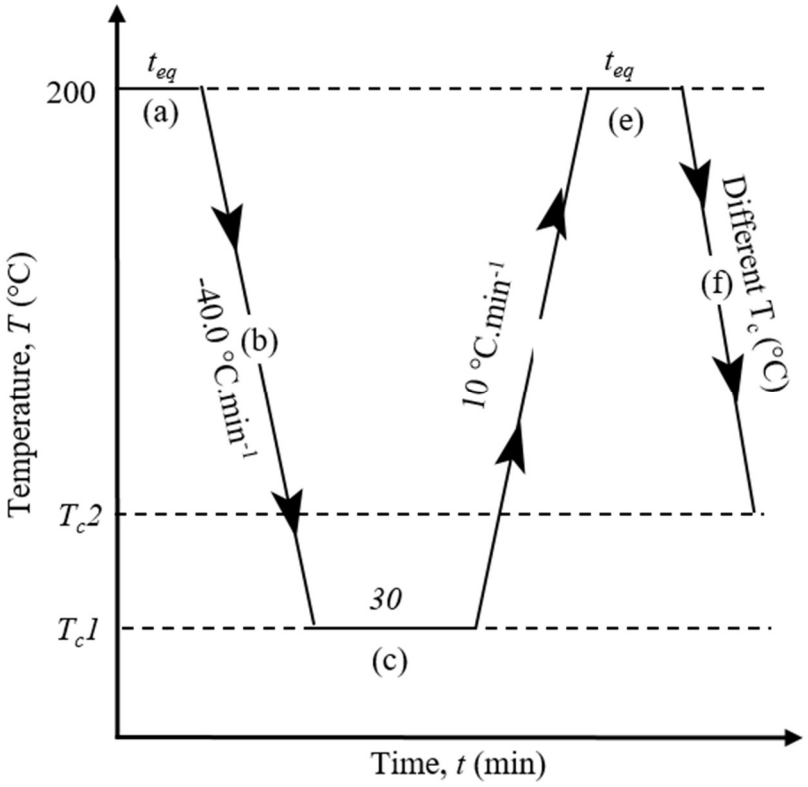

Figure 5.6. *Schematic representation of the isothermal crystallization procedure. The alphabets specify the thermal protocol involved.*

5.1.6. Dynamical Mechanical Thermal Analysis (DMTA)

DMTA experiments were performed on a DMTA Q800 instrument (TA Instrument, New Castle, DE, USA). A commercial Trios Analysis software version 4.1.0 (TA Instruments) was used for data analysis.

The dynamical mechanical thermal properties of the extruded sheets were investigated using a single cantilever bending mode at a frequency of 1 Hz and a deformation of 0.02% (LVE). The temperature range was set from 30 ºC to 105 ºC at a heating rate of 2 ºC.min^{-1}. Samples with nominal dimensions of 17.5 x 12 x 1 mm^3 were extracted from the centre of the

extruded sheets in the MD. The storage modulus (E'), the loss modulus (E'') and the mechanical loss factor (tan δ) were determined according to the standard procedure.

5.2. Rheological Dynamic Analysis (RDA)

5.2.1. Sample conditioning

The initial X_c exhibited by a polymer may significantly affect its viscoelastic behaviour when rheological experiments are performed in its rubbery state above T_g ($T_g < T < T_m$). Thus, the temperature dependence over a large range of temperatures could be meaningless if this crystalline phase is not previously removed.

Prior to testing, amorphous samples were prepared in order to enlarge the temperature window for dynamic measurements. In a typical procedure, sheet parts were vacuum-dried using silica gel as dessicant at 55 °C overnight and subsequently melted at 5 °C above their respective melting temperature for 2 minutes between two steel plates in a hot plate press. Then, they were quickly quenched in an ice water bath (2 ± 2 °C) for 5 minutes in order to avoid crystallization. After drying, disks with 25 mm in diameter were extracted from the centre of the sheet and vacuum-dried overnight at room temperature using silica gel as dessicant.

5.2.2. Testing conditions

In order to characterize the rheological properties, disks of 25 mm diameter were prepared by extracting it from the centre of the extruded sheets. Dynamic rheological measurements were performed on an AR-G2 magnetic bearing rheometer (TA Instruments, New Castle, DE, USA) in parallel plate (25 mm) configuration with a constant gap of 1 mm. All tests were conducted under dry nitrogen atmosphere in order to minimize degradation

throughout rheological testing. Prior to testing, samples were vacuum-dried overnight at 55 °C over silica gel. Dynamic frequency sweeps were carried out over an angular frequency (ω) range from 628 to 0.0628 rad.s^{-1} at 175, 180, 190 and 200 °C under stress controlled conditions (2 %, LVR).

5.3. Mechanical Characterization

The mechanical characterization was carried out using uniaxial tensile tests according to the ASTM D638 standard. Specimens of type I *(c.f. figure 5.7)* were extracted from the centre of the sheet, parallel to the MD direction and following the protocol described in *section 4.1.4* (*c.f. chapter 4*). Tests were performed at room temperature (26 ± 3°C) using a Zwick Roell Z010 Allround testing machine coupled with makroXtens extensometer (Zwick Roell, Ulm, Germany) that is equipped with a 10 kN load cell.

Engineering stress–strain curves were computed based from the resultant load and deformation data following the equations below:

$$\sigma = F/A \tag{5.15}$$

where σ is engineering stress (in Newtons per square metre, N.m^{-2} or, equivalently, Pascals, Pa). F is force (in Newtons, N), and A is the cross-sectional area of the tensile specimens before deformation has taken place.

$$\epsilon = \frac{\Delta l}{l_0}.100 = \frac{l - l_0}{l_0}.100 \tag{5.16}$$

where ε is engineering strain, Δl is the increase in the specimen length between gauge marks and l_0 is the gauge length of the initial specimen (50 mm).

The Young's Modulus (E), yield strength (σ_y), yield strain (ε_y) and strain at break (ε_b) were determined from the engineering stress–strain curves plotted. All reported values are average readings of ten valid tests.

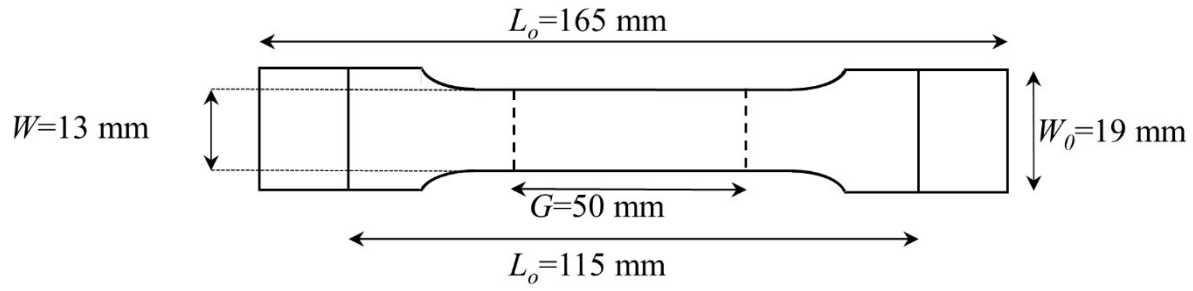

Figure 5.7. *Tensile specimen of Type I with sample dimensions. L_o: length overall, D: distance between grips, G: gauge length, W_o: width overall, W: width of the narrow section (based on ASTM D638 standard).*

5.4. Fracture Characterization

Due to the fast physical aging of nature of PLA, essential work of fracture (EWF) analysis can only be successfully applied in de-aged material. A ductile-brittle transition behaviour can be observed after being exposed to de-aging treatment. All the tested sample shows exhibit a ductile behaviour.

Identical devices as described in the mechanical characterization section (*c.f. section 5.10*) were used to perform uniaxial fracture tests and to measure displacement of the process zone. Tests were performed with a crosshead speed of 1 mm.min^{-1} at room temperature (26 ± 3 ºC). Deeply double-edge notched test (DDENT) samples were mechanized from the centre of the sheet, parallel to the MD direction with the following dimensions: Length L=105 mm, width W=65 mm, thickness t=1 mm and distance between grips ZG=65 mm (*c.f. figure 5.7*). Ten ligament lengths, ranging from 6 to 24 mm, were tested. Each of them was repeated three

times using fresh samples. Prior to testing, initial cracks were sharpened using a fresh razor blade with an edge radius of 0.13 μm. The work required for the whole fracture process (W_f) was measured by integrating the corresponding area underneath the load-displacement curve for each ligament length.

After testing, the accurate ligament length (l) and the height (h) of the outer process deformation zone (OPDZ) or "plastic" zone, surrounding the ligament length, were measured using a binocular lens microscope (Carton, Pathumthani, Thailand). This allowed for the determination of the shape factor (β), calculated from the slope of h versus l using a linear regression analysis. In addition, a video monitoring system (two digital cameras Xenoplan 1.4/23-0.902, Schneider Kreuznach, Bad Kreuznach, Germany) coupled to an optical strain measurement system (ARAMIS®, GOM GmbH, Braunschweig, Germany) was employed for an advanced strain analysis using digital image correlation (DIC).

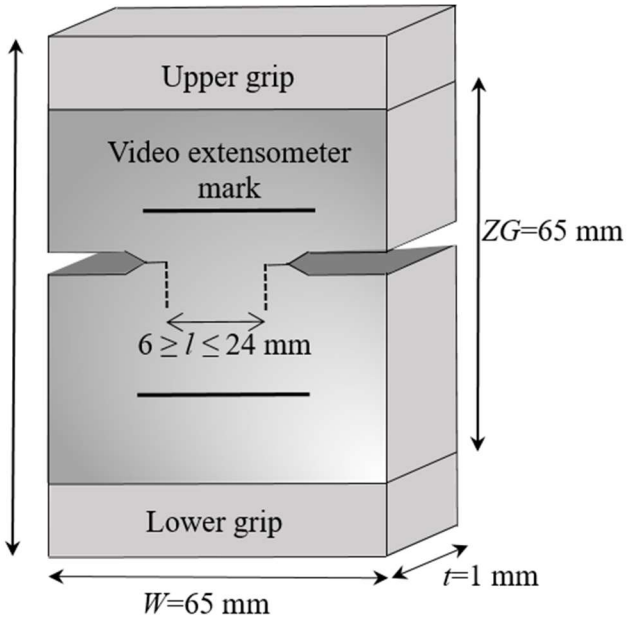

Figure 5.8. *Schematic representation of the deeply double-edge notched test (DDENT) geometry with sample dimensions.*

5.5. Fractography Characterization

5.5.1. Transmission Electron Microscopy (TEM) Analysis

The state of dispersion/intercalation of clay particles into the calendered sheets was investigated using high-resolution transmission electron microscopy (TEM). TEM images were obtained from approximately 100 nm thick slices using a JEOL TEM 2100 (JEOL Ltd., Tokyo, Japan) device operating at 200 kV under vacuum. Analyzed samples were initially micro-tomed by a diamond blade into slices with a thickness around 100 nm. Microtoming was performed with the sample being initially flash freezed using liquid nitrogen between -120 and -160°C. Slices were then taken parallel to the extruded sheet surface.

5.5.2. Scanning Electron Microscopy (SEM) Analysis

The fractured surface of tensile specimens was inspected using a JEOL JSM-5610 Scanning Electron Microscopy (JEOL Ltd., Tokyo, Japan) operating at 12 kV under vacuum. Prior to testing, samples were coated with a thin layer of gold in argon atmosphere.

5.5.3. Optical Microscopy

The morphology of the surface normal to the fracture plane of the tensile samples was inspected using optical microscopy. Observations were performed using a polarized light microscopy (Nikon, Optiphot-Pol XTP-11, Japan) coupled to both a ProgRes® CT3 Camera (JENOPTIK Optical Systems GmbH, Jena, Germany) and a commercial ProgRes CapturePro version 2.5 software.

5.6. Investigation of hydrophilicity and hydrophobicity of nanofillers used.

PLA is easily hydrolyzed in the presence of moisture, and its hydrolyzed products are non-toxic. It absorbs water when exposed to moist or humid environments and expedites its

process of decomposition. Although PLA can degrade through the hydrolysis of its backbone ester groups, PLA have been known to be relatively hydrophobic (Farah et al., 2016; Xiao et al., 2012). Generally, pure PLA films possess low surface energy with contact angles on the order of 80° which makes it hydrophobic (Hendrick and Frey, 2014; Ouyang et al., 2009). Hence, it would be advantageous that nanofillers used will also be hydrophobic making it thermodynamically miscible with PLA (Le Bolay et al., 2012).

Hydrophobic nanofillers are considered as nano-sized particles which displays water resistant properties because of its nanostructure and chemical properties. When introduced to a surface of a material, the nanofillers will adhere to the host material and prevent liquids from permeating through. The water will only come into contact with the tip of the nanoparticles coating the outside of the host material. Due to lack of surface attraction, the water is then repelled from the hydrophobic nanofillers.

Pristine MMT was well noted to possess hydrophilic properties owing to the presence of inorganic cations on their surface and thereby incorporating it into hydrophobic polymers could potentially reduce it efficacy. With regards to organically modified nanoclays, surface modifications of o-MMT with alkyl quaternary ammonium ions have resulted it being transform into hydrophobic hence facilitating better interactions with PLA (*c.f. figure 5.9 a*).

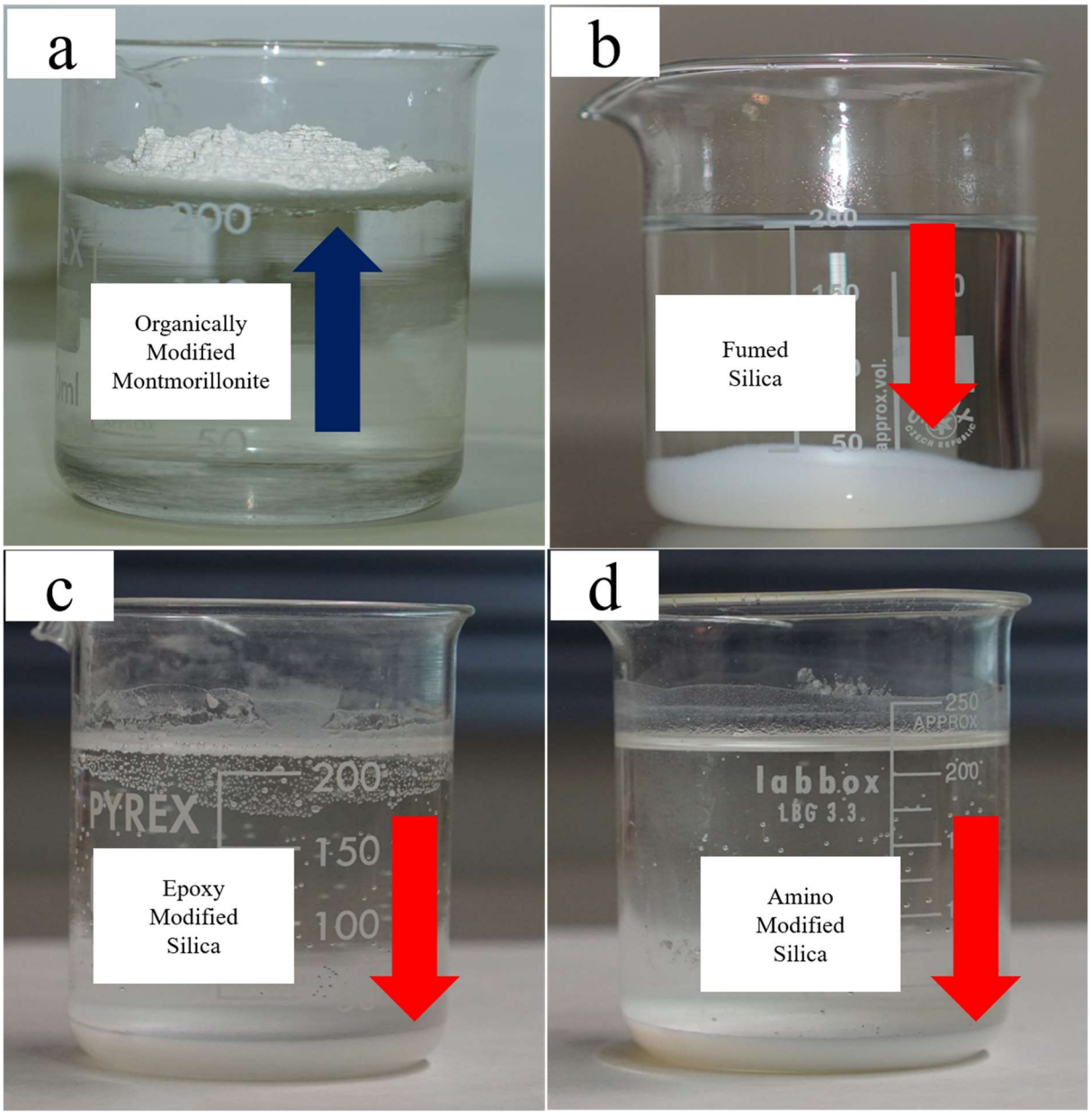

Figure 5.9. *Demonstration of hydrophobicity of (a) o-MMT with respect to the hydrophilicity of non-modified and surface modified nanosilica of (b) SiO_2, (c) SiO_2-E and (d) SiO_2-A, respectively.*

Fumed silica can either be hydrophilic or hydrophobic. Hydrophilic fumed silica are silicon dioxide with hydroxyl groups which is chemically bonded to the silicon atoms on the surface of the silica particles. This predominantly took place during manufacturing of fumed

silica powders which is produced via flame hydrolysis of silicon tetrachloride ($SiCl_4$) in an O_2(air)/H_2 flame (Zhuravlev, 2000). This makes the fumed silica hydrophilic and capable creating hydrogen bonding with suitable molecules. SiO_2 nanofiller exploited in this work is an untreated fumed silica with a trade name of CAB-O-SIL EH-5 which is supplied by Cabot Corporation. This SiO_2 nanofiller is hydrophilic which is not beneficial to the filler/matrix miscibility with PLA which could lead to poor interaction between these two components (*c.f. figure 5.9 b*).

However, surface modifications of fumed silica by substituting it with epoxy moieties does not seem to overhaul its inherent hydrophilic properties (*c.f. figure 5.9 c*). Likewise, surface modifications of SiO_2 by aminopropyl still render it hydrophilic (*c.f. figure 5.9 d*). In this respect, comparative images are shown here.

The hydrophobicity of o-MMT when incorporated into hydrophobic PLA should improve it compatibilities especially evident in the enhanced dispersion and distribution of nanofiller particles throughout the PLA matrix. Accompanied with its high surface to volume ratio and reduced sensitivity towards moisture, PLA and REX-PLA nanocomposites with o-MMT should display optimal thermal, physical, mechanical and fracture properties.

On the other hand, hydrophilicity of SiO_2, SiO_2-E and SiO_2-A have rendered it thermodynamically immiscible with PLA since PLA is hydrophobic. This could purportedly lead to poor distribution and adhesion between the two components, and consequently poor and irreproducible performances in thermal, physical, mechanical and fracture properties.

Results and Discussions

Chapter 6. REX-PLA/o-MMT Nanocomposites

6.1. Laboratory scale: Internal mixer study

6.1.1. Effect of o-MMT on the reaction profile of PLA and modified PLA composites

In the beginning, the influence of o-MMT on PLA and modified PLA composites torque trace was investigated in an internal mixer. In order to accomplish this, *Figure 6.1 (a)* depicting torque (Γ) while *figure 6.1 (b)* displayed the bulk temperature (T_b) over extended mixing time (t = 30 minutes) respectively were plotted to monitor the progression of the reactions of PLA, REX-PLA and PLA composites with o-MMT. The torque measurements recorded were then used to calculate the specific mechanical energy (SME) according to *equation 6.1* (Redl et al., 1999).

$$SME = \frac{\omega}{m} \int_{4}^{t_{max}} \Gamma(t) d(t) \tag{6.1}$$

where ω is the screw speed (rad.s^{-1}), m the sample weight (g), $\Gamma(t)$ is the torque at a time, t (Nm) and t_{max} the mixing time (s). The SME elucidates the sum of the energy that was imparted to the melted blend due to the motion of the rotor shaft for mixing and dispersing the fillers in the melted polymer within the mixing chamber up to a specific time. In the present case, a completely molten state was observed for all samples within 4 minutes. On this basis, $\Gamma(t)$ was integrated from 4 to 30 minutes. Computed results are given in *Table 6.1*.

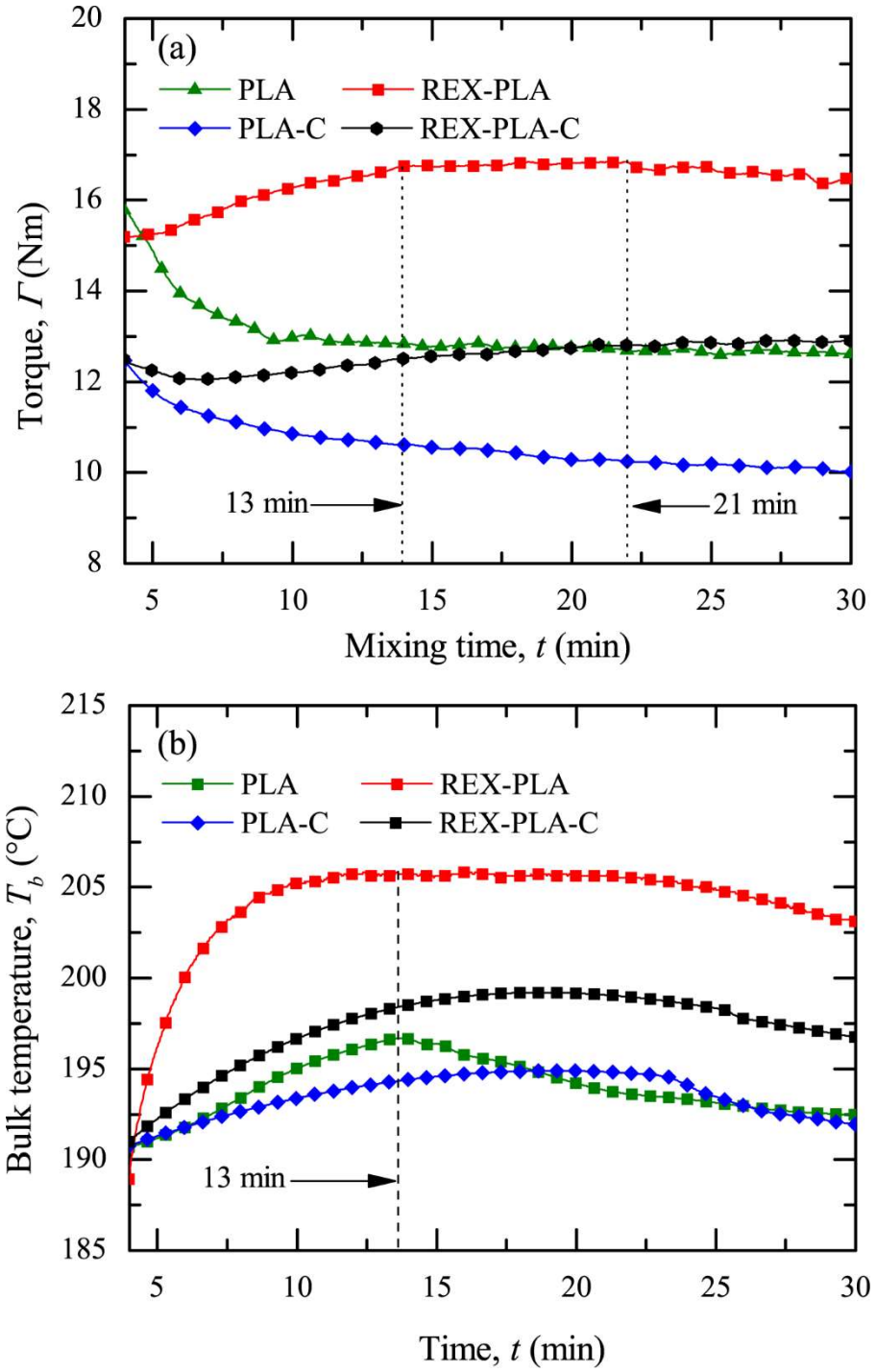

Figure 6.1. *Influence of o-MMT on the (a) torque trace (Γ) and (b) bulk temperature (T_b) as a function of the mixing time (t) at 180 °C of PLA and modified PLA composites.*

Table 6.1. *Influence of o-MMT on specific mechanical energy of PLA and modified PLA composites.*

Sample Nomenclature	SME ($J.g^{-1}$)
PLA	364 ±13
REX-PLA	507 ±17
PLA-C	325 ±21
REX-PLA-C	390 ±19

The torque trace of PLA sample decreased monotonically over mixing time, as shown in *figure 6.1*. This trend indicates that several random thermo-oxidative mechanisms took place during mixing, which leads to a decrease in the molecular weight of the raw PLA resins which has been similarly reported elsewhere (Cailloux, 2015; Carrasco et al., 2011b; Carrasco et al., 2015). In contrast, strong torque increase was observed with the incorporation of SAmfE (*i.e.* REX-PLA). The torque increase monotonously until it reached a plateau at approximately 13 minutes as indicated by a dashed line. This trend is also reflected in the higher SME values reported for REX-PLA (*i.e.* $SME_{REX\text{-}PLA} > SME_{PLA}$) and is in line with study of Cailloux et al. (2013) and Corre et al. (2011a).

The observed trend may be attributed to the higher amount of functional end groups of PLA generated due to thermal degradation during processing that promotes the reaction towards SAmfE. An increase in molecular weight (as indicated by the higher torque reading) due to chemical bonding of several PLA chains to one SAmfE molecule could have occurred due to the multifunctionality nature of SAmfE reactive agent ($f_n \approx 12$) (Cailloux, 2015; Cailloux et al., 2013; Cailloux et al., 2015). The thermo-oxidative reactions could therefore being minimized thus leading to a possible increase in molecular weight and modification of the

molecular topology, as already reported elsewhere (Cailloux et al., 2015; Corre et al., 2011a). Slight torque fluctuations were also observed between 20-35 min (indicated by an arrow). This might be a consequence of the stick and split behaviour on the wall of the mixing chamber. Based on a stick-slip mechanism as elucidated by Shenoy (1999), it is purported that, above a critical shear stress due to a possible increase in the melt elasticity, the polymer melt experiences intermittent slipping due to a lack of adhesion between itself and the mixing chamber wall, in order to relieve the excessive deformation energy adsorbed during the flow.

With regards to PLA's bulk temperature, it saw an increase of up to 195 °C even though the mixing temperature were initially set at 180 °C. This increase in temperature is likely to be related to shearing or stretching of the polymer between the rotating mixing screw and stationary mixing chamber wall. However with SAmfE content, the bulk temperature of modified PLA saw a temperature surge from 180 to 205 °C. The bulk temperature increase was influenced by both the mechanical shearing on the polymer melt and the effect of the exothermic nature of the chemical reaction. Comparing to REX-PLA, PLA samples exhibited a smaller SME value attributed to lower viscous dissipations hence the slightly lower bulk temperature observed (Cailloux, 2015; Cailloux et al., 2013).

While PLA and REX-PLA exhibited almost similar torque values at 4 minutes, addition of o-MMT causes approximately 20% decrease of torque (*i.e.* PLA-C and REX-PLA-C). The decrease in initial torque happened even though the processing conditions of both masterbatches were carefully designed in order to minimize thermo-mechanical degradations of raw PLA during processing. Thus, this trend could primarily be attributed to a possible plasticizing effect induced by the low MW of the organo-modifier of the filler (*i.e.* MW ≥ 404.8

g.mol^{-1}) rather than the possible minor variations in the molecular weight of the processed PLA.

Addition of o-MMT causes the torque trace of PLA-C sample to decrease monotonously over mixing time until it reached a plateau at approximately 21 min (indicated by a dotted line), which is lower than PLA torque trace. This trend is in agreement with both the calculated SME values and a large number of studies (Bigg, 2005; Castiello et al., 2012; Corre et al., 2011a; Pluta, 2006). This suggest that o-MMT addition decreases the thermal stability of PLA during mixing. The surfactant decomposition products in organomodified clay act as catalyst agent, which significantly enhances the random chain scission reaction of PLA at elevated temperatures, as already published by Bordes and colleagues (2009).

Unlike o-MMT, modified PLA matrix increased the melt stability REX-PLA-C sample. However, a slower and less pronounced torque increase were observed when compared to REX-PLA samples. The torque curve increase over mixing time until it reached a plateau at approximately 21 minutes as shown in *figure 6.1*. It is hypothesized this trend were due to the higher interaction between -OH functional end groups of o-MMT with the epoxy groups of SAmfE in the melted bulk. This leads to SAmfE agent being grafted onto the clay surface through the ester linkage formation thus limiting further possible reaction between PLA and SAmfE. Consequently, the enhancement of the REX-PLA-C melt properties is likely to be reduced, leading to lower torque values.

With regards to bulk temperature, PLA-C saw an increase from 180 to 195 °C which is relatively similar to PLA. On the other hand, REX-PLA-C saw an increase 180 °C to approximately 198 °C. However when compared to REX-PLA, the increase in bulk temperature of REX-PLA-C temperature were slightly lower. It is hypothesize that the bulk temperature increase observed in REX-PLA-C was also influenced by both the mechanical shearing on the polymer melt and the effect of the exothermic nature of the chemical reaction between SAmfE and o-MMT. This trend may have also substantiated the observations made for REX-PLA-C in which possible reaction limitation of between PLA and SAmfE may have resulted in slightly lower increase in bulk temperature.

6.1.2. Expected chain topologies of PLA and modified PLA composites with o-MMT.

It has been established that both PLA functional end groups (i.e. -COOH and -OH groups) can react with the epoxy groups of SAmfE and these reactions have been described at length by Cailloux and co-workers (2013). Due to the nature of SAmfE that has a functionality of 12, it is hypothesized that several PLA chains could react and become covalently bonded to one SAmfE molecule. However, little reactivity of PLA terminal end groups towards SAmfE is initially expected, as most PLA functional end groups might be end-capped. This is common practice during production of commercial PLA grades in which PLA chains were end-capped with hydroxyl groups in order to enhance the hydrolysis resistance and prevent severe degradation (Bigg, 2005; Cailloux, 2015; Liu et al., 2010).

On the other hand, the organic treatment of the o-MMT resulted in presence of high concentration of $-CH_2CH_2OH$ groups. The combination of low MW of the quaternary ammonium ion and high concentration of $-CH_2CH_2OH$ groups in o-MMT surfactants became

a major influence in enhancing the diffusivity of the -OH functional end groups of o-MMT towards the epoxy groups. Thus it is hypothesized that SAmfE agent could be grafted onto o-MMT clay surface via the -C-O-C- ester linkage formation (*c.f. I* in *figure 6.2*) whilst mitigating further possible reaction between PLA and SAmfE.

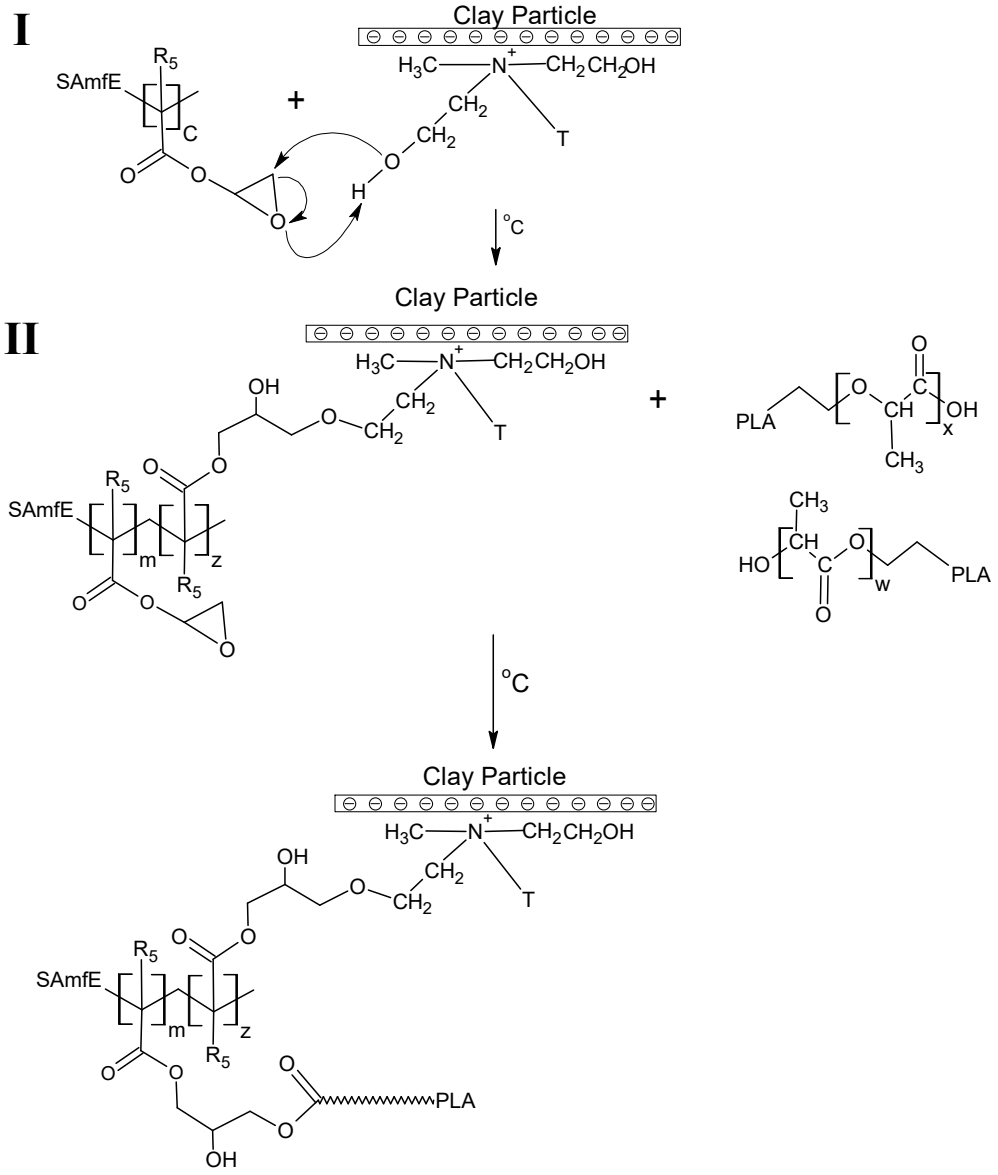

Figure 6.2. *Proposed reaction mechanisms of PLA/o-MMT in the presence of SAmfE.*

However, at longer reaction times, the formation of new terminal -COOH and -OH groups in PLA (i.e. shorter PLA chains and/or oligo PLA) due to various thermo-mechanically induced degradation mechanisms at high temperatures were expected. Due to the multi-functionality nature of SAmfE ($f_n \approx 12$), the residual free epoxy groups will react with the new PLA terminal groups forming covalent bonds between the clay and the polymer chains (*c.f.* II in *figure 6.2)*. This leads to a topological modifications that are not trivial and are deemed to be a mixture of several types of non-uniform structures in MW, in architectures and in number of branch per macromolecules (Cailloux et al., 2015).

6.1.3. Characterization of the reactivity between organo-modifier of clay with SAmfE and its effect on the dispersion of o-MMT.

Attenuated total reflectance Fourier transform infrared (ATR FT-IR) spectroscopic investigation were performed in order to assess the possible reactions between montmorillonite platelets and SAmfE. The absorbance relations of IR-identifiable spectra of Si-OH and -CH_2-OH groups from the organic treatment of montmorillonite and epoxy ring of SAmfE were used to quantify the reactivity of the analyzed groups and this study would remain independent of the influence of sample thickness. Initially, 4 grams of SAmfE and 2 grams of pre-dried clay (in powder form) were charged in a 150 mL beaker and manually mixed at 180 °C for 20 minutes. SAmfE was added in excess in order to enhance the formation of -C-O-C- linkage. Clay-SAmfE samples were extracted at an interval of 0, 5, 10 and 20 minutes, cooled to room temperature and then powdered using mortar and pestle. *Figure 6.3* shows the change in FT-IR absorbance spectra of the clays as function of the reaction time with SAmfE.

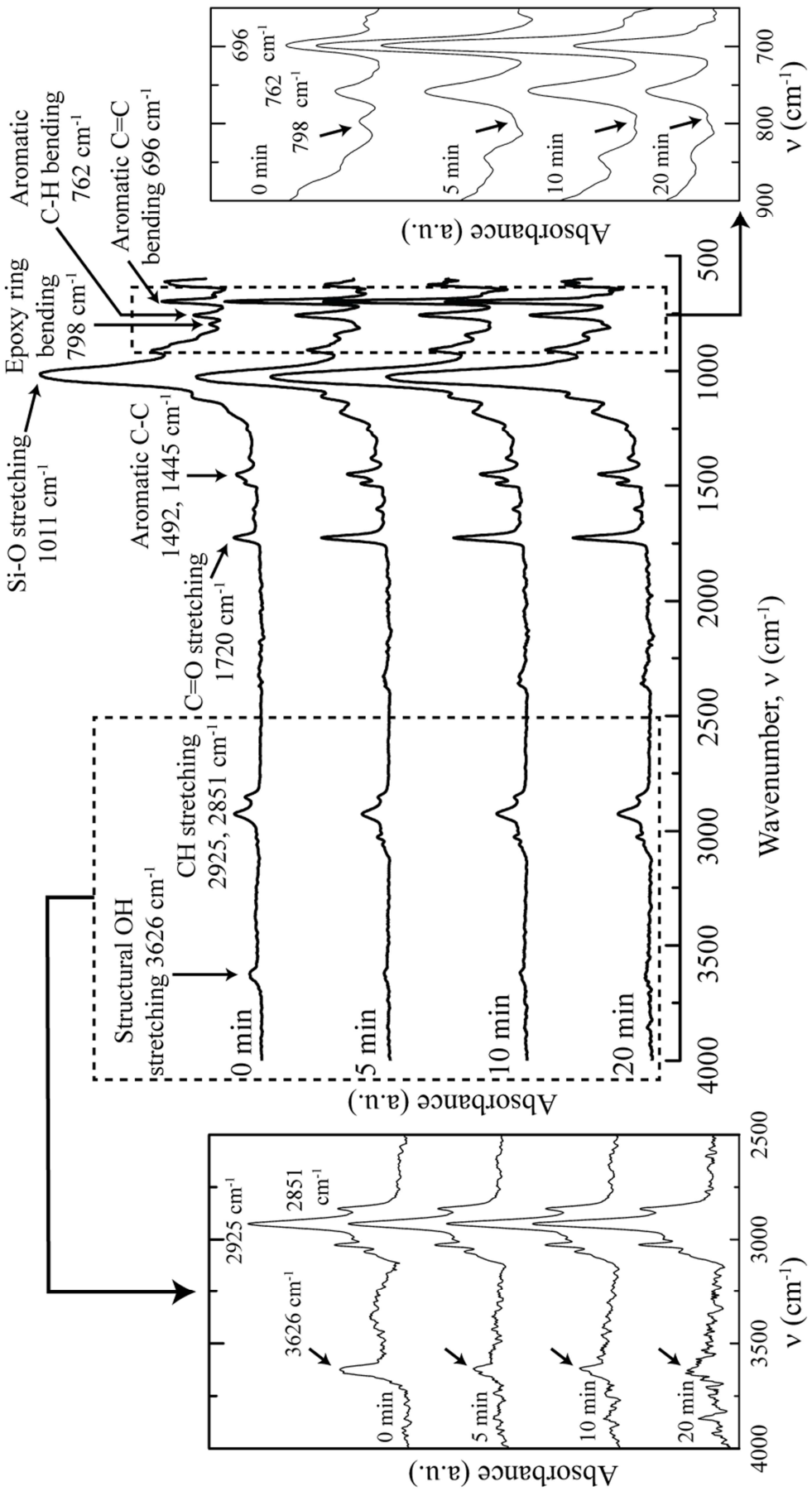

Figure 6.3. *FT-IR spectra of clay-SAmfE samples at the indicated reaction times.*

The peak intensity of the corresponding Si-OH and -CH_2-OH groups of the montmorillonite platelets and the organic treatment versus epoxy ring of SAmfE at several time intervals were then compared and contrasted. In order to impart clarity, absorbance spectra that encompasses the respective functional groups were enlarged. For Si-OH and -CH_2-OH groups of the montmorillonite platelets and the organic treatment, the absorbance spectra between 4000 and 2500 cm^{-1} at different reaction times were selected. While absorbance spectra between 900 and 650 cm^{-1} which corresponds to epoxy ring of the SAmfE at different reaction times were chosen.

The absorption peaks of clay particles are characterized at 1011 cm^{-1} for Si-O stretching, 2925 and 2851 cm^{-1} for C-H stretching, which corresponds to the hydrocarbon chains of the organic ammonium ions, and at 3626 cm^{-1} for the structural -OH stretching of both silanol groups (i.e. Si-OH) and the organic modifier (i.e. -CH_2-OH) (Korobko et al., 2011; Pattanayak and Jana, 2005). The absorption peaks of SAmfE are characterized at 696 cm^{-1} for aromatic C=C vibration, at 762 cm^{-1} for aromatic C-H bending, at 798 cm^{-1} for epoxy ring bending, at 1492 and 1445 cm^{-1} for aromatic C-C vibration and at 1720 cm^{-1} for C=O stretching (Najafi et al., 2012b; Pretsch et al., 2001).

However, the band characteristic of Si-O stretching (1011 cm^{-1}) overlaps -C-O-C- stereo symmetric characteristic band, which are located between 1055 - 870 cm^{-1}. Thus, the absorbance band at 3626 cm^{-1} (i.e. structural -OH stretching) and at 798 cm^{-1} (i.e. epoxy ring bending) were selected for monitoring of Clay-SAmfE reactions. *Figure 6.3* presents an enlarged version of the FT-IR spectra between 4000 - 2500 cm^{-1} and 900 - 650 cm^{-1} corresponding to the structural -OH group (3626 cm^{-1}) and epoxy groups (798 cm^{-1}) respectively to demonstrate the evolution of the peak as a function of reaction time.

Figure 6.3 reveals that there is a decrease of intensity of both peaks as the reaction time increases (as indicated by the arrow in both inserts). It was observed that the absorbance peak in the epoxy group band was negligibly small compared to structural -OH group peak for reacted clay-SAmfE samples. It is established that the peak intensity is proportional to the concentration of absorbing species. It can be assumed that the diminishment of the 798 cm^{-1} peak was due to total consumption of the available epoxy groups during mixing or to a low remaining concentration of epoxy groups that is below the detection limits of the FT-IR analysis.

To quantify the decrease in the amount of structural -OH groups (referred to as α), an internal standard FT-IR method was devised. It is determined from the ratio of absorbance area of structural -OH group at 3626 cm^{-1} against internal standard, as given as by *equation 6.2.* The characteristic band associated with stretching of C-H_2 groups at 2925 and 2851 cm^{-1} were selected as the internal standard.

$$\alpha = \left[1 - \left(\frac{A_{-OH}}{A_{-CH_2}} \right)_{t=0\,\mathrm{min}} \times \left(\frac{A_{-CH_2}}{A_{-OH}} \right)_{t} \right] \times 100 \qquad (6.2)$$

Where A_{-OH} and A_{-CH2} are the area under the peak corresponding to the structural -OH stretching (at 3626 cm^{-1}) and to the CH stretching (at 2925 and 2851 cm^{-1}), respectively. *t* is the reaction time. The computed value of α as function of reaction times of reacted clay-SAmfE samples are plotted in *Figure 6.4*.

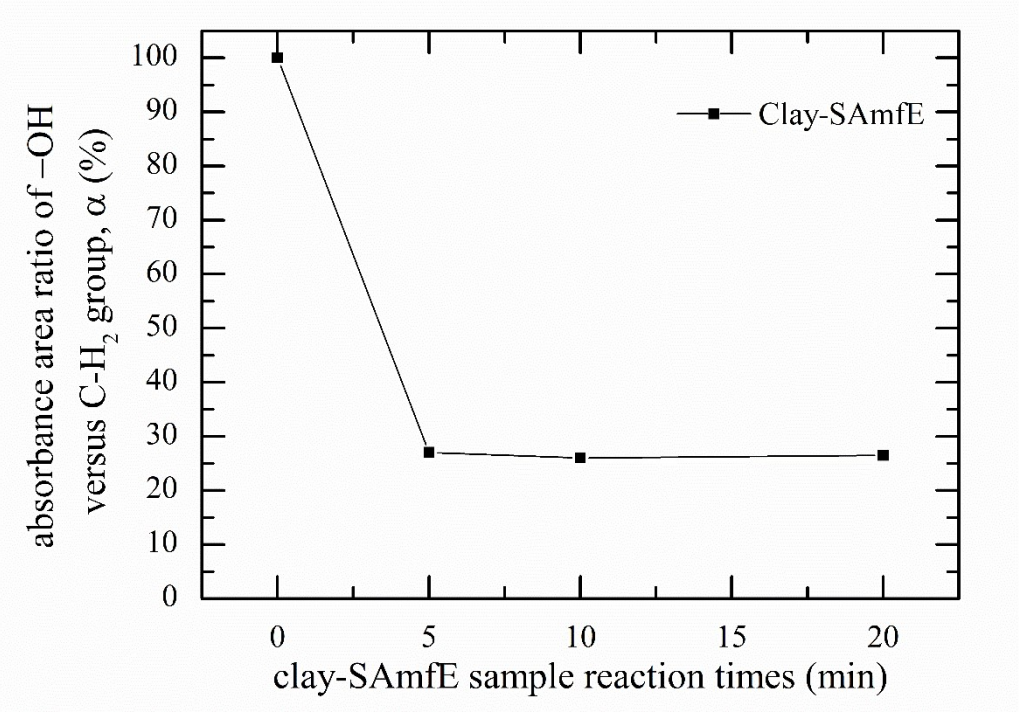

Figure 6.4. *Computed value of absorbance area ratio of -OH group versus C-H_2 group as function of reaction times of reacted clay-SAmfE samples.*

By calculations, there is a steep decrease of the relative amount of structural -OH groups when the reaction time reaches 5 minutes (-73 %). As the reaction time increases, within the statistical error of the experiments *α* value reaches a plateau. These observations verifies the aforementioned hypothesis. A facile and fast chemical grafting reactions between SAmfE and the clays took place via the reaction between the epoxy groups and the -OH functionalities which are carried by both the surface of the platelets (*i.e.* Si-OH) and the organic modifying agent (*i.e.* -CH_2-OH).

For the purpose of verifying the intercalation of SAmfE molecules into the o-MMT galleries, raw o-MMT powder and clay-SAmfE samples extracted after 5 minutes of mixing (referred to as clay/SAmfE$_{t=5}$) were analyzed using WAXD measurements. The WAXD diffractogram of all samples are illustrated in *figure 6.5.* The interlayer spacing of each sample was determined from the angular location of the peak and are calculated using Bragg equation (*c.f. Equation. 5.1*)

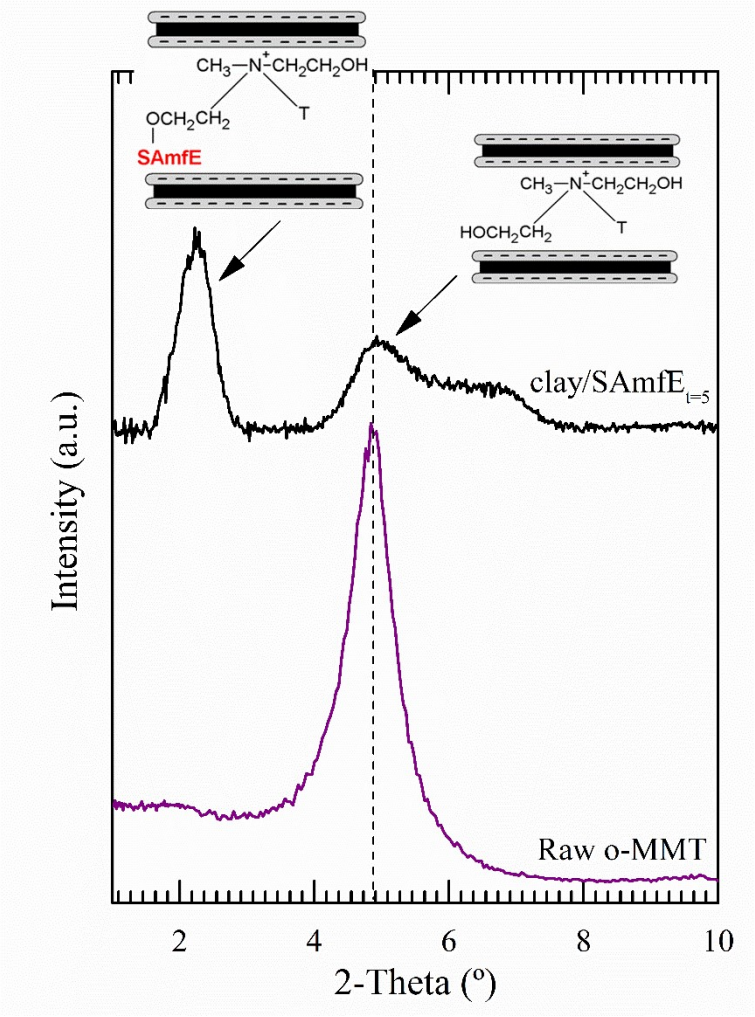

Figure 6.5. *Influence of the reactivity exhibited by the -OH functionalities of the clays towards epoxy group on the interlayer spacing.*

In *Figure 6.5*, raw o-MMT powder featured a clear sharp peak at 2θ = 4.8° (indicated by a dashed line) which agrees to the theoretical basal spacing (d_{001}) of 1.86 nm provided by suppliers's technical data (Southern Clay Products, 2005). However for o-MMT/SAmfE$_{t=5}$, two peaks emerged specifically a unique sharp peak at 2θ = 4.8°; corresponding to the basal spacing of the raw o-MMT and relatively sharp peak at 2θ = 2.3° which suggests that the basal *d*-spacing between clay platelets have increased from 1.86 to 3.84 nm. These results are suggestive that the increased interlayer spacing are caused by the intercalation of SAmfE species in between the clay galleries heights due to the reactivity exhibited by the -OH functionalities of the organic modifying agent towards epoxy groups. This result also is in keeping with those obtained by FT-IR observations. However, there is an additional shoulder in the high 2θ tail of the remaining pristine o-MMT peak (*i.e.* 2θ = 4.8°) which could be attributed to the degradation of the organic modifier. The decomposition of the organic modifier provokes a collapse of the clay mineral particles in the interlayer spacing which results in clay agglomeration (Scaffaro and Botta, 2014).

In regards of these analyses, it can be hypothesize that SAmfE will preferentially reacts with o-MMT organic modifier which is located in the interlamellar spaces between the clay galleries. This could potentially improve interface interactions between o-MMT and PLA matrix, making it more adherent to the polymer matrix while at the same time improving the degree of intercalation of o-MMT.

6.2. Scaling up of the reactive extrusion processing

6.2.1. Molecular characterization: SEC-DRI analysis of PLA and modified PLA composites with o-MMT

In order to determine the molecular modifications of PLA and modified PLA composites resulting from the addition of clay particles during reactive extrusion processing, the MWD was investigated using SEC-DRI. It has been reported in the literature that the multifunctional reactive agent that were used in this study yields the formation of sparsely LCB and/or complex topological structures (Cailloux, 2015; Cailloux et al., 2013; Corre et al., 2011a; Corre et al., 2011b).

The molecular weight determined by classical SEC technique (employing a single concentration detector; *e.g.* DRI) can provide a reliable MW estimation of linear polymers but it can suffer from limitations to accurately determine the MW of branched polymers. This is due to the analysis of branched polymers that are based on calibration standards made using linear polymer. Since separation in SEC columns are based on the hydrodynamic volume of a polymer, linear and branched polymers of equal molecular weight possess different hydrodynamic volumes. Their measured molecular weight will be different and thus the obtained molecular weights of the branched samples could be lower than the true values (Abt et al., 2012). While SEC-DRI data are likely to be flawed due to co-elution issues, van Ruymbeke et al. (2005) and Cailloux et al. (2015) stated that the error on the MWD are considered to be statistically insignificant for low levels of structural modifications. Based on these findings, standard SEC-DRI equipment was utilized to perform MW analysis. *Figure 6.6* shows the MWD of all extruded sheets while *table 6.2* tabulate the corresponding MW values.

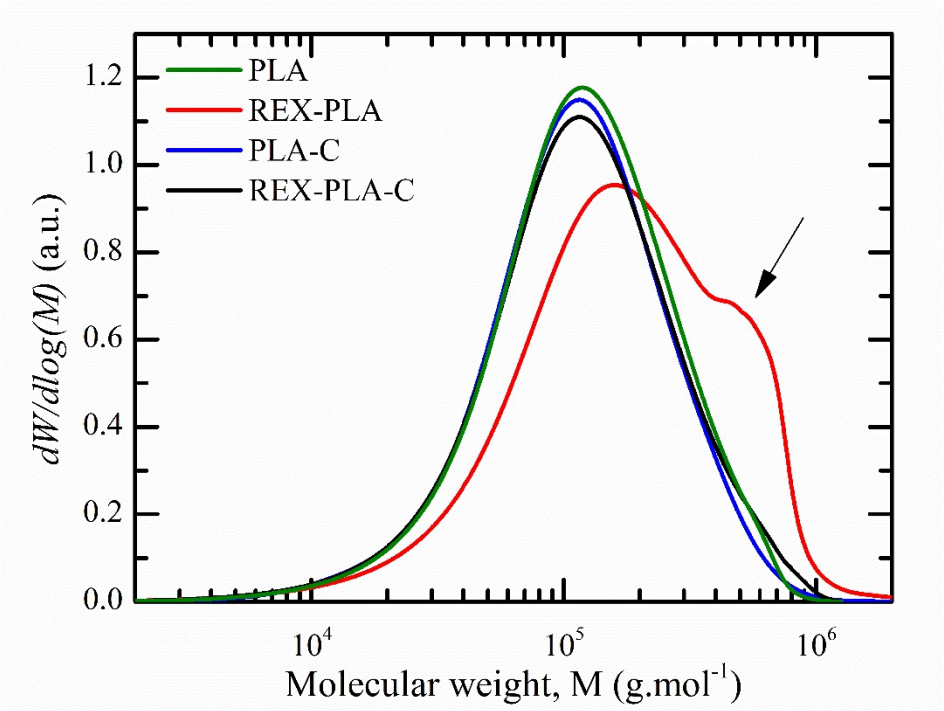

Figure 6.6. *Effect of the clay addition on the shape of the MWD of PLA and modified PLA composites.*

Table 6.2. *Numerical analysis of the MWD depicted in figure 6.6.*

Sample Nomenclature	M_n* (kg.mol^{-1})	M_w* (kg.mol^{-1})	M_z* (kg.mol^{-1})	PDI*
PLA pellets	77 ±1	165 ±4	298 ±34	2.1 ±0.1
PLA	74 ±4	158 ±1	277 ±21	2.1 ±0.1
REX-PLA	96 ±3	241 ±11	427 ±42	2.5 ±0.2
PLA-C	73 ±2	152 ±2	271 ±3	2.1 ±0.1
REX-PLA-C	73 ±2	160 ±3	293 ±7	2.0 ±0.1

*Relative MW values based on PMMA standards in HFIP. They were calculated from the average of three experiments based on fresh samples.

Looking at *figure 6.6,* it is apparent that both PLA and PLA-C samples displayed a slight decrease in MWs when compared to PLA raw materials (*i.e.* PLA pellets). However from *table 6.2*, it can be seen that reduction in MW averages measured were less than 9 % when compared to PLA pellets. The result obtained suggests that optimization of the processing conditions (*i.e.* nitrogen blanket, relatively low profile temperature, vacuum, etc.) have been successful at minimizing the effect of different thermo-oxidative degradations during reactive extrusion.

While both PLA and PLA-C samples displayed a narrow monomodal MWD, presence of SAmfE broadened the REX-PLA spectrum. A high molar mass shoulder appeared (indicated by an arrow) and naturally increases the average molar mass as reported in *table 6.2*. These trends were expected and match those observed in earlier studies (Cailloux et al., 2013; Cailloux et al., 2015). Authors proposed that these transformations are attributed to an increased population of high MW linear chains and/or the presence of a combination of several types of non-uniform branched structures (*i.e.* in MW and in architecture).

However, the most striking observation to emerge was the anticipated MW increase for REX-PLA-C samples was not realized. Closer inspection of the MW measurements revealed that raw PLA pellets, PLA, PLA-C and REX-PLA-C MW averages ranged within 10 %. These could be cause by a combination two factors. Firstly, even though MW was not enhanced, this does not necessarily exclude the occurrence of topological changes in REX-PLA-C samples during processing. Possible explanation for these could be that possible premature reactions between epoxy rings and -OH functionalities of the clays could have taken place, possibly reducing chain extension/branching reactions. Secondly, the following issue of REX-PLA-C

samples were being previously filtered before SEC analyses is highlighted. Thus, possible PLA macromolecules, which could be grafted to both SAmfE molecules and clay particles might have been removed during filtering process, eliminating the higher MWs fractions especially reducing M_z values.

6.2.2. Effect of clay addition on the rheological behaviour of PLA and modified PLA composites.

The viscoelastic functions were investigated to determine whether REX-PLA-C sample showed any behaviour consistence with the presence of clay-PLA tethering with presence of clay in the modified PLA matrix. Within the linear viscoelastic regime, investigation of the temperature dependence of the dynamic experiments, which were performed at different temperatures, can provides useful information about the molecular structure.

Wood-Adams and Costeux (2001) have introduced a new representation in order to validate the application of time-temperature superposition (TTS) using plots of the magnitude of the complex modulus $|G^*|$ vs the product of zero-shear viscosity and frequency, $\eta_0.\omega$ as shown in *Figure 6.7.* For the superposition principle to apply, the sample must be homogeneous, isotropic and amorphous. The material must be and remain linear viscoelastic under the deformations range of interest*, i.e.,* the deformation must be expressed as a linear function of the stress by applying very small strains. The study states that if the plot is temperature independent for thermorheologically simple polymer (*i.e.* linear polymers), all data will superpose into the same curve for TTS to be successfully applied. While for thermorheologically complex materials, data will not superpose into the same curve suggesting applying TTS is not possible.

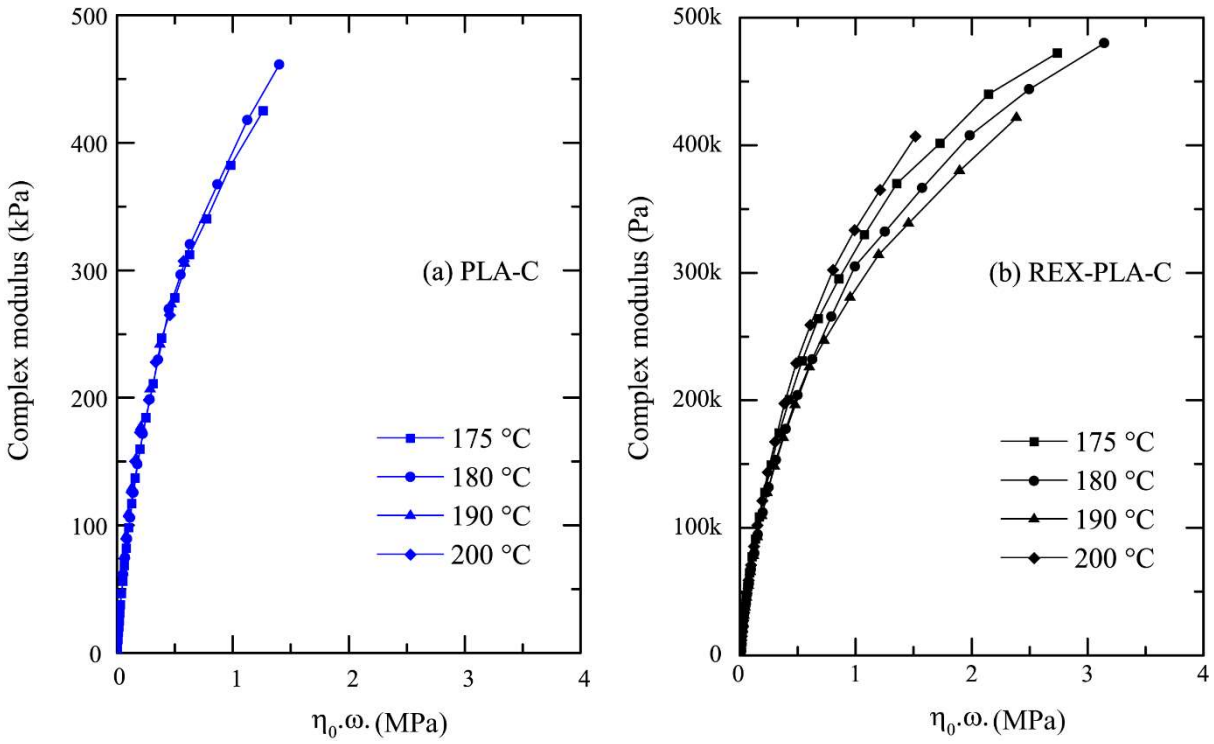

Figure 6.7. *Effect of (a) the clay in PLA matrix and (b) clay in modified PLA matrix on the validity of the TTS principle. Experimental data correspond to isothermal frequency measurements collected at the indicated temperature.*

It was observed that PLA and PLA-C samples displayed similar temperature independence of $|G^*|$ versus $\eta_0.\omega$. On the other hand, REX-PLA and REX-PLA-C displayed an opposite trend. For the sake of clarity, only PLA-C and REX-PLA-C datasets are shown in *figure 6.7*. With regards to TTS criterion, isothermal measurements collected at 175, 180, 190 and 200 °C of PLA-C superpose suggesting that both PLA and PLA-C samples (*c.f. figure 6.7a*) displayed thermorheologically simple behaviour. It seems that the addition of o-MMT in PLA matrix did not seem to modify both the molecular relaxation sequence and relaxation time at different testing temperatures.

On the contrary, a clear deviation of the TTS criterion was observed for REX-PLA-C samples (*c.f. figure 6.7b*). It was observed that plots of $|G^*|$ versus $\eta_0.\omega.$ at temperatures of 175, 180, 190 and 200 °C did not superpose. As a result of SAmfE presence in the modified PLA matrix, the mechanical response curves of REX-PLA and REX-PLA-C samples were not able to merge signifying of a material possessing thermorheologically complex behaviour. The display of thermorheologically complex behaviour is usually attributed the presence of LCB polymers, as already discussed by Lohse et al. (2002) and Wood-Adams and Costeux (2001) for LCB polyolefins and Al-Itry et al. (2014) and Cailloux et al. (2015) for randomly LCB-PLA.

In a thermorheologically complex material, the rate of molecular motion as well as the sequence of molecular processes is affected by changes in temperature. The architecturally modified macromolecules could have become sufficiently long to entangle and hinder the segmental motions of the neighbouring chains; leading to a modification of the sequence of the molecular relaxations by changing the temperature of measurement. The melt response time have significantly increase and the mechanical response curves cannot be superimposed to form a master curve by a simple transition along the frequency axis.

It is known that SAmfE is a multifunctional reactive agent, several PLA chains and/or clay particles could be grafted to one SAmfE molecule. Since the addition of o-MMT alone apparently does not modify the temperature dependence of viscoelastic measurements, the observed thermorheologically complex behaviour is dominantly caused by the formation of different non-uniform branched structures, which possibly exhibit LCB.

For the TTS principle to hold, samples must possess an extremely slow crystallization kinetics and the materials must be linear viscoelastic under the deformations of interest, *i.e.,* the deformation must be expressed as a linear function of the stress by applying very small strains. Additionally, isothermal frequency measurements must also reach the terminal regime for TTS to be valid. Considering that the temperature-independence of PLA and PLA-C is based on the consideration of zero-shear rate viscosity (η_0) values, data analysis would be invalid if η_0 is not accurately estimated for each temperature.

With regards to the above considerations, the effects of o-MMT addition in PLA on the temperature dependence of the viscoelastic functions were studied using the activation energy (E_a). Since the concept of a single activation energy is meaningless if the temperature sensitivity is time-dependent, consequently, E_a was solely calculated for samples that exhibit a thermorheologically simple behaviour (*i.e.* PLA and PLA-C samples) over the temperature range considered. The complex viscosity ($|\eta^*|$) and storage modulus (G') functions were chosen for the shifting process since η_0 can be observed for PLA and PLA-C samples in both the frequency range and the temperature experimental windows evaluated. Both complex viscosity ($|\eta^*|$) and storage modulus (G') curves measured at 175, 180, 190 and 200 °C were shifted along the frequency axis to 180 °C using the TTS principle, as illustrated in *figure 6.8 (a)* and *figure 6.8 (b)* for PLA and PLA-C samples, respectively.

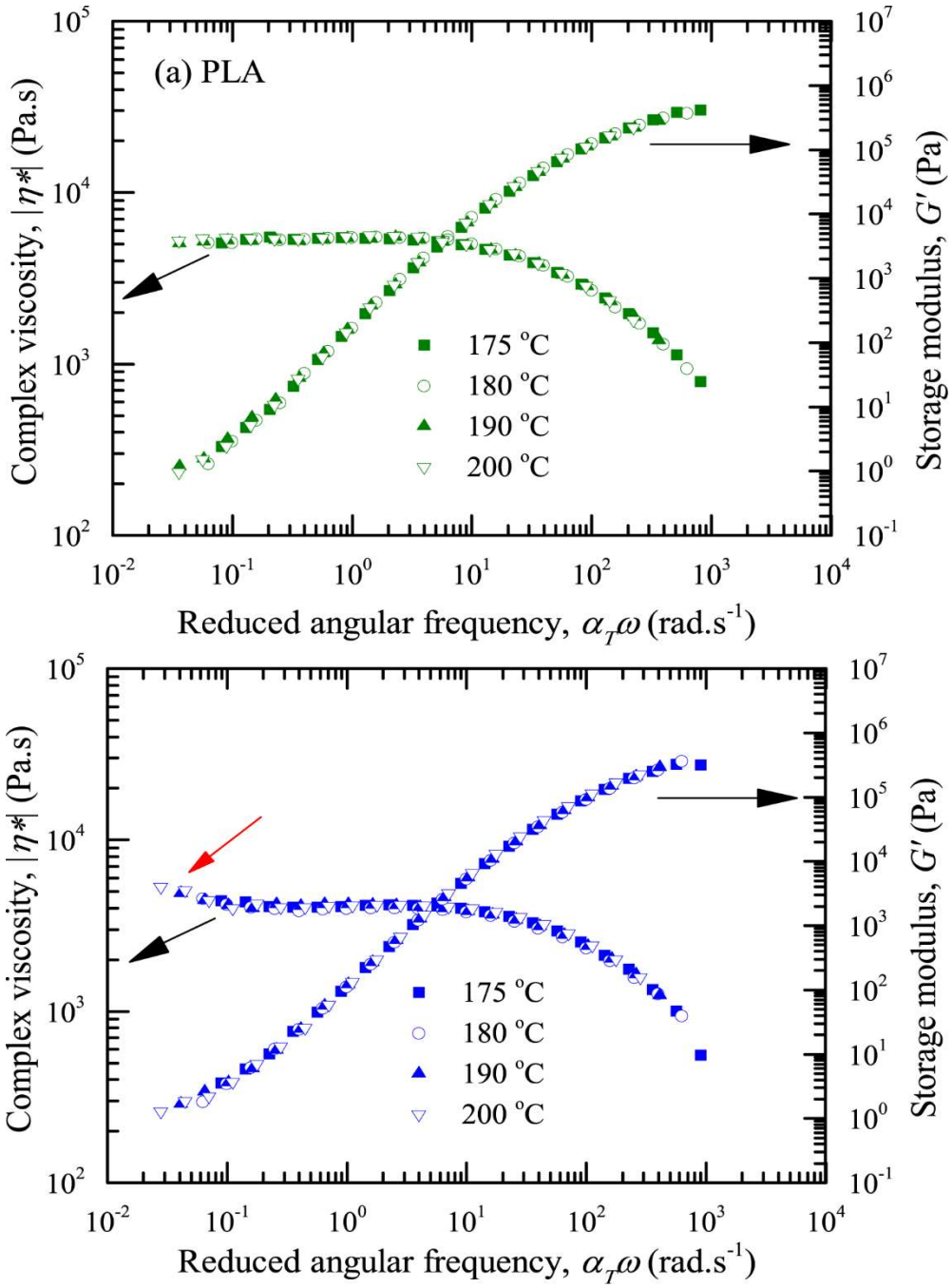

Figure 6.8. *Complex viscosity (|η*|) and storage modulus (G') functions versus reduced frequency for (a) PLA and (b) PLA-C samples. Master curves obtained by application of time–temperature superposition. The reference temperature is 180 ºC. For each temperature measurements, only three points/decade are reported for brevity and improved clarity on the TTS graph.*

The good superposition between all the measurements enables the construction of the temperature dependence of a_T over 7 decades of temperatures for PLA and PLA-C samples, as shown in *figure 6.8.* However in *figure 6.8(b)*, a slight increase in $|\eta^*|$ and G' values were observed in the lower range of $a_T\omega$ (as indicated with a red arrow). This non-plateau behaviour at low $a_T\omega$ could be attributed to the retardation of molecular relaxation processes from presence of o-MMT that induced geometric constraints due to probable particle–particle and/or particle–polymer interactions on the molecular relaxation of the polymer matrix.

Since the viscoelastic measurements were available only over a relatively narrow temperature range, the horizontal shift factor, a_T, follows an Arrhenius relation with temperature, as given by *equation 2.12* (*c.f. chapter 2, section 2.6.3*). E_a was obtained from the best linear regression of a set of values represented in a graph plotting the natural logarithmic values of a_T versus $1/T$, as shown in *figure 6.9* while results are listed in *table 6.3.*

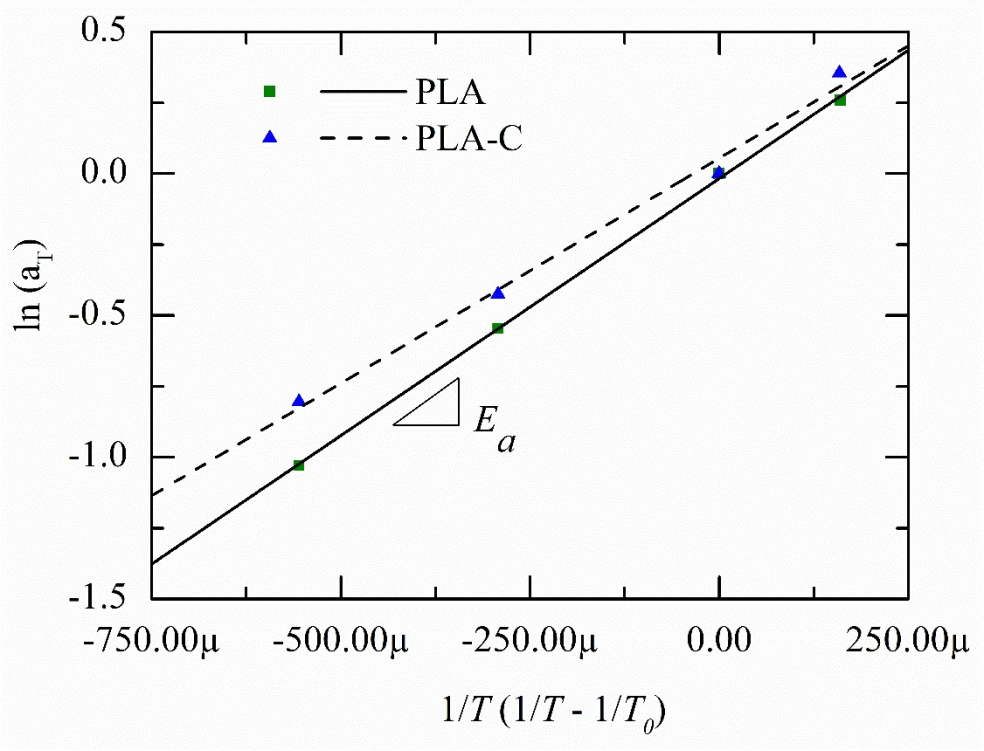

Figure 6.9. *Horizontal shift factor (a_T) versus 1/T (1/T-1/T_0) for PLA and PLA-C samples with 180 °C as reference temperatures. The statistical errors derived from the master curve construction are not shown as they were smaller than the symbol size. The different lines represent the Arrhenius experimental data fits according to equation 2.12 (c.f. chapter 2, section 2.6.3).*

Table 6.3. *Activation energy for PLA and PLA-C samples. The reference temperature is 180 °C.*

Sample Nomenclature	PLA	PLA-C
E_a (kJ.mol^{-1})	88 ±3	84 ±9
R^2	0.9991	0.9882

From *table 6.3*, the computed flow activation values of PLA sample is 88 kJ.mol^{-1} which is consistent with the values reported by Cailloux (2015) (ranged between 85 to 88 kJ.mol^{-1}) and Dorgan et al. (1999) (ranged between 79 and 92 kJ.mol^{-1}) with regards to linear PLA polymers. However, it is revealed that presence of o-MMT reduces E_a measurements of PLA-C from 88 to 84 kJ.mol^{-1} within the margin of error of the experiment.

While the temperature range is narrow by normal commodity polymer standards, it is seen that there is little difference between the activation energies as a function of presence of o-MMT. However, Dorgan et al. (1999) and Cailloux (2015) have also stated the temperature dependency of the viscoelastic functions is independent of the MW but mainly depends on local segmental relaxations rather than large-scale relaxation mechanisms (*e.g.* reptation, constraint release, etc) distinguished by mere calculation E_a value. The possible factor that contributed to this E_a decline could be due to the modest effects of the reduced MW of PLA-C. Presence of hydroxyl-groups belonging to the silicate layers could have increase hydrolytic degradation rate of PLA. This gives rise to formation shorter chain of PLA which could have increased a small scale of local motions of the polymer chain hence the lower E_a value.

In order to substantiate the presence of topological modifications in REX-PLA and REX-PLA-C, its viscoelastic functions within the linear viscoelastic (LVE) regime in comparison with PLA and PLA-C were evaluated. The complex viscosity, $|\eta^*(\omega)|$ and the storage modulus, $G'(\omega)$ obtained from frequency sweeps at 180 °C, is presented in *figure 6.10.* This temperature was selected due to its good compromise between flow properties and thermal stability throughout rheological testing. Additionally, it is also the most representative of the processing temperature used for the manufacturing of PLA/o-MMT nanocomposites sheets.

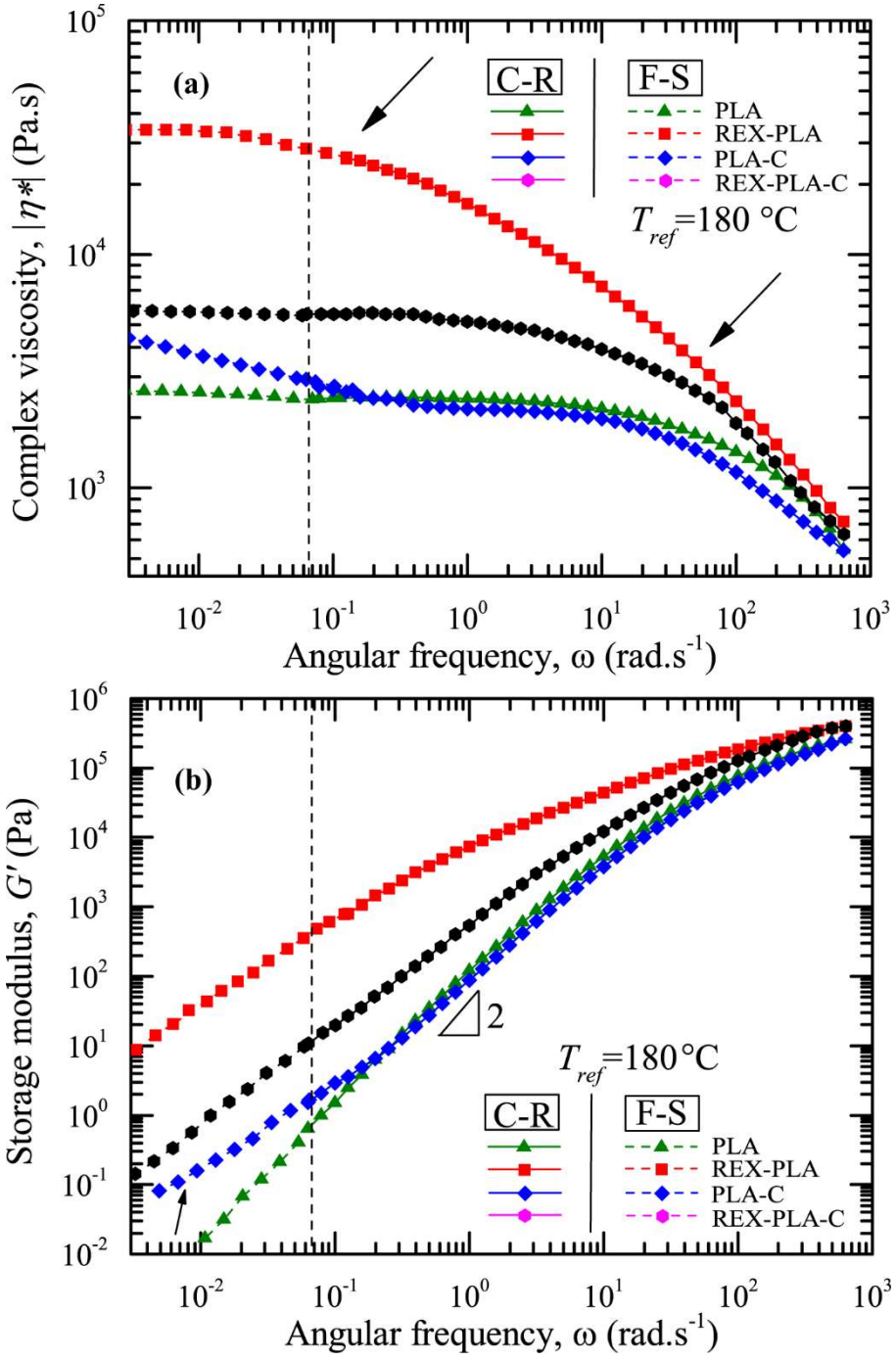

Figure 6.10. *Influence of the clay addition in PLA and modified PLA composites on (a) complex viscosity and (b) storage modulus as function of angular frequency at 180 °C. C-R: conversion of the creep-recovery data calculated from retardation spectrum. F-S: frequency sweep data reduced to master curve. Arrows indicate the geometric effects of the clay particles.*

Looking at *figure 6.10(a)*, it can be seen that the linear newtonian regime was achieved (around 1 rad.s^{-1}) for PLA samples. However, the lowest reachable ω (0.0628 rad.s^{-1}) using a frequency sweep experiment failed to achieved terminal zone for REX-PLA sample. This is because neither $|\eta^*(\omega)|$ reached a plateau nor $G'(\omega)$ reached the terminal double logarithmic slopes of 2, as shown in *figure 6.10(b)*. It has been established that REX-PLA behaves as a thermorheologically complex materials due to the modification of the chain architecture achieved. According to Van Gurp and Palmen (1998), the TTS principle will not hold for materials that has been changed chemically or physically. Therefore, the rheological measurement performed on REX-PLA will not obey the TTS principle. In order to circumvent this issue, combination of a frequency sweep and the conversion of the creep-recovery data at 180 °C was proposed in order to expand rheological measurements towards lower ω as illustrated in figure *figure 6.10(a)* and *(b)*.

From *figure 6.10(a)* and *(b)*, it can be seen that both frequency sweep and the conversion of the creep-recovery data merges with each other. All the investigated sample viscosities converges at high angular frequency (between 10^2 and 10^3 rad.s^{-1}). At this high shearing level, chain orientation (disentanglement) and thermal energy dissipation could be responsible for these similar rheological behaviour. These factors are very influential for the processability of the samples because typical extrusion shear rate lies in the range of 100 up to 500 s^{-1}.

Looking at *figure 6.10 (a)*, it can be seen that PLA displayed a terminal region over a wide range of ω followed by the pseudo-plastic regime with increasing ω. The observed viscoelastic curves of PLA mimics the rheological behaviour of linear chain polymers. The

zero shear viscosity, η_0 and terminal zone slopes of $G'(\omega)$ of all the investigated samples are presented in *table 6.4.*

Table 6.4. *Zero shear viscosity, η_0 and terminal slopes of $G'(\omega)$ of all the investigated samples.*

Sample Nomenclature	Zero shear viscosity, η_0 (kPa.s)	Terminal slopes of $G'(\omega)$
PLA	2.8	2.0
REX-PLA	34.0	1.3
PLA-C	4.2	1.2
REX-PLA-C	5.7	1.5

In the case of PLA-C, its qualitative behaviour of $|\eta^*(\omega)|$ and $G'(\omega)$ is essentially similar albeit marginally lower to PLA up to 10^0 rad.s^{-1}. This could be primarily attributed to the lower MW values as measured using SEC-DRI (*c.f. table 6.2*). However at lower ω region (< 10^0 rad.s^{-1}), $|\eta^*(\omega)|$ and $G'(\omega)$ starts to monotonically increased with decreasing ω (indicated by an arrow). The theoretical double logarithmic slope of $G'(\omega)$ of PLA-C also were reduced to 1.2. Okamoto (2012) have also observed and reported similar rheological response in his PLA/organically modified MMT nanocomposites samples. The higher absolute values of the dynamic moduli may have indicate that reptation mode of the polymer chains in PLA-C were impeded. A possible explanation for this result could be from presence of o-MMT that induced geometric constraints due to probable particle–particle and/or particle–polymer interactions that may have obstructed molecular relaxation of the polymer matrix.

However, REX-PLA sample displayed significantly different rheological behaviour from those of PLA and PLA-C in several key aspects. SAmfE presence in the modified PLA matrix has enlarge the transition zone between the terminal and power-law region. It was observed that the theoretical double logarithmic slope of $G'(\omega)$ does not reached to 2. However, $|\eta^*(\omega)|$ of REX-PLA sample does reached a plateau regime using convergence of frequency sweep and conversion of the creep-recovery data. At low ω, G' values of REX-PLA also increased and became less shear-sensitive as compared to PLA. This behaviour indicates an increase in the melt elasticity (and thus in the melt strength) which is in line with the significant increases in MW as measured using SEC-DRI (*c.f. table 6.2*). Numerous studies has observed similar findings and have attributed the result to the restriction of molecular mobility due to the increase in MW and the chain extension/branching reactions resulting from the reactive process.(Al-Itry et al., 2014; Corre et al., 2011a; Dorgan et al., 1999; Mihai et al., 2010; Najafi et al., 2012a)

On the contrary, the viscosity enhancement with presence of clay particles in a REX-PLA matrix was not as anticipated. $|\eta^*(\omega)|$ were only slightly enhanced for REX-PLA-C (η_0 = 5.7) as compared to REX-PLA (η_0 = 34.0). Surprisingly, the slight increase in $|\eta^*|$ and G' values in the lowest ω range induced by the clays in PLA-C was also not present for REX-PLA-C samples. Since the corresponding onset frequency of this transition is related to the size, the size distribution and the interfacial tension between clays and the polymeric matrix, the lower the onset frequency, the smaller the size of the particle and the larger the interfacial tension causing clay particles to adhere more strongly to the polymer matrix. Thus, it is suggested that the slight increase in G' and $|\eta^*|$ values might have been shifted to lower ω due

better clay dispersion caused by the higher local shear field coupled with the possible clay–polymer tethering.

For the purpose of verifying the modifications in the frequency onset of the transition in PLA-C and REX-PLA-C, the out-of-phase of component of $|\eta^*|$, η'' was analysed. Ostensibly, the complex viscosity $|\eta^*|$ can be broken into an in-phase component (η') and out-of-phase component (η''). η'' is defined as the ratio of the storage modulus (G') to the angular frequency (ω) determined during dynamic measurements. Since dynamic viscosity (η') describes the viscous part of complex viscosity term, utilizing η'' values can gives an insight into the elastic part of the complex viscosity of the material analysed. The double logarithmic derivative of η'' versus log ω in combination with $d^2(\log(\eta''))/d(\log(\omega))^2$, for PLA-C and REX-PLA-C was plotted in *figure 6.11.*

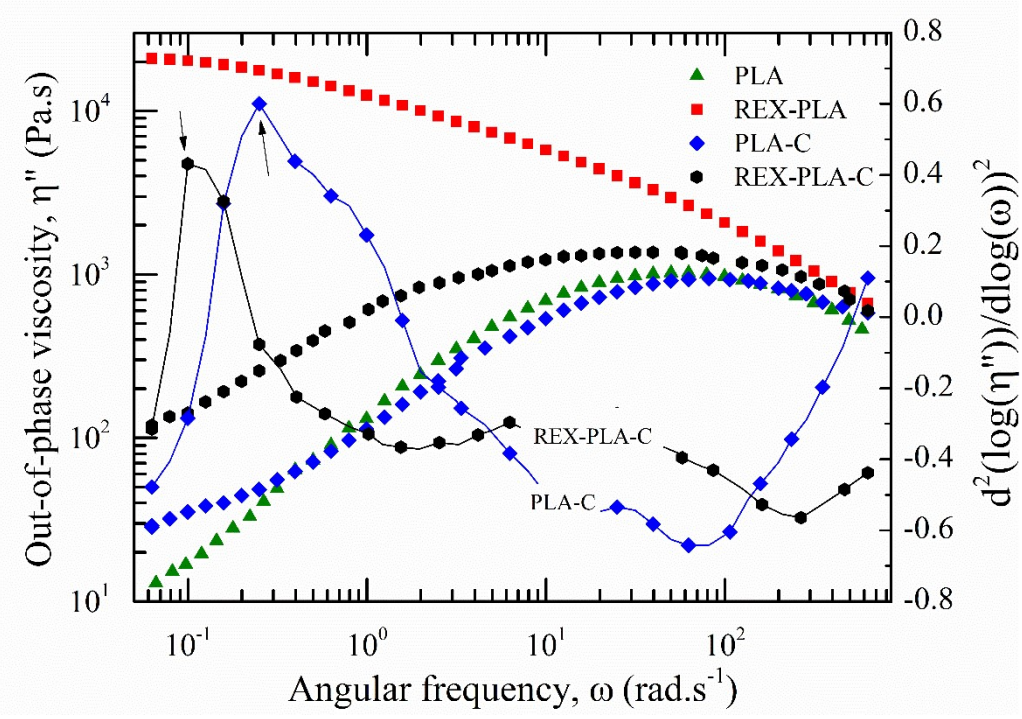

Figure 6.11. *Effect of clay particles on PLA matrix versus modified PLA matrix on the onset frequency of the transition of η'' at 180 °C.*

As shown in *figure 6.11.*, presence of SAmfE clearly modifies the onset frequency of the transition in REX-PLA-C compared to PLA-C. Trend-wise, one can see an evident displacement of the peak maximum of the second derivative (indicated by an arrow) to lower ω. Peak maximum of the second derivative for REX-PLA-C samples was observed at approximately 0.1 $rad.s^{-1}$ compared to 0.3 $rad.s^{-1}$ for PLA-C samples signifying better clay dispersion was achieved in REX-PLA-C.

In general, a good dispersion of filler agglomerates can be achieved when the cohesive forces of the agglomerates are exceeded by the hydrodynamic separating forces applied by the fluid polymer (Majesté, 2016). However, relying only on hydrodynamic stress is insufficient to ensure good dispersion state of nanoparticles in polymer matrix as evidenced in PLA-C. Creation of appropriate filler–matrix interactions from clay–polymer tethering through SAmfE molecules may have resulted in the chemical weakening of agglomerates and improving the efficiency of hydrodynamic forces. This resulted in an increased interfacial tension in REX-PLA-C samples hence improved o-MMT dispersion.

6.2.3. Investigation of clay dispersion in PLA and modified PLA composites.

The X-ray diffraction (XRD) profiles of PLA-C and REX-PLA-C samples are displayed in *Figure 6.12.* Initally, it can be observed that an intense reflection appeared at 2θ = 2.4° for PLA-C. However in REX-PLA-C, basal plane reflection of PLA-C observed was shifted to a lower diffraction angles (2θ = 1.9°) and broadened in the modified PLA matrix. The shifting of these peaks to lower angles translates into an increase of *d*-spacing of initial interlayer distance of raw o-MMT from 1.86 nm to 3.7 nm and to 4.6 nm for PLA-C and REX-PLA-C, respectively, which signifies clay intercalation.

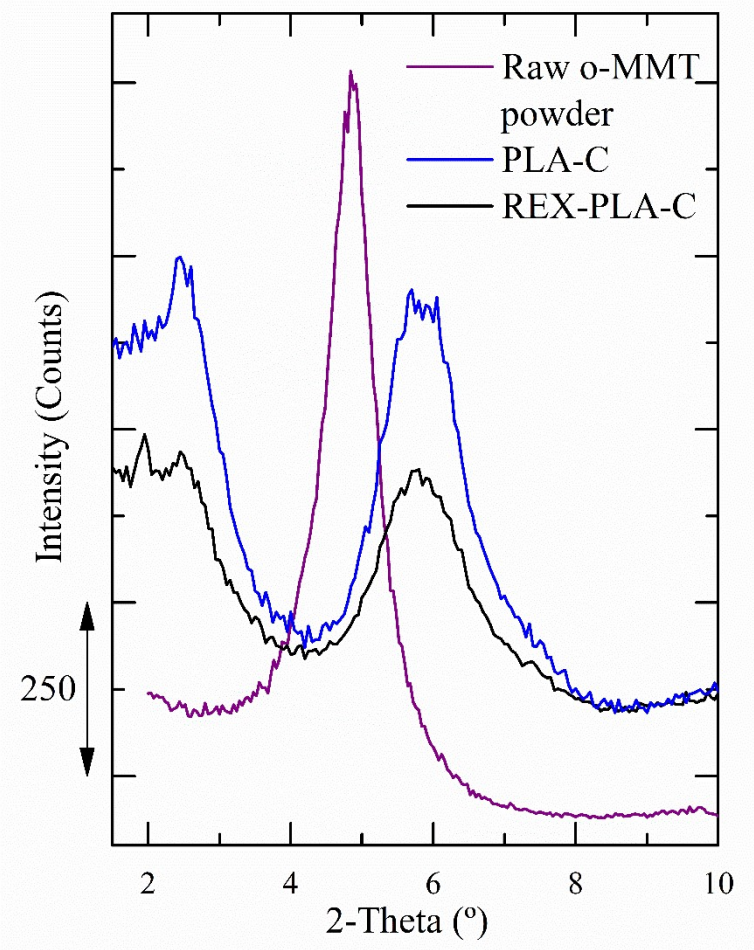

Figure 6.12. *State of dispersion of clay particles in PLA and modified PLA matrix. Raw o-MMT powder was included for comparison purposes.*

Meanwhile, another peak was also observed at 5.8° for both composite materials. Similar observations was made by Fillipi et al. (2011) that attributed these peaks to a clay gallery collapse due to decomposition of the organo-modifying agent. Additionally, an appreciable decrease of diffracted intensity of REX-PLA-C when compared to PLA-C may be attributed to the partial disruption of parallel stacking order and/or interlayer galleries of the clay platelets (*i.e.* delamination). In order to evidence this hypothesis, transmission electron microscopy (TEM) study were undertaken to better understand the final nanocomposite morphology of PLA-C and REX-PLA-C.

Figure 6.13 show the TEM micrographs at several magnifications of sections of both PLA composites, in which dark entities are the cross section of o-MMT layers. As observed in *figure 6.13 (a)*, a relatively homogeneous and uniform clay distribution was observed in both PLA-C and REX-PLA-C (*c.f.* magnification 8000X). It also noticed that the clay orientation is predominantly oriented in the direction of flow extrusion.

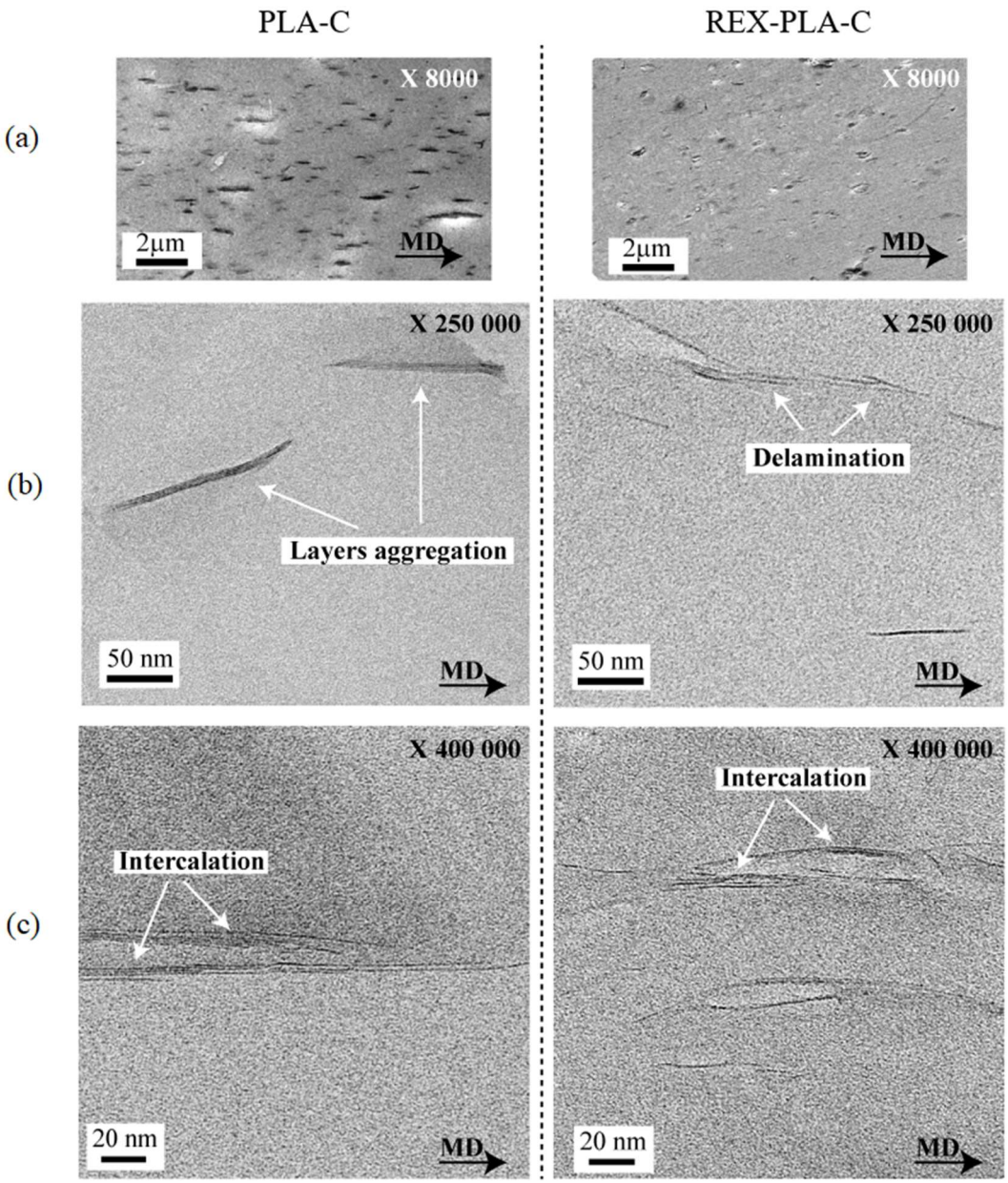

Figure 6.13. *The clay dispersion of PLA-C and REX-PLA-C samples as observed with TEM at the indicated magnification. The micrographs are arranged in an ascending order of magnification, namely (a) X8000, (B) X250 000 and (c) X400 000.*

Comparing to PLA-C, it can be suggested that the clay layers are more homogeneously and finely dispersed in REX-PLA-C. There also seems to be an improvement on the degree of clay delamination and intercalation in REX-PLA-C compared to PLA-C as evidenced in *figure*

6.13 (b) and *(c)*. This finding could have been due to the combined effects of clay–polymer tethering through SAmfE molecules and higher shear viscosity during clay–polymer mixing due to the different flow rates between the melt and o-MMT platelets (*c.f. figure 6.10*). The local shearing field that exists along the clay platelets may have increased during mixing; hence disrupting the o-MMT ordered structures. Succinctly, it can be articulated that the inferences made in XRD analysis was corroborated in *figure 6.13* and agrees with the study of Najafi et al. (2012a).

However, evidences of delamination and intercalation but not so much of effective exfoliation were observed in REX-PLA-C. This is consistent with the intercalated structure reported by so many nanocomposite researchers, who successfully prepare only intercalated (not exfoliated) nanocomposites via melt extrusion technique (Arroyo et al., 2010; Carrasco et al., 2011a; Pluta et al., 2006; Sinha Ray et al., 2003b; Wu et al., 2009). Yoshida et al (2006) and Okamoto (2012) has suggested that amount of shear stress applied during processing has little effect on the exfoliation of the o-MMT layer. Achieving complete exfoliation of layered fillers requires an innovative compounding technique in order to possess nanoscale control of the layered nanofillers and achieved complete exfoliation (Saito et al., 2007).

6.2.4. Effect of clay on the thermal behaviour of PLA and modified PLA composites.

a) Extruded sheets: "As received analysis"

The investigation of the thermal behaviour of PLA, REX-PLA and PLA composites with o-MMT using DSC was performed following the thermal protocol described in *section 5.5.* The first DSC heating scans (H1) at 10 ºC.min^{-1} of all the investigated samples stored for 1 week at room temperature after de-aging treatment are shown in *figure 6.14*. Thermal properties obtained from the corresponding heating scans are tabulated in *table 6.5.*

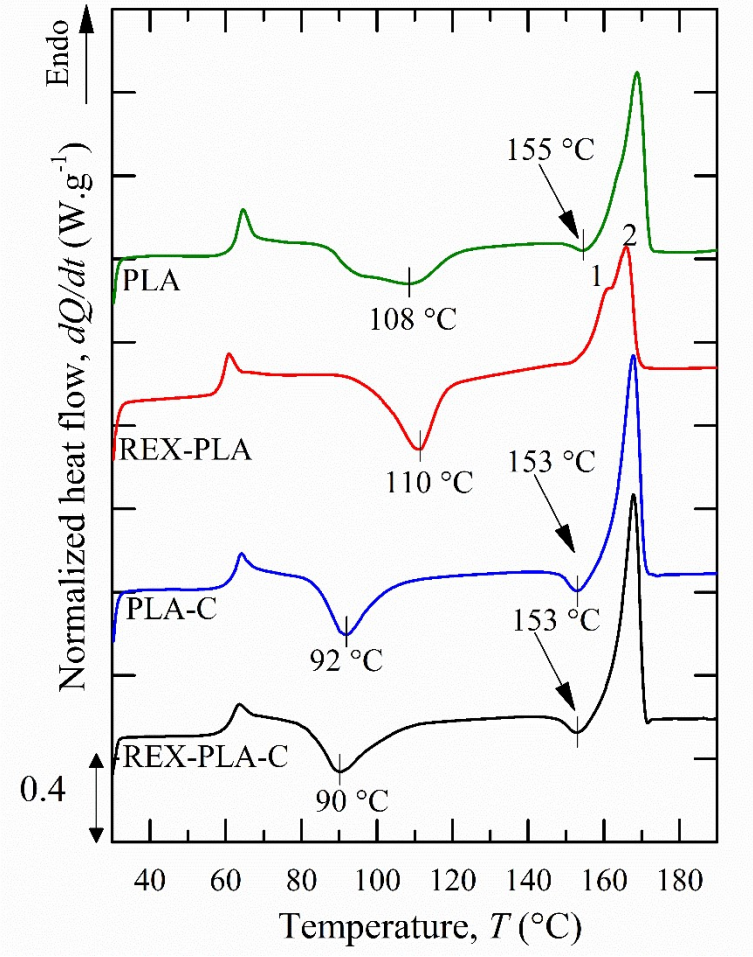

Figure 6.14. *First DSC heating scan (H1) of all investigated samples stored for 1 week at room temperature after de-aging treatment. Arrows indicated small exothermic peak prior to dominant melting peak together with the corresponding temperature.*

Table 6.5. *Calorimetric properties of PLA and REX-PLA/o-MMT nanocomposites from first heating scan.*

Parameters	Materials			
	PLA	**REX-PLA**	**PLA-C**	**REX-PLA-C**
$T_{g,m}$ (°C)	61.5 ± 0.3	62 ± 2	61.3 ± 0.1	61.2 ± 0.4
T_{cc} (°C)	107.6 ±1.7	109.7 ±0.4	91.7 ±0.2	89.4 ±1.2
ΔH_{cc} (J g^{-1})	29 ±2	29 ±1	25 ±1	23 ±4
$X_{c,cc}$ (%)	31 ±2	31 ±2	27 ±2	25 ±4
T_{mp1} (°C)	168.9 ±0.3	160.6 ±0.6	168.1 ±0.3	167.5 ±0.5
T_{mp2} (°C)	n/a	165.3 ±0.1	n/a	n/a
ΔH_m (J g^{-1})	34 ±1	31 ±1	34 ±1	35 ±1
$X_{c,m}$ (%)	36 ±1	32 ±1	38 ±1	38 ±2
X_c (%)	5 ±1	2 ±1	10 ±1	14 ±1

n/a: not available

In general, presence of either SAmfE and/or o-MMT does not appear to affect the midpoint $T_{g,m}$ of REX-PLA, PLA-C and REX-PLA-C as shown in *table 6.5*. However, for all the samples, the endothermic peak intensity related to the enthalpy relaxation observed in the vicinity of $T_{g,m}$ appeared to be overlapped by glass transition. According to Pan et al. (2008), this is attributed to a large change in the potential energy within T_g region due to the alteration of locally ordered domains to a more disordered conformational state, upon heating.

Within the statistical error, SAmfE in the modified PLA matrix does not modifies T_{cc} of REX-PLA. Similarly, $X_{c,cc}$ of REX-PLA computed is also similar to PLA. Similar studies suggested that maximum degree of cold-crystallization should decrease due to the observed increase in MW (*c.f. table 6.2*) and introduction of microstructural defects (e.g. branching) which could possibly encumbers the reptation-like mobility of chains to crystallization sites (Baratian et al., 2001; Bigg, 2005; Saeidlou et al., 2012).

In contrast, addition of o-MMT has reduced T_{cc} to lower temperature (-15%). However, $X_{c,cc}$ of PLA-C were similar to PLA within the experimental error. Similar trends was reported by Chow and Lok (2009), Day et al. (2006), Lee et al. (2003) and Lewitus et al. (2006). Usually, a lower T_{cc} on heating indicates faster crystallization rate. All the studies suggested that the observed trends were attributed the nucleating effect of the nanosized clay. The increased nucleating sites are likely to facilitate the PLA crystallization process in the nanocomposite systems thus T_{cc} is decreased by the addition of nanoclays. In the case of REX-PLA-C, within the T_{cc} and ΔH_{cc} does not seem to be significantly modified within the statistical error with the presence of o-MMT when compared to PLA-C. It seems that factors such as increased surface area of intercalated o-MMT due to clay-polymer tethering coupled with nucleating effect of o-MMT does not seem to play a significant role facilitating further crystallization process.

With regards to the melting transition region, a small exotherm were observed in all of the investigated samples (indicated by an arrow in *figure 6.11*) prior to a single dominant melting peak. According to Pan and colleagues (2007), the appearance of the exothermic peak could be caused by the α-to-α' transition of the possible α'-crystals formed during the cold-crystallization process. On the other hand, the single dominant melting endotherm observed in PLA, PLA-C and REX-PLA-C samples hints that only a single population size of crystal is present. However for REX-PLA, the presence of SAmfE in the modified PLA matrix induced a separation of the shoulder from the dominant endotherm into two separated peaks. This behaviour might be attributed to the melt-recrystallization mechanism. The low-temperature shoulder may be attributed to the melting of the original crystals, while the high-temperature endothermic melting peak may be due to the melting of crystals that developed during the melt-

recrystallization mechanism during heating. This observation is also inline with the ones reported by Pan et al. (2008) and Cailloux et al. (2014).

However, the presence of SAmfE in the modified PLA matrix does not seem to modify the melting temperature of REX-PLA. T_m of REX-PLA was roughly similar compared to other investigated samples (≈ 2%). Several studies have stated that T_m will simultaneously increase with MW up to a critical value (M_n ≈80-100 kg.mol^{-1}) and thereafter reaches a constant value upon further increase (Auras et al., 2010; Cailloux, 2015; Ikada and Tsuji, 2000). Similarly, o-MMT presence does not seem to cause a significant change in T_m of PLA-C and REX-PLA-C. As reported by Paul et al. (2003) and Vasanthan et al. (2011), o-MMT presence does not influence the T_g and the T_m of the PLA matrix.

Looking at the X_c values, PLA and REX-PLA samples are amorphous due to the low crystalline fraction (*i.e.* 5 and 1%, respectively) developed during processing. The low crystallinity is attributed to the slow crystallization kinetics of PLA and REX-PLA due to the relative fast cooling rate applied to the melted material at the die exit during reactive extrusion. However, X_c values observed for PLA-C and REX-PLA-C have increased to 11 and 14% respectively. Day et al. (2006) reported that the presence of the o-MMT nanoparticle influences the nucleation and crystal growth rate of the PLA. The crystallization rate of PLA is enhanced by the addition of nanoclay. In semi-crystalline PLA, chain conformation and developed crystallinity are sensitive to surface interactions. It is possible, in the case of nanocomposites, that the high surface interaction between the polymer chains and the nanoclay surface tends to increase the degree of crystallinity because of the heterogeneous nucleation effect of o-MMT.

b) Thermal transitions under controlled cooling/heating ramps of PLA, REX-PLA and PLA based composites with o-MMT

The following DSC analysis will examine the effects of o-MMT on the thermal behaviour of PLA and modified PLA composites excluding the previous thermo-mechanical characteristics generated by the REX-calendering stage. *Figure 6.15* show the controlled cooling **(C)** and second heating **(H2)** scans, respectively. *Table 6.6* summarizes the thermal properties determined from **C** and **H2** cycles.

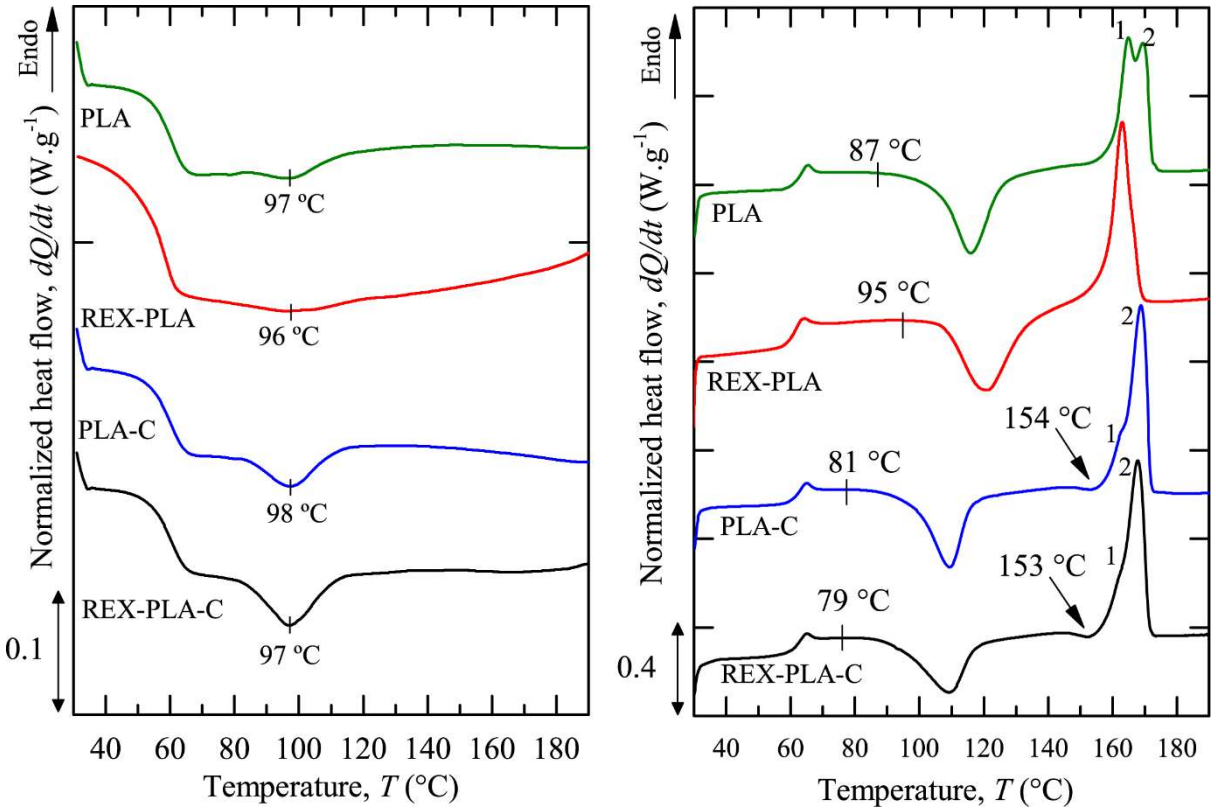

Figure 6.15. *DSC (a) controlled cooling scan* ***(C)*** *and (b) second heating scan* ***(H2)*** *both at 10 ºC.min^{-1} of all investigated samples. Arrows indicated small exothermic peak prior to dominant melting peak together with the corresponding temperature.*

Table 6.6. *Thermal properties determined from the **C** and **H2** runs.*

	Parameters	PLA	REX-PLA	PLA-C	REX-PLA-C
Cooling (C)	$T_{c,0}$ (°C)	119.2 ±0.2	123.0 ±0.2	120.4 ±0.8	120.7 ±0.5
	T_c (°C)	97.7 ±0.3	96.3 ±0.3	97.5 ±0.2	97.2 ±0.3
	$\Delta H_{c,c}$ (J g^{-1})	2 ±1	2 ±1	3 ±1	4 ±1
	$X_{c,c}$ (%)	2 ±1	2 ±1	3 ±1	4 ±1
2nd Heating (H2)	$T_{g.\ m}$	61.9 ± 0.1	60.9 ±0.2	61.6 ± 0.1	61.8 ± 0.1
	$T_{cc,0}$ (°C)	86.7 ± 0.3	95.2 ±0.2	81.3 ± 0.2	79.4 ± 0.3
	T_{cc} (°C)	115.9 ±0.1	112.8 ±0.4	109.2 ±0.1	109.5 ±0.4
	ΔH_{cc} (J g^{-1})	37 ±1	33 ±2	29 ±1	26 ±1
	T_{mp1} (°C)	164.7 ±0.2	165.0 ±0.2	164.2 ±0.1	162.1 ±0.1
	T_{mp2} (°C)	169.4 ±0.2	n/a	168.7 ±0.3	167.9 ±0.1
	ΔH_m (J g^{-1})	39 ±1	35 ±1	34 ±1	32 ±1
	X_c (%)	2 ±1	2 ±1	4 ±1	5 ±1

n/a: not available

Under the cooling conditions used in the current study, PLA samples exhibited a weak crystallization exotherm with T_c peak at 97 °C during the controlled cooling run **(C)** (*c.f. figure 6.15a*). However, REX-PLA samples displayed a broadened crystallization transition while the crystallization exotherm were shifted to 123 °C. Similar trends were also observed by Cailloux (2015) following the evaluation of his modified PLA sheets. This trend can be explicated by the MW increase due to introduction of sparsely branched topology of REX-PLA (*c.f. table 6.2*). These microstructural defects will then consequently increase the steric hindrance and restrict the movement and reorientation of the PLA chains to form a more thermodynamically favourable crystalline state.

With regards to both PLA-C and REX-PLA-C, it was found that o-MMT does not significantly changes the crystalline structure of PLA chain. Within the statistical error, the calculated $X_{c,c}$ content for both PLA-C and REX-PLA-C reported were similar to PLA and REX-PLA. However, the crystallization transition of both PLA-C and REX-PLA-C does

appear to be broader and sharper albeit having similar $T_{c,0}$ and T_c with PLA. The broadened transition can be explained by possible "lubricating" effect induced by the low MW of the organo-modifier of o-MMT that counteracts the decrease in molecular mobility during cooling. Murariu et al. (2015) have reported similar trends for his PLA/o-MMT nanocomposites. In order to gain a better understanding of this trend, relative percentage conversion as function of temperature graph of all the investigated samples were plotted in *figure 6.16*.

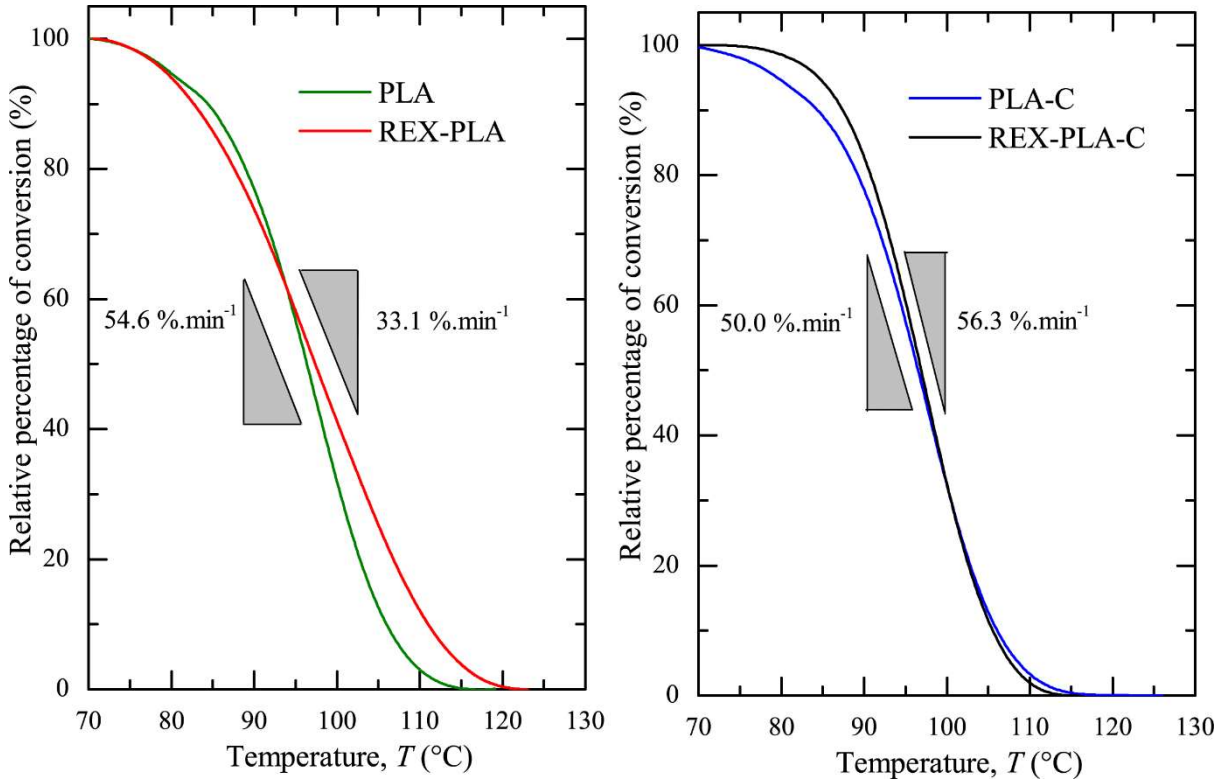

Figure 6.16 *Relative percentage of conversion as a function of the temperature for (a) PLA and REX-PLA and (b) PLA based nanocomposites samples upon cooling at 10 ºC.min^{-1}. The maximum rate of conversion is indicated for each sample.*

Looking at *figure 6.16(a),* although $T_{c,o}$ of REX-PLA was higher than PLA, a decline in the ability to crystallize upon cooling is apparent. It is seen that maximum rate of conversion

of REX-PLA saw -39% decrease compared to PLA. These tendencies validates the summation made by several studies that introduction of microstructural defects due to presence of SAmfE retarded reptation motion due to the PLA chain immobilization and hamper crystal growth rate (Cailloux, 2015; Henton et al., 2005; Lim et al., 2008; Pan et al., 2007).

Referring to *figure 6.16(b),* it seems $T_{c,o}$ of PLA-C and REX-PLA-C remained insensitive towards presence of o-MMT. Likewise, maximum rate of conversion of both PLA-C and REX-PLA-C also remained similar to PLA. It can be surmised that o-MMT presence in PLA-C and REX-PLA-C neither promote nor hampers the crystallization of PLA.

At the second controlled heating scan (**H2)**, the midpoint T_g remained unaffected to presence of SAmfE and/or o-MMT for all the investigated samples, as shown in *table 6.6*. This trend are similar to studies reported by Dorgan et al. (2000), Korhonen et al. (2001) and Nofar et al. (2011) regarding LCB, star- and comb-like (4-9 arms) PLA architectures and by Chow and Lok (2009), Paul et al. (2003) and Vasanthan et al. (2011) regarding PLA/o-MMT nanocomposites.

However, during the cold-crystallization process, REX-PLA samples showed a decrease in the onset temperature and T_{cc} compared to PLA samples. This result is probably due to the overlapping of the cold-crystallization and melting processes, respectively. Addition of o-MMT cause the onset of the cold-crystallization temperature and T_{cc} shifted to lower temperatures for PLA-C and REX-PLA-C samples which is in correlation with *section 6.2.4a*. An improvement in the cold-crystallization ability with the presence of o-MMT upon reheating is perceptible as shown in *table 6.4*. Similar observations were observed and discussed by Day

et al. (2006) and Lewitus et al. (2006) which attributed all these trends to the nucleating effect of the nanosized clay. The introduction of o-MMT increases the available nucleating sites which are likely to facilitate the crystallization process.

At the melting endotherm, PLA samples displayed a well-defined double melting peak (marked as 1 and 2). This trend is contrary to the other samples in which a small exotherm followed by shoulder or low temperature peak is formed in the melting endotherm. Consequently, T_{mp1} and T_{mp2} values declined with SAmfE presence in the modified PLA matrix. The reduction in T_{mp} values found for REX-PLA was probably due to the increase in microstructural defects (*e.g.* branching) which promoted the crystallization of thinner and inhomogeneous lamellar crystals. However with the introduction of o-MMT, T_{mp} values of PLA-C and REX-PLA-C within the statistical error remain similar to PLA. Upon reheating, it seems that presence of o-MMT have become hindrance in macromolecular chain medium-range transport movement for formation of thicker and homogeneous lamellar crystals.

6.2.5. Effect of clay addition on non-isothermal crystallization of PLA and modified PLA based composites.

Evaluation of the non-isothermal crystallization behaviour from the melt of PLA, REX-PLA and its composites with o-MMT was carried out using the DSC technique. *Figure 6.16* shows the comparative DSC ramps at different cooling rates of PLA, REX-PLA and its composites with o-MMT.

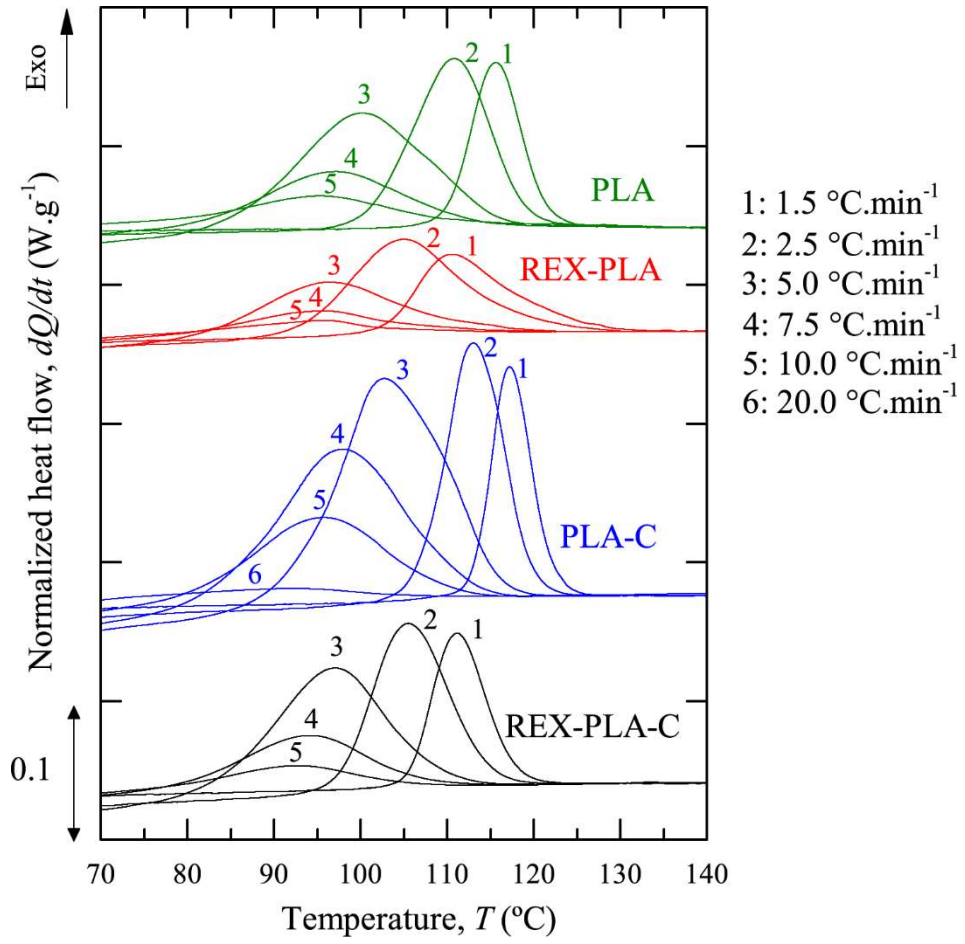

Figure 6.17. *Non-isothermal crystallization DSC traces at the indicated cooling rates (°C min^{-1}) for all investigated samples.*

It must be noted that all the curves have been translated in vertical direction for clearer interpretations. It can be seen that from *figure 6.17,* both the position and the shape of the exothermic signal corresponding to the crystallization process are contingent on the cooling rate. It is also observed that the exothermic signal became wider and shifted towards lower temperatures with increasing cooling rate. This observation is general for all the samples investigated.

PLA displayed single crystallization exotherms at relatively slow cooling rates (*i.e.* 1.5, 2.5, 5, 7.5 and 10 °C.min^{-1}). It is widely-accepted that PLA possess slow crystallization kinetics and this trend reinforces this understanding which is also in line with the results of the thermal analysis (*c.f. chapter 6, section 6.2.4)*. In regards to REX-PLA, the thermal "windows" of crystallization (temperature range where the crystallization process is recorded) appear to be similar to PLA. However, the thermal windows have been displaced towards lower temperatures in REX-PLA. The crystallization exotherms exhibited were also broader and less intense than PLA especially evident at slower cooling rates. Evidently, SAmfE presence in the modified PLA matrix seems to slightly reduce the crystallizability of REX-PLA. This result indicate that REX-PLA possess very slow crystallization kinetics which could be influenced by existence of microstructural defects (e.g. branching) that could hinder the mobility of chains towards crystallization sites.

Interestingly, o-MMT presence seems to improve the crystallization behaviour of PLA-C, as shown in *figure 6.17*. It seems that the cooling rate windows were enlarged (*i.e.* 1.5, 2.5, 5, 7.5, 10 and 20 °C.min^{-1}). It is apparent that in a non-isothermal conditions that the presence of o-MMT impart a nucleating effect on PLA, which might enhance crystallization. However, o-MMT presence in a modified PLA matrix negated the effectiveness of o-MMT in enhancing the crystallizability of REX-PLA-C. Comparing with the respective cooling rate, the exothermic signals were broader and less intense in comparison to PLA-C. It is known that SAmfE is a multifunctional reactive agent, several PLA chains and clay particles could be grafted to one SAmfE molecule. Crystallization rate of a polymer is determined by the nucleation rate and mobility of polymer chains. Even though the nucleation rate increases with presence of o-MMT, the mobility of polymer chains has been reduced due to induced

topological modifications of REX-PLA and possible clay-polymer tethering hence reducing the crystallizability of REX-PLA-C.

Subsequently, valuable informations such as peak crystallization temperature, T_c and the proportion (percentage) of the crystalline fraction, X_c were extracted from *figure 6.17.* Next, both T_c and X_c as a function of the applied cooling speed were plotted and are presented in *figure 6.18.*

Looking at *figure 6.18,* both T_c and X_c are inversely proportional to the applied cooling rate. It is evident in which both T_c and X_c decrease with increasing cooling rates. It is also noted that as cooling rates starts to increase to 10 °C.min^{-1}, the crystallinity fraction barely reaches ≈8 % and ≈3 % crystallinity for PLA-C and the other samples, respectively. Additionally, it is also observed that PLA-C samples also achieved the highest peak crystallization temperature and crystalline fraction compared to the other samples. This observation substantiate the nucleating effect of o-MMT has on PLA matrix as has been elucidated in the above paragraphs.

From *figures 6.18,* both REX-PLA and REX-PLA-C had the lowest T_c and X_c compared to other samples. This also confirms the hypothesis that the existence of topological modifications in REX-PLA and possible clay-polymer tethering in REX-PLA-C could hinder the mobility of chains towards crystallization sites hence reducing the crystallizability of both REX-PLA and REX-PLA-C.

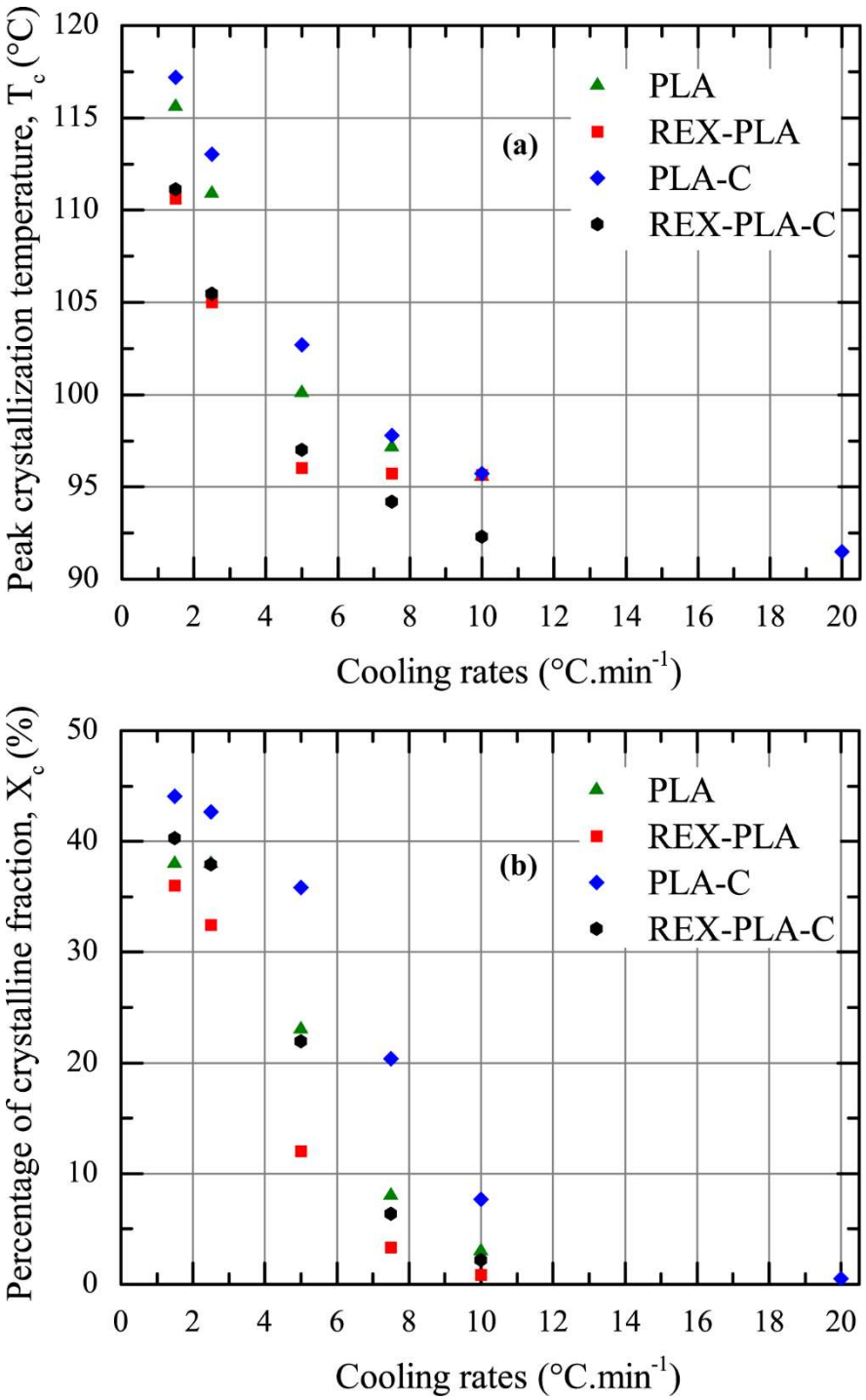

Figure 6.18. *Variation of cooling rate against (a) peak crystallization temperature and (b) percentage of the crystalline fraction of PLA and modified PLA composites.*

Another significant aspect to understand the influence of o-MMT in both PLA or modified PLA matrix on crystallization is by determination of the "activation energy" of the crystallization process (ΔE) using well-defined model. For this study, this analysis was performed using Friedman model. The Friedman model attempts to express the activation energy required as a function of the conversion speed that is recorded at a given conversion percentage at a certain temperature under an applied cooling speed. This analysis could perhaps offer a clearer interpretation and allows a more "immediate" comparison between different formulations.

The Friedman model can be mathematically expressed as:

$$Ln\left(\frac{dX(t)}{dt}\right) = -\frac{\Delta E}{RT} - Lnf\left(\frac{dX(t)}{dt}\right) \quad 6.5$$

Or alternatively:

$$Ln\left(\frac{dX(T)}{dT}\varphi\right) = -\frac{\Delta E}{RT} - Lnf\left(\frac{dX(t)}{dt}\right) \quad 6.6$$

Where:

dX(t)/dt: conversion rate (crystallization)
f(dX(t)/dt): pre-exponential factor
ΔE: "Activation energy" of the process
T: Temperature at the specific degree of conversion.
φ: cooling rate applied.

The basic calculation procedure is the graphic representation of the terms on the right hand side of the equation versus $1/T_c$. From the slope and the intercept obtained after the linear regression, ΔE and the "pre-exponential" function were determined in each case. A generic

representation made according to the Friedman models proposed for a relative degree of conversion of 40% are illustrated in *Figure 6.19* while the calculated activation energy are listed in *Table 6.6.*

It is evident from *figure 6.19* that the first applications of the Friedman methods immediately brought to light the issue of variable activation energy which is evident in REX-PLA sample. It is observed that the representation of the Friedman model (relative isoconversion speed) for the REX-PLA formulation possess two slopes. This indicates that the process could not be described by a single activation energy. This is due to the occurrence of secondary crystallization regime probably caused by calendaring process during extrusion. However, it can be seen that all other the samples excluding REX-PLA exhibit only primary crystallization regime.

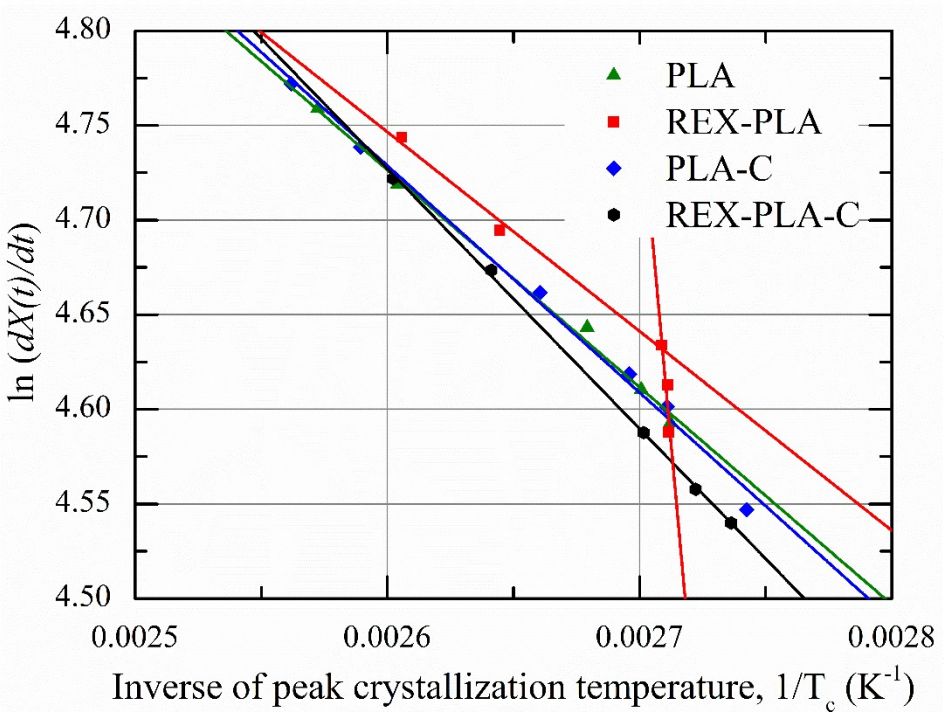

Figure 6.19. *The Arrhenius plot of natural logarithm of conversion rate versus reciprocal of peak crystallization temperature at relative conversion percentage of 40%.*

Table 6.7. *Calculated activation energy of primary crystallization for all the investigated sample at relative conversion percentage of 20, 40, 60 and 80 %.*

Relative conversion percentage, X(t) (%)	Activation energy, ΔE (kJ.mol^{-1}.K^{-1})			
	PLA	REX-PLA	PLA-C	REX-PLA-C
20	-0.3	-0.4	-0.5	-0.6
40	-8.9	-10.9	-9.4	-11.4
60	-11.9	-12.1	-11.7	-14.1
80	-16.1	-22.7	-14.6	-13.9

From *table 6.7*, all the computed values of ΔE are negative, indicating that the rate of crystallization increases with decreasing T_c. For all the sample analyzed, ΔE is found to increase with increasing relative crystallinity, suggesting that as the crystallization progresses it is more difficult for all samples to crystallize which is similarly proposed by Li et al. (2010). At relative crystallinity up 60%, the ΔE value of all the samples are relatively similar. This indicates that the presence of o-MMT in PLA and modified PLA composites neither reduces nor enhances drastically transportation ability of polymer chains and affects the mobility of PLA molecular segments. However at 80% relative crystallinity, the presence of SAmfE in REX-PLA leads to an increase of ΔE value. It could be hypothesize that the chain topology modifications brought about by SAmfE in REX-PLA, may have imposed a limitation in the "self-diffusion" (transportability) factor of the polymer chains and impede crystalline growth.

6.2.6. Effect of clay addition on isothermal crystallization of PLA and modified PLA composites.

Investigation of isothermal crystallization of PLA, REX-PLA and PLA based composites with o-MMT were performed at various crystallization temperatures (T_c) are shown in *figure 6.21*. Initially, isothermal crystallization of PLA was analyzed with T_c ranging from

122 to 116 ºC. However, addition of o-MMT exhibited comparable primary crystallization as PLA at lower range of T_c from 120 to 114 ºC hence the isothermal crystallizations was investigated at the aforementioned temperatures. On the other hand, REX-PLA sample displayed a broader and less intense crystallization exotherms at T_c ranging from 120 to 112 ºC. Interestingly, REX-PLA-C display almost similar primary crystallization at similar T_c range hence isothermal crystallizations was studied at the said temperatures.

The general pattern that emerges from *figure 6.20* is that a single and monomodal exothermic signal at each T_c were observed for all the formulations. However, the exothermic peak shifted to longer duration and becomes broader with increasing T_c. This behaviour indicates that a slower exotherm reaction will take place with increasing T_c. Turning now to exotherm enthalpy, the decrease in the exotherm enthalpy (*i.e.* the total exotherm peak area) observed in REX-PLA and REX-PLA-C can be attributed to SAmfE and/or o-MMT presence. This observation implies a decrease in the maximum X_c for REX-PLA and REX-PLA-C as compared to PLA and PLA-C.

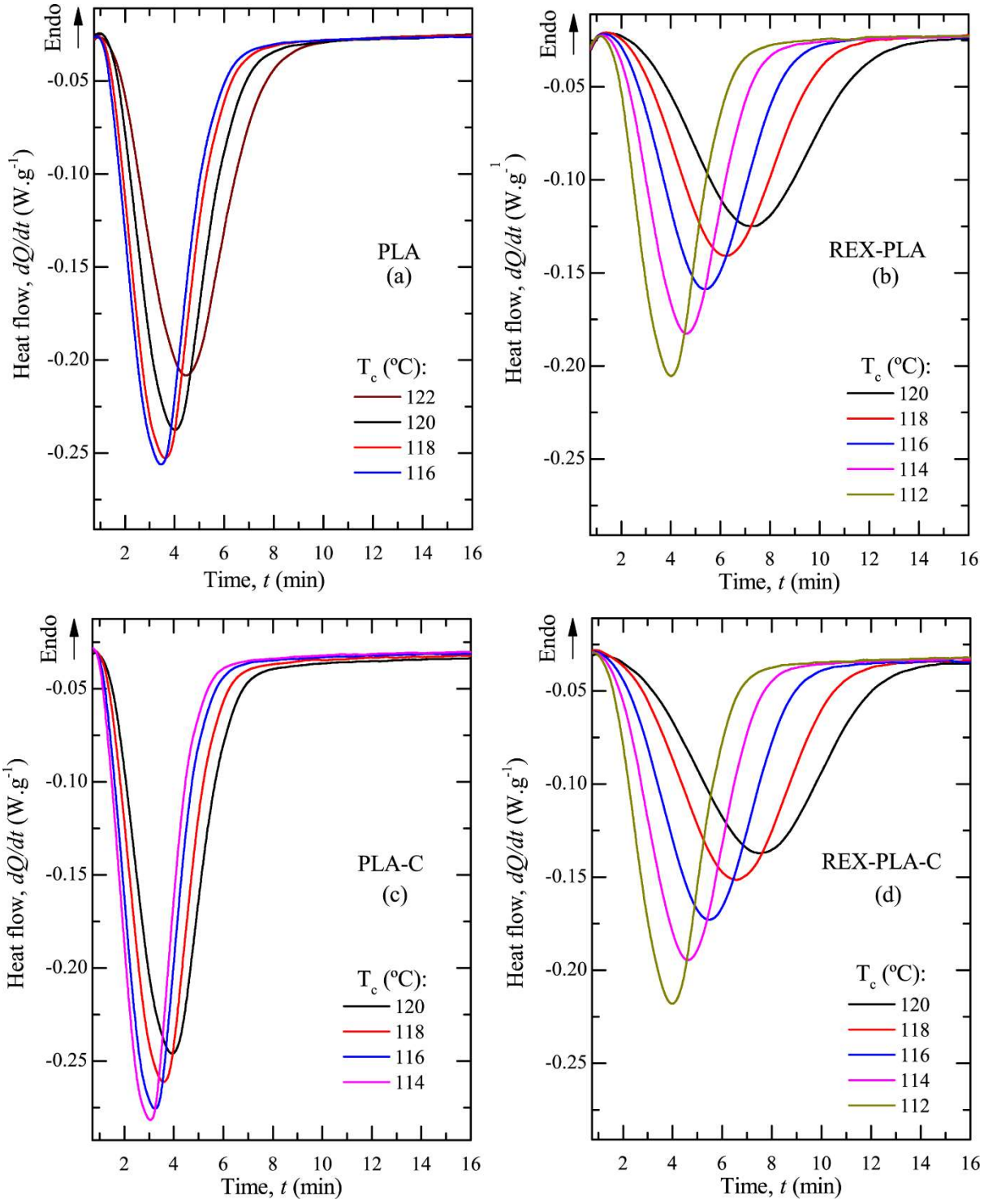

Figure 6.20. *Heat flow as a function of time during isothermal crystallization of (a) PLA, (b) REX-PLA, (c) PLA-C and (d) REX-PLA-C at the indicated crystallization temperatures (T_c).*

Alternatively, the determination of crystallization half-time ($t_{0.5}$) value can be utilized to investigate the effect of o-MMT on the overall crystallization rate. $t_{0.5}$ is the time duration needed to obtain 50% of the final crystallinity from the crystallization onset (t_0) in an isothermal test. It can be derived directly from the relative crystallinity as a function of time plot. Determination of overall crystallization rate, G, which is defined as the inverse of $t_{0.5}$, can be utilized as an indication of the crystallization rate at the respective temperature. For the sake of comparison, relative crystallinity (X_t) versus time at T_c of 120 °C for all the formulation are compared in *figure 6.21.* To demonstrate clearer comparison between $t_{0.5}$, induction time (t_i) of all the investigated samples, defined as time before the start of crystallization which is indicative of the efficiency of the nucleating effect of nano-SiO_2 were omitted from the graph. Instead t_i, $t_{0.5}$ and G values calculated from the analysis were compiled in *table 6.8*. T_c at 120 °C was chosen because it is the only common temperature in which the primary crystallization process occurs in PLA and REX-PLA/o-MMT composites.

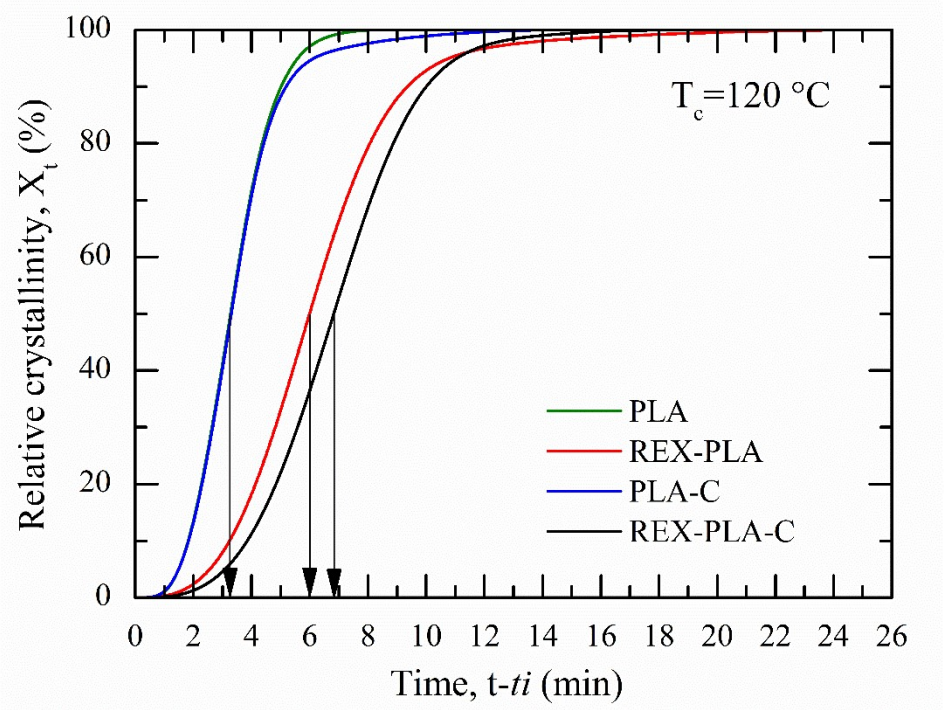

Figure 6.21. *Comparison of the relative degree of crystallization as function of time between all the formulations for isothermal experiments performed at T_c = 120 °C. Arrows indicate $t_{0.5}$ of the respective samples.*

Table 6.8. Comparative t_i, $t_{0.5}$ and G values under Isothermal Crystallization at T_c = 120 °C.

Sample Nomenclature	Induction time, t_i (min)	$t_{0.5}$ (min)	G (min^{-1})
PLA	0.9	3.3	0.30
REX-PLA	1.0	5.8	0.17
PLA-C	0.9	3.3	0.30
REX-PLA-C	0.9	6.8	0.15

From *table 6.8,* it can be seen that PLA-C generate similar t_i and $t_{0.5}$ values as PLA. This trend suggest that the addition of o-MMT does not seem modify the crystallization behaviour of PLA. This trend however is in contrast with results suggested by several studies (Day et al., 2006; Vasanthan et al., 2011). PLA crystallization is governed by several parameters. However, in the present case, the particle dimensions could be the reason for the observed trend. It is hypothesize that the presence of o-MMT agglomeration could have negated the nucleation ability of o-MMT. Agglomeration of o-MMT could ultimately encumbers macromolecular chain short-range transport movement for formation of spherical crystal hence no improvement in t_i, $t_{0.5}$ and G values. Comparing to REX-PLA, $t_{0.5}$ values increase (by about 76%) while G decrease with the addition of SAmfE while t_i remain insensitive to the presence of SAmfE. This indicate that REX-PLA possess very slow crystallization kinetics which could be influenced by existence of microstructural defects (e.g. branching) that could hinder the mobility of chains towards crystallization sites This trend agrees with the observation made in non-isothermal crystallization analysis (*c.f. chapter 6, section 6.2.5*).

Meanwhile, presence of o-MMT in the modified PLA matrix increase the $t_{0.5}$ values even further (by about 106%) while G simultaneously decrease. However, while t_i remain unchanged. It is known that crystallization rate of a polymer is determined by the nucleation rate and mobility of polymer chains. SAmfE is a multifunctional reactive agent, it is hypothesized that several PLA chains and clay particles could have been grafted to one SAmfE molecule. The mobility of polymer chains could have been suppressed due to induced topological modifications of REX-PLA and possible clay-polymer tethering hence reduced crystallizability of REX-PLA-C.

From *figure 6.20*, the relative crystallinity (X_t) is the ratio of the exothermic peak area at time, *t* to the total heat generated up to the end of the crystallization process. It was calculated using the following equation:

$$X_t = \frac{\int_0^t \left(\frac{dQ}{dt}\right) dt}{\int_0^\infty \left(\frac{dQ}{dt}\right) dt} \tag{6.7}$$

Where *dQ* is the measured heat flow released during an infinitesimal time interval, *dt*; the limits *t* and ∞ are to denote the elapsed time during the course of crystallization and at the end of the crystallization process respectively. *Figure 6.22* shows the calculated relative degree of crystallization as function of time of all the formulations at the indicated T_c.

The Avrami model (1939) has been the most commonly used for obtaining crystallization kinetics information even though newer isothermal macrokinetic models such as Evans (1945), Tobin (1974) and Malkin models (1984) has been proposed. Its widespread use is in part due to the relative ease with which the analysis can be applied. Avrami model was deemed to be most suitable to quantitatively describe the evolution of the crystallinity versus crystallization time, *t* for the early stages of crystallization during isothermal crystallization. The classical Avrami equation in its simplest form is:

$$1 - X_t(t) = \exp(-k(t)^n) \tag{6.8}$$

Where X_t is the relative crystallinity as a function of time, *t*, *k* is the Avrami crystallization rate constant and *n* is the Avrami exponent of time. *k* is a constant that is reliant on the shape of the growing crystalline entities and the amount and type of nucleation while exponent *n* is a constant that is dependent upon the nucleation type and growth geometry.

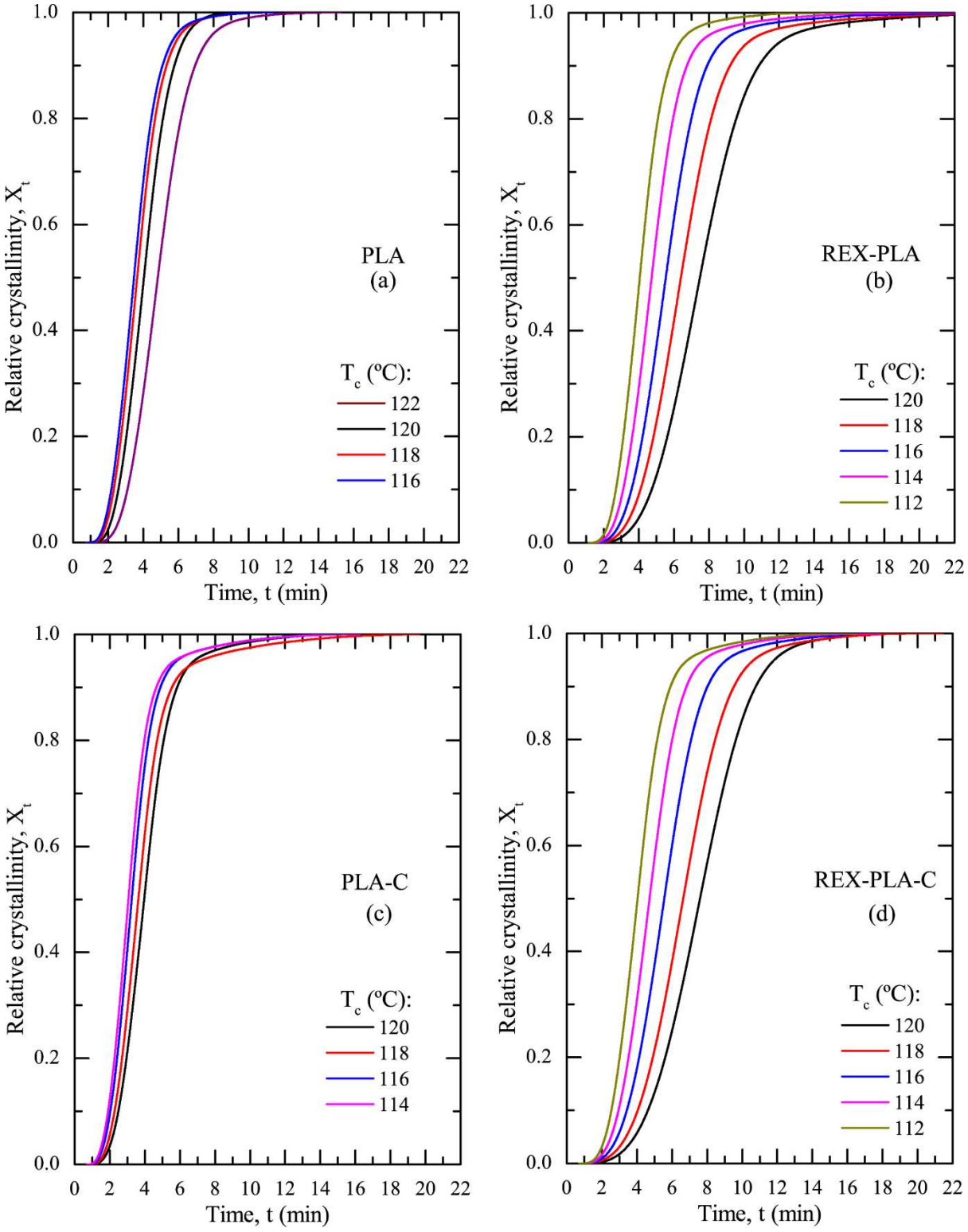

Figure 6.22. *Relative degree of crystallization as function of time for isothermal crystallization of (a) PLA, (b) REX-PLA, (c) PLA-C and (d) REX-PLA-C at the indicated crystallization temperatures (T_c).*

A minor modification to include experimental induction time, t_0 is introduced into the Avrami classical equation. The extended Avrami equation according to Lorenzo et al. (2007) is:

$$1 - X_t(t - t_0) = \exp(-k(t - t_0)^n) \quad (6.9)$$

In order to calculate the Avrami parameters (n, k), it is necessary to linearize the above equation into:

$$\log[-\ln[1 - X_t(t - t_0)]] = n\, log(t - t_0) + log\, k \quad (6.10)$$

The values of n can be obtained from the slope of the straight line and the values of k can be obtained from the intersection with the y-axis.

Plots of log [-ln(1-X_t)] versus log t according to *equation (6.10)* are shown in *figure 6.23* and Avrami parameters are listed in *table 6.9*. However, the linear form of the Avrami equation is inaccurate at both high and low extents of crystallization. Usually, non-linearity in the Avrami plot at low extent of crystallization can be attributed to the experimental errors during the first stages of the crystallization process cause by the slow stabilization of the equipment and the small quantity of heat evolved (Müller et al., 2016). For kinetics analysis, the rate of crystallization in this region may be neglected since the parameter is very low. However at high extents of crystallization, the non-linearity in the Avrami plot could be due to the secondary crystallization processes taking place (Lehmann and Karger-Kocsis, 2009).

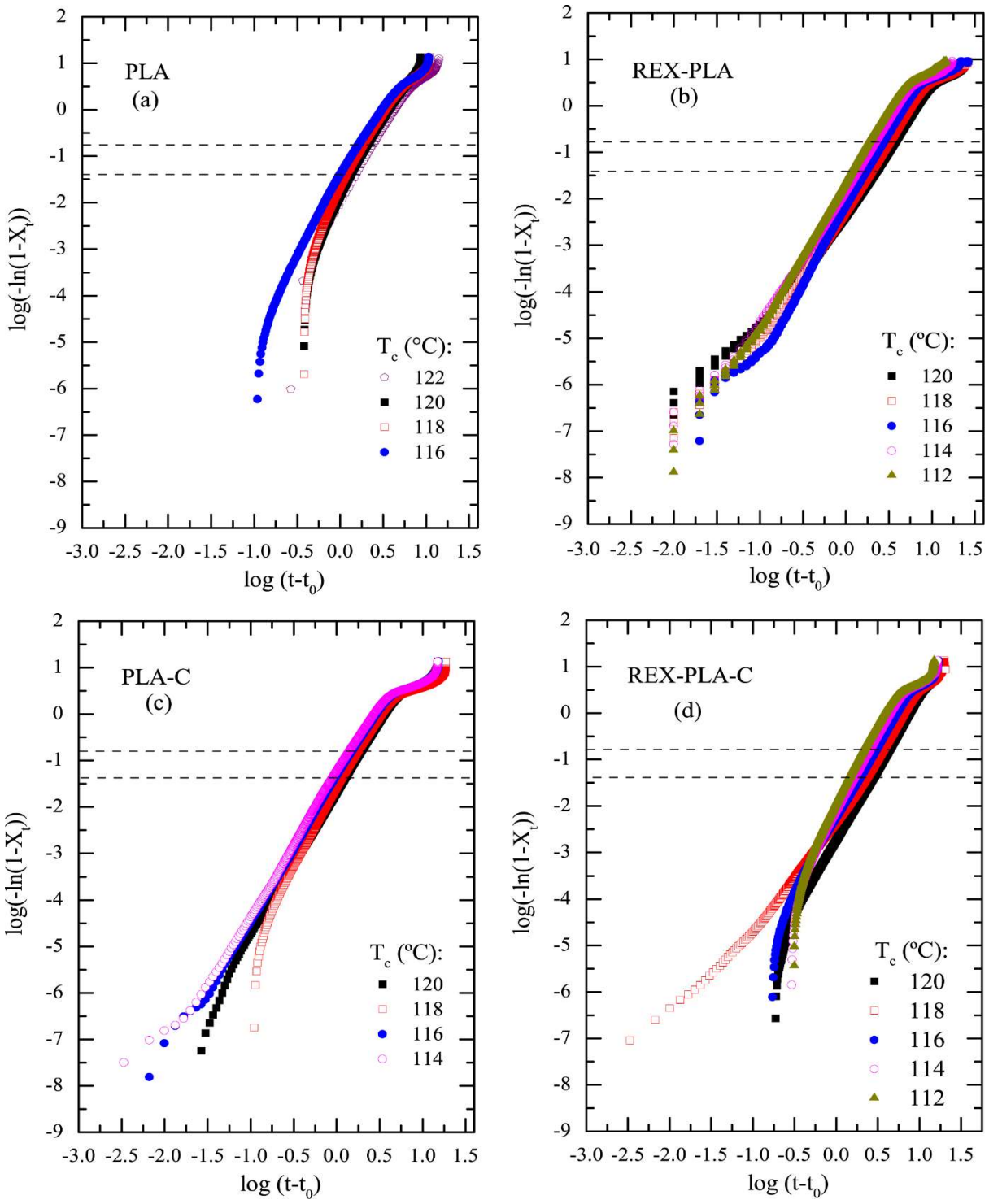

Figure 6.23. *Avrami plots of log(-ln(1-X_t)) vs. log (t-t_o) of (a) PLA, (b) REX-PLA, (c) PLA-C and (d) REX-PLA-C crystallized at different crystallization temperature. Experimental data between the dashed lines indicate the linear region that covers the relative conversion range between 8 and 70% that were analyzed in the Avrami plot.*

Table 6.9. *Kinetic parameters of isothermal crystallization from the Avrami equation (T_c: the crystallization temperature, k: the crystallization rate constant, n: the Avrami exponent).*

Material	T_c (°C)	n^a	$k^a.10^{-3}$ (min^{-n})
PLA	122	3.03	1.92
	120	2.84	1.60
	118	3.00	1.55
	116	2.81	1.36
REX-PLA	120	2.97	3.41
	118	3.05	4.79
	116	3.10	7.24
	114	3.04	14.51
	112	3.04	25.01
PLA-C	120	2.98	1.64
	118	3.00	1.53
	116	2.86	1.31
	114	2.80	1.21
REX-PLA-C	120	3.22	2.84
	118	3.12	2.55
	116	3.16	2.32
	114	3.24	2.12
	112	3.29	1.90

[a] *n* and *k* value were calculated from *figure 6.23.*

According to Rybnik (1963), the elucidation of secondary crystallization mechanism may be divided into two groups. The proponents of the first group define secondary crystallization as a reorganization of the remaining amorphous phase, where the variation of crystallinity or of other quantities proportional to the crystallinity is linearly related to the logarithm of time (Collins, 1958; Majer, 1960). On the other hand, the proponents of the second group postulated that the process of secondary crystallization is analogous to the relaxation process, where the logarithm of crystallinity change is linearly proportional to the time (Buckser and Tung, 1959; Zachmann and Stuart, 1960). However for the sake of repeatability

and consistency, only primary crystallization processes were analyzed using Avrami plot that covers a relative conversion range between 8 and 70% (*i.e.* linear region).

The results as tabulated in *table 6.9* indicate that independent of the o-MMT presence in PLA and modified PLA matrix, generally all the samples show an Avrami exponent of $n \approx 3$ which does not appear to have any systematic trend across the crystallization temperatures investigated. These results are in agreement with previous works published on PLA (Iannace and Nicolais, 1997; Kolstad, 1996) and on PLA/o-MMT nanocomposites (Chu and Wu, 2007; Papageorgiou et al., 2010). Avrami theory have indicated that $n \approx 3$ suggest either athermal nucleation with three dimensional spherical crystal growth or thermal nucleation with two-dimensional disc crystal (Hiemenz and Lodge, 2007). Previous studies have also suggested that PLA and PLA/o-MMT nanocomposites crystallization correspond to prevalent spherical crystal growth morphology with an athermal nucleation (Di Lorenzo, 2005; Huang et al., 2010; Papageorgiou et al., 2010; Tsuji and Ikada, 1996).

From *table 6.9*, *n* values for PLA-C samples are slightly lower than those calculated for PLA and REX-PLA. Principally, the slight decrease of *n* value is explained by presence o-MMT particles that could cause spherulite growth impingement, so that the growth form in spherulite mode become restricted leading to lower values of *n*.

Avrami rate of crystallization constant, *k* is a kinetic constant which is dependent on *n* constant that provides insight on both nucleation and crystallization growth rate (min^{-1}). The computed *k* value of all the investigated samples are plotted in *figure 6.24*. With the exception of REX-PLA, the trend that can be observed for *k* value is that it decreases with reducing T_c.

From *table 6.9*, it can be observed that REX-PLA$_2$ displayed the highest *k* value when compared to the other investigated samples. The *k* values of REX-PLA which are in the range of 3.41 to 25.01 when compared to PLA *k* values which is between 1.92 to 1.36. It is hypothesized that the highly entangled network in REX-PLA due to introduction of sparsely branched structure due to SAmfE could possibly have encumbers the reptation-like mobility of chains to crystallize. Thus, at higher T_c, REX-PLA may have gained higher chain mobility to overcome the entangled network of REX-PLA to crystallize hence the higher *k* values.

On the other hand, *k* values of PLA-C were almost similar to REX-PLA-C which is between 1.21 to 1.64 compared to 2.84 to 1.90, respectively. This could mean that the o-MMT addition in either PLA or modified PLA matrix does not modify the crystallization rate of PLA-C and REX-PLA-C composites, respectively.

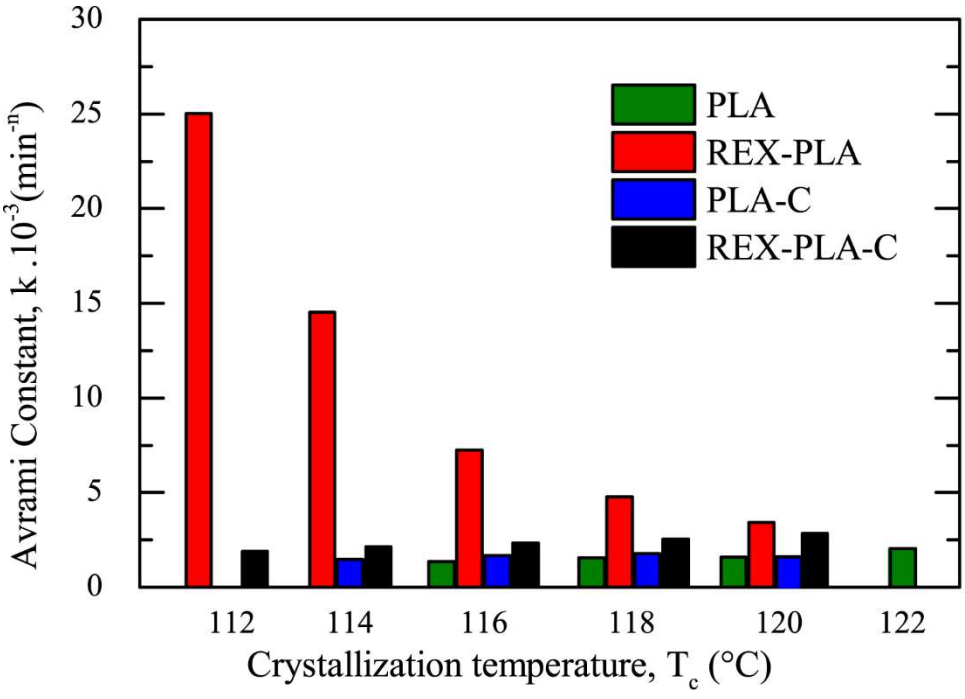

Figure 6.24. *Comparison of Avrami constant, k of PLA, REX-PLA and their respective composites.*

Apparent activation energy (E_c) gives insight about the rate of crystallization in which E_c is inversely proportional to the rate of crystallization (Hemlata and Maiti, 2012). The *n* value in *table 6.9* was used to determine an apparent activation energy for crystallization during isothermal conditions, at intermediate degree of conversion. It is assumed that the crystallization rate constant (K) from *equation 6.10* is temperature dependent and can be approximately written as:

$$K^{1/n} = K_0 \exp(-\frac{E_C}{RT_c}) \tag{6.11}$$

Taking natural logarithm of Arrhenius equation yields:

$$\frac{1}{n} lnK = lnK_0 - E_c/RT_c \tag{6.12}$$

Where E_c is the apparent activation energy (kJ.mol^{-1}), R is universal gas constant (L.bar.K^{-1}.mol^{-1}) and T_c is the corresponding crystallization temperature (K). The apparent activation energy for crystallization can be determined by plotting ln(K/n) versus $1/T_c$. The slope of the straight line is used to determines E_c. Plot ln[(K/n)] versus $1/T_c$ are shown in *figure 6.25* and the computed E_c and R^2 values are summarized in *table 6.10*.

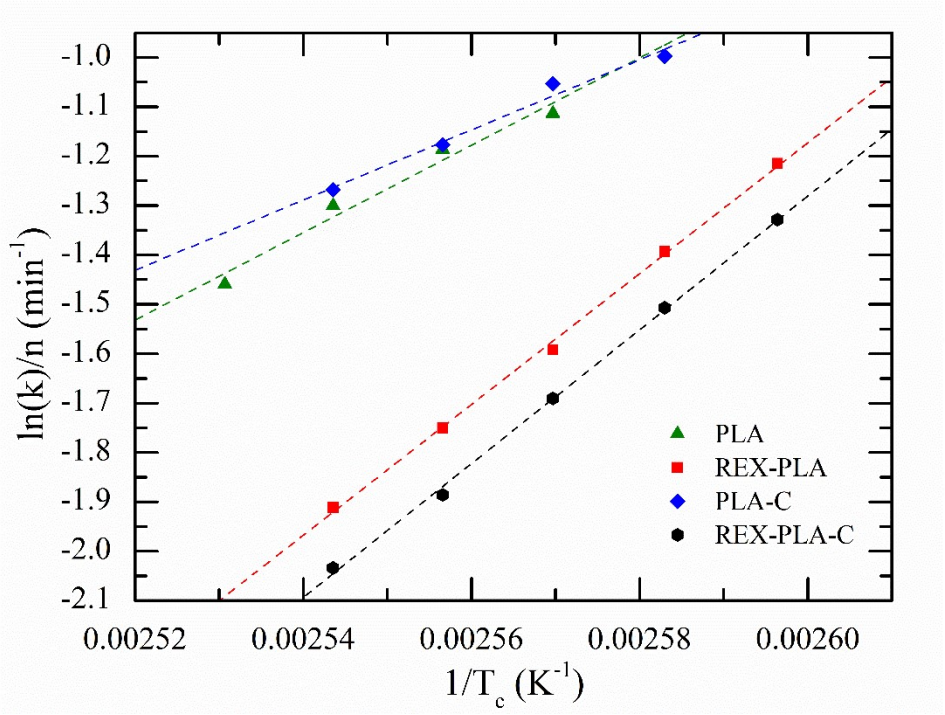

Figure 6.25. *Plots of ln(K)/n versus 1/T_c of all the investigated samples determined from isothermal crystallization experiments.*

Table 6.10. *Apparent activation energy and R^2 value of PLA, REX-PLA and PLA coomposites with o-MMT.*

Material	E_c (kJ.mol^{-1})	R^2
PLA	88 ±10	0.957
REX-PLA	132 ±3	0.998
PLA-C	71 ±7	0.972
REX-PLA-C	135 ±3	0.998

From *table 6.10,* it can be seen that E_c for PLA is 88 kJ.mol^{-1}. This E_c value is very similar to the E_c value of neat PLA reported by Wu et al. (2008) (≈83 kJ.mol^{-1}). With regards to PLA-C, it can be seen that decrease E_c value approximately by 19% in comparison to PLA were observed. Similar trends were reported by Wu et al. (2008) and Lee et al. (2008) for their PLA/o-MMT composites. Both of these studies attributed the E_c decrease to the nature of o-MMT that acts as heterogeneous nucleating agent thus facilitated the crystallization of PLA.

Meanwhile, o-MMT presence in PLA and modified PLA composites increases the E_c value of REX-PLA and REX-PLA-C approximately 50% and 53%, respectively. Generally the lower the E_c value is, the easier the polymer melt crystallize (Run et al., 2007). However in the case of REX-PLA, microstructural defects present (*e.g.* sparsely branched PLA) in the REX-PLA could possibly encumbers the short-range transport movement for formation of crystals hence higher E_c. Comparably in the case of REX-PLA-C, combination of induced topological modifications in the modified PLA matrix and possible clay-polymer tethering could have impeded the nucleation and growth of crystals. This could possibly diminish macromolecules segmental mobility by a significant margin hence an increase in E_c value.

6.2.7. Effect of clay presence on dynamic mechanical properties of PLA and modified PLA composites

DMTA analysis was performed using a single cantilever bending mode to evaluate the effects of o-MMT on the dynamic mechanical properties of "as-received" PLA and modified PLA composites sheets. The "as-received" analyzed samples have been subjected to 1 week of physical aging at room temperature to mimic the common industrial conditioning of these prepared sheets. The thermomechanical spectrum of PLA and modified PLA composites with o-MMT sheets which were recorded from 30 to 105 ºC are depicted in *figure 6.26,* in the form of storage modulus, E' and the loss tangent, tan $\delta = E''/E'$ respectively. Meanwhile, loss modulus (E'') traces are shown in the appendix.

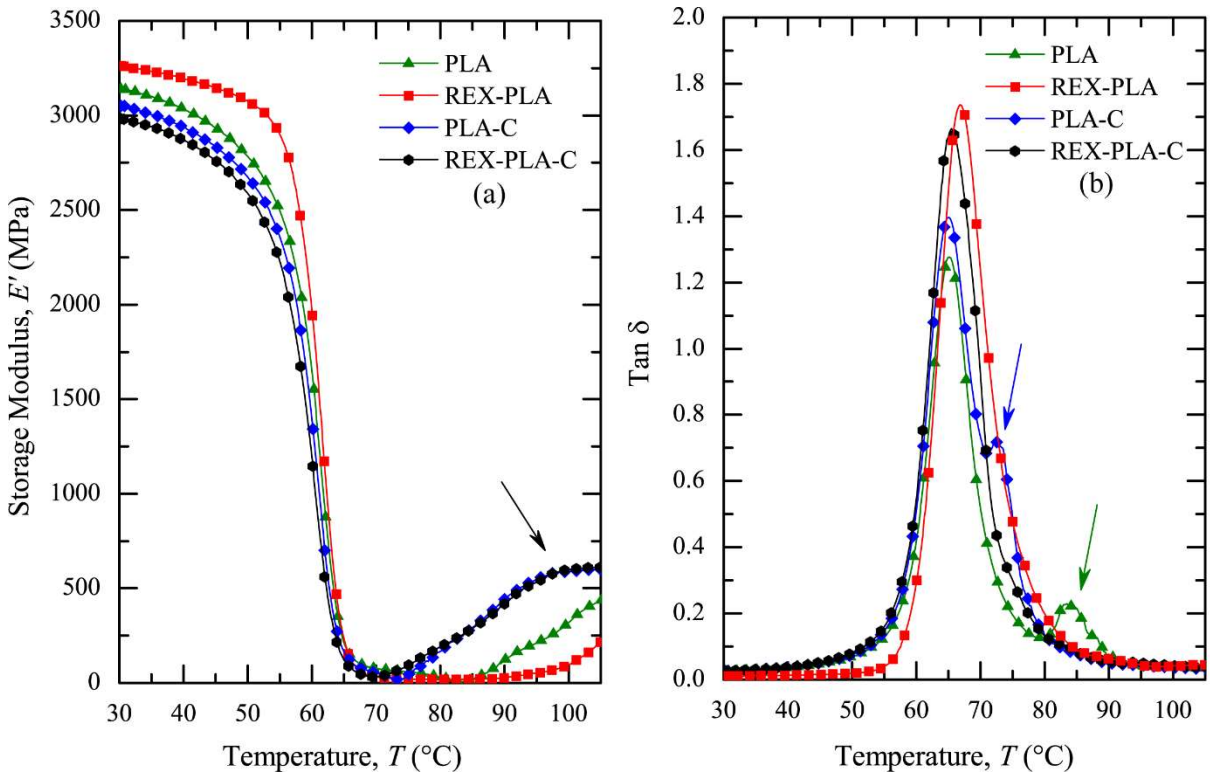

Figure 6.26. *(a) Storage modulus and (b) tan δ traces of all the investigated samples tested at 2 °C.min^{-1}. Black arrow indicate E' value increase while green and blue arrows indicates additional peak in tan δ curves of PLA and PLA-C, respectively.*

The following results will be derived from *figure 6.26* and tabulated in *Table 6.11*:

- The storage modulus at 30 ºC, $E'_{(30ºC)}$, at 60 ºC, $E'_{(60ºC)}$ and at 105 ºC, $E'_{(105ºC)}$, respectively
- The glass transition temperature, T_g. It was determined as the point where tan δ (referred to as T_g (tan δ)) and E'' (referred to as T_g (E'')) reached a maximum, respectively.
- The drop percentage in E' between 30 and 60 ºC. It was calculated as per *equation 6.13*. This parameter was studied in order to observe thermomechanical behaviours of the

investigated materials as the testing temperature approach their respective glass transition temperature.

- Temperature at *E'* at 1.5 GPa that coincides with heat distortion temperature (HDT) of PLA.

$$Drop\ (\%) = \frac{E'_{30°C} - E'_{60°C}E'_{60°C}}{E'_{30°C}} * 100 \quad (6.13)$$

Table 6.11. *DMTA parameters for PLA, REX-PLA, PLA composites with o-MMT tested at 2°C.min^{-1}.*

Sample Nomenclature	$E'_{(30°C)}$ (GPa)	$E'_{(60°C)}$ (GPa)	Drop (%)	$E'_{(105°C)}$ (GPa)	Maximum value of T_g (E'') (°C)	Maximum value of T_g (tan δ) (°C)	Temperature at E' at 1.5 GPa (°C)
PLA	3.1 ±0.1	1.6 ±0.2	48.2 ±0.1	0.5 ±0.1	61.3 ±0.2	65 ±1	60.5 ±0.1
REX-PLA	3.3 ±0.1	1.8 ±0.2	45.5 ±0.2	0.3 ±0.1	61.9 ±0.1	66 ±1	61.2 ±0.1
PLA-C	3.0 ±0.2	1.3 ±0.1	56.0 ±0.1	0.6 ±0.2	60.7 ±0.1	65 ±1	59.7 ±0.3
REX-PLA-C	3.0 ±0.3	1.1 ±0.2	61.6 ±0.1	0.6 ±0.2	60.4 ±0.2	65 ±2	59.0 ±0.2

From *figure 6.26*, it can be seen that generally all the samples exhibit almost similar *E'* at 30 ºC within the statistical error for a given thermal history. However in the T_g region, all the samples experienced a drastic decrease in *E'* values which drop between 30 and 60 ºC. Comparing to the other samples, REX-PLA samples experience the least reduction. It seems that the increase in MW and formation of sparsely branched structures in the modified PLA might have improved the calculated $E'_{(60°C)}$ values.

Meanwhile, PLA-C and REX-PLA-C exhibited sharpest decrease in *E'* with increasing the temperature comparing to the other samples. The calculated $E'_{(60°C)}$ values of PLA-C and REX-PLA-C was reduced by 19% and 31% respectively in comparison to PLA. However, it

must be considered beforehand that the comparison is made with the understanding that all of the investigated samples are in an equilibrated aged state that were reached in 1 week storage at room temperature according to previous work published by our group (Maspoch et al., 2015). This trend could be explained with domain relaxation model proposed by Lu and Nutt (2003) in their study of epoxy/o-MMT nanocomposites.

It is known that the enthalpy relaxation during the physical aging process is related to the degree of chain segmental relaxation, it is hypothesized that the slower relaxation rate of chain segments could be cause by restrictions provided by embedded o-MMT particles. In the case of PLA-C, this outcome could be due to the decrease in the rate of physical aging. That is, presence of o-MMT decrease the rate of segmental relaxation over time that leads to a high remaining molecular mobility after being aged for 1 week hence lower $E'_{(60ºC)}$ values. For REX-PLA-C, topological modifications in the modified PLA matrix and possible clay-polymer tethering induced by o-MMT addition could have decrease rate of physical aging even higher, thus leading to an even larger remaining molecular mobility after 1week aging resulting into a steeper decrease of $E'_{(60ºC)}$.

Meanwhile at 105 ºC, presence of o-MMT both in PLA-C and REX-PLA-C saw an increase in $E'_{(105ºC)}$ values (indicated by a black arrow) compared to PLA and modified PLA samples. The $E'_{(105ºC)}$ values increase could be attributed to the decrease of the onset temperature of cold-crystallization process occurring during heating due to nucleating effect of o-MMT. The nucleating effect that o-MMT possess is well known, thus this trend reinforces this datum and is in agreement with the thermal behaviour analysis (*chapter 6, section 6.2.4*).

The $E'_{(105°C)}$ increase observed in PLA-C and REX-PLA-C samples is especially useful in increasing the range of geometrical stability of samples containing o-MMT. This would be very advantageous as it would lead to a more stable dimension control and integrity of product especially during thermoforming.

Even though $E'_{(105°C)}$ values of both PLA-C and REX-PLA-C were higher compared to PLA and REX-PLA samples, the $E'_{(105°C)}$ increase does not reach a critical value that can modify the softening temperature (heat distortion temperature, HDT) of all of the investigated samples. HDT can be defined as macroscopic measure of the "stiffness" of a material when the temperature increases. It is also a useful measure of the relative service temperature for a polymer when used in load-bearing parts. Typically, *E'* values at approximately 1.5 GPa has a particular physical significance since it usually coincides with the HDT of PLA. From *table 6.11*, it can be seen that temperature at *E'* at 1.5 GPa of all the samples were similar. Even though convincing evidences of o-MMT delamination and intercalation and clay-polymer tethering in REX-PLA-C have been presented and discussed in *section 6.2.3* and *section 6.1.3* respectively, these modifications were still insufficient to significantly modifies the thermomechanical properties of the resultant modified PLA composites with o-MMT specifically HDT parameter.

Referring to *figure 6.26(b),* an additional peak in the tan δ curves (indicated by a green arrow) with further increase in temperature in PLA was also observed. This trend might be explained by SAmfE absence. The absence of SAmfE produces lower concentration of "defects" or "disruption" in the crystal arrangement hence facilitates the increase in the molecular mobility of PLA for crystallization. Another additional peak in PLA-C in the tan δ

curves was also noted (indicated by a blue arrow). This peak could be attributed cold crystallization process in PLA-C as the onset temperature of cold crystallization were lowered with presence of o-MMT. This also agrees with the previously discussed DSC data (*c.f. table 6.5*).

According to *table 6.11,* the temperatures that correspond to tan δ and/or *E"* peaks (referred to as T_g), remained fairly insusceptible to modifications brought about by o-MMT filler. The T_g values were also similar to previously reported DSC data (*c.f. table 6.5*). However, an increased height of the tan δ peak in modified PLA and modified PLA composites with o-MMT was observed. This suggest that REX-PLA and REX-PLA-C samples exhibit improved damping properties which could be attributed to the increase in MW (*c.f. table 6.2*) The formation of non-uniform branched structures for REX-PLA and clay-polymer tethering for REX-PLA-C might have decrease the rate of segmental relaxation over time, thus leading to a remaining larger molecular mobility after being aged for 1 week thus improved damping properties.

6.2.8. Effect of clay addition on mechanical properties of PLA and modified PLA composites

A typical engineering stress-strain curves are plotted in *figure 6.27*. All the tensile specimens showcase a typical yield point in the engineering stress (σ_y). It is observed that PLA exhibit brittle fracture (fragile) without any perceptible deformation while the rest of the samples exhibit ductile behaviours sans any appreciable cold drawing. This behaviour could be due to the formation of crazes that prevents the propagation of a stable neck. *Table 6.12* summarizes the mechanical parameters of all the investigated samples.

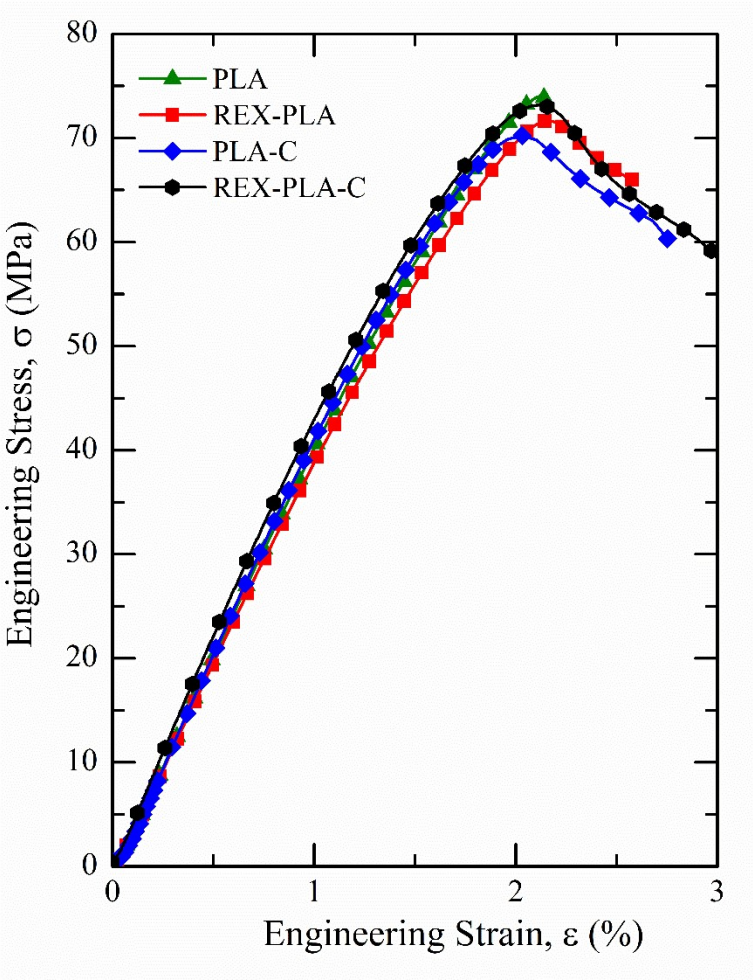

Figure 6.27. *Typical tensile engineering stress–strain curves at 10 mm.min^{-1}.*

Table 6.12. *Influence of clays on the uniaxial tensile parameters at 10 mm.min^{-1}.*

Sample nomenclature	E (GPa)	σ_y (MPa)	ε_y (%)	ε_b (%)
PLA	3.5 ±0.1	74 ±2	2.2 ±0.1	2.2 ±0.1
REX-PLA	3.3 ±0.1	73 ±1	2.18 ±0.03	2.5 ±0.1
PLA-C	3.7 ±0.1	73 ±3	2.17 ±0.01	2.82 ±0.01
REX-PLA-C	3.9 ±0.1	72 ±2	2.3 ±0.1	3.00 ±0.05

Visual inspection on *figure 6.28* reveals PLA and REX-PLA tensile specimens yielded a relatively flat fractured plane. Examining the respective micrographs revealed that crazes formed in both PLA and REX-PLA is very nearly perpendicular to the direction of the applied

tensile stress. It is also imperative to note that REX-PLA samples displayed comparatively higher amount of short crazes around the fractured region than PLA samples. Similar observation were also reported by Cailloux et al. (2014). When this happens, plastic deformation becomes localized to the surrounding craze region. This large amounts of highly localized plastic deformation surrounding the crazes could then have enhanced ε_b slightly, as reported in *table 6.12.* However, E, σ_y and ε_y values within the experimental error remain insensitive to the modification of the molecular architecture brought about by SAmfE.

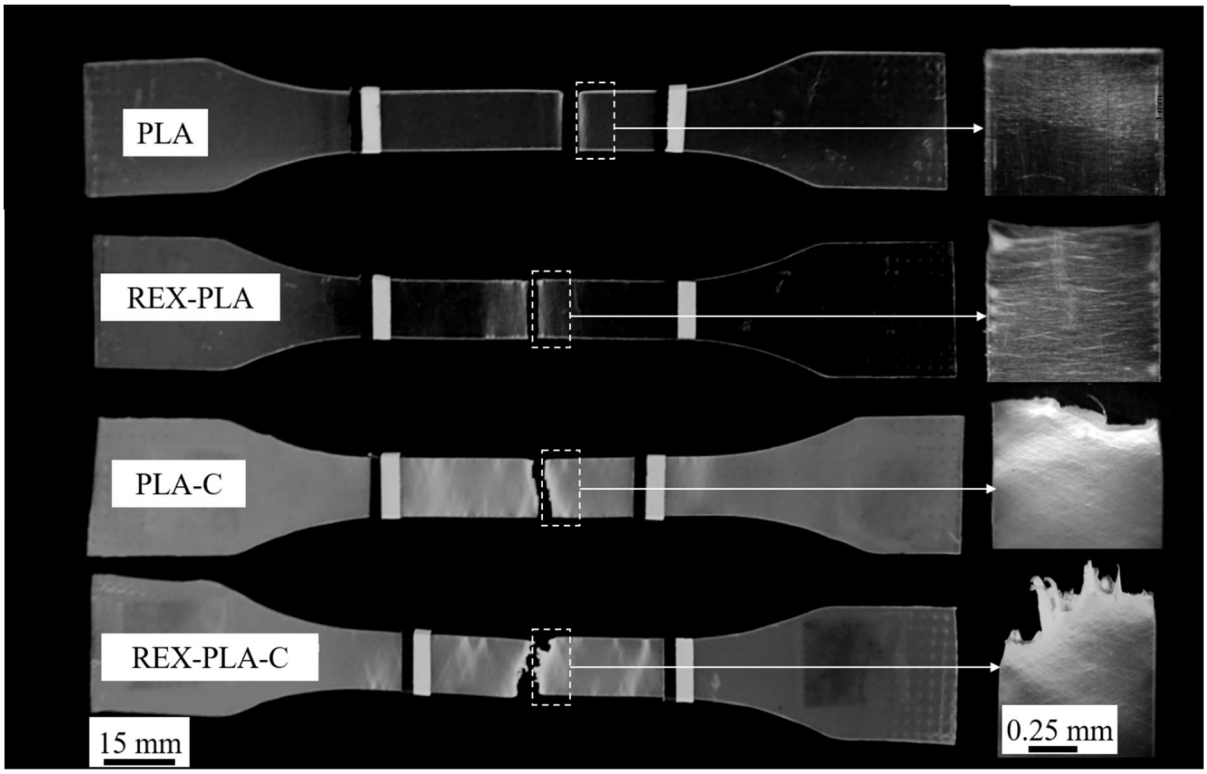

Figure 6.28. *Macrophotographs of PLA and modified PLA composites with o-MMT specimens after testing at 10 mm.min^{-1}. Micrographs were taken in the vicinity of the fractured part of each sample.*

In contrast, o-MMT presence modifies the deformation mechanisms observed in PLA-C and REX-PLA-C. From *figure 6.28*, it was observed that PLA-C and REX-PLA-C exhibit a mixed deformation mechanism between crazing and localized shear banding throughout the specimens gauge length. Additionally, REX-PLA-C samples exhibited plastic tearing in the fracture surface.

From *table 6.12*, it can be seen that the tensile modulus showed 6% and 11% increase for PLA-C and REX-PLA-C samples, respectively. The improved modulus in PLA/o-MMT nanocomposites as similarly reported by numerous studies (Chow et al., 2014; Jiang et al., 2007; Lee et al., 2003; Najafi et al., 2012a; Wang et al., 2012; Zou et al., 2012), may have been predominantly attributed to high L/D ratio of o-MMT and its orientation along the tensile stress direction (Fornes and Paul, 2003). Nevertheless, neither σ_y nor ε_y values within the experimental error appeared to be significantly improved with o-MMT incorporation. Meanwhile, it was observed that ε_b value increased for both PLA-C and REX-PLA-C samples. To investigate this trend further, fractographic analysis of the fractured surface were performed in order to observe the interfacial interactions between PLA, PLA-C and REX-PLA-C, as shown in *figure 6.29*.

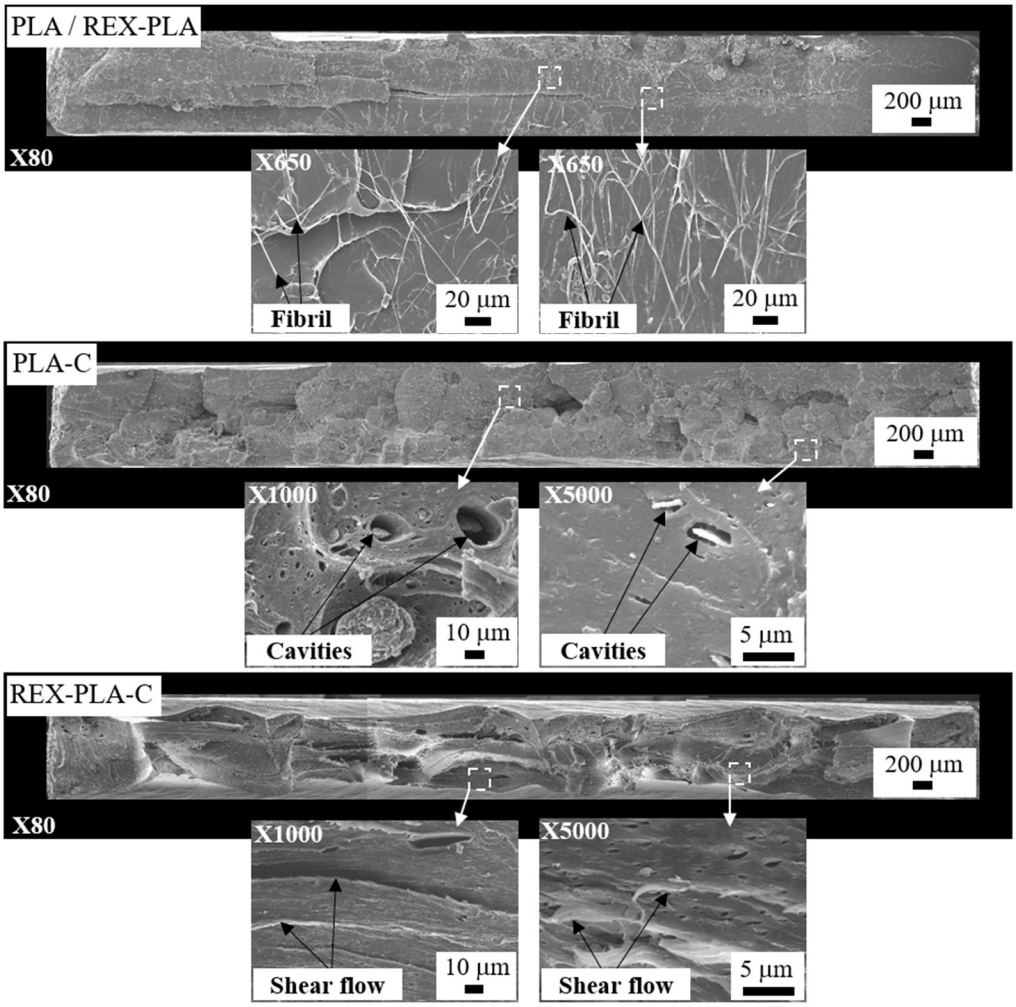

Figure 6.29. *SEM micrographs of PLA, PLA-C and REX-PLA-C fractured surfaces.*

Comparing between PLA and REX-PLA samples, both samples displayed almost indistinguishable fracture surface morphologies. Subsequently, only PLA micrographs are shown in *figure 6.29*. PLA exhibited a relatively smooth fracture surface with formations of thin fibril indicating a continuous plastic flow. This morphology typically leads to craze formations resulting in brittle failure. However, o-MMT presence in PLA-C leads to an increase in the roughness of the fractured surface. In addition, cavities were also observed at the interface between clays and polymer matrix. In general, there are two types of cavitation that can be observed in fillers reinforced polymer system. The first is internal cavitation which

is defined as cavities formed within the filler particle which occurs when the interfacial bonding is strong between the filler and matrix. Secondly, debonding cavitation which occurs when there is poor particle/matrix interfacial bonding. It could be speculated that a combination of cavities formed either in the filler particle (internal cavitation) and debonding at the PLA/o-MMT interface (debonding cavitation) could have occurred simultaneously. This could have relieved the local triaxial stress state and thereby promoted void formation. Subsequently, this could possibly increase ε_b under further uniaxial loading, as suggested by Kim and Michler (1998).

In contrast to earlier observations, o-MMT presence in modified PLA matrix will enhanced shearing deformation mechanism in REX-PLA-C samples. From TEM micrographs, it was shown that REX-PLA-C exhibited a finer clay dispersion than PLA-C (*c.f. figure 6.13*). Thus, it is assumed that the phase adhesion between o-MMT and polymer matrix has been enhanced due to possible reaction between remnants of epoxy groups in SAmfE with the o-MMT organomodifier and PLA degradation products in the modified PLA matrix (*c.f. figure 6.2*). Hence, these possible interactions could behaved as a "phase adhesive", possibly delaying the interfacial debonding mechanism up to a "critical" stretch point under uniaxial loading. When this threshold has been exceeded, the higher and finer dispersion of the clays in the polymeric matrix could have augmented creation of multiple cavitation. However, the triaxial stress concentration will be locally released corresponding to further enhanced shear flow of the modified PLA matrix under further uniaxial loading.

6.2.9. Effect of clay addition on fracture behaviour of PLA and modified PLA composites

The influence of o-MMT on de-aged fracture behaviours of PLA and modified PLA composites were investigated using the Post-Yielding Fracture Mechanics (PYFM). The decision that only de-aged samples would be analyzed were based on the recommendations by previous works published by our group (Cailloux et al., 2014; Gamez-Perez et al., 2011b; Maspoch et al., 2015). From the aforementioned studies, it was demonstrated that the EWF analysis can only be successfully applied in the non-aged material due to the transient ductile-brittle behaviour observed after all the investigated samples were subjected to 1 hour of de-aging treatment

Investigation of modifications of the micromechanism of deformation between all the investigated samples was performed using Scanning Electron Microscopy (SEM). The fracture behaviour of all the samples was evaluated using Deeply Double Edge-Notched Tension (DDENT) specimens. Under uniaxial loading, a large plastic deformation was observed at both crack tips; suggesting the applicability of the *post-yielding fracture mechanisms* through *the Essential Work of Fracture* (EWF) concept. These observations are consistent with those already published by Gámez-Pérez et al. (2011b), Maspoch et al.(2015) and Cailloux (2015).

The DDENT sample geometry was selected because it meets the two crucial requirement of the European Structural Integrity Society-Technical Committee 4 (ESIS-TC4). First, the ligament length must Secondly, a near constant mechanical constraint must be achieved so that the magnitude of plastic zone along the ligament commensurate with the ligament length (Anderson, 2005; Clutton, 2001; Duan et al., 2006).

The presentation of the EWF results is divided in two subsections:

- Validation of the EWF experiment.
- Influence of the o-MMT presence on fracture behaviour of PLA and modified PLA composites.

a) Validation of the Essential Work of Fracture methodology

Figure 6.30 presents the load-displacement curves for PLA, REX-PLA and PLA composites with o-MMT. It is observed that the load-displacement traces were self-similar in terms of the load increased with the ligament size but that the overall shape of the stress–strain curve remained the same. Therefore, these curves fulfil one of the main prerequisite of the validity of the EWF methodology, as already reported elsewhere (Duan et al., 2006; Karger-Kocsis and Czigány, 2000; Martinez et al., 2009). This self-similarity trend assures that the cracks propagate under similar stress state in the whole ligament lengths range, independent of ligament length (l).

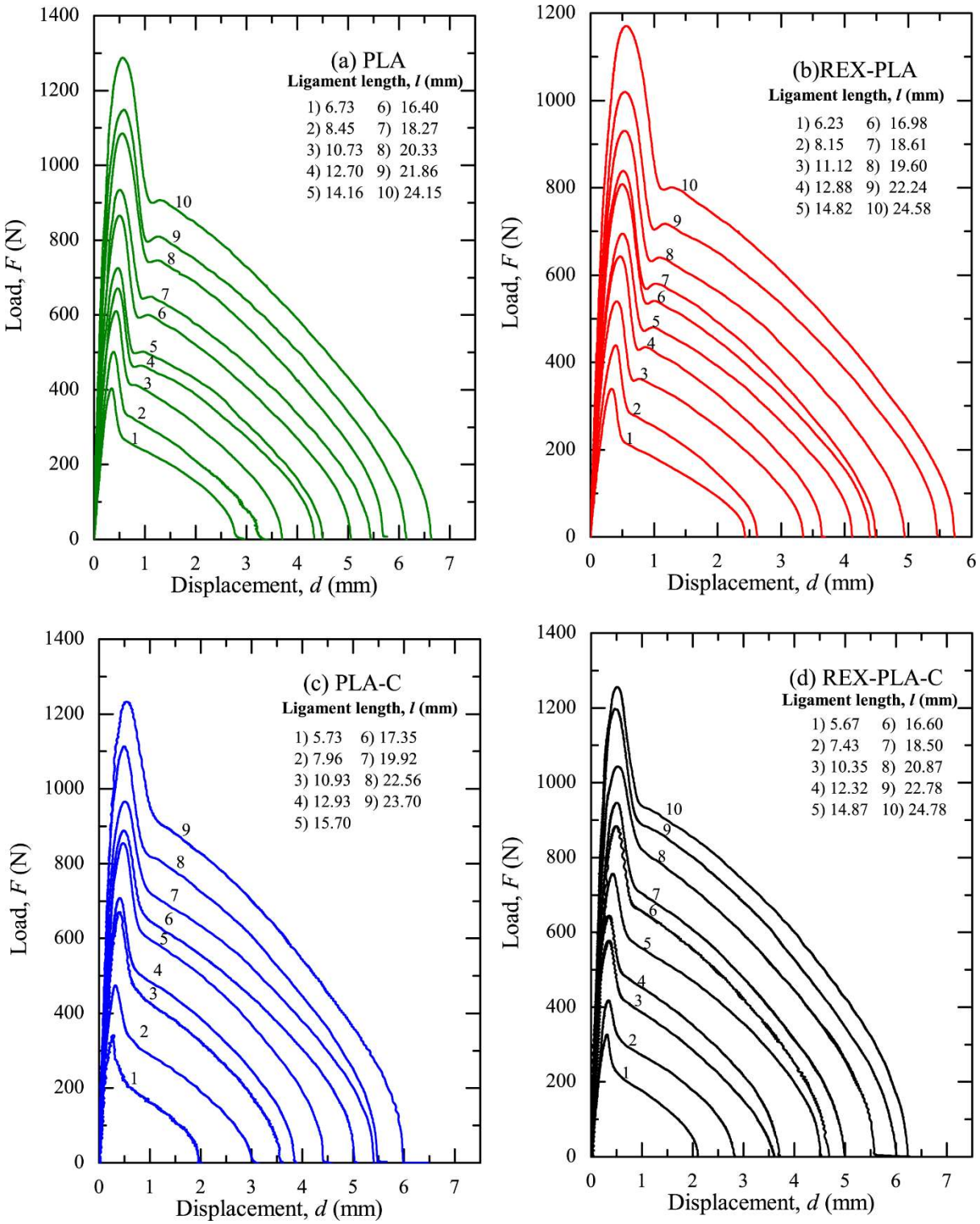

Figure 6.30. *Comparison of the load vs. displacement curves at different ligament length of de-aged (a) PLA, (b) REX-PLA, (c) PLA-C and (d) REX-PLA-C samples tested at 1 mm.min^{-1}.*

A further validity check is linked to the full ligament yielding prior to final fracture. *Figure 6.31* displays typical engineering stress (σ) vs. normalized displacement (d_N) curves obtained from the EWF tests for de-aged PLA, REX-PLA and PLA composites with o-MMT samples. Digital Image Correlation (DIC) analysis was used to determine the strain field encompassing the ligament length as similarly performed by Gamez-Perez et al. (2011b) and Cailloux et al (2014). It was observed that in all of the investigated samples, the yielding process was initiated prior to reaching the maximum load and possibly from both sides of co-linear notches in the DDENT specimen cut due to its considerably higher stress concentration points. For reference, the crack propagation onset was distinguished at the point indicated by the arrows as shown in *figure 6.31*. This shows that the specimen ligaments are fully yielded prior to maximum stress and possibly from both side of co-linear notches in the specimen cut due to its considerably higher stress concentration points. This results should meet the crucial requirement of the full length ligament yielding prior to final fracture (Duan et al., 2006; Karger-Kocsis and Czigány, 2000; Martinez et al., 2009).

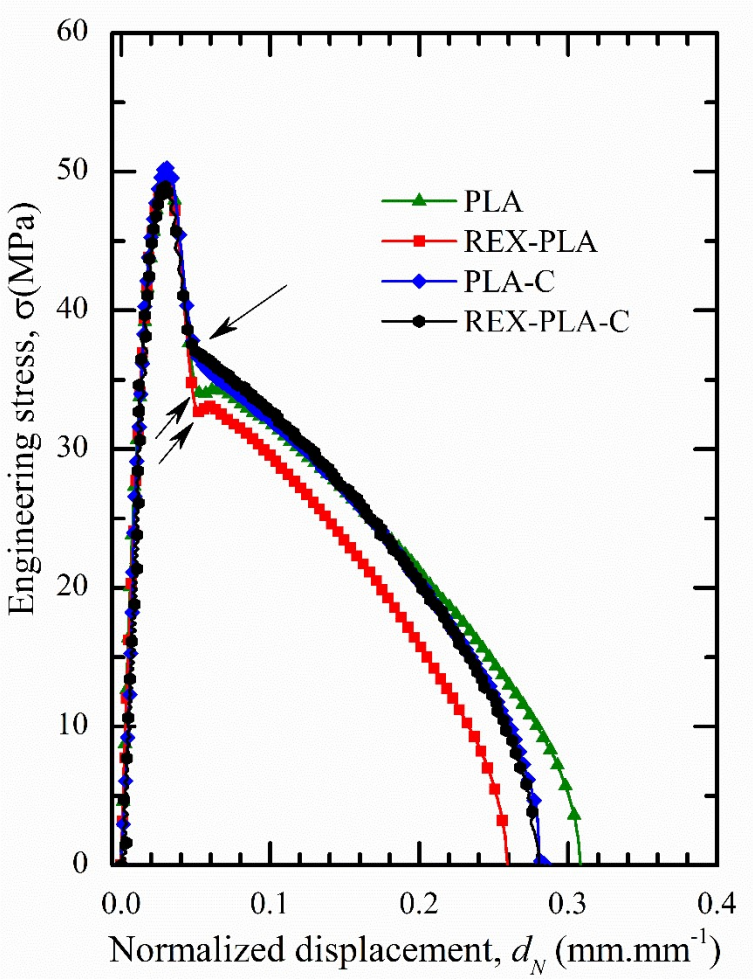

Figure 6.31. *Engineering stress versus normalized displacement (by l of 16 mm) curves for PLA and modified PLA composites with o-MMT samples tested at 1mm.min^{-1}.*

Referring to *figure 6.31*, it was observed that addition of o-MMT seems to suppress the necking process (strain softening) independent of the types matrix used (either PLA or REX-PLA matrix). This is evident from onset point prior to crack propagation becomes less sharp compared to PLA and REX-PLA samples (as indicated with an arrow). This could possibly be due to the manifestation of blunting effect of the notch due to the formation of o-MMT cavities in this zone which would be substantiated in the morphological analysis of fractured samples.

From the figure above, it was also observed that tear resistance of PLA is higher than REX-PLA. This is also in agreement with results discussed by Cailloux (2015) and Cailloux et al. (2014). In contrast to PLA-C and REX-PLA-C, it was observed that addition of o-MMT does not make any distinction between either type of matrix used. The discussion of these observations will be discussed in conjunction with the computed EWF parameters in the upcoming paragraphs.

In order to ensure that the EWF measurements were performed in a uniform stress state, the results were verified using the *equation* below (Clutton, 2001):

$$0.9\sigma_m \leq \sigma_{max} \leq 1.1\sigma_m \tag{6.14}$$

Figure 6.32 displayed the maximum stress (σ_{max}) vs ligament length (l) for PLA and modified PLA composites with o-MMT samples. Trend-wise, σ_{max} values decrease with increase l between the 1.1-0.9 σ_m limits hence this implies that all the EWF experiments were conducted under uniform stress state or pure plane stress.

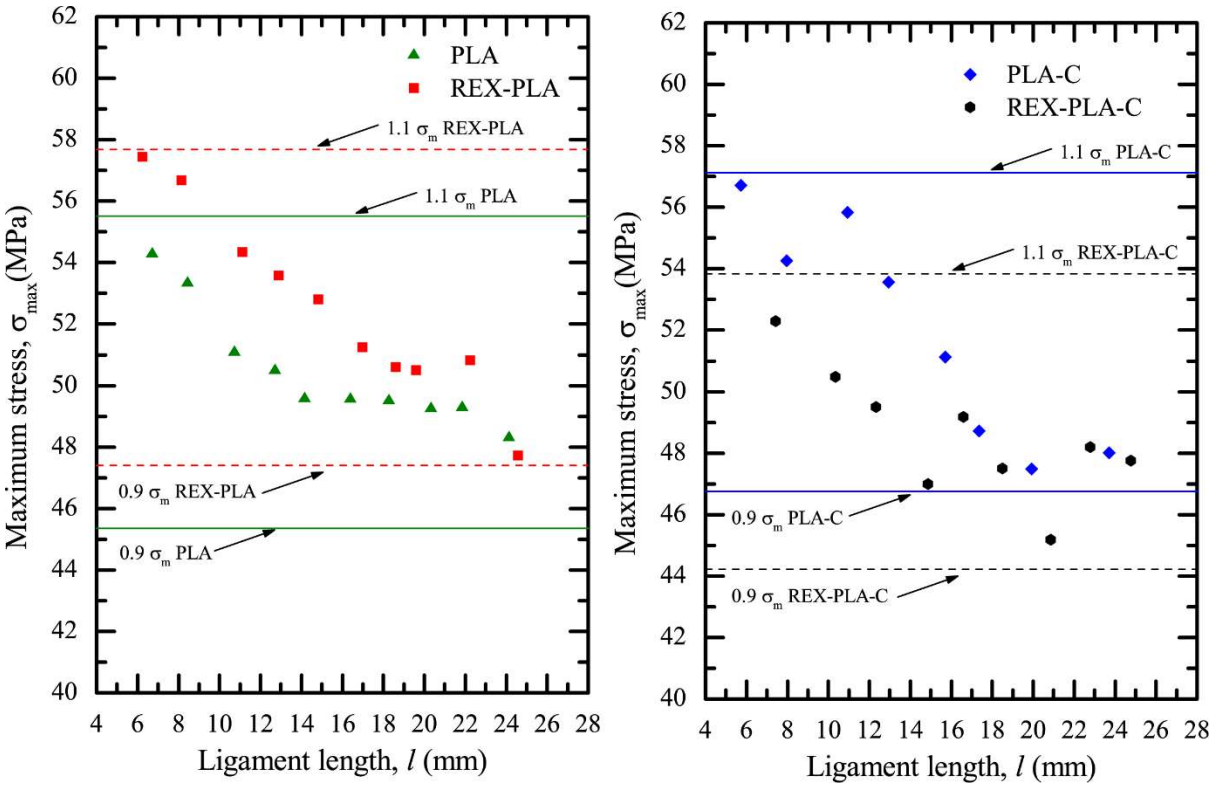

Figure 6.32. *The specific total work of fracture, w_f, as a function of the ligament length, l of de-aged PLA and modified PLA composites with o-MMT.*

Studies by Karger-Kocsis et al. (1998), Karger-Kocsis and Moskala (2000) and Maspoch et al. (1999) has suggested that verification of linear correlation between the specific total work of fracture, w_f and ligament length, l could be utilized as another approach to substantiate that all the EWF experiments were conducted under uniform stress state. *Figure 6.33* shows w_f versus l for de-aged PLA and REX-PLA/o-MMT nanocomposite samples. From the figure, it was observed that all of the investigated samples have demonstrated a linear relation have been obtained between w_f and l values. This validates the prerequisite of performing all the experiments under uniform stress state as per recommended by the ESIS protocol for EWF.

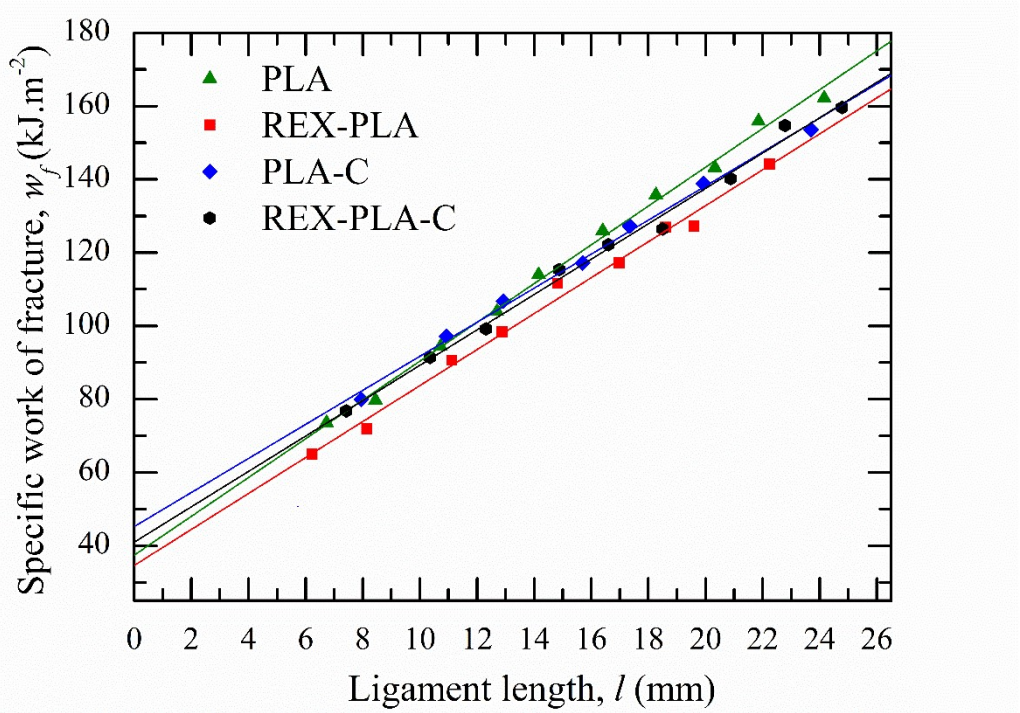

Figure 6.33. *Specific work of fracture (w_f) as a function of the ligament length (l) for de-aged PLA, REX-PLA and PLA composites with o-MMT.*

b) Fracture parameters

Taking into consideration that all prerequisites have been validated, *equation 6.14* was used for the analysis. Using best fit regression line, a linear relation is obtained in which Y-axis intercept and slope are w_e and βw_p respectively. All the EWF parameters were analyzed and results are reported in *table 6.13* based from *figure 6.33*.

$$\frac{W_f}{lt} = w_f = w_e + \beta w_p l \tag{6.14}$$

Table 6.13. *Influence of clays incorporation on the EWF parameters of de-aged PLA and modified PLA composites.*

Sample Nomenclature	w_e (kJ.m^{-2})	βw_p (MJ.m^{-3})	β (10^{-2})	w_p (MJ.m^{-3})	R^2 (w_f *vs.* l)
PLA	37 ±2	5.3 ±0.1	8.3 ±0.6	63.9 ±0.1	0.998
REX-PLA	34 ±2	4.9 ±0.2	6.1 ±0.5	80.3 ±0.2	0.996
PLA-C	45 ±2	4.7 ±0.1	12.6 ±1.4	37.0 ±0.1	0.995
REX-PLA-C	41 ±3	4.8 ±0.1	10.4 ±0.9	46.5 ±0.1	0.993

From *table 6.13,* it was observed that w_e value of REX-PLA samples were almost similar compared to PLA within the experimental error. This could indicate that the topological modifications induced by SAmfE addition remained insensitive to the essential work required for total plastic collapse of the ligament prior to necking of the ligament section. Similarly, Gámez-Pérez et al. (2011b) and Cailloux et al. (2014) have reported comparable w_e values for de-aged PLA films with a nominal thickness of 0.3 mm. This seem to be consistent with other publications which states that that the specific essential work of fracture is a material constant which remain independent of specimen geometry and MW under plane stress condition. (Cailloux et al., 2014; Hashemi, 1997; Karger-Kocsis and Moskala, 1997; Martinez et al., 2009; Wu and Mai, 1996). Furthermore, Karger-Kocsis et al. (1998) added that w_e values would not be influenced within the range of 2-50 mm.min^{-1}.

However, βw_p values appeared to be slightly reduce with chain architecture modifications. This decrease can be seen best when comparing PLA and REX-PLA samples as shown in *table 6.13*. This trend correlates with the lower crack propagating behaviours (tear resistance) observed for REX-PLA compared to PLA samples in *figure 6.31* and highlighted in the above paragraphs. The chain architecture modifications might have been attributed for lower plastic energy being dissipated outside the fracture process zone. The topological modifications achieved in REX-PLA resulted in a highly entangled network. This leads to a decrease in the ability to orientate the molecular chains under uniaxial loading thus leading to lower βw_p values (Cailloux et al., 2014).

According to Cailloux et al. (2014), the deformation mechanism which controls the extent of network stretching under uniaxial loading was predominantly reliant on of the extent of entangled network of REX-PLA. It was pointed out that beyond the yield point, a highly entangled network could only effectuate shorter network extension in comparison to a less-entangled structure. This could be due to the reduced stretching level of the backbone chain been caused by the reduced molecular weight between entanglements. Consequently, highly entangled network leads to a constraint in dispersing and relieving the stress in a higher volume of deformed material (decrease β value). This in turn will contribute to an increase in the mechanical work required to generate plastic flow which results in an increase of w_p value. (Basu et al., 2005; Cailloux et al., 2014; Chen and Wu, 2007).

Addition of o-MMT on the other hand seems to be a greater influence on the fracture parameters under plane stress condition observed. For PLA-C, it was observed that w_e value increased while simultaneously βw_p value decreased. Due to o-MMT higher specific surface

area and size, initiation requires considerable fracture energy resulting in higher fracture toughness. This trends bodes well with studies reported on various polymer nanocomposites using identical o-MMT (Bureau et al., 2004; Karger-Kocsis et al., 2013; Maspoch et al., 2009; Maspoch et al., 2015). The former effect can be attributed to a decrease in the interparticle distance due to agglomeration in this kind of filler which strongly favours the voiding (cavitation) and yielding of PLA matrix. As a result, the work expended in the fracture zone (i.e. process zone) becomes greater. While the latter effect is attributed to the o-MMT particles exerting a greater internal constraint on the polymer which restricts its ability for bulk deformation to form a larger plastic zone. This could explain the trend in which w_e value changes adversely with βw_p value as a function of the filler presence (Karger-Kocsis et al., 2013).

However in REX-PLA-C, the improvement on the w_e value expected from nanoparticles appears to be slightly limited, or obscured, by the presence of topological modifications and possible clay-PLA tethering with addition of clay. The w_e value and βw_p value of REX-PLA-C remain similar to PLA-C within the statistical error. A combined effect of the chain architecture modifications and improved o-MMT dispersion due to clay-polymer tethering might have been the factors responsible for this outcome. This observation will be further elucidated in the analysis of the plastic term, βw_p below.

To evaluate further the influence of o-MMT addition on the specific plastic or non-essential work of fracture (w_p) in PLA and modified PLA composites, a detailed analysis of the βw_p term was needed. In spite of this, w_p cannot be directly calculated from *equation 6.14* due to its combination with the shape factor, β term. After testing, a visual examination performed

indicates that the plastic zone formed in all of the test specimens featured a parabolic shaped geometry. The summation of combined height of the OPDZ, h, surrounding the ligament length, l, was measured. β was obtained from the best linear regression of a set of values represented in a graph plotting h versus l values and using *equation 6.15.*

$$\beta = \frac{2h}{3l} \tag{6.15}$$

Considering the data computed for PLA and REX-PLA, results suggest that β values decreased with structural modifications induced by SAmfE; thus indicating a significant decrease in the volume of deformed material surrounding the ligament length. On the other hand, a significant rise in w_p was obtained, indicating an increase in the energy density dissipated in the plastic deformation process surrounding the plane of crack propagation. Similar observations were also reported by Cailloux et al. (2014) and Cailloux (2015) with his modified PLA sheets.

In contrast to PLA, presence of o-MMT reverses this trend. It was observed that the shape parameter, β increases significantly (≈ 52%) while w_p (i.e. the plastic work dissipated per unit volume) decreases markedly (≈ 42%) for PLA-C. The fracture behaviour of the PLA-C can be explained by these two effects. The specific non-essential work of fracture (w_p) decreases with the presence of the o-MMT particles, as a result of the hampering effect of the clay on the plastic flow. On the other hand, presence of o-MMT particles also promotes a stress transfer effect. This trait is reflected in the enhancement of the outer plastic zone, reflected in higher values of β, which compensates the reduction of w_p as similarly reported by Maspoch et al. (2009).

Comparing PLA-C to REX-PLA-C, even though βw_p value were similar within the statistical error, β and w_p values individually were slightly modified. In REX-PLA-C, β value seems to decrease while w_p value seems to increase. From the WAXD analysis and TEM micrographs (*section 6.2.3*), it can be assumed that a relatively homogeneous clay distribution with smaller clay particles was observed in PLA-REX-C compared to PLA-C. Michler and Baltá-Calleja have concluded that composites with smaller particles would exhibit a larger reduction in the amount of deformable matrix because, at any given nominal filler content, the total interfacial area between fillers and polymer is larger for smaller filler particles (Michler and Baltá-Calleja, 2012). Additionally, it is also noted that plastic deformation of localized ligaments between the o-MMT particles within the matrix following particles-matrix decohesion and voiding can also contribute to enhancement of w_p value. Due to more a homogeneous and finely dispersed o-MMT distribution in REX-PLA-C, it is hypothesized that a higher mechanical work content is needed to produce plastic deformation especially during decohesion of o-MMT particles from PLA matrix which releases the local triaxiality. With these assumptions, the specific plastic work, w_p of REX-PLA-C would have increased compared to PLA-C at the detriment of the formation of plastic zone, which is reflected in lower values of β.

In order to morphologically analyze the effect of o-MMT in PLA and modified PLA matrix, inspection of the fractured surfaces of both PLA-C and REX-PLA-C were performed using SEM after fracture experiments. *Figure 6.34* shows the images taken from the usual plastic zone of the broken DDENT specimens and the SEM images of the corresponding fractured surfaces ahead of the crack tip.

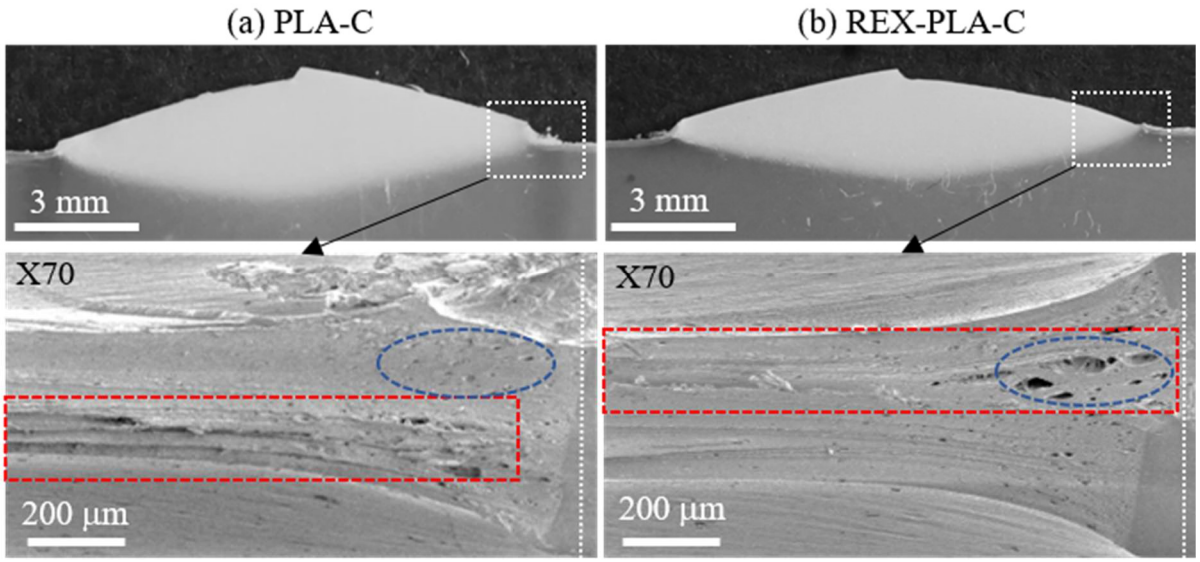

Figure 6.34. *Images were taken from the plastic zone of the broken DDENT samples of (a) PLA-C and (b) REX-PLA-C both at nominal ligament length of 16 mm tested at crosshead speed of 1 mm.min^{-1}. The fractured surface ahead of the crack tip (white dashed rectangle) was observed by SEM. The white dashed line indicates the initial crack tip.*

From *figure 6.34*, fracture surfaces of PLA-C samples revealed formation of small voids just ahead of the crack tip (highlighted in the blue dashed oval). It is also notice that the voids were small and were mostly present in the vicinity of the crack tip. These voids formation could be ascribed to the typical high crack-tip stress triaxiality and lower measure of toughness during the initial loading state (Argon et al., 1992). Additionally, formation of multiple ridges parallel to the crack propagation direction coupled with massive elongated voids were also observed in PLA -C (highlighted in red rectangle).

From TEM and XRD analyses (*c.f. section 6.2.3*), it can be inferred that o-MMT particles in PLA-C have poor particle–polymer interactions due to its inferior filler dispersion compared to REX-PLA-C. It is well known that voiding is caused by the filler particles, acting as stress concentrators, and easily detaching from the matrix while stress concentrations related to filler particles are proportional to their nominal surface area in the loading plane. Lower surface area of o-MMT in PLA-C due to presence of agglomerates causes void initiation to occur at significantly lower stresses due to the lack of reinforcement of the matrix. Once these voids were initiated, it grew in size under plastic flow until it coalesced with neighbouring voids. This trend augurs well with the decrease in non-essential term, βw_p values when compared to PLA as observed in *table 6.13*.

On the other hand, the fractured surfaces of REX-PLA-C displayed a relatively smoother fracture surface with formation of several massive cavities accompanied with smaller ones ahead of the crack tip. The massive voids in REX-PLA-C were mostly present at the beginning of the crack tip (highlighted in the blue dashed oval). Similar to PLA-C, the development of these voids near crack tip are to be expected since during the initial loading state, there is a high levels of stress triaxiality near the crack tip.

However, fracture surfaces of REX-PLA-C are quite different in that it possesses huge cavitation exclusively near the crack tip which is not present in PLA-C. These massive cavities formed signifies a higher degree of o-MMT debonding with REX-PLA as a matrix compared to PLA-C. It is known that from TEM and XRD analyses (*c.f. section 6.2.3*), REX-PLA-C still possess a notable amount o-MMT aggregates regardless of clay-polymer tethering evidenced in *section 6.1.3.* It is postulated that these voids initiation were instigated by o-MMT aggregates that are poorly bonded to the modified PLA matrix.

However, the fracture surfaces of REX-PLA-C also features multiple ridges with presence of small and evenly dispersed voids in the modified PLA matrix (highlighted in red rectangle). It is also known that from TEM and XRD analyses (*c.f. section 6.2.3*), REX-PLA-C possess higher and more homogenous clay particle distribution even though complete exfoliation, *i.e.,* complete separation of individual clay layers, could not be obtained irrespective of the modified PLA matrix. It is believed that the voids formed in REX-PLA-C is smaller in size due to higher o-MMT particle distribution. Once axial loading was applied and small voids and crazes were initiated, the small void and craze will propagate in conjunction with extensive fibrillation (shear yielding). However, the voids growth and coalescence are also governed by the stability of the fibrils extension and the resistance of the particle-matrix interface. It is hypothesize that clay-polymer tethering could have behave as a "phase adhesive" that impeded the generation of larger plastic deformation in REX-PLA-C hence slightly decreasing βw_p values compared to PLA-C.

6.3. Summary

Initial investigation using torque as function of mixing time in an internal mixer revealed that torque trace of PLA sample decreased monotonically over mixing time. This indicates that several random thermo-oxidative mechanisms took place during mixing, which leads to a decrease in the molecular weight of PLA. Conversely, significant torque hike was observed for REX-PLA sample compared to PLA. This could be ascribed to the higher reactivity of epoxy group of SAmfE towards higher content of terminal functional groups of PLA (hydroxyl and carboxyl groups) generated during mixing. In contrast, addition of o-MMT causes the torque trace of PLA-C sample to decrease monotonously over mixing time. This could be attributed to a possible plasticizing effect induced by the low MW of the organo-

modifier of the filler. However, a slow and gradual torque increase were observed for REX-PLA-C samples which can be attributed to reaction between the -OH functional end groups in surfactants in o-MMT with the remnants epoxy groups in the modified PLA matrix. This increased reactivity would then lead to remnant epoxy group being grafted onto the clay surface through the -C-O-C- linkage formation. FT-IR measurements on o-MMT and SAmfE blends revealed that a relatively fast chemical grafting reactions between the epoxy groups of SAmfE and the -OH functionalities of o-MMT did took place validating the outcome of the internal mixer analysis.

Conventional chromatographic SEC-DRI analysis revealed a significant increase in the molecular weight of REX-PLA samples compared to PLA which is reflected in the increase of the MW averages. The molecular weight spectra were also modified and a shoulder appeared in the high molecular weight tails. o-MMT addition made no significant difference in the molecular weight of PLA-C and REX-PLA-C. The narrow monomodal molecular weight spectras attained were similar to PLA. SAXS profiles and TEM morphologies revealed relatively homogeneous o-MMT distribution with partial intercalation was achieved in REX-PLA-C.

Rheological measurements showed that the addition of o-MMT decreases the complex viscosity of PLA-C compared to PLA while viscosity enhancement of REX-PLA-C were marginal. However, $|\eta^*(\omega)|$ and $G'(\omega)$ of PLA-C starts to monotonically increased with decreasing ω ($< 10^0$ rad.s^{-1}). This is due to geometric constraints from probable particle–particle and/or particle–polymer interactions that may have obstructed molecular relaxation of

the PLA matrix. On the other hand, REX-PLA-C displayed thermorheologically complex behaviour which validates the presence of clay-PLA tethering reactions.

On the other hand, T_g were not significantly modified with the addition of o-MMT during heating. However, o-MMT reduces T_{cc} and increases X_c of both PLA-C and REX-PLA-C during heating. o-MMT act as nucleating agent and facilitates crystallization of the polymer matrix during heating. With regards to cold-crystallization, o-MMT presence in PLA-C and REX-PLA-C neither promote nor hampers the crystallization of PLA during cooling. Upon reheating, it seems that presence of o-MMT have become hindrance in macromolecular chain medium-range transport movement for formation of thicker and homogeneous lamellar crystals.

The thermomechanical spectrum of PLA and modified PLA composites with o-MMT sheets revealed that o-MMT decreases the onset temperature of cold crystallization process. tan δ curves of PLA-C also exhibit additional peak attributed cold crystallization process in PLA-C. Both of these observations could be attributed to the nucleating effect of o-MMT. This observation is in agreement with the thermal behaviour analysis.

The tensile properties of PLA-C and REX-PLA-C samples were remained statistically similar to its neat homologues. However, tensile modulus showed 6% and 11% increase for PLA-C and REX-PLA-C samples, respectively. o-MMT addition also modifies the deformation mechanisms observed in PLA-C and REX-PLA-C. Both samples exhibit a mixed deformation mechanism between crazing and localized shear banding throughout the specimens gauge length as evidenced by the appearance of a stress-whitening zones appearing

along the gauge length attributed to the matrix-particle debonding and the consequent cavities growth.

The essential work of fracture (EWF) approach confirmed the enhancement of the fracture toughness of PLA composites with o-MMT. Considerable improvements of the specific essential work of fracture parameter (w_e) were observed in both PLA-C and REX-PLA-C compared to PLA and REX-PLA. However, the specific plastic work of dissipation (βw_p) of REX-PLA-C did not see any improvement compared to PLA-C.

Chapter 7: REX-PLA/nano-SiO_2 composites

7.1. Laboratory Scale: Internal mixer study

7.1.1. Verification of surface modification of silica used

For verification of the surface functionalization of the nanosilica used, its respective IR spectra were investigated using Fourier transform infrared spectroscopy in attenuated total reflectance mode (ATR-FT-IR). *Figure 7.1* shows the IR absorbance spectra of fumed silica, epoxy and aminopropyl functionalized silica, respectively. With the exception of SiO_2-E, all the nanosilica exhibited the characteristic bands assigned to SiO_2 at 811 cm^{-1} and 1087 cm^{-1} for symmetrical and asymmetric vibrations of the Si–O–Si bond (Hernández-Morales et al., 2012; Pretsch et al., 2009). Similarly, broad band centered at 3325 for SiO_2, 3433 for SiO_2-E and 3310 for SiO_2-A which is characteristic of physically absorbed molecular water interacting by H-bonding with silanol groups were also observed (Pretsch et al., 2009). Due to the epoxy surface functionalization of SiO_2-E, the appearance of absorption band at 798 cm^{-1} for epoxy ring bending overlapped symmetrical Si–O–Si absorption bands at 811 cm^{-1} (Pretsch et al., 2009).

On the other hand, the aminopropyl functionalization of SiO_2-A resulted in the appearance of band at 1552 cm^{-1} assigned to vibrations of N–H bond of amino groups as well as bands at 1467 cm^{-1} which is assigned to stretching and bending vibrations of CH_2 groups in aminopropyl (Antsiferova et al., 2013; Pretsch et al., 2009).

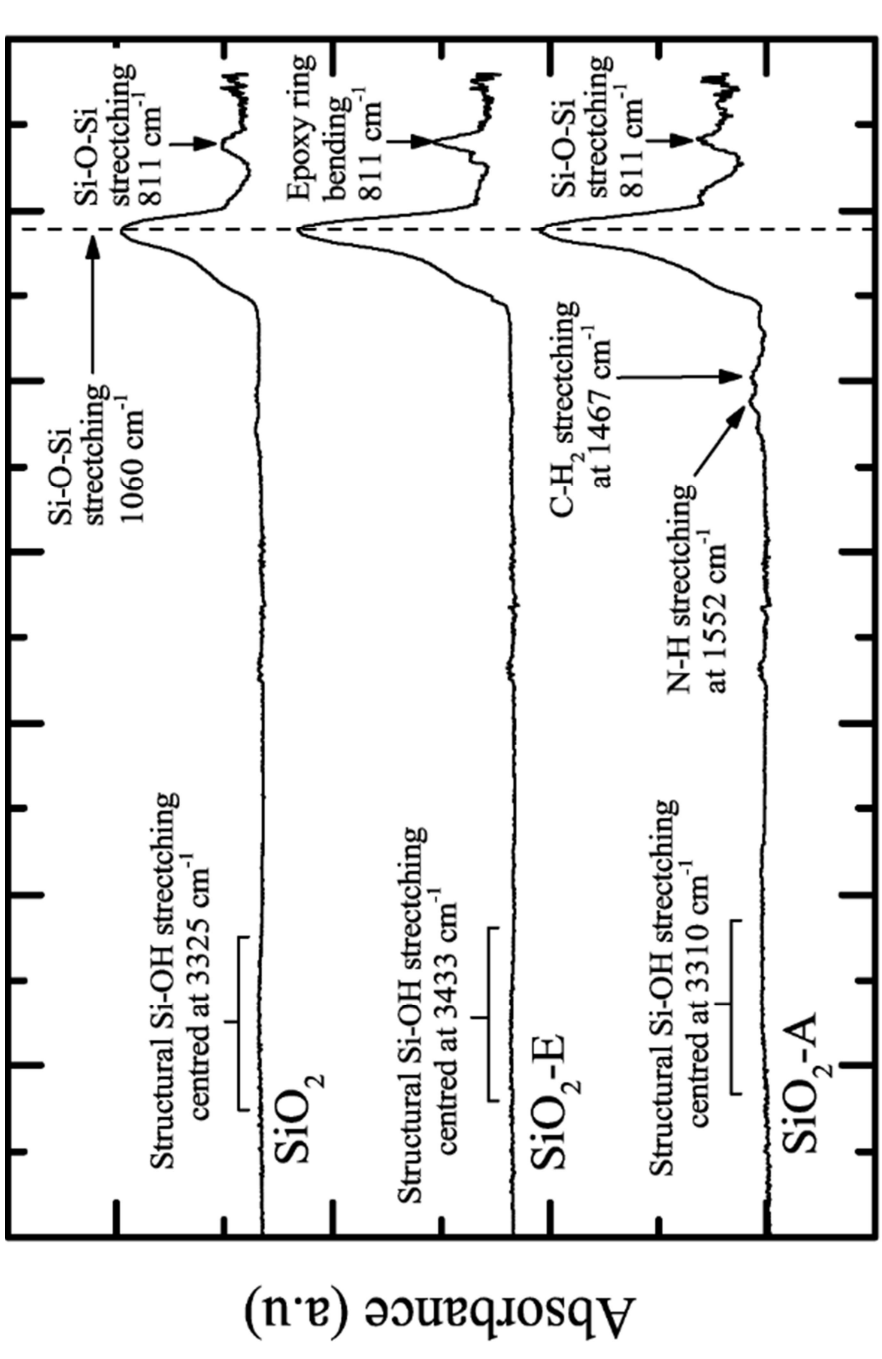

Figure 7.1. *FT-IR spectra of non-functionalized, epoxy and aminopropyl functionalized nano-SiO_2.*

7.1.2. Effect of nano-SiO_2 on the reaction profile of modified PLA composites

In the beginning, REX-PLA was chosen to be used exclusively as the matrix for the preparation of all PLA composites with nano-SiO_2. The influence of nano-SiO_2 on modified PLA torque trace was initially investigated using internal mixer. The progression of the torque trace (Γ) and the bulk temperature (T_b) as function of mixing time (t = 30 minutes) are observed and depicted in *figure 7.2(a)* and *7.2(b)* respectively. The torque measurements recorded were then used to compute the specific mechanical energy (SME) using *equation 6.1* (Redl et al., 1999) as has been elucidated in *chapter 6, section 6.1.1*. Results are given in *Table 7.1*.

From *figure 7.2*, it is seen that the torque trace of REX-PLA torque monotonically increase until it reached a plateau at approximately 13 minutes (indicated by a dashed line). This is in contrast to the observed torque of PLA melt which saw monotonous decrease up to 13 minutes. As has been discussed in *chapter 6, section 6.1.1.,* the trend may indicate that probable chemical bonding of several PLA chains to one SAmfE molecule could have taken place. The thermo-mechanical reactions could therefore be minimized thus leading to a possible increase in molecular weight and modification of the molecular topology as similarly reported by Cailloux et al. (2015) and Corre et al. (2011a). An increase of bulk temperature to 205 °C were also observed even though the set temperature was 180 °C. The increase of bulk temperature is causally associated with dissipation of energy as heat due to mechanical shearing of blends and the exothermic nature of the possible reaction between SAmfE and PLA.

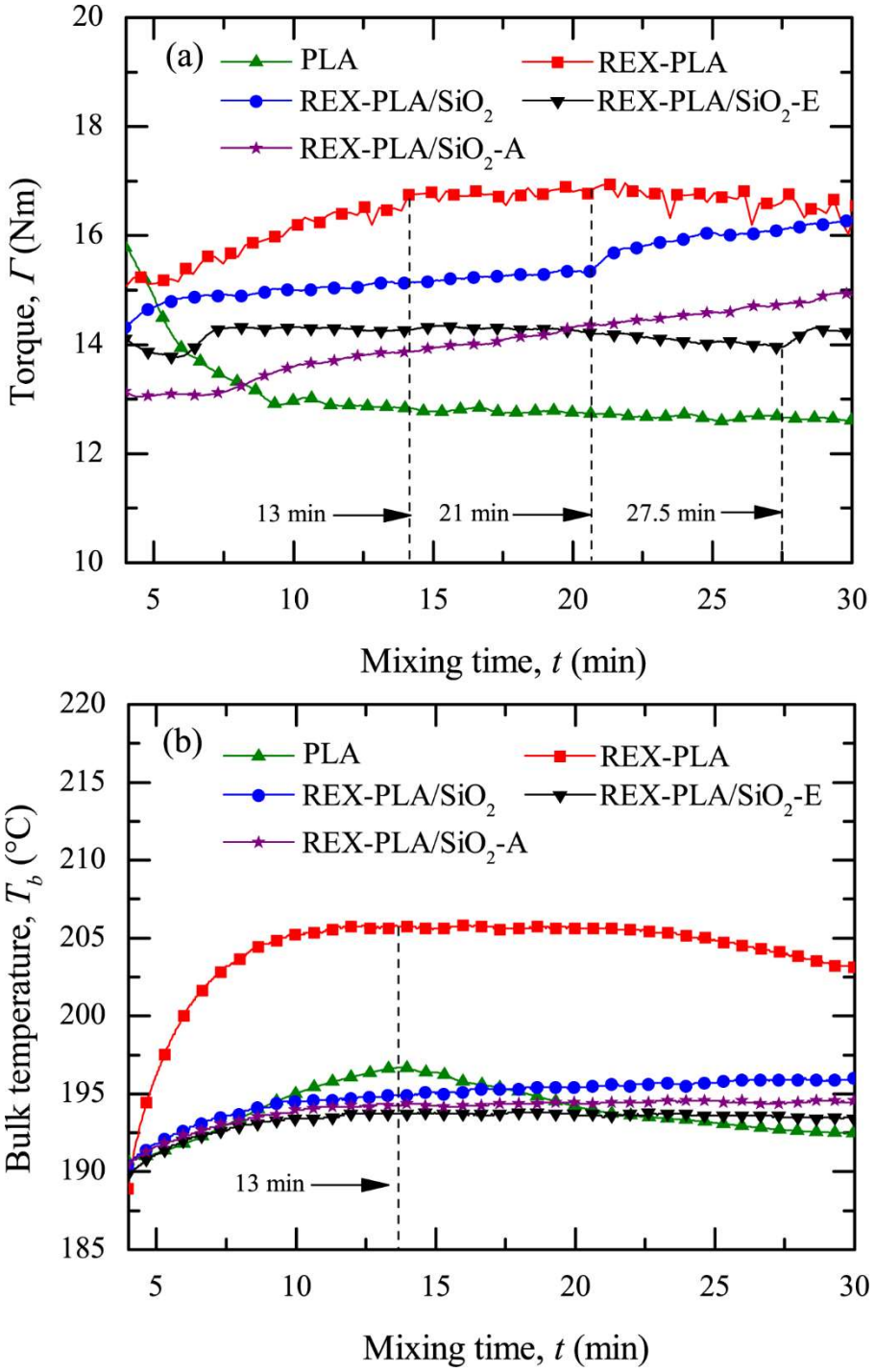

Figure 7.2. *Influence of nano-SiO_2 on the (a) torque trace (Γ) and (b) bulk temperature (T_b) as a function of the mixing time (t) at 180 °C of modified PLA composites.*

Table 7.1. *Influence of nano-SiO_2 on specific mechanical energy of modified PLA composites.*

Sample Nomenclature	SME ($J.g^{-1}$)
PLA	364 ±13
REX-PLA	507 ±17
REX-PLA/SiO_2	401 ±13
REX-PLA/SiO_2-E	365 ±24
REX-PLA/SiO_2-A	368 ±22

In the case of REX-PLA/SiO_2 blends, addition of SiO_2 causes a slight decrease of initial torque (≤1 Nm) compared to REX-PLA. The decrease in the initial torque still occurs even though all the necessary steps were taken to minimize thermo-mechanical degradations of both masterbatches (*i.e.* MB_{SAmfE} and MB_{SiO2}). This trend could be then solely attributed to the incorporation SiO_2 filler in to REX-PLA matrix. Apart from being used as reinforcing fillers, fumed silica possesses thixotropic (shear-thinning) behaviour in a liquid systems and are used as additives for viscosity control, anti-sag and anti-settling behaviour, and for general rheological enhancement. So when a system is at a constant shear rate and the viscosity of the system will decrease over time (Cabot Corporation, 2010). The shear-thinning behaviour of fumed silica is attributed to its spherical particles shapes and smooth non-porous surfaces, which would lower the friction coefficient causing its melt blends to decrease in viscosity (Kim et al., 2003). Due to the constant mechanical shearing during mixing at extended mixing time (*i.e.* 50 rpm at 30 minutes), fumed silica may have reduced the viscosity of the REX-PLA/SiO_2 blends which is reflected in torque reading. This trend is also mirrored in the lower SME values reported for REX-PLA/SiO_2 blends (*i.e.* $SME_{REX\text{-}PLA} > SME_{REX\text{-}PLA/SiO2}$).

As the mixing time progresses, a spike of torque reading was observed at approximately 21 minutes and continues to rise to up to 30 minutes. The increase in viscosity with addition of SiO_2 is most probably related to the development of a deformation sensitive microscopic structure. It is hypothesized that the torque increase is caused by the modified PLA matrix becoming confined and immobilized within and between "occluded volumes" which is shielded against deformation during mixing. Kosinski and Caruthers (1985) have similarly observed this trend in their poly(dimethylsiloxane)/fumed silica composites and elucidated it at length.

In general, SiO_2 possess small primary particle size, high specific surface area and silanol (hydroxyl) groups on its particle surface which renders it hydrophilic. In combination with its incompatibility with PLA, SiO_2 possess a high tendency to aggregate and form agglomerates. During melt mixing, these large agglomerates of SiO_2 particles in REX-PLA/SiO_2 blends will be broken down to smaller sizes due to high shear. However, some SiO_2 particles would remained in the form of smaller agglomerates due to the strong cohesive forces prevailing among SiO_2 particles and some as individual nanoparticles.

The individual SiO_2 particles, due to high cohesive energy, would have a tendency to form a network-like structure within the polymer matrix where they are either physically attached to each other or remained in close vicinity to each other. Thus in a REX-PLA/SiO_2 blends, network formation by SiO_2 particles throughout the modified PLA matrix, could occlude part of the continuous polymer phase in their inter-network voids. This is generally known as ‘‘occluded volume,’’ and leads to polymer matrix being confined and immobilized within the occluded volumes and would act as part of the fumed silica volume fraction.

With regards to the bulk temperature, an increase to 193 °C from the set temperature was observed. The bulk temperature increase could be attributed to high mechanical shearing due to the combination of melting of REX-PLA granules and diminution of the SiO_2 aggregates into smaller particles.

In contrast, the torque vs time of REX-PLA/SiO_2-E traces confounded expectations. Instead of an increase in torque, the addition of epoxy modified silica gradually decreases the torque value over mixing time. However at approximately 27.5 minutes (indicated by a dotted line), a minor spike of torque were observed. Nevertheless, the overall torque value was still lower than REX-PLA/SiO_2 torque trace. This trend is also in agreement with the calculated SME values of both blends(*i.e.* $SME_{REX\text{-}PLA/SiO2} > SME_{REX\text{-}PLA/SiO2\text{-}E}$). The marked decrease in torque can be attributed to the silica that imparts thixotropy that reduces the viscosity of the REX-PLA/SiO_2-E. It can also be assumed that the epoxy functional end group in SiO_2-E does not react with the remnants epoxy groups in the melted bulk of modified PLA. This hypothesis also is supported by the comparison of bulk temperature between REX-PLA/SiO_2-E and REX-PLA/SiO_2. However, this is higher when compared to the bulk temperature of PLA neat. Even though the bulk temperature of REX-PLA/SiO_2-E recorded is higher than the set temperature, it is evident that the temperature remained flat throughout the mixing time. Both of these trends are general indications of little or no chemical interactions happened within REX-PLA/SiO_2-E blends.

Unlike SiO_2-E, SiO_2-A presence monotonically increase torque value of REX-PLA/SiO_2-A blends. However, the initial torque of REX-PLA/SiO_2-A were approximately

13% lower than REX-PLA. Subsequently, the torque reading started to increase at approximately 8 minutes and gradually improved throughout the mixing time that could probably indicate nano-SiO_2-polymer tethering reaction. Nevertheless, torque level recorded were still lower when compared to REX-PLA samples which is also reflected in the calculated SME values of both blends(*i.e.* $SME_{REX\text{-}PLA} > SME_{REX\text{-}PLA/SiO2\text{-}A}$). It is hypothesized that the amino in SiO_2-A enhances the diffusivity of the SiO_2-A towards the epoxy groups in REX-PLA. The slight increased reactivity would lead to SAmfE agent being grafted onto the SiO_2-A through the -C-N linkage formation. However, silica plays a role in reducing the viscosity of melt blends due to its thixotropic behaviour. Thus, the enhancement of the REX-PLA/SiO_2-A melt properties is likely to be reduced, leading to lower torque values. Interestingly, the bulk temperature of REX-PLA/SiO_2-A blend observed were lower than REX-PLA/SiO_2 blend. This is probably due to lower shear heating due to higher viscous dissipation of REX-PLA/SiO_2-A blend compared to REX-PLA/SiO_2.

7.1.3. Proposed reactions of REX-PLA onto nano-SiO_2 particles

To begin with, PLA was initially reacted with styrene-acrylic multifunctional oligomeric agent (SAmfE) to obtain REX-PLA. As has been similarly discussed in *section 6.1.2.*, it is well known that carboxyl groups from PLA can react with epoxy functional groups from SAmfE and these reactions have been described at length by Cailloux et al. (2013). It has been demonstrated that there are residual unreacted epoxy groups present in REX-PLA due to the nature of SAmfE that has a functionality of 12 (Cailloux, 2015). Consequently, the remaining epoxy groups could have reacted towards -OH from silanol groups on the SiO_2 surface which results in grafting of REX-PLA onto SiO_2 particles (*c.f. figure* 7.3 [Scheme I]).

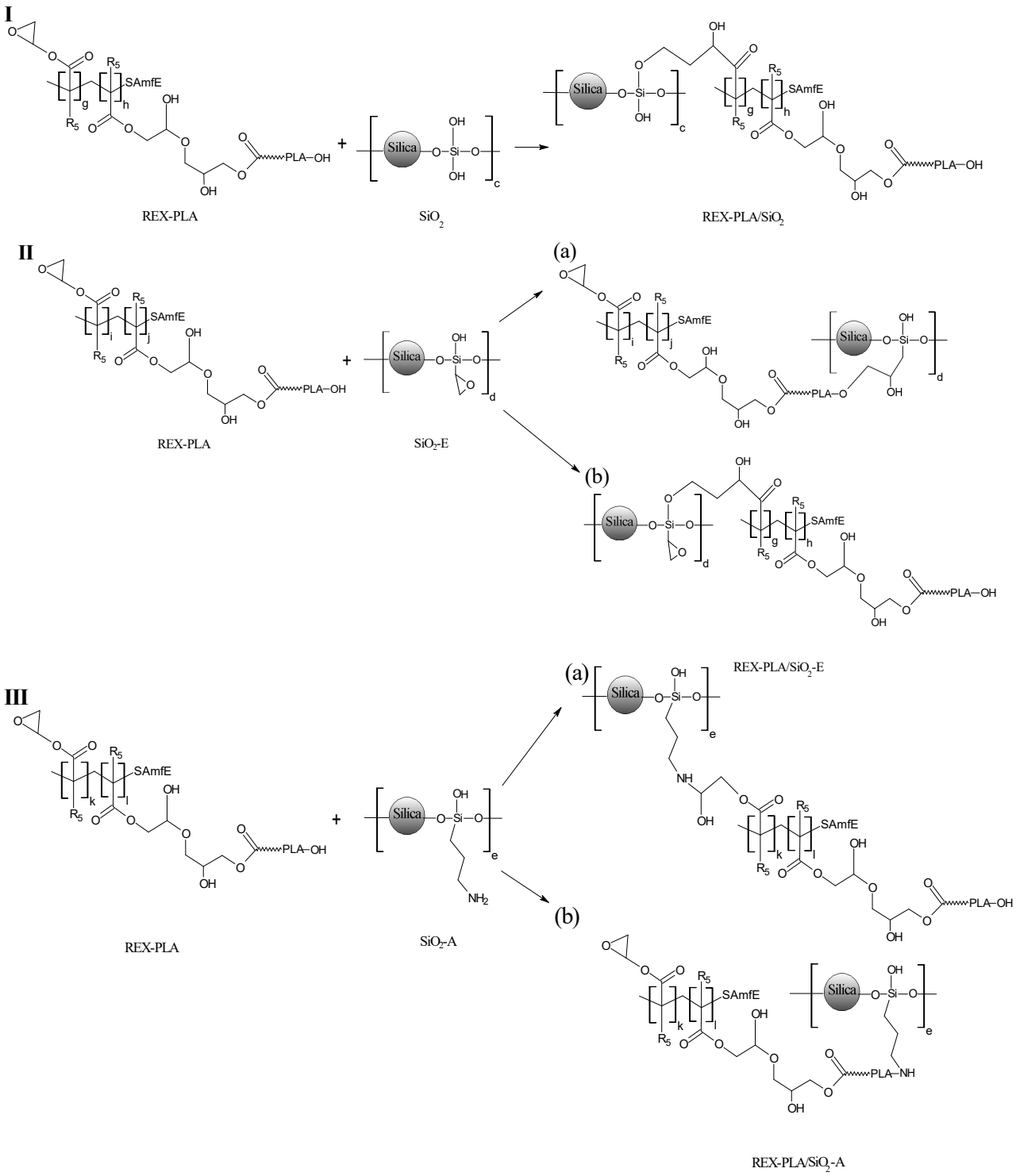

Figure 7.3. *Proposed reaction mechanisms of REX-PLA with (I) SiO_2, (II) SiO_2-E and (III) SiO_2-A.*

Introducing surface modification by replacing the surfaces of the unmodified particles that are generally covered by silanol groups (Si–OH) with either epoxy or amino functional group have the potential to interact with the epoxy group of SAmfE or carboxyl groups of PLA, through covalent attachment of end-functionalized polymers to the surface of nano-SiO_2. Such interactions are expected to significantly affect the physical properties of the dispersion, especially for initial particles with smaller diameters.

It is known that epoxy groups can react with both PLA functional end groups creating covalent bonds (i.e. -COOH and -OH groups). However, due to the strong polarization of the hydroxyl groups of carboxylic acid, a higher reactivity of epoxy towards the carboxyl groups compared to hydroxyl groups was reported (Bikiaris and Karayannidis, 1996). Nevertheless, the epoxy functionalization of SiO_2 could have resulted in an increased concentration of epoxy group in SiO_2-E. Epoxy group in SiO_2-E could have reacted towards remaining -OH functional end groups from REX-PLA which results in grafting of SiO_2-E particles onto REX-PLA (*c.f. Figure 7.3* [Scheme II a]). Conversely, due to presence of residual epoxy group from SAmfE, epoxy group in REX-PLA could have also reacted towards remaining -OH from silanol groups in SiO_2-E which also results to grafting of REX-PLA onto SiO_2-E particles (*c.f. figure 7.3* [Scheme II b]). The reaction between epoxy and silanol group have also been previously reported by Xue et al. (2008b).

With regards to amine treated silica, primary amine groups from SiO_2-A is also able to react towards REX-PLA functional end groups (-OH and –COOH). However, the reaction of epoxide with amino is a more predominant reaction as was previously reported (Shechter et al., 1956; Vladimirov et al., 1980). Amino group in SiO_2-A will primarily react with the remaining epoxy group of SAmfE in REX-PLA. Reaction between amino groups in SiO_2-A with epoxy rings via ring-opening reaction could have created a covalent -C-N bonds will results in grafting of SiO_2-A particles onto REX-PLA (*c.f. figure 7.3* [Scheme III a]). On the other hand, -NH_2 group from SiO_2-A could have also reacted towards -OH groups from REX-PLA which also results to grafting of SiO_2-A particles onto REX-PLA (*c.f. figure 7.3* [Scheme II]).

7.1.4. Characterization of reactivity between nano-SiO_2 and SAmfE

To obtain more information regarding the grafting of nano-SiO_2 onto REX-PLA, all the film samples were evaluated by monitoring the of absorption bands using FT-IR in the spectral regions of 4000 to 2750 cm^{-1} and 850 to 775 cm^{-1}. *Figure 7.4* depicts the IR absorbance spectra of REX-PLA and REX-PLA/nano-SiO_2 composites. Correction of the spectra were applied for direct comparison between all of the analyzed samples. The absorption peaks of PLA are characterized at 1080 and 1183 cm^{-1} for C-O-C stretching, at 1360 and 1380 cm^{-1} for C-H bending and at 2991 and 2945 cm^{-1} for C-H stretching (Pretsch et al., 2009). The absorption peaks of SAmfE are characterized at 700 cm^{-1} for aromatic C=C vibration, 750 cm^{-1} for aromatic C-H bending, at 798 cm^{-1} for epoxy ring bending and at 1748 cm^{-1} for C=O stretching (Najafi et al., 2012b; Pretsch et al., 2001). While the absorption peaks of all nano-SiO_2 particles that are visible were only at 3298 cm^{-1} for the structural -OH stretching of silanol groups (i.e. Si-OH). Unfortunately, absorption peaks of epoxy and aminopropyl surface functionalized groups were not detectable due to being overlapped by the principal bands of PLA.

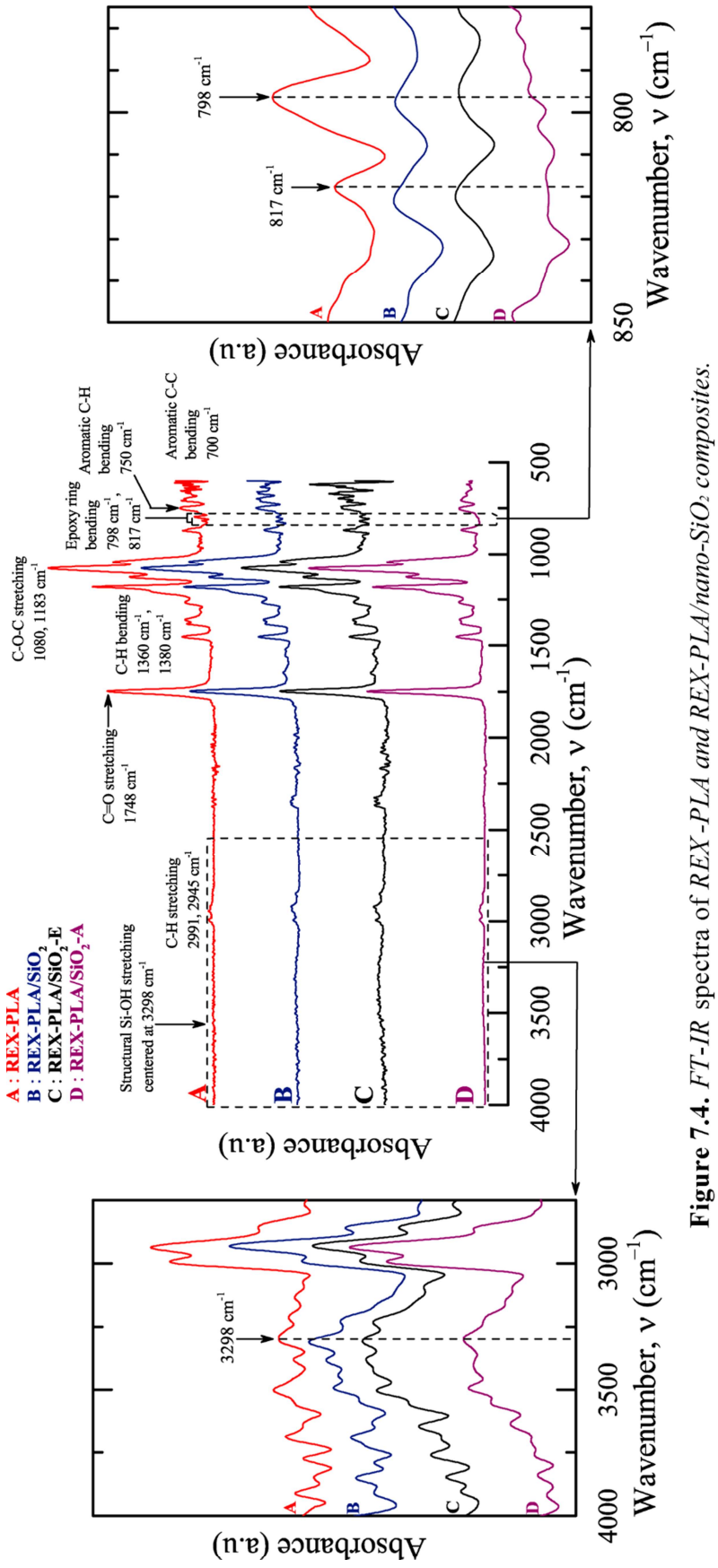

Figure 7.4. *FT-IR* spectra of *REX-PLA and REX-PLA/nano-SiO_2 composites.*

Due to the aforementioned difficulties, only the absorption band at 817 and 796 cm^{-1} which corresponds to epoxy ring of SAmfE and the weak broad peak at 3298 cm^{-1} that corresponds to structural -OH stretching of nano-SiO_2 fillers were used for the monitoring of nano-SiO_2–REX-PLA reactions.

Addition of SiO_2 in REX-PLA increases the intensity of broad structural -OH absorption peaks (3298 cm^{-1}) compared to REX-PLA due to surface -OH from silanol group of SiO_2 in *figure 7.4 (B)*. From the absorbance band of 850 to 775 cm^{-1}, it was observed that the increase of structural -OH peaks coincided simultaneously with partial diminishment of both epoxy absorption band (*i.e.* at 817 and 796 cm^{-1}). It is known that the intensity of the absorption band is directly correlated with the concentration of reactants. This observation could indicate that a potential albeit weak interactions may have taken place via residual epoxy group of REX-PLA with hydroxyl group on the surface of SiO_2. Comparable trend was observed for REX-PLA/SiO_2-E thus indicating similar reaction between epoxy and -OH functionalities may have taken place as depicted in *figure 7.4 (C)*.

It is postulated that amino group in SiO_2-A will primarily react with the remaining epoxy group of SAmfE in REX-PLA. The introduction of SiO_2-A decreases the intensity of both epoxy absorbance peaks, eventually becoming negligibly small (817 and 796 cm^{-1}) in tandem with the diminishment of absorption band at 1552 cm^{-1} (i.e. N–H) and at 1467 cm^{-1} (i.e. -CH_2) which is assigned to the aminopropyl functionalization of SiO_2-A as observed in *figure 7.4(D)*. This trend was probably due to a near total consumption of the available epoxy groups or to a remaining concentration of epoxy groups below the detection limit of the FT-IR analysis. Thus, SiO_2-polymer tethering reaction in REX-PLA/SiO_2-A may have occurred.

7.2 Scaling up of the reactive extrusion processing

7.2.1. Molecular characterization: MW Determination by Intrinsic Viscosity

Since the main emphasis of this dissertation is one-step reactive extrusion processing technique in a pilot plant, only calendered films manufactured in this method will be considered for further analyses. In order to determine the molecular modifications of PLA resulting from the addition of nano-SiO_2 particles and SAmfE agent during processing, intrinsic viscosities ([η]) of all the manufactured films were determined using *figure 7.5* in which its [η] values are related to the viscosity-average molecular weight, (M_v) by means of the Mark-Houwink-Sakurada equation which was listed in *equation 5.9 (c.f. chapter 5, section 5.1.4)*.

Even though size exclusion chromatography (SEC) is a faster and more convenient method for determining the molecular weight distribution of polymers, intrinsic viscosities measurement was chosen for this study to circumvent the drawbacks encountered based from previous MW measurements of REX-PLA/o-MMT nanocomposites performed using SEC-DRI technique namely, probable removal of PLA macromolecules during separation of o-MMT prior to performing the analysis. *Table 7.2* summarizes the corresponding MW values calculated from measured intrinsic viscosity using *equation 5.10 (c.f. chapter 5, section 5.1.4)*.

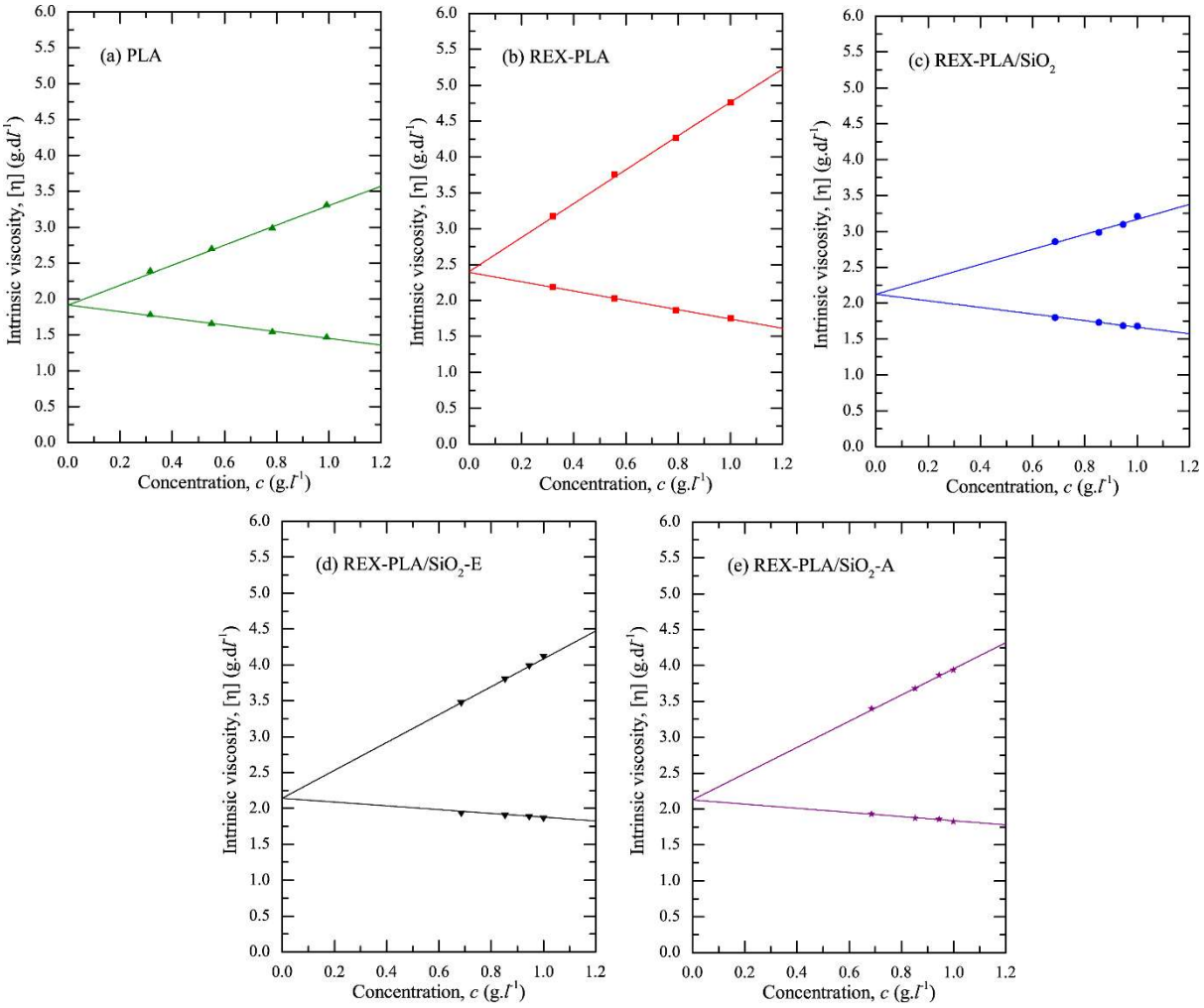

Figure 7. 5. *Plot of (a) PLA, (b) REX-PLA, (c)REX-PLA/SiO₂, (d) REX-PLA/SiO₂-E and (e) REX-PLA/SiO₂-A to determine intrinsic viscosity,* [η] *(limiting viscosity number).*

Table 7.2. *Effect of nanosilica addition on intrinsic viscosities and estimation of molecular weight averages of REX-PLA and REX-PLA/nano-SiO_2 composites.*

Sample Nomenclature	Intrinsic Viscosity, $[\eta]$ (dl/g)	M_v[a] (kg.mol^{-1})	M_n[b] (kg.mol^{-1})	M_w[c] (kg.mol^{-1})
PLA	1.94 ± 0.01	132	70	140
REX-PLA	2.40 ± 0.01	175	92	185
REX-PLA/SiO_2	2.28 ± 0.03	163	86	173
REX-PLA/SiO_2-E	2.31 ± 0.02	165	88	175
REX-PLA/SiO_2-A	2.30 ± 0.02	165	87	174

[a]M_v were calculated using Mark-Houwink-Sakurada equation (*c.f. equation 5.9, chapter 5; section 5.1.4)*.
[b]M_n were calculated based on $\frac{M_v}{M_n} = 1.89$ (Schindler and Harper, 1979).
[c]M_w were calculated using *equation 5.11* (*c.f. chapter 5; section 5.1.4)*.

Using Mark-Houwink-Sakurada equation, the calculated *K'* values for PLA (*K'* = 0.3) showed that the chloroform represents a good solvent for the PLA nanocomposites, indicating that the hydrodynamic volume of the polymer chain shrinks with favourable interaction between polymer and solvent (Al-Itry et al., 2012). Additionally, calculation of M_n using relation of M_v/M_n =1.89 were based on Schindler and Harper (1979) findings for racemic PLA which were dissolved in chloroform.

From *table 7.2,* it can be seen that REX-PLA displayed the highest $[\eta]$ value compared to PLA and REX-PLA/nano-SiO_2 composites. This could be attributed to the topological modifications induced by SAmfE that increases the hydrodynamic volume of REX-PLA which in turn increases the viscosities of the dissolved REX-PLA solution. Calculation of M_n using relation of M_v/M_n =1.89 shows that M_n of PLA and REX-PLA computed were approximately

within 5% and 4% of M_n of PLA and REX-PLA respectively which was estimated using SEC technique (*c.f. Chapter 6; section 6.2.1,*). This suggest that that the estimation of M_n using relation M_v/M_n =1.89 were reliable.

With regards to M_w, M_w of PLA computed using *equation 5.11* were approximately within 10% of M_w estimated using SEC technique. On the other hand, M_w value of REX-PLA calculated using *equation 5.11* were 23% less than the M_w of REX-PLA estimated using SEC technique. This could be attributed to the increased in the population of sparsely branched structures brought about by presence SAmfE in REX-PLA that may have resulted in the inaccuracies in the M_w calculated. This hints that M_w estimation using *equation 5.11* as suggested by Fried (2003) and Hiemenz and Lodge, (2003) were only suitable to be used for M_w estimation of linear polymer.

With regards to REX-PLA/SiO_2, solute molecules such as fumed silica that have a tendency to associate and formed well-defined aggregates can also increase the intrinsic viscosity of a solution (Zou et al., 2008). In contrast, $[\eta]$ values observed for REX-PLA/SiO_2 were the lowest measured. Similar trends were reported by Hahm et al. (2004) and Todorov and Viana (2007) using PET/SiO_2 nanocomposites. The reasons for this could probably due to the spherical particles shapes and smooth non-porous surfaces of the fumed silica, which would lower the intrinsic viscosity of solution. Poor or limited SiO_2-polymer tethering reaction between SiO_2 and REX-PLA may have also contributed to this observation.

As in the case of SiO_2-E and SiO_2-A, a slight increase of $[\eta]$ values compared to REX-PLA/SiO_2 were observed. Probable improved interactions between surface functionalized

silica and REX-PLA may have contributed to this. However, both [η] values were still lower than [η] values recorded for REX-PLA. This could also be attributed to the geometric shapes of nano-SiO_2 that are spherical particles. A possible mechanism that can explained this trend is called "ball bearing" effect. Xie et al. (2004) have proposed that the spherical nanoparticles can serve as 'ball bearings', reducing the interlayer interaction of the polymer matrix and thereby decreasing the viscosity of nanocomposites. An illustration depicting this effect is presented in *figure 7.6.* This effect is based on the idea that when a polymer containing spherical particles is subjected to a shear flow, a high local shear is developed in the narrow gap between two nearby spherical particles, which may cause them to rotate and lead the chains between them to disentangle hence an observed lower viscosity.

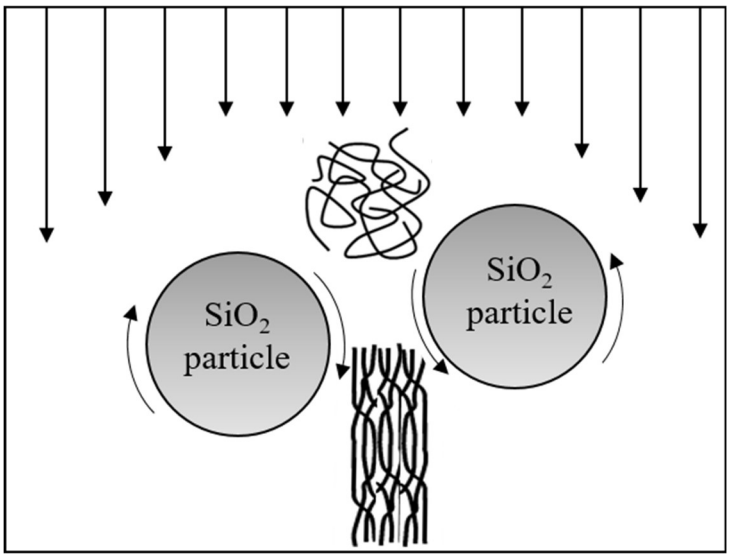

Figure 7.6. *Illustration of "ball bearing" effect in which entangled chain becomes disentangled when subjected to high shear flow in the vicinity of spherical SiO_2 particles.*

From *table 7.2*, the trend observed suggest that addition of nano-SiO_2 seems to reduce the [η] values measured. It can be hypothesize that possible SiO_2-polymer tethering induced

by SAmfE and nano-SiO_2 addition were negligibly small. This combine with geometric shapes of nano-SiO_2 may have contributed to the decrease of [η] values.

7.2.2. Effect of nano-SiO_2 addition on the rheological behaviour of modified PLA composites.

The viscoelastic functions of REX-PLA and REX-PLA/SiO_2 nanocomposites within LVE regime were investigated to verify the presence of SiO_2-PLA tethering within all the investigated samples. The frequency sweeps and creep-recovery experiments of all the manufactured films were performed at 180 °C with 0.2 % strain amplitude (LVE). According to Cailloux et al. (2015), the frequency sweeps and conversion of the creep-recovery traces should superpose if all the experiments were performed within the LVE regime. The combination of both tests could assist in characterizing the viscoelastic behaviour of REX-PLA and REX-PLA/SiO_2 nanocomposites over a larger range of times or frequencies. Additionally, $|\eta^*(\omega)|$ of PLA samples was added in *figure 7.7* for comparison purposes. Thus, *figure 7.7* shows the $|\eta^*(\omega)|$ master curve for PLA, REX-PLA, REX-PLA/SiO_2, REX-PLA/SiO_2-E and REX-PLA/SiO_2-A samples.

The $|\eta^*(\omega)$ master curve of all samples were made by merging frequency sweep and the conversion of the creep-recovery data at 180 °C. The merged dynamic mechanical graphs encompasses of seven magnitudes of angular frequency, comprises of data attained from the frequency sweep test in the range of 2.10^{-1} - 10^3 rad.s^{-1} and the data from the conversion of the creep-recovery test in the range of 3.10^{-3} - 10^{-1} rad.s^{-1} derived from retardation spectrum.

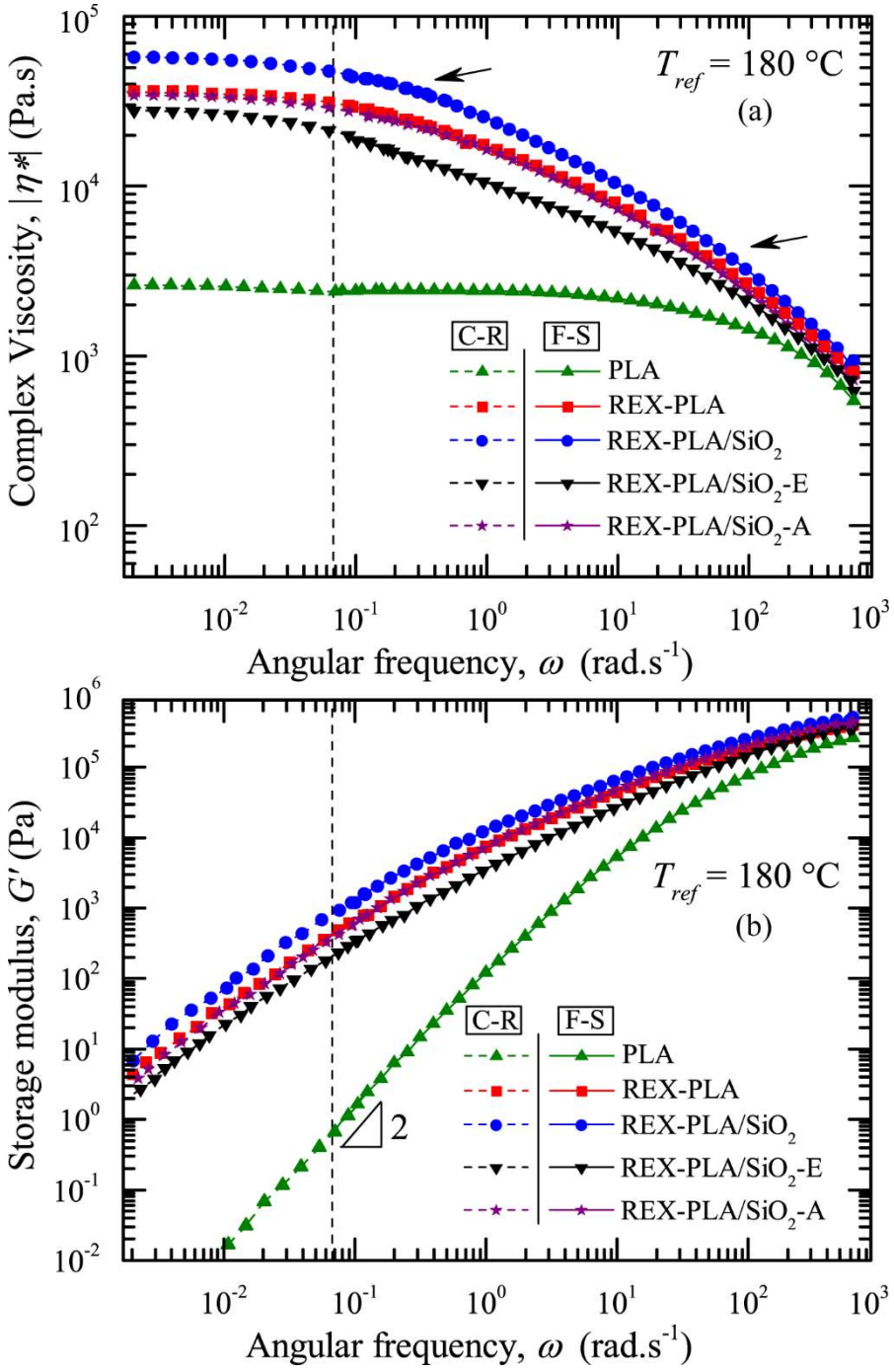

Figure 7.7. *Effect of the addition of nano-SiO_2 on (a) complex viscosity and (b) storage modulus versus angular frequencies of modified PLA composites at a reference temperature of 180 ºC. C-R: conversion of the creep-recovery data calculated from retardation spectrum. F-S: frequency sweep data reduced to master curve. The arrows indicate the two different curvatures in the transition zone between the terminal and power-law region.*

From *figure 7.7(a)* and *(b)*, both frequency sweeps and creep-recovery spectrums superpose well for all the investigated samples despite exhibiting contradictory relaxation behaviour between PLA versus REX-PLA and REX-PLA/SiO_2 nanocomposites. Observing *figure 7.7(a)* and *(b)* reveals that the linear terminal regime of PLA was reached (around 1 rad.s^{-1}). However, at the lowest ω (0.0628 rad.s^{-1}) attainable using a frequency sweep experiment neither $|\eta^*(\omega)|$ reached the terminal (Newtonian) region nor $G'(\omega)$ reached the terminal double logarithmic slopes of 2 in REX-PLA and REX-PLA/SiO_2 nanocomposites. Additionally, a significant increase in $\eta^*(\omega)$ value and the shifting of the onset of the terminal region to lower ω were also observed for REX-PLA and REX-PLA/SiO_2 nanocomposites. The transition zone between the terminal and power-law region was also enlarged and two different curvatures were observed specifically in REX-PLA and REX-PLA/SiO_2 nanocomposites (indicated by arrows).

As has been discussed and established in the TTS validation discussion of REX-PLA/o-MMT composites in the foregoing chapter (*c.f. Chapter 6; section 6.2.2*) that REX-PLA exhibited thermorheologically complex behaviour which is attributed the presence of LCB polymers. Since all the other REX-PLA/SiO_2 nanocomposites spectrums mimics these behaviours, it can be assumed that all REX-PLA/SiO_2 nanocomposites samples also possess thermorheologically complex behaviour.

From the *figure 7.7(a)* and *(b)*, it can be generalized that $|\eta^*(\omega)|$ and $G'(\omega)$ values of all the investigated sample seems to converge towards approximately similar value at high angular frequency (between 10^2 and 10^3 rad.s^{-1}). PLA displayed a Newtonian plateau region over a wide range of ω signalling a relatively fast chain relaxation process followed by a

smooth transition to the power-law region with increasing ω. This thermorheological simple behaviour exhibited by PLA are characteristic of a linear polymer. In contrast to PLA, the addition of SAmfE leads to shifting of the onset terminal region to lower ω ($\approx 10^{-1}$ rad.s^{-1}) and a significant increase in η_0. REX-PLA sample displayed Newtonian plateau region followed by a smooth but broadened transition zone with 2 different curvature (indicated by arrows) between zero-shear viscosity plateau and power law region. The zero shear viscosity, η_0 and terminal zone slopes of $G'(\omega)$ of all the investigated samples are presented in *table 7.3*.

Table 7.3. *Zero shear viscosity, η_0 and terminal slopes of $G'(\omega)$ of PLA, REX-PLA and REX-PLA/SiO_2 nanocomposites.*

Sample Nomenclature	Zero shear viscosity, η_0 (kPa.s)	Terminal slopes of $G'(\omega)$
PLA	2.8	2.0
REX-PLA	34.0	1.3
REX-PLA/SiO_2	57.0	1.3
REX-PLA/SiO_2-E	28.0	1.2
REX-PLA/SiO_2-A	33.0	1.3

Looking at *figure 7.7(a)* and *(b)*, it is apparent that REX-PLA/SiO_2 exhibited similar rheological behaviour as REX-PLA sample almost throughout the whole frequency scan. REX-PLA/SiO_2 displayed a terminal region followed by a broad transition zone to pseudo-plastic regime with increasing ω. The terminal zone slopes of $G'(\omega)$ of REX-PLA/SiO_2 were also similar to REX-PLA (≈1.3). However, η_0 values of REX-PLA/SiO_2 sample were markedly higher when compared to REX-PLA. This trends match those observed in HDPE-SiO_2 nanocomposites studied by Nandi et al. (2013). The increased η_0 values could be attributed to physical characteristics of SiO_2 having high specific surface area and presence of surface silanol

(hydroxyl) groups that made it easily adhered to each other through hydrogen bonding and formed large agglomerates. It would then have a tendency to form a network-like structure within the polymer matrix where it will be physically attached or remained in close vicinity to each other. Thus, the SiO_2 network formation throughout the REX-PLA matrix may possibly occlude part of the continuous polymer phase in their inter-network voids. This is generally known as "occluded volume" and that lead to a larger effective phase volume than that of the primary aggregate SiO_2 particles. The polymer phase trapped and immobilized within and between these occluded volumes will be shielded against deformation under stress and would act as part of the fumed silica volume fraction (Nandi et al., 2013). This in turn may have impeded the reptation of the polymer chains in REX-PLA/SiO_2 hence the higher η_0 values.

On the contrary, addition of epoxy modified silica slight lowers $|\eta(\omega)|$ of REX-PLA/SiO_2-E compared to REX-PLA/SiO_2 which is especially evident between $\omega \approx 0.1$ to 1 rad.s^{-1}. This results in 17% decrease in η_0 values of REX-PLA/SiO_2-E in comparison to REX-PLA/SiO_2. The terminal zone slopes of $G'(\omega)$ of REX-PLA/SiO_2-E were also reduced to 1.2. Possible explanations for the decrease in η_0 values and terminal zone slopes of $G'(\omega)$ would be that addition of SiO_2-E particles may have disrupted the regularity of the REX-PLA chain structures and increased the space between the chains and promoted the mobility of the chain segments in the direction of flow. Another possible factor could be the manifestations of the relatively poor interactions between SiO_2-E and polymer matrix. This shows that there is little or minimal SiO_2-E-polymer tethering that would have otherwise increase the η_0 values. However, REX-PLA/SiO_2-E possess similar rheological behaviour as REX-PLA sample with enlarged transition zone between the terminal and power-law region as opposed to PLA. This thermorheologically complex behaviour could be primarily attributed to addition of SAmfE

that increases the melt elasticity due to possible modification of the molecular topology which is in line with the significant increases in MW as measured using IV measurements (*c.f. table 7.2*).

Referring to REX-PLA/SiO_2-A, presence of SiO_2-A retains similar rheological behaviour as REX-PLA sample with enlarged transition zone between the terminal and power-law region. It seems that addition of amino modified silica yielded almost identical η_0 values and terminal zone slopes of $G'(\omega)$ with REX-PLA (≈1.3). From the internal mixer analysis (*c.f. chapter 7; section 7.1.1)* it was observed that addition of SiO_2-A could have decrease viscosity due to the geometrical nature of SiO_2-A particle that promotes the mobility of polymer chain. However, it is hypothesize that probable SiO_2-polymer tethering as evidenced in the FT-IR analysis (*c.f. chapter 7; section 7.1.3)* may have compensated for this phenomenon. The postulated SiO_2-A -polymer tethering may have perturbed the normal flow of the REX-PLA matrix and hindered the mobility of the chain segments in the direction of flow and as a result yielded very similar η_0 values as REX-PLA.

In order to interpret the feature of $|\eta^*(\omega)|$ of all of the investigated samples in a numerical expression, the Carreau Yasuda extended (CY-Ext) models as proposed by Cailloux (2015) were used to fit $|\eta^*(\omega)|$ experimental data of PLA, REX-PLA and REX-PLA/nano-SiO_2 composites. The CY-Ext model used are displayed below as *equation 7.1.*

$$|\eta^*(\omega)| = \frac{\eta_0}{\left[(1+(\tau_1\omega)^{2a_1})^{\frac{1-\nu_1}{2a_1}}\right]\left[(1+(\tau_2\omega)^{2a_2})^{\frac{1-\nu_2}{2a_2}}\right]} \quad (7.1)$$

The entire set of superposed frequency sweeps and conversion of the creep-recovery measurement data of PLA, REX-PLA and REX-PLA/nano-SiO_2 composites were fitted using the preceding equation using the least squares approach. In order to ascertain whether the CY-Ext models can be utilized to describe $|\eta^*(\omega)|$ functions of REX-PLA and REX-PLA/nano-SiO_2 composites, the double logarithmic slope $d\log|\eta^*(\omega)|/d\log\omega$ as a function of ω were plotted in *figure 7.8.*

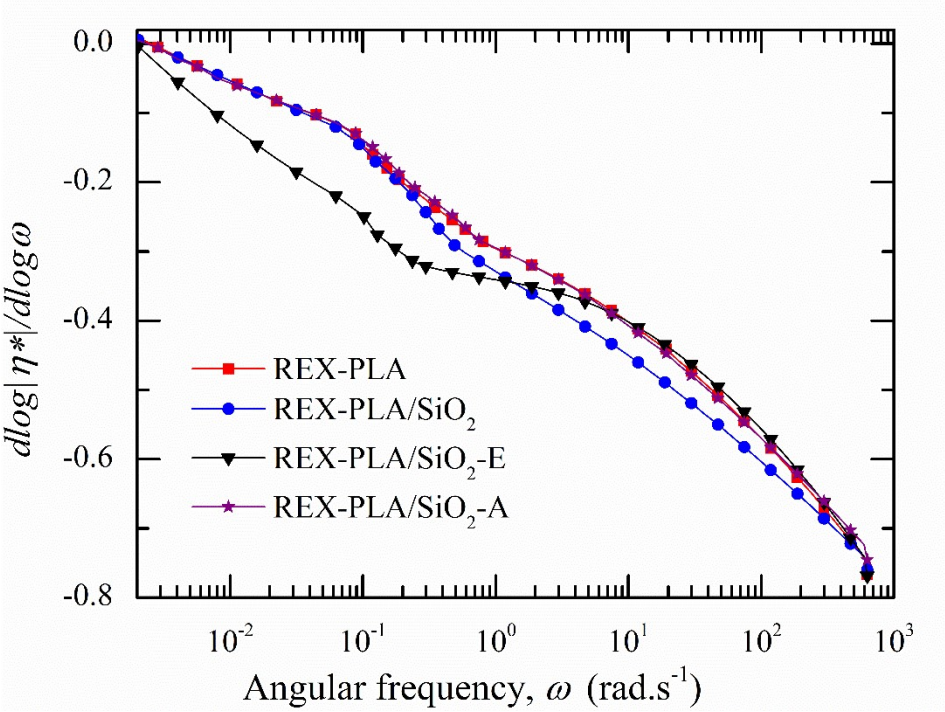

Figure 7.8. *Double logarithmic derivative of the viscosity functions of REX-PLA and REX-PLA/nano-SiO_2 composites.*

It was recommended by Cailloux (2015) that the double logarithmic slope $d\log|\eta^*(\omega)|/d\log\omega$ has to monotonously increase with decreasing ω for the fitting to hold. From *figure 7.8*, it was observed that $d\log|\eta^*(\omega)|/d\log\omega$ of REX-PLA and REX-PLA/nano-SiO_2 composites increase with decreasing ω which would indicate that the CY-Ext models can

be used to fit $|\eta^*(\omega)|$ data. It was also observed that all the investigated samples exhibited double curvature within the transition region between the terminal and pseudo-plastic region which also corroborates the assumption of thermorheologically complex behaviour of REX-PLA/nano-SiO_2 composites. Henceforth, the CY-Ext model fitting was performed with *figure 7.9* demonstrating the general trace of $|\eta^*(\omega)|$ functions which display two separated relaxation processes in the transition region with the different parameters of *equations 7.1*. The computed parameters are listed in *table 7.4* while the outcome of CY-Ext fitting of PLA, REX-PLA and REX-PLA/nano-SiO_2 composites are illustrated in *figure 7.10.*

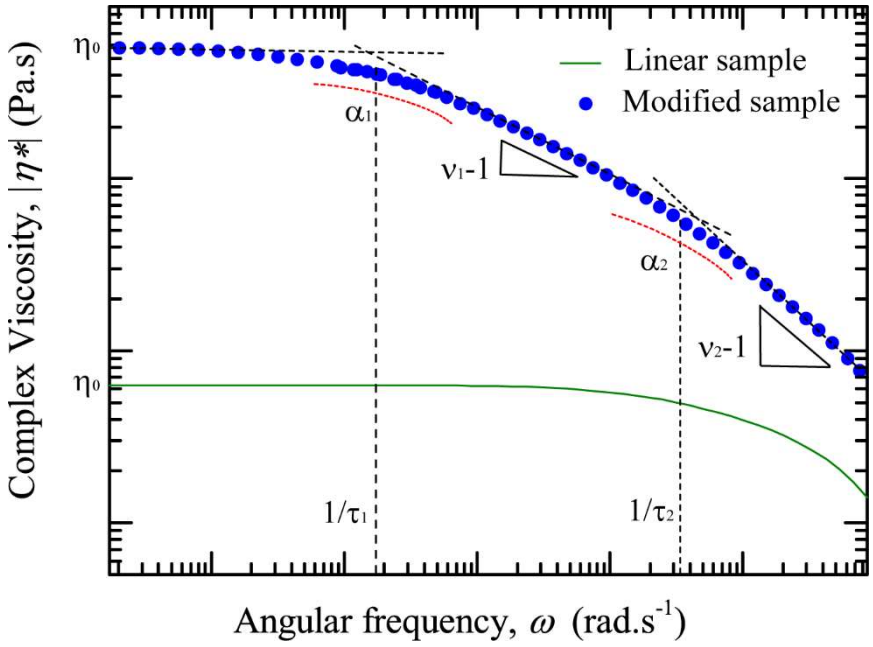

Figure 7.9. *General representation of $|\eta^*(\omega)|$ functions demonstrating two types relaxation regimes within the transition zone. Parameters computed in the Carreau Yasuda Extended model is stated within the graph.*

Table 7.4. *Numerical results of the Carreau-Yasuda Extended model fitting at 180 °C.*

Sample Nomenclature	η_0 (kPa.s)	τ_1 (s)	α_1	ν_1	τ_2 (s)	α_2	ν_2
PLA	2.8	$7.9.10^{-3}$	0.656	1.850	-	-	-
REX-PLA	35	13.997	1.526	0.842	0.137	5.253	1.044
REX-PLA/SiO_2	58	47.495	1.959	0.932	0.905	5.939	0.386
REX-PLA/SiO_2-E	28	26.619	2.401	0.892	0.040	3.757	0.593
REX-PLA/SiO_2-A	34	12.180	2.025	0.881	0.159	4.114	0.541

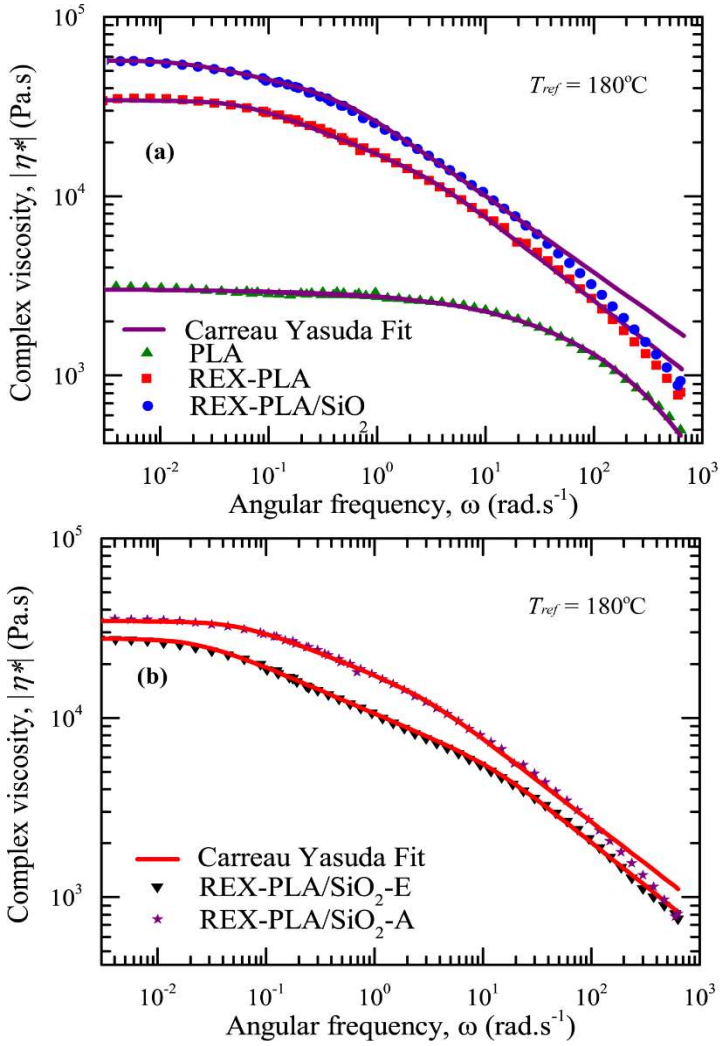

Figure 7.10. *Master curve of complex viscosity functions for (a) PLA, REX-PLA and REX-PLA/SiO_2 and (b) REX-PLA/SiO_2-E and REX-PLA/SiO_2-A samples at a reference temperature of 180 ºC. Solid lines are Carreau Yasuda model predictions according to equation 7.1.*

As displayed in *table 7.4,* the first relaxation time (τ_1) increased significantly for REX-PLA and REX-PLA/nano-SiO_2 composites compared to PLA. These results suggest that the transition zone between the Newtonian and the power-law region was broadened due to the modification of the chain architecture achieved in the modified PLA matrix. It was also observed that REX-PLA/SiO_2 exhibited the highest τ_1 which concomitantly increases η_0 compared to the other samples. As has been discussed in the preceding paragraphs, this could possibly be attributed to possible "occluded volume" factor that may have hindered the reptation of the polymer chains in REX-PLA/SiO_2.

With regards to width of the first transition region curvature (α_1), all REX-PLA/nano-SiO_2 composites samples exhibit higher α_1 compared to PLA and REX-PLA samples. Additionally, addition of nano-SiO_2 also seems to decrease the values of v_2 which could imply that $|\eta^*(\omega)|$ was more shear-sensitive in REX-PLA/nano-SiO_2 composites. These aforementioned trends could be attributed to the modification of the molecular mobility due to the presence nanoparticles in the modified PLA matrix.

However, inferences about the higher order structures and degree of dispersion of the filler cannot solely be deduced from *figure 7.10*. Several researchers have suggested the use Cole–Cole plots to observe the modifications of the relaxation behaviour of polymer composites due to presence of higher order filler structures (Ábrányi et al., 2006; Khan et al., 2011; Zhu et al., 2010). In the Cole-Cole plot, the imaginary part of complex viscosity (η'') is plotted against its real component of complex viscosity (η'). The plot should be a perfect arc if higher order structures are absent, and the relaxation behaviour of the melt can be described by a single relaxation time (Cole and Cole, 1941; Havriliak and Negami, 1966). On the other

hand, the presence of higher order structure due to formation of filler inter-network could broaden the relaxation time spectrum leads to a formation of a second arc, whereas formation of aggregates may result in the appearance of a tail (Ábrányi et al., 2006; Zhu et al., 2010). Thus, the Cole–Cole plots of PLA, REX-PLA and REX-PLA/SiO_2 nanocomposites are plotted in *figure 7.11*.

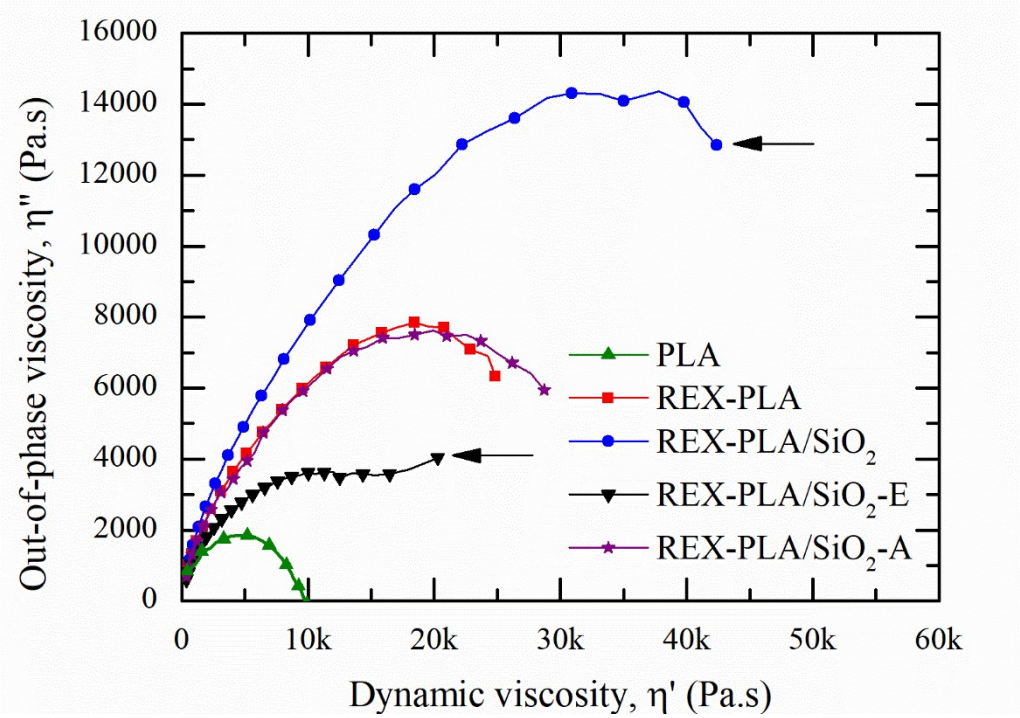

Figure 7.11. *Cole-Cole representation of PLA, REX-PLA and REX-PLA/SiO_2 nanocomposites. Arrows indicate presence of either an upturn or tail.*

Based on the Cole-Cole representation, it is observed that for PLA were arc-like and the relaxation process were extremely short. This trend suggest that PLA sample is displaying behaviour similar to a linear polymer. However, SAmfE presence seems to shifts the Cole-Cole plot of REX-PLA to higher values of η' and η'' that leads to formation of a skewered arc. This trend verifies presence of a higher order structures from

the modification of the molecular topology achieved in REX-PLA as has been reported by Cailloux et al. (2015) and Corre et al. (2011a).

Addition of SiO_2 sees a significant increase in both η' and η'' in the Cole–Cole plot of REX-PLA/SiO_2 nanocomposite that resulted in an appearance of a second arc (indicated with an arrow). The upturn might indicate the presence of two relaxation mechanisms as a result of the high number of SiO_2 aggregates formation and greater heterogeneity within the REX-PLA matrix, stemming from the incompatibility which correlates well with the inference made in complex viscosity versus ω analysis. The significant increase of η' and η'' compared to REX-PLA could be caused by formation of filler–network structure instead of SiO_2 -polymer tethering. The SiO_2-polymer interaction which is determined by the dispersive component of SiO_2 particle surface energy is lower than the inter-particle interaction which is supported by polar silanol groups. Consequently, the poor compatibility with the polymer and the strong filler-filler interaction due to high surface activity lead to a more developed filler network. Thus, a probable higher order structure (a filler–network structure) may have been present as has been similarly observed by Zhu et al. (2010).

In contrast, presence of SiO_2-E reduces η'' and η' when compared to REX-PLA. The appearance of a second arc (also indicated by an arrow) which is also apparent in Cole-Cole plot of REX-PLA/SiO_2-E. The existence of the second arc which could be interpreted as presence of aggregates due SiO_2-E particles tendency to adhere to one another despite being surface-functionalized. The surface activity of SiO_2-E were modified by surface treatment which reduce the concentration of high energy sites that should have weakens the interaggregate interactions and promotes SiO_2-E-polymer interactions. Even though it was

suggested that in the previous section that probable reaction between epoxide remnant group in the modified PLA matrix and -OH moieties in the silanol group may have taken place, FT-IR analysis has indicated otherwise (*c.f.*, *Chapter 7; Section 7.1.3*). Due to these poor interactions, the tendency for SiO_2-E to form particles cluster becomes greater hence the appearance of second arc in Cole-Cole plot.

On the other hand, presence of SiO_2-A generated almost similar η'' and η' values of Cole-Cole plot as REX-PLA. However, no tail was observed in the Cole-Cole plot. Favourable interaction between amino group from SiO_2-A and epoxy group from SAmfE seems to contributes to a better filler dispersion which is directly evident from absence of a tail. However, the postulated interactions between SiO_2-A and REX-PLA chain does not seem to highly restrain the movements of chain segments hence reinforcing effects of homogenous filler dispersion was not immediately evident from the Cole-Cole plot.

7.2.3. Effect of surface modification on the nano-SiO_2 particles dispersion in the REX-PLA matrix

The mechanical properties of nanocomposites are highly influenced by the degree of dispersion of nano-SiO_2 in the nanocomposites. Thus, REX-PLA/nano-SiO_2 composite films were investigated using TEM to examine the effect of surface functionalization on dispersion of nano-SiO_2, are shown in *figure 7.12.*

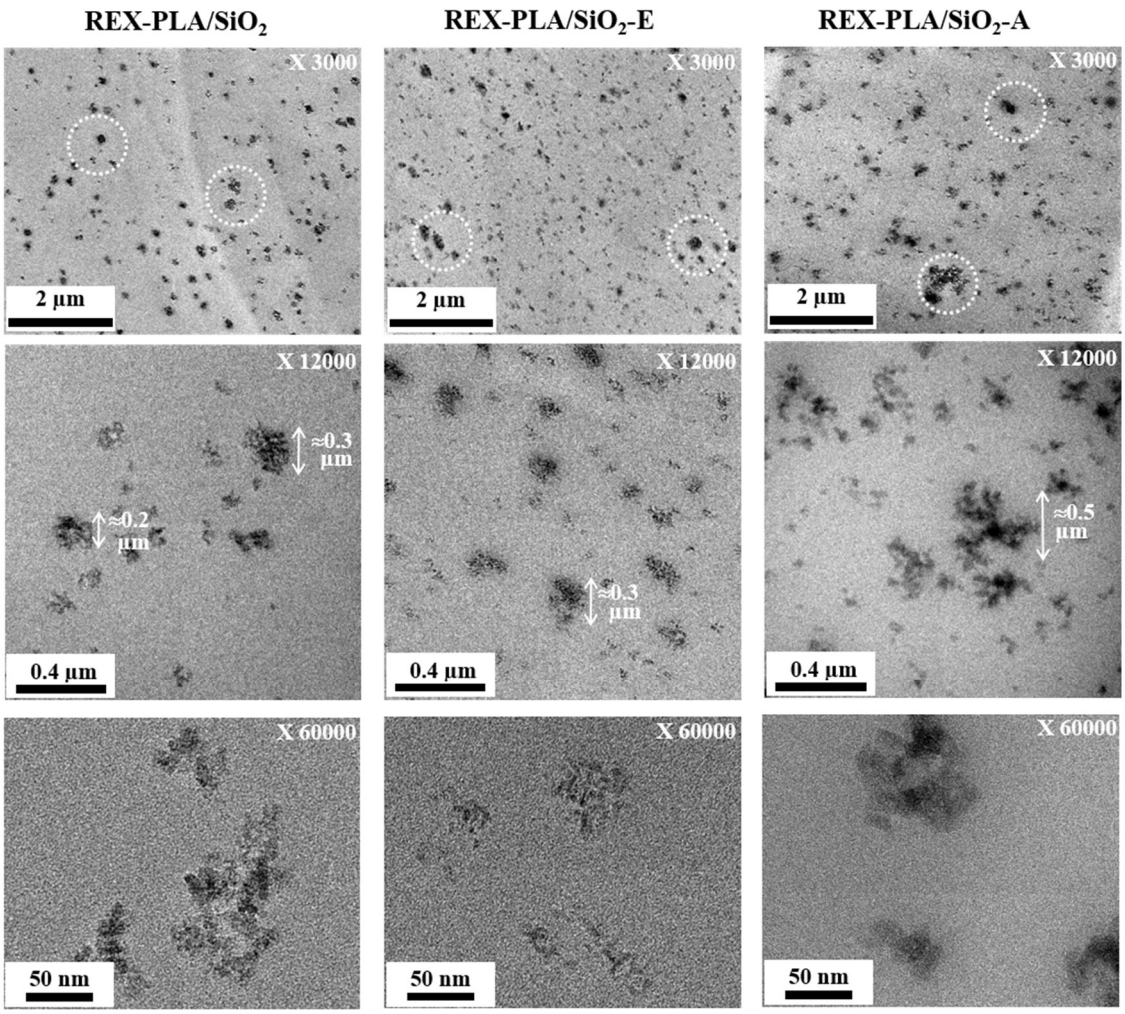

Figure 7.12. *Effect of surface functionalization of SiO_2 on the nano-SiO_2 dispersion for REX-PLA/nano-SiO_2 composites as observed with TEM at the indicated magnification. The micrographs are arranged from low to high magnification.*

At lower magnification (*i.e.* x3000), the micrographs of all the nano-SiO_2 types investigated suggest a relatively homogeneous and sub-micro nano-SiO_2 dispersion in the REX-PLA matrix was observed. However, the formation of aggregates (indicated by white dashed circles) cannot be denied due to strong cohesive forces prevailing among nano-SiO_2 particles from the hydroxyl groups. Additionally, the incompatibility of REX-PLA matrix and

nano-SiO_2 due to hydrophobicity-hydrophilicity mismatch (*c.f. Chapter 5; Section 5.6*) may also have consequently contributed to this trend.

As expected, REX-PLA/SiO_2 exhibits clearly aggregates ranging from 200 - 300 nm due to the high polarity of the surface –OH groups which could form due to hydrogen bonds. In its pristine state, SiO_2 itself exist as fractal clusters. However even at relatively low concentration (*i.e.* 2.5 wt. %.), these individual SiO_2 clusters start to attach itself each other primarily due to hydrogen bonding between the silanol groups on the particle surface resulting in a dense aggregation. For this reason, nano-SiO_2 aggregates is present and it will be very difficult to break down during processing even when high shear rates are employed as in the reactive extrusion unless all the surface –OH groups can be replaced with other functional groups.

It is found that surface functionalization does not entirely prevent formation nano-SiO_2 aggregation. However, epoxy functionalization of SiO_2 have shown improved SiO_2 dispersion with a lower number of aggregates comparing with REX-PLA/SiO_2. Nevertheless, aggregates in REX-PLA/SiO_2-E with similar sizes of about 300 nm is still present which is probably due to the poor miscibility between SiO_2-E and REX-PLA matrix due to hydrophobic-hydrophilicity mismatch. Similar observations can be seen for REX-PLA/SiO_2-A. Even with amino functionalization of SiO_2, aggregates are still present in the REX-PLA matrix. However, aggregates in REX-PLA/SiO_2-A with slightly larger size of about 500 nm can be seen at X12 000 magnifications.

These phenomena may be related to the fact that during REX-calendering process, REX-PLA matrix may have been chemically grafted onto SiO_2-E and SiO_2-A particles, which have either epoxy and NH_2 groups on their surface. Due to this, a layer of crosslinked molecules may have surrounds these clusters of aggregates encapsulating them within the matrix itself and are therefore not dispersible anymore since they are already chemically bonded.

To substantiate the chemical grafting of REX-PLA chains on surface-treated nano-SiO_2, the topography of the cryo-fractured surfaces of REX-PLA/nano-SiO_2 composites is of particular interest. *Figure 7.13* shows SEM micrographs of the cryo-fractured surfaces of REX-PLA/nano-SiO_2 composites. As shown in the figure below, cohesive interactions between both surface-modified SiO_2 types and the REX-PLA matrix is evident on the cryogenically fractured surface of REX-PLA/SiO_2-E and REX-PLA/SiO_2-A formulations, suggesting SiO_2-polymer tethering. However, similar interactions were absent on the fractured surface of REX-PLA/SiO_2 samples suggesting poor filler-polymer interactions.

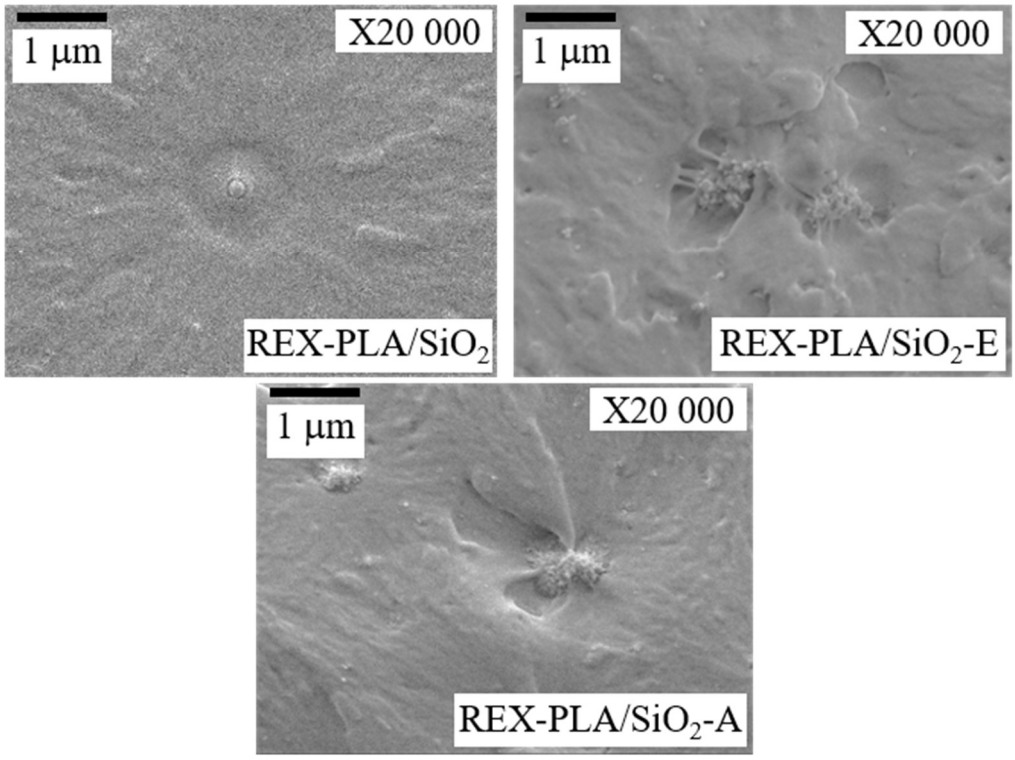

Figure 7.13. *SEM micrographs of the cryo-fractured surfaces of REX-PLA/nano-SiO_2 composites.*

7.2.4. Effect of nano-SiO_2 addition on the thermal behaviour of modified PLA composites.

The thermal behaviour of REX-PLA and REX-PLA/nano-SiO_2 composites were investigated using DSC measurements. The first heating, cooling scans and second heating are shown in *figure 7.14 (a), (b) and (c)*, respectively. Midpoint glass transition temperature (T_g), cold-crystallization temperature (T_{cc}), cold-crystallization enthalpy (ΔH_{cc}), melting temperature (T_m), melting enthalpy (ΔH_m), crystallization temperature onset ($T_{c,0}$), crystallization temperature (T_c), crystallization enthalpy (ΔH_c) and the degree of crystallinity (X_c) results derived from DSC analysis are compiled in *table 7.5.*

From *figure 7.14 (a),* it can be seen that T_g remained unaffected within the experimental error of the measurements upon heating regardless of the incorporation of SiO_2 particles. In contrast, T_{cc} were shifted to lower temperatures for REX-PLA/nano-SiO_2 composites irrespective of the SiO_2 type. This behaviour is commonly attributed to the presence of solid particles with high surface area, actuating as nucleating agent throughout heating as similarly reported by Wen et al. (2009). Regarding the melting transition, any significant differences between all the formulations have not been observed. However, all samples displayed a small exotherm [indicated by an arrow in *figure 7.14 (a)*] prior to a dominant melting peak that featured two overlapped endotherms (marked as 1 and 2). Numerous authors attributed this exothermic signal to the α'-to-α transition of the α'-crystals generated during the cold crystallization process. While the double melting peak is usually associated to the melt-recrystallization mechanism (Di Lorenzo, 2006; Pan et al., 2007). According to the reactive extrusion conditions used in this study, the addition of SiO_2 with different surface treatment did not modified the amorphous state of the manufactured films as reported in *table 7.5*.

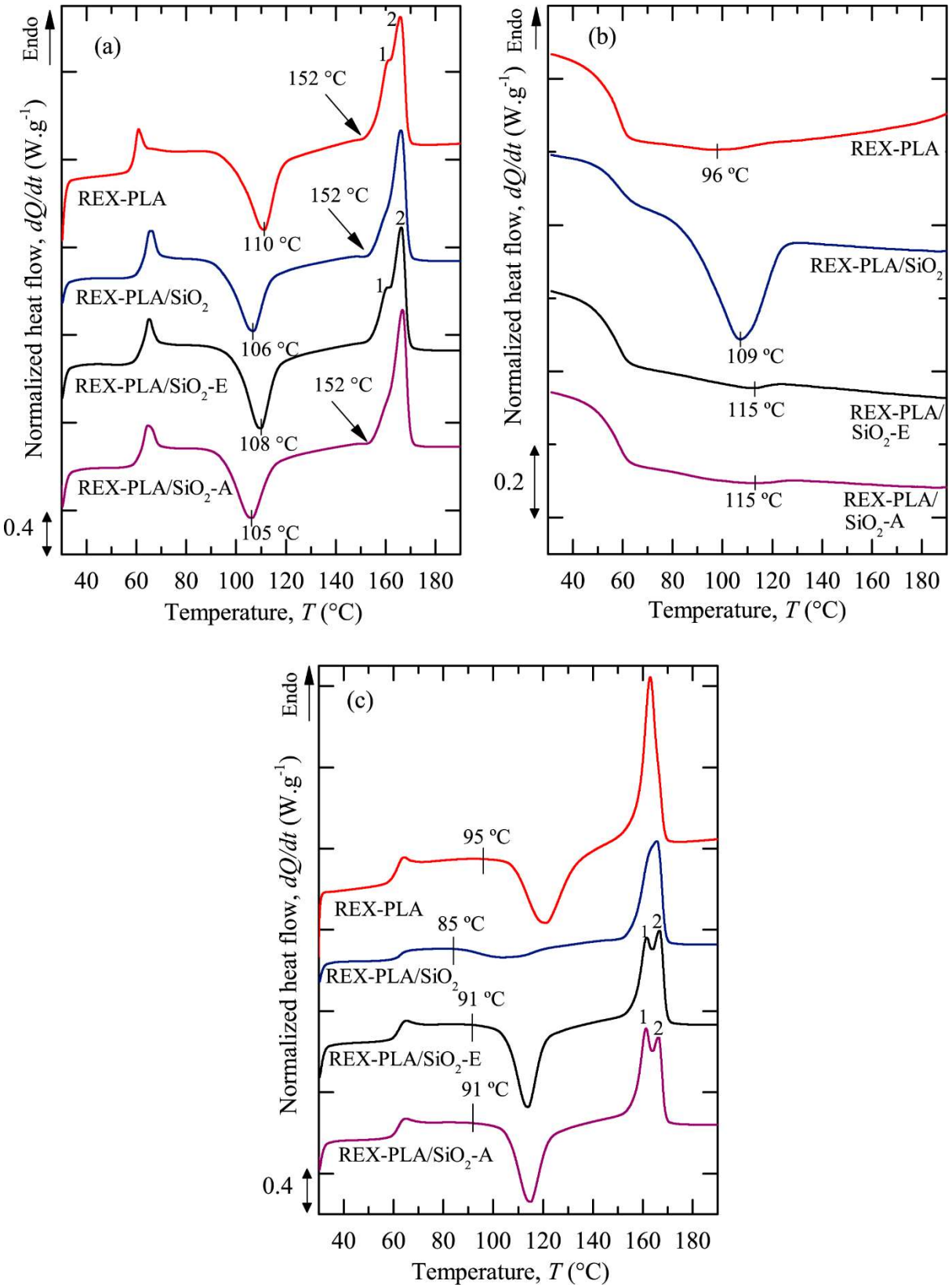

Figure 7.14. *DSC (a) first heating (b) cooling scan and (c) second heating at 10 °C.min*$^{-1}$ *for all investigated samples.*

Table 7.5. *Comparative thermal properties from the first DSC heating and cooling scans, respectively.*

	Parameters	REX- PLA	REX-PLA/ SiO_2	REX-PLA/ SiO_2-E	REX-PLA/ SiO_2-A
1st Heating	T_g	62 ± 2	63 ±2	63 ±2	62 ±2
	T_{cc} (°C)	109.7 ±0.4	106 ±1	108.3 ±0.9	105 ±1
	ΔH_{cc} (J g^{-1})	29 ±1	28 ±3	29 ±0.9	27 ±2
	T_{mp1} (°C)	160.6 ±0.6	166.2 ±0.1	161 ±0.2	166.8 ±0.4
	T_{mp2} (°C)	165.3 ±0.1	n/a	166.4 ±0.3	n/a
	ΔH_m (J g^{-1})	31 ±1	29 ±1	29.0 ±0.3	30 ±1
	X_c [b] (%)	1 ±1	1 ±1	0 ±1	3 ±1
Cooling	T_g (°C)	61.7 ±0.5	63 ±1	63.4 ±0.7	62 ±1
	$T_{c,0}$ (°C)	123.0 ±0.2	130.4 ±0.6	125.2±0.3	130.3 ±0.3
	T_c (°C)	96.3 ±0.3	109 ±1	115.1±0.5	115.4 ±0.5
	ΔH_c (J g^{-1})	2 ±1	25±2	2.0±0.2	2.6±0.4
	X_c (%)	1 ±1	26 ±1	1 ±1	1 ±1
2nd Heating	T_g	60.9 ± 0.2	61.2 ±0.1	60.3 ± 0.1	60.3 ± 0.3
	T_{cc} (°C)	112.8 ±0.1	106.2 ±3.3	114.5 ±0.3	113.4 ±0.4
	ΔH_{cc} (J g^{-1})	22 ±2	7 ±1	32 ±1	32 ±1
	T_{mp1} [a] (°C)	165.5 ±0.2	165.0 ±0.1	161.2 ±0.1	160.9 ±0.4
	T_{mp2} [a] (°C)	n/a	n/a	165.8 ±0.1	166.0 ±0.2
	ΔH_m (J g^{-1})	35 ±1	37 ±1	35 ±1	35 ±1
	X_c (%)	14 ±1	32 ±3	4 ±2	3 ±1

[a] *Temperature of the first (T_{mp1}) and second (T_{mp2}) melting peak, respectively.*
[b] *Crystallinity calculated by considering an enthalpy of 93.6 J.g^{-1} for 100% crystalline PLA.*

Under controlled cooling rate, REX-PLA exhibits a weak crystallization exotherm, as shown in *figure 7.14(b).* This behaviour could be attributed to the slow kinetics of crystallization exhibited by PLA resins, as already reported elsewhere.(Miyata and Masuko, 1998; Pan et al., 2007). Irrespective of the SiO_2 type, $T_{c,0}$ shifted to higher temperatures with the addition of the nanofillers. These results suggest that SiO_2 particles could act as nucleation sites for REX-PLA, thus lowering the free energy barrier towards nucleation which enable crystallization at higher temperature upon cooling.

Regarding the crystallization process, it has been observed that the addition of both surface-treated SiO_2 did not seem to enhance PLA crystallization (*i.e.* presence of a weak and undefined exothermic signal). By contrast, a well-defined crystallization transition was observed with the addition of untreated SiO_2 nanofillers, thus drastically improving REX-PLA crystallinity (up to 19%). The observed trends may be due to two different effects. On one hand, the higher specific surface area exhibited by untreated SiO_2 particles as compared with surface-treated ones not only have act as heterogenous nucleants but also seems to accelerate the crystal growth of the modified PLA matrix. This may have resulted in the formation of a larger fraction of heterogeneous crystal nucleation sites and corresponding faster crystal growth rate resulting in an increase of ultimate crystallinity. On the other hand, the aforementioned SiO_2-polymer tethering reactions between REX-PLA and the surface treated SiO_2 nanofillers may have impede the macromolecular chain short-range transport movements thus suppressing crystallization observed in REX-PLA/SiO_2-E and REX-PLA/SiO_2-A.

Referring to *figure 7.14(c),* the midpoint T_g remained unaffected to presence of nano-SiO_2 for all the modified PLA composites at the second controlled heating scan (**H2)**, as shown in *table 7.5*. During the cold-crystallization process, it seems that $T_{c,o}$ of REX-PLA, REX-PLA/SiO_2-E and REX-PLA/SiO_2-A remained almost similar within the experimental error. It was found that surface modified SiO_2 does not significantly changes REX-PLA chain. Conversely, REX-PLA/SiO_2 sees a decrease of $T_{c,o}$.

Addition of SiO_2 cause the onset of the cold-crystallization temperature and T_{cc} shifted to lower temperatures for REX-PLA/SiO_2 samples which is in correlation with the preceding paragraphs. An improvement in the cold-crystallization ability with the presence of SiO_2 upon reheating is perceptible as shown in *table 7.5*. Similar trends were observed and discussed by Murariu et al. (2015) and Lai et al. (2015) in their PLA/SiO_2 nanocomposites. Both attributed this trend to the excellent nucleating nature of fumed silica used. The introduction SiO_2 increases the available nucleating sites which are likely to facilitate and concomitantly accelerate the crystallization process of REX-PLA/SiO_2 samples.

At the melting endotherm, both REX-PLA and REX-PLA/SiO_2 samples displayed a single melting endotherm peak. The single dominant melting endotherm observed in both REX-PLA and REX-PLA/SiO_2 samples hints that only a single population size of crystal is present. In contrary, both REX-PLA/SiO_2-E and REX-PLA/SiO_2-A displayed a well-defined double melting peak (marked as 1 and 2) which is consistent with the mechanism of melt-recrystallization. However in contrast to REX-PLA/SiO_2-E, the lower-temperature melting peak in REX-PLA/SiO_2-A is more dominant than the higher-temperature melting peak.

It is suggested that the melt-recrystallization in REX-PLA/SiO_2-E initially induced smaller and less perfect crystals which transforms successively into more stable crystal through the melt-recrystallization mechanism hence the more dominant higher-temperature melting peak. On the other hand, REX-PLA/SiO_2-A initially produced more developed and perfect crystals. However due to purported SiO_2-A-polymer tethering in REX-PLA/SiO_2-A, it is postulated that mobility and ability of chains to further melt and recrystallize the original crystals became suppressed. Thus, there are less recrystallized crystals that was newly

developed during the melt-recrystallization mechanism (reduced peak 2) compared to the original crystals melt.

7.2.5. Effect of nano-SiO_2 addition on the non-isothermal crystallization of modified PLA composites.

It is well known that PLA crystallization is a key issue during its large-scale production and many efforts were made by both academia and industry in order to tackle it. It is worth pointing out that the addition of the selected nano-SiO_2 fillers show nucleating effect for REX-PLA, which might enhance crystallization. Based on this premise and within the context of the of industrial production, a first trial to evaluate the non-isothermal crystallization behaviour from the melt of REX-PLA/nano-SiO_2 composites was carried out using the DSC technique. *Figure 7.15* shows the comparative DSC ramps at different cooling rates of REX-PLA and REX-PLA/nano-SiO_2 composites.

As shown in *figure 7.15*, both the position and the shape of the exothermic signal corresponding to the crystallization process depend on the cooling rate. With increasing cooling rate, the exothermic signal became wider and shifted towards lower temperatures. The observation is general for all the samples investigated regardless of the type of nano-SiO_2.

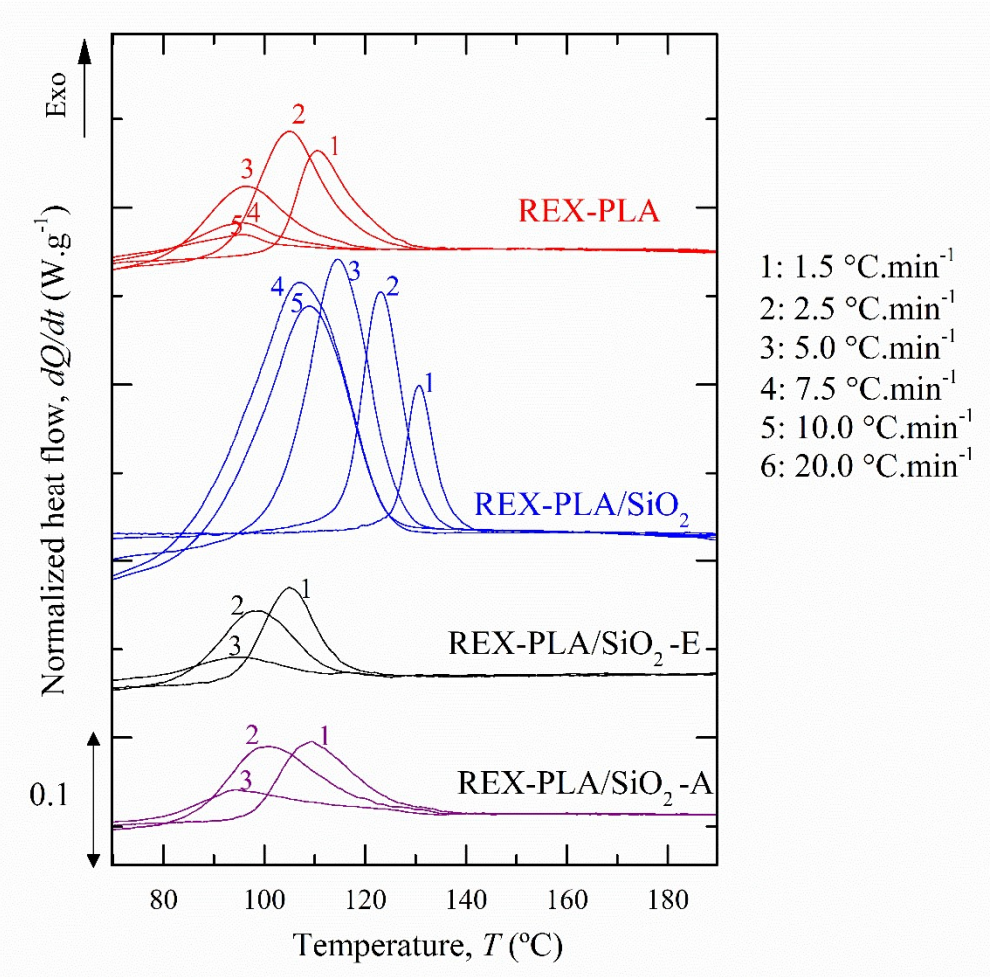

Figure 7.15. *Non-isothermal crystallization DSC traces at the indicated cooling rates (°C.min^{-1}) for all the formulations.*

As expected, REX-PLA exhibited solely crystallization exotherms at relatively slow cooling rates (*i.e.* 1.5, 2.5 and 5 °C.min^{-1}). This behaviour is in line with the results of the thermal analysis and can be principally attributed to the slow kinetics of crystallization exhibited by PLA resins. However, no significant differences were apparent between REX-PLA/SiO_2-E and REX-PLA/SiO_2-A formulations, as shown in *figure 7.15*,. Additionally, surface-treated SiO_2 addition seems to slightly reduce the crystallizability of the blends, since the intensity of the exothermic signal recorded at 5 °C.min^{-1} upon cooling from the melt was

reduced. Bearing in mind that REX-PLA chains might have been grafted onto surface-treated SiO_2 particles during processing, possibly minimizing the medium-range translation processes on the chain folding needed for crystallization.

In contrast, significant differences were observed in the crystallization behaviour of REX-PLA/SiO_2. That is, the cooling rate windows leading to REX-PLA crystallization is enlarged, the exothermic signals are better defined, the heat of the crystallization peaks increased and the peak temperatures shifted to higher temperature (for the corresponding cooling rate). This trend could be due to the inertness and high surface area of untreated SiO_2 particles behaves as centre of germination and nucleation thereby promoting nucleation of the modified PLA matrix and enhances the crystallization ability of REX-PLA.

In order to gain a better understanding of the effects of nano-SiO_2 addition on the non-isothermal crystallization of modified PLA composites, peak crystallization temperature, T_c and the proportion (percentage) of the crystalline fraction, X_c data were extracted from *figure 7.15*. Concomitantly, both T_c and X_c as a function of the applied cooling speed were plotted in *figure 7.16.*

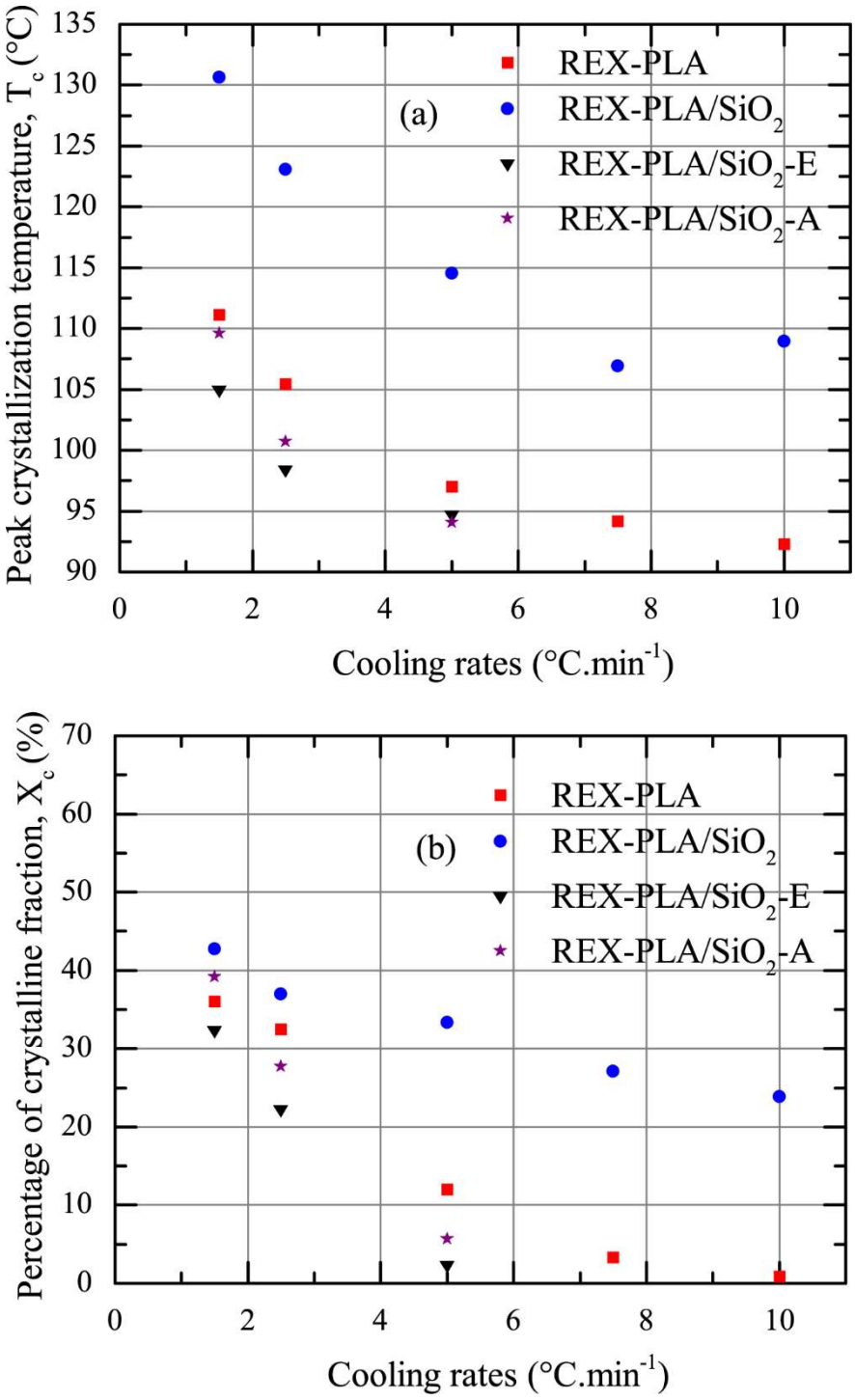

Figure 7.16. *Variation of cooling rate against (a) peak crystallization temperature and (b) percentage of the crystalline fraction of REX-PLA and REX-PLA/nano-SiO₂ composites.*

Independent of the types of nano-SiO_2, it is evident that both T_c and X_c decrease with increasing cooling rates as observed in *figure 7.16*. It is also noted that as cooling rates starts to increase to 5 °C.min^{-1}, the relative final crystallinity of REX-PLA/SiO_2 is still able to reach 34 %. On the other hand, relative crystallinity percentage of REX-PLA have drastically declined to ≈12 %. Comparably, similar decline in the relative crystallinity percentage achieved in REX-PLA/SiO_2-E and REX-PLA/SiO_2-A were observed (≈2 and ≈6 %, respectively). However at cooling rate 7.5 °C.min^{-1} and higher, it was observed REX-PLA/SiO_2-E and REX-PLA/SiO_2-A did not crystallize at all. Correspondingly, it is also observed that REX-PLA/SiO_2 samples also achieved the highest peak crystallization temperature and crystalline fraction compared to the other samples. Similar non-isothermal crystallization tendency were observed and discussed by Papageorgiu et al. (2010) in their PLA/SiO_2 nanocomposites. This observation suggest that in comparison to the surface-modified nano-SiO_2, non-modified SiO_2 have nucleated PLA crystallization more effectively and enhances the crystallization process of REX-PLA/SiO_2.

From *figures 7.16,* both REX-PLA/SiO_2-E and REX-PLA/SiO_2-A had the lowest T_c and X_c compared to other samples. This could also corroborates that the existence possible SiO_2 -polymer tethering could hinder the mobility of chains towards crystallization sites hence reducing the crystallizability of both REX-PLA/SiO_2-E and REX-PLA/SiO_2-A.

Another significant aspect to understand the influence of nano-SiO_2 in modified PLA matrix on crystallization is by determination of the "activation energy" of the crystallization process (ΔE) using well-defined model. For this study, this analysis was performed using Friedman model as has been previously elucidated in the preceding chapter (*c.f. Chapter 6;*

section 6.2.5). This analysis allows for direct comparison between different formulations and a clearer interpretation of the effect of nano-SiO_2 in modified PLA matrix.

A generic representation made according to the Friedman models proposed for a relative degree of conversion of 40% are illustrated in *Figure 7.17* while the calculated activation energy are listed in *Table 7.6.*

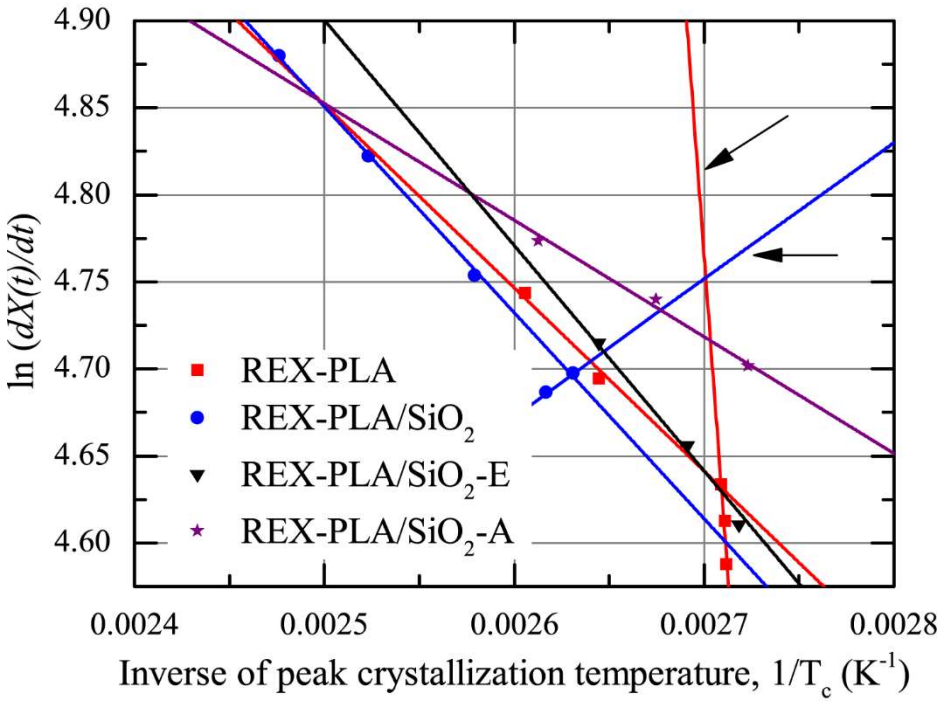

Figure 7.17. *The Arrhenius plot of natural logarithm of conversion rate versus reciprocal of peak crystallization temperature at relative conversion percentage of 40%. Arrows indicate Arrhenius plot of secondary crystallization in REX-PLA and REX-PLA/SiO_2.*

It is evident from *figure 7.17* that the fitting of the Friedman methods reveal the variable activation energy which is evident in REX-PLA and REX-PLA/SiO_2 sample. The representation of the Friedman model (relative isoconversion speed) for the REX-PLA and REX-PLA/SiO_2 sample formulation possess two slopes. This indicates that the process could not be described by a single activation energy due to the occurrence of secondary crystallization regime. However, it can be seen that REX-PLA/SiO_2-E and REX-PLA/SiO_2-A exhibit only primary crystallization regime.

Table 7.6. *Calculated activation energy of primary crystallization for REX-PLA and REX-PLA/nano-SiO_2 composites at relative conversion percentage of 20, 40, 60 and 80 %.*

Relative conversion percentage, X(t) (%)	Activation energy, ΔE (kJ.mol^{-1}.K^{-1})			
	REX-PLA	REX-PLA/SiO_2	REX-PLA/SiO_2-E	REX-PLA/SiO_2-A
20	-0.4	-7.3	-10.5	-4.4
40	-10.9	-9.2	-11.8	-6.9
60	-12.1	-11.5	-13.2	-9.1
80	-22.7	-15.3	-15.1	-11.3

The calculated values of ΔE of REX-PLA and REX-PLA/nano-SiO_2 composites as tabulated in *table 7.6* are negative which indicates that the rate of crystallization increases with decreasing T_c. The general trend observed in all the sample analyzed shows that ΔE increases with increasing relative crystallinity which indicates that it is more difficult for all samples to crystallize as the crystallization progresses. At relative crystallinity up 80%, the ΔE value of REX-PLA were approximately 33% higher compared to REX-PLA/SiO_2 and REX-PLA/SiO_2-E. As previously discussed, this could be due to the chain topology modifications in REX-PLA

may have hindered transportability factor of the polymer chains and encumbered crystalline growth.

With regards to nano-SiO_2, it was observed that ΔE value of REX-PLA/SiO_2-A were approximately 25% lower compared to REX-PLA/SiO_2 and REX-PLA/SiO_2-E. This trend confounded expectations because from the analysis in the preceding paragraphs it was anticipated that REX-PLA/SiO_2 would have yielded the lowest ΔE value. This analysis becomes ambiguous for these formulations (especially for REX-PLA/SiO_2-E and REX-PLA/SiO_2-A) due to the limited crystallization windows upon cooling from the melt which can lead to untrustworthy results (*i.e.* 1.5, 2.5 and 5 C.°min^{-1}). On this basis, isothermal crystallization analysis was favoured to investigate the effectiveness of nano-SiO_2 type on REX-PLA crystallization.

7.2.6. Effect of nano-SiO_2 addition on the isothermal crystallization of modified PLA composites.

Isothermal crystallization of REX-PLA, REX-PLA/SiO_2-E and REX-PLA/SiO_2-A were performed at a range of crystallization temperatures (T_c) varying between 120 to 112 °C are shown in *figure 7.18*. In view of the fact that SiO_2 nanoparticles displaced crystallization process to higher temperatures as observed in *figure 7.14 (b)* (*c.f. section 7.2.4*), the isothermal crystallizations of REX-PLA/SiO_2 were performed at higher range of T_c from 130 to 120 ºC and are also depicted in *figure 7.18.*

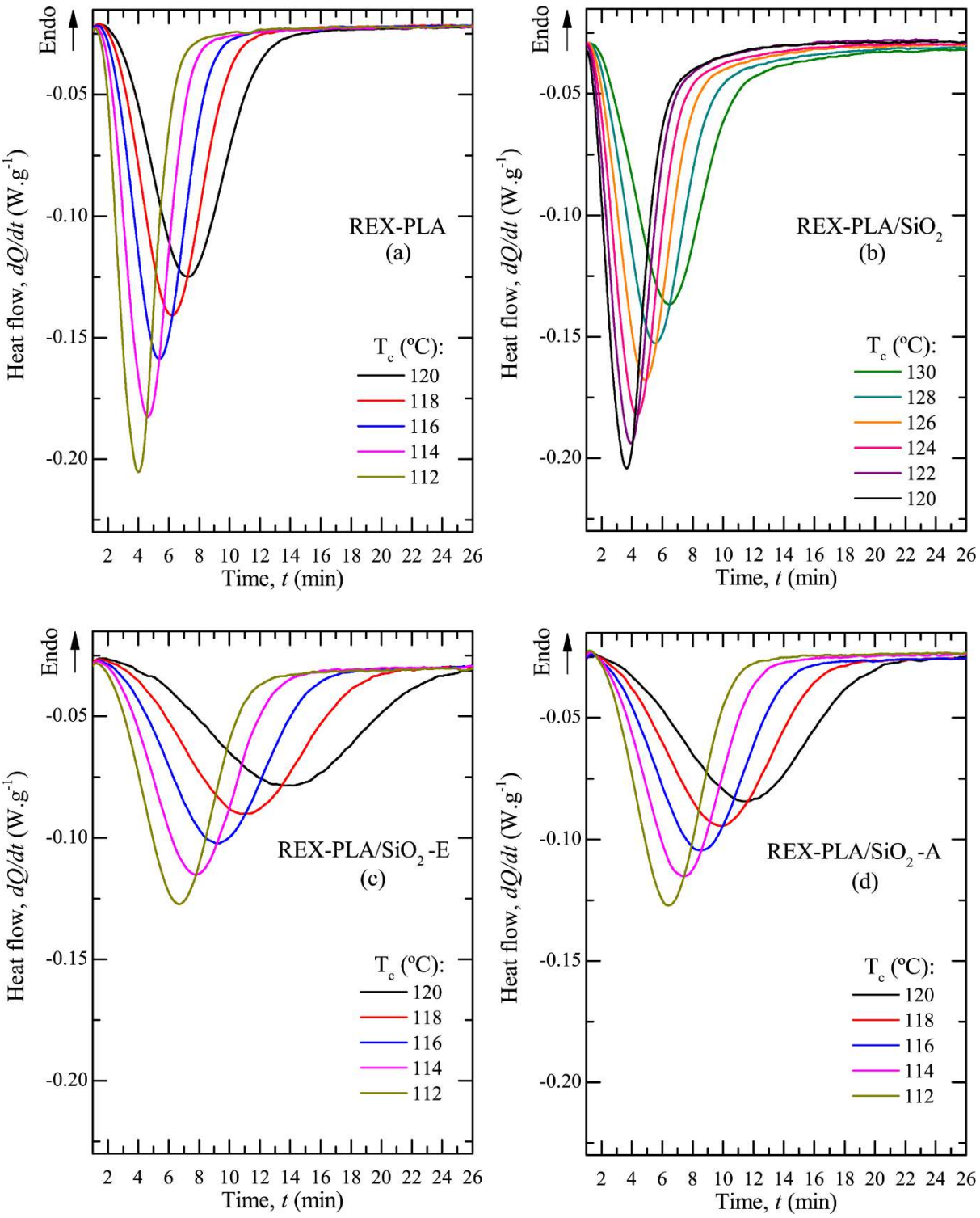

Figure 7.18. T*he isothermal crystallization exotherms of (a)REX-PLA, (b)REX-PLA/SiO₂, (c) REX-PLA/SiO₂-E and (d) REX-PLA/SiO₂-A as function of time at the indicated crystallization temperature (T_c).*

A general observation is that a monomodal exothermic signal at each T_c were observed for all the samples. The exothermic peak shifted to longer time and become broader with increasing T_c. This behaviour indicates that a longer time is necessary to complete crystallization with increasing T_c. Additionally, the exotherm enthalpy, as defined by the total exotherm area, seems to decrease with the addition of both surface-modified SiO_2 nanoparticles irrespective to the range of T_c. This trend suggests a decrease in the maximum X_c achievable for REX-PLA/SiO_2-E and REX-PLA/SiO2-A as compared to REX-PLA under this crystallization condition.

The relative crystallinity (X_t) was calculated using *equation 6.7 (c.f. chapter 6, section 6.2.6)*. *Figure 7.19* shows the computed relative degree of crystallization as function of time of all the samples at the indicated T_c.

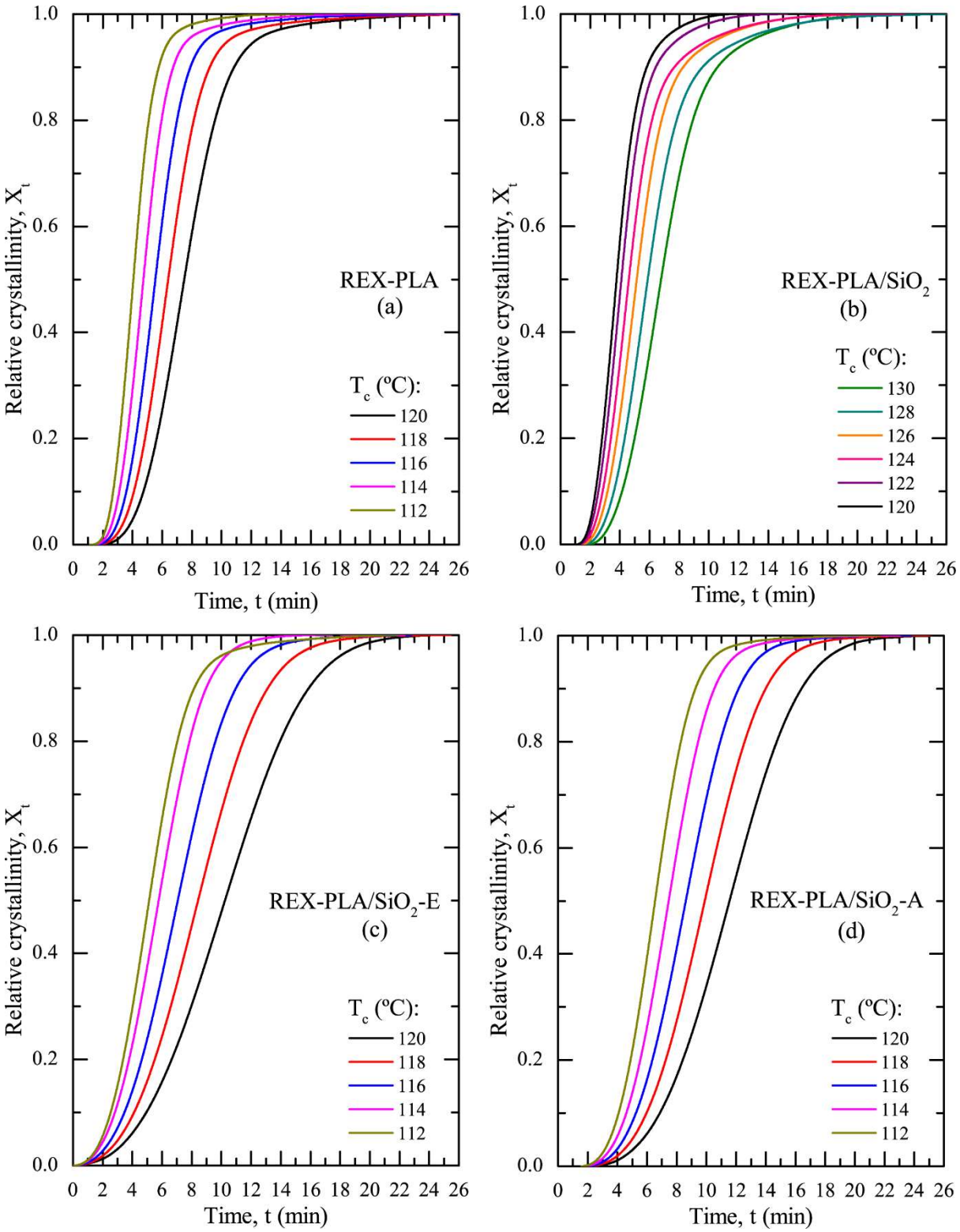

Figure 7.19. *The relative degree of crystallization of (a) REX-PLA, (b) REX-PLA/SiO_2, (c) REX-PLA/SiO_2-E and (d) REX-PLA/SiO_2-A as function of time at the indicated crystallization temperature (Tc).*

To investigate the efficacy of different SiO_2 types as heterogeneous nucleating agent on the overall crystallization rate, determination of $t_{0.5}$ (the elapsed time from the onset of the crystallization (t_0) to the point where the crystallization is 50% completed) was suggested by several researchers (Liao et al., 2007; Wang and Qiu, 2012). It can be derived directly from the relative crystallinity as a function of time plot. $t_{0.5}$ values derived from this graph for all the investigated samples are indicated by vertical dashed lines.. On the other hand, the overall crystallization rate, *G*, is defined as the multiplicative inverse of $t_{0.5}$, which is direct measure of the crystallization rate at the considered temperature (Kang et al., 2013). Di Lorenzo (2005) have established that the optimum crystallization rate of PLA were achieved between 100 and 120 °C under isothermal conditions.

For the sake of comparison, comparison of relative crystallinity versus time at T_c of 120 °C are shown in *figure 7.20*. To demonstrate clearer comparison between $t_{0.5}$, induction time (t_i) of all the investigated samples, defined as time before the start of crystallization which is indicative of the efficiency of the nucleating effect of nano-SiO_2 were omitted from the graph. Instead t_i, $t_{0.5}$ and *G* values derived from the analysis are tabulated in *table 7.7*.

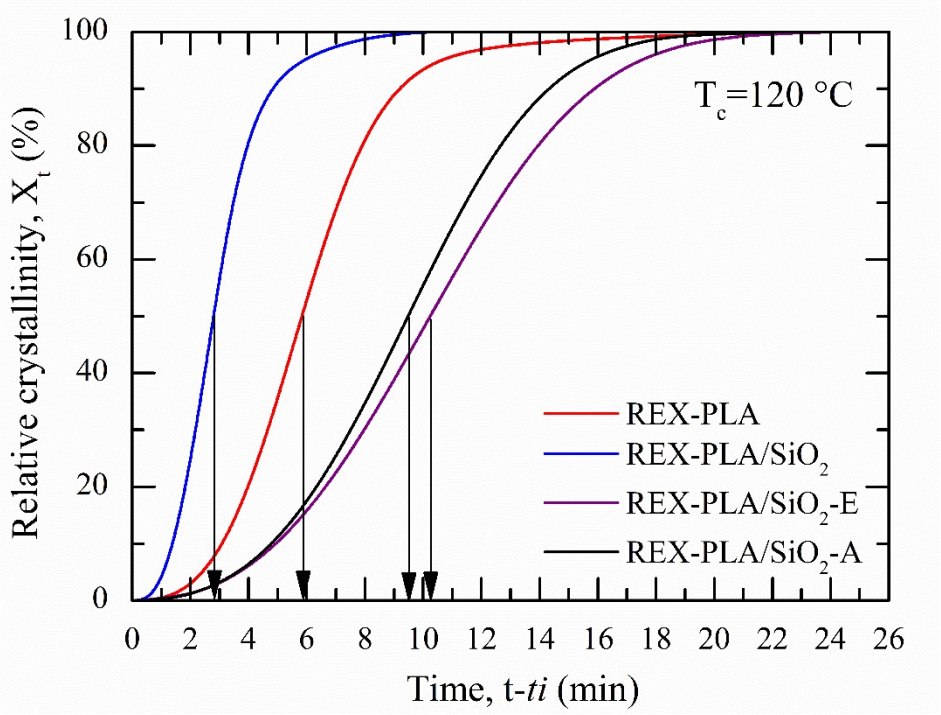

Figure 7.20. *Comparison of the relative degree of crystallization as function of time between all the formulations for isothermal experiments performed at T_c=120 °C. Arrows indicate $t_{0.5}$ of the respective samples.*

Table 7.7. *Comparison of t_i, $t_{0.5}$ and G values under isothermal crystallization at T_c = 120 °C.*

Sample Nomenclature	Induction time, t_i (min)	$t_{0.5}$ (min)	G (min^{-1})
REX-PLA	1.7	5.8	0.17
REX-PLA/SiO_2	1.0	2.8	0.36
REX-PLA/SiO_2-E	3.7	10.3	0.10
REX-PLA/SiO_2-A	2.1	9.5	0.11

The most striking result to emerge from *figure 7.20* and *table 7.7* is that REX-PLA/SiO_2 have the lowest t_i and $t_{0.5}$ value compared to the other samples. Comparing to REX-PLA, t_i and $t_{0.5}$ value of REX-PLA/SiO_2 (improved by 41 and 52%, respectively) while G were the highest indicating that it has the fastest overall crystallization rate. This trends suggest that the crystallization rate of REX-PLA/SiO_2 seems to be enhanced with presence of untreated SiO_2. Similar trends were observed by Bouaziz et al. (2014) in their PP/SiO_2 composites. This observed trend was attributed to the inertness and high surface area properties of untreated SiO_2 particles which behaves as centre of germination and nucleation. This in turn promoted the nucleation of the polymer matrix by inducing higher nucleation density under isothermal condition (Bouziz et al., 2014).

On the other hand, REX-PLA slower crystallization rate was principally attributed to the slow kinetics of crystallization exhibited by PLA resins. While possible SiO_2-polymer tethering reactions in both REX-PLA/SiO_2-E and REX-PLA/SiO_2-A could be responsible for confining or restricting the molecular ability of REX-PLA matrix to crystallize thus inhibiting crystallization rate. All these trends agree with previous results of non-isothermal crystallization analysis and the cooling scan discussed in the previous sections (*c.f. section 7.2.4 and 7.2.5*).

Even though several macrokinetic models such as Evans, Tobin, Malkin, Dietz and Nakamura models are available, Avrami model was deemed to be most suitable to quantitatively describe the evolution of the crystallinity versus crystallization time, *t* for the early stages of crystallization during isothermal crystallization (Supaphol and Spruiell, 2000). The Avrami equation has been introduced in the preceding *equation 6.8 (c.f. chapter 6, section 6.2.6)*.

Plots of log [-ln(1-X_t)] versus log *t* according to *equation 6.10 (c.f. chapter 6, section 6.2.6)* are shown in *figure 7.21* and Avrami parameters are listed in *table 7.8*. However, the linear form of the Avrami equation is inaccurate at both high and low extents of crystallization. Usually, non-linearity in the Avrami plot at low extent of crystallization can be attributed to the experimental errors during the first stages of the crystallization process cause by the slow stabilization of the equipment and the small quantity of heat evolved (Müller et al., 2016). For kinetics analysis, the rate of crystallization in this region may be neglected since the parameter is very low. However at high extents of crystallization, the non-linearity in the Avrami plot could be due to the secondary crystallization processes taking place (Lehmann and Karger-Kocsis, 2009). So in order to accurately analyze primary crystallization processes, only linear region (8 – 70%) in the Avrami plot were used in the analysis.

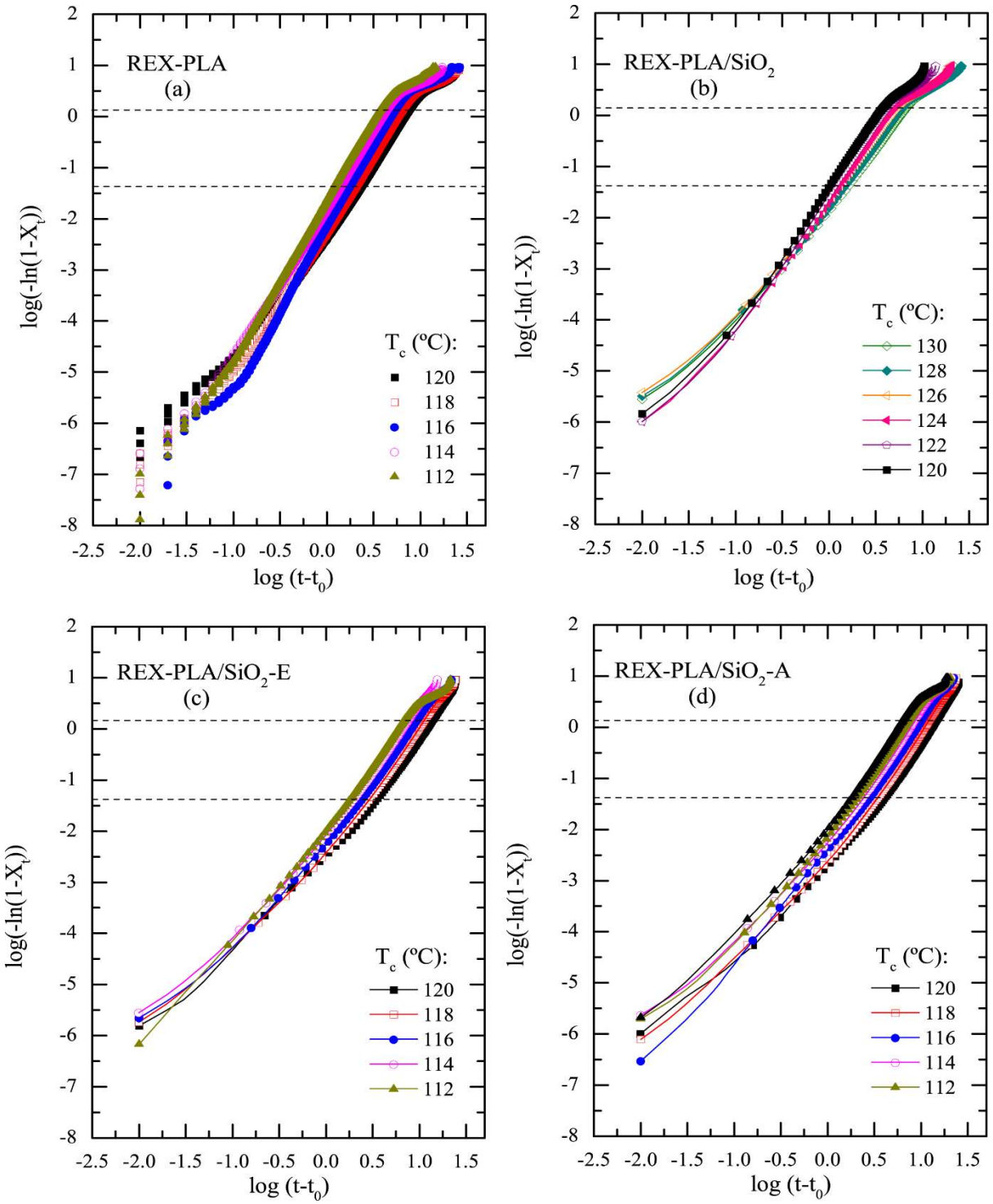

Figure 7.21. *Selected Avrami plots of (a) REX-PLA, (b) REX-PLA/SiO_2, (c) REX-PLA/SiO_2-E and (d) REX-PLA/SiO_2-A composites crystallized at different crystallization temperature. Experimental data between the dashed lines indicate the linear region that covers the relative conversion range between 8 and 70% that were analyzed in the Avrami plot.*

Table 7.8. *Kinetic parameters of the Avrami Analysis for Isothermal Crystallization REX-PLA and REX-PLA composites with nano-SiO_2.*

Material	T_c (°C)	n^a	$k^a.10^{-3}$ (min^{-n})
REX-PLA	120	2.97	3.41
	118	3.05	4.79
	116	3.10	7.24
	114	3.04	14.51
	112	3.04	25.01
REX-PLA/SiO_2	130	2.54	11.02
	128	2.56	14.46
	126	2.64	18.46
	124	2.71	21.09
	122	2.71	30.12
	120	2.65	41.86
REX-PLA/SiO_2-E	120	2.64	1.41
	118	2.68	2.15
	116	2.70	3.30
	114	2.69	5.83
	112	2.72	7.55
REX-PLA/SiO_2-A	120	2.82	1.14
	118	2.77	2.13
	116	2.79	3.13
	114	2.83	4.53
	112	2.82	7.00

[a] n and k value were calculated from plots of log [-ln(1-X_t)] versus log t.

n is a characteristic parameter which qualitatively describes the crystallization mechanism which in turn controls the morphology *i.e.* dimension of growth of the crystallites. In general, the trend shows that n values increase marginally to an extent with decreasing T_c. From the data in *table 7.8*, it can be observed that REX-PLA shows an Avrami exponent of $n \approx 3$, corresponding to prevalent spherical crystal growth morphology (Lehmann and Karger-Kocsis, 2009). While the n values for nanocomposites samples decreases to $2.5 < n < 2.8$ which is lower than those calculated for REX-PLA. An Avrami exponent of $2.5 < n < 2.8$, indicates crystal morphology of nucleation with two-dimensional crystal growth (Lehmann and Karger-Kocsis, 2009). Principally, the decrease of n value is explained by the basis of a modification in crystal growth mechanisms due to the addition of nano-SiO_2 (Papageorgiou et al., 2006).

Nano-SiO_2 causes spherulite growth impingement in REX-PLA, so that the growth form in spherulite mode become restricted leading to solely two-dimensional crystal growth hence lower values of *n*.

Avrami rate of crystallization constant, *k* is a kinetic constant which is dependent on *n* constant that provides insight on both nucleation and crystallization growth rate (min^{-1}). The computed *k* value of all the investigated samples are plotted in *figure 7.22*. Generally, the trend that can be observed for *k* value is that it increases with reducing T_c. From *table 7.8*, it can be observed that REX-PLA/SiO_2 displayed the highest *k* value when compared to the other investigated samples. The *k* values of REX-PLA/SiO_2 which are significantly enhanced are in the range 11.02 to 41.86 when compared to REX-PLA *k* values which is between 3.41 to 25.01. While *k* values of REX-PLA/SiO_2-A between REX-PLA/SiO_2-E are significantly lower and almost similar which is between 1.14 to 7.55.

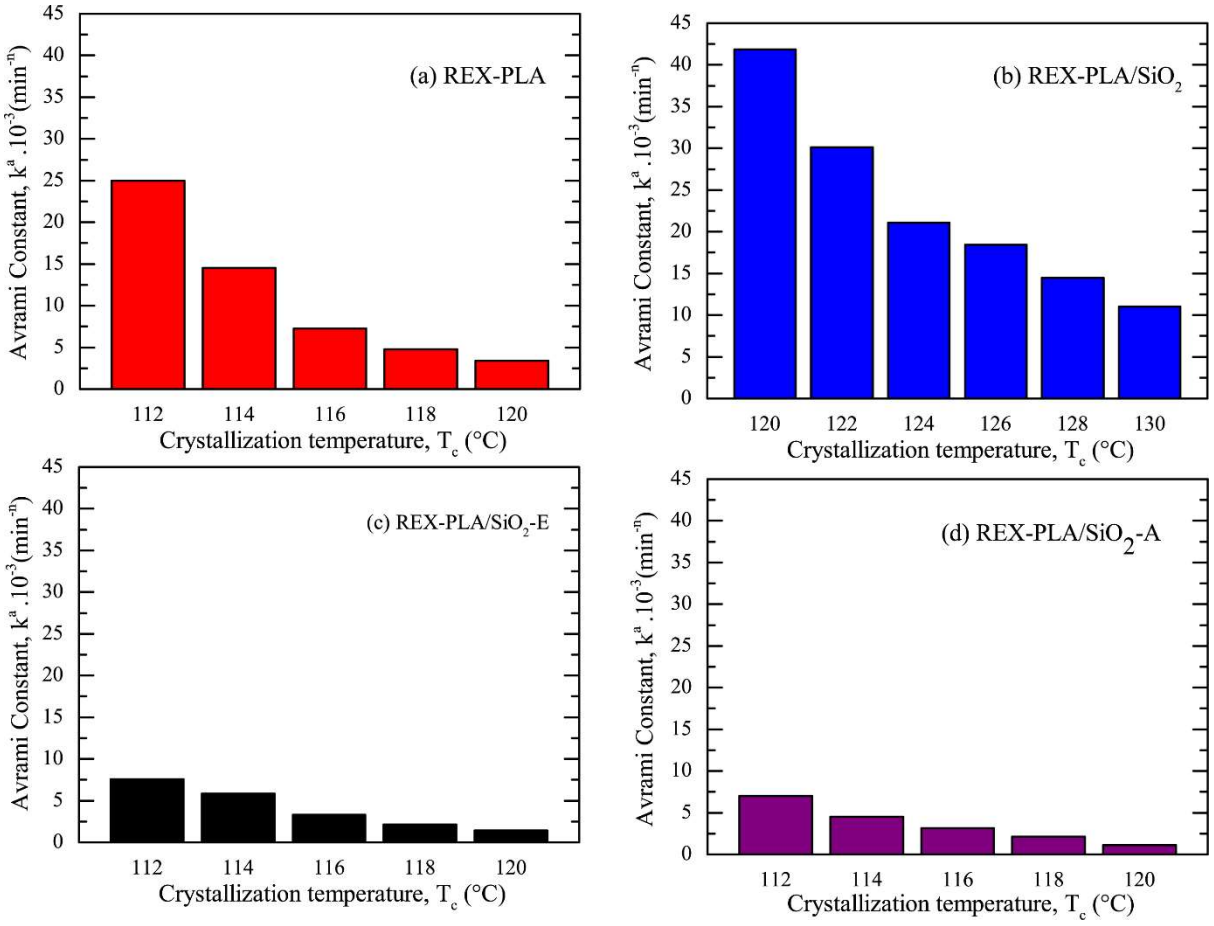

Figure 7.22. *Comparison of Avrami Constant, k of (a) REX-PLA, (b) REX-PLA/SiO₂, (c) REX-PLA/SiO₂-E and (d) REX-PLA/SiO₂-A composites.*

Apparent activation energy (E_c) gives insight about the rate of crystallization and ability of growth of chain segments (Hemlata and Maiti, 2012). If E_c is higher, then the rate of crystallization will be lower. The *n* value in *table 7.8* can be used to determine an apparent activation energy for crystallization during isothermal conditions, at intermediate degree of conversion. It is assumed that the crystallization rate constant (K) from *equation 6.10 (c.f. chapter 6, section 6.2.6)* is temperature dependent and have been expressed in the previous chapter as *equation 6.11(c.f. chapter 6, section 6.2.6).* Graph of $\ln[(K/n)]$ versus $1/T_c$ are plotted and shown in *figure 7.23* and all the relevant parameters are summarized in *table 7.9.*

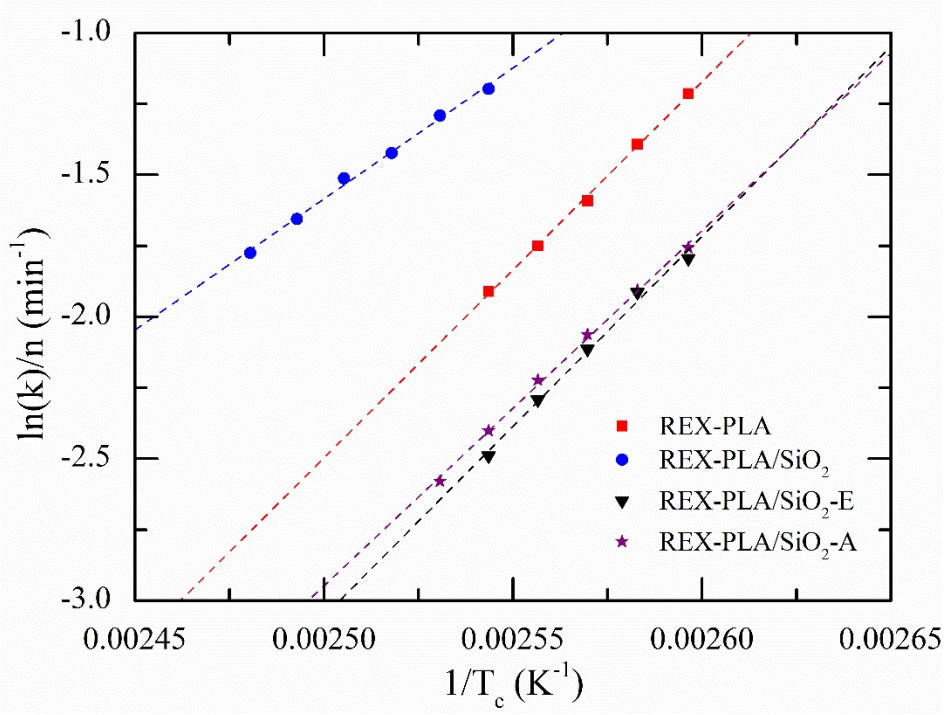

Figure 7.23. *Apparent activation energy determined from isothermal crystallization of REX-PLA and REX-PLA/nano-SiO_2 composites.*

Table 7.9. *Apparent activation energy, E_c and linear regression coefficient, R^2 calculated for isothermal crystallization of REX-PLA and REX-PLA/nano-SiO_2 composites.*

Nomenclature	Apparent activation energy, E_c (kJ.mol^{-1})	R^2
REX-PLA	141 ±2	0.999
REX-PLA/SiO_2	109 ±4	0.999
REX-PLA/SiO_2-E	143 ±8	0.990
REX-PLA/SiO_2-A	135 ±4	0.996

It can be observed that the R^2 values of REX-PLA and REX-PLA/nano-SiO_2 composites represents a very good fit and the apparent activation energy readings can be considered reliable. It can be seen that the addition of surface-treated nano-SiO_2 (i.e. REX-PLA/SiO_2-E =143 kJ.mol^{-1} and REX-PLA/SiO_2-A = 135 kJ.mol^{-1} respectively) does not significantly increase nor decrease E_c in comparison to REX-PLA. However, introduction of non-treated nano-SiO_2 sees a reduction of E_c value of approximately 24% to 109 kJ.mol^{-1}.

Generally, the lower the E_c value is, the higher the probability of the polymer melt to transform into a crystalline state (Run et al., 2007). In an isothermal crystallization conditions, E_c decreases with the presence of non-treated nano-SiO_2. Factors such as its high surface area and its chemical inertness towards REX-PLA matrix makes SiO_2 particles behaves as centre of germination and nucleation. This could have played a role to increase the density and rate of nucleation substrate, giving rise to a reduction in the apparent activation energy hence enhancing the crystallization rate during isothermal crystallization process.

However, REX-PLA/SiO_2-E and REX-PLA/SiO_2-A yield almost similar E_c values as REX-PLA (i.e. 141 kJ.mol^{-1}). Dissimilar to non-treated silica, this indicate that SiO_2-polymer tethering reactions of SiO_2-E and SiO_2-A were achieved (*c.f. figure 7.2 Scheme II and Scheme III*; *section 7.1.2*) and its interactions could have impeded the nucleation and growth of crystals. This however neither diminish nor enhance macromolecules segmental mobility by a significant margin which would affect the E_c values of its respective REX-PLA/nano-SiO_2 composites.

7.2.7. Effect of nano-SiO_2 addition on dynamic mechanical properties of modified PLA composites.

DMTA analysis was performed using a single cantilever bending mode to evaluate the effects of nano-SiO_2 addition on the dynamic mechanical properties of REX-PLA and REX-PLA/nano-SiO_2 composites. All of the analyzed samples have been subjected to 1 week of physical aging at room temperature to mimic the common industrial conditioning of these prepared sheets. The thermomechanical spectrum of REX-PLA and REX-PLA/nano-SiO_2 composites which were recorded from 30 to 120 ºC are depicted in *figure 7.24,* in the form of storage modulus, *E'* and the loss tangent, tan $\delta = E''/E'$ respectively. Meanwhile, loss modulus (*E''*) traces are shown in the appendix.

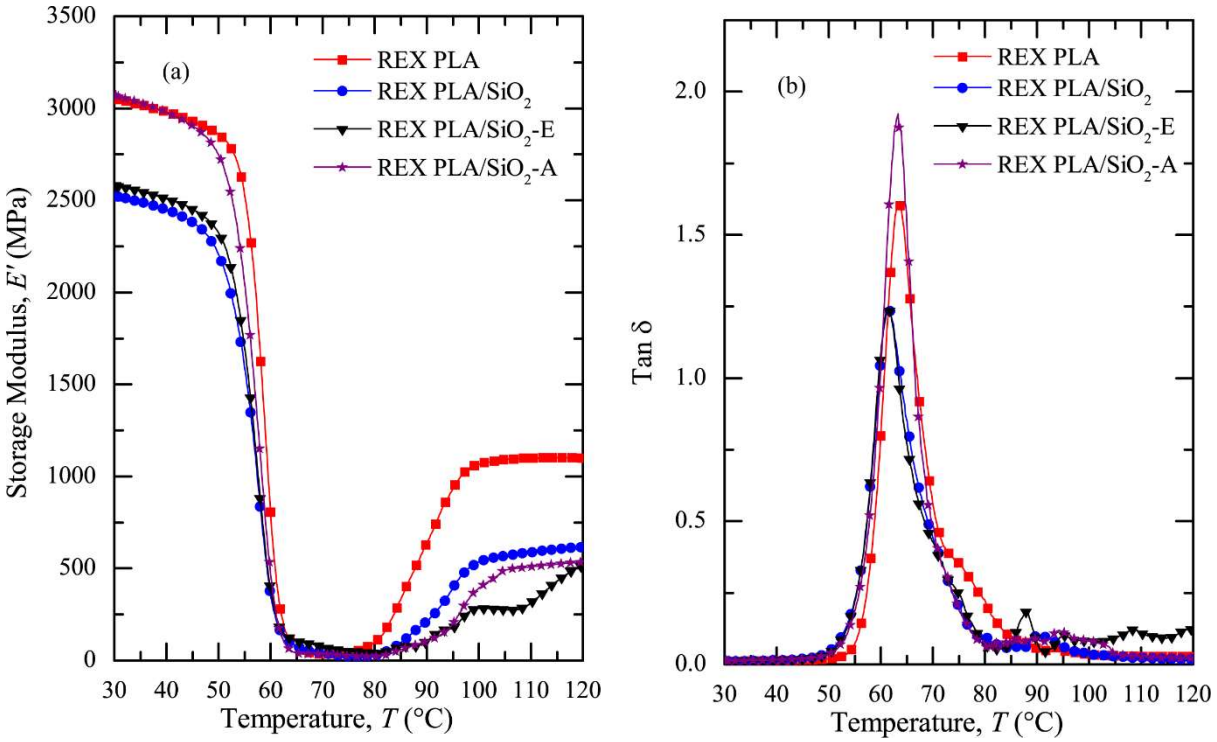

Figure 7.24.*(a) Storage modulus and (b) tan δ traces of REX-PLA and REX-PLA/nano-SiO_2 composites tested at 2 °C.min^{-1}.*

The following results will be derived from *figure 7.24* and *Table 7.10* tabulated the following results:

- The storage modulus at 30 ºC, $E'_{(30ºC)}$, and at 60 ºC, $E'_{(60ºC)}$, respectively
- The glass transition temperature, T_g. It was determined as the point where tan δ (referred to as T_g (tan δ)) and *E"* (referred to as T_g (*E"*)) reached a maximum, respectively.
- The drop percentage in *E'* between 30 and 60 ºC. It was calculated as per *equation 6.13 (c.f. chapter 6, section 6.2.7).* This parameter was studied in order to observe thermomechanical behaviours of the investigated materials as the testing temperature approach their respective glass transition temperature.
- Temperature at *E'* at 1.5 GPa that coincides with heat distortion temperature (HDT) of PLA.

Table 7.10. *DMTA parameters for REX-PLA and REX-PLA/nano-SiO_2 composites tested at 2°C.min^{-1}.*

Sample Nomenclature	$E'_{(30ºC)}$ (GPa)	$E'_{(60ºC)}$ (GPa)	Drop (%)	$E'_{(120ºC)}$ (GPa)	Maximum value of T_g (*E"*) (°C)	Maximum value of T_g (tan δ) (°C)	Temperature at *E'* at 1.5 GPa (°C)
REX-PLA	3.1 ±0.1	0.8 ±0.2	74.2 ±0.2	1.1 ±0.1	59.3 ±0.2	63.4 ±1.4	58.5 ±0.1
REX-PLA/SiO_2	2.5 ±0.1	0.3 ±0.2	88.0 ±0.2	0.7 ±0.1	58.2 ±0.3	61.7 ±1.8	55.5 ±0.1
REX-PLA/SiO_2-E	2.5 ±0.2	0.4 ±0.1	84.0 ±0.1	0.6 ±0.1	58.1 ±0.1	61.5 ±1.3	56.1 ±0.1
REX-PLA/SiO_2-A	3.1 ±0.3	0.5 ±0.2	83.9 ±0.1	0.6 ±0.1	58.0 ±0.2	63.3 ±1.2	57.0 ±0.1

Figure 7.24 reveals that REX-PLA and REX-PLA/SiO_2-A exhibit similar *E'* at 30 ºC within the statistical error for a given thermal history. However, addition of SiO_2 and SiO_2-E reduces the *E'* value at 30 ºC to 2.5 GPa. This trend could be attributed to an increase in the ability to dissipate energy through molecular motions due to the manifestations of the relatively

poor filler-polymer interactions between SiO_2 and SiO_2-E against polymer matrix. In the case of SiO_2, high concentration of surface -OH groups of SiO_2 made it chemically inert toward polymers. While for SiO_2-E as observed in the FT-IR analysis (*c.f. section 7.1.3*), little or minimal SiO_2-E-polymer tethering could have principally influenced the decrease in the *E'* value at 30 ºC.

The general pattern observed in glassy region (between 30 and 55 ºC) is that all the samples experienced a significant reduction that is reflected in the calculated $E'_{(60^{\circ}C)}$ values with increasing temperature. Comparing to the other samples, REX-PLA samples seems to exhibit the least amount of reduction. The increase in MW and formation of non-uniform branched structures brought about by SAmfE addition might have improved the calculated $E'_{(60^{\circ}C)}$ values.

Meanwhile, addition of nano-SiO_2 seems to exhibit a more pronounced decreased of calculated $E'_{(60^{\circ}C)}$ values. The calculated $E'_{(60^{\circ}C)}$ values of REX-PLA/SiO_2, REX-PLA/SiO_2-E and REX-PLA/SiO_2-A were reduced by 63 %, 50 % and 38% respectively in comparison to REX-PLA. It is well established that finer nano-SiO_2 dispersion and strong interfacial interactions between particles and polymer matrix will restrict the movement of matrix molecules that will translate into improved $E'_{(60^{\circ}C)}$ values. However, the decrease of $E'_{(60^{\circ}C)}$ values of REX-PLA/nano-SiO_2 composites can be explained by these two aforementioned factors. From the TEM micrographs and FT-IR analyses (*c.f. section 7.1.3 and 7.2.3)*, REX-PLA/SiO_2 seems to exhibit highest number of agglomerates with minimal interactions with REX-PLA matrix. The combination of these factors may have contributed to the increased chain mobility of polymer matrix and it is reflected in the steepest decrease in $E'_{(60^{\circ}C)}$ values.

On the other hand, finer dispersion of surface-modified nano-SiO_2 particles coupled with possible SiO_2-polymer tethering reactions in both REX-PLA/SiO_2-E and REX-PLA/SiO_2-A could be responsible for confining or restricting the molecular ability of REX-PLA matrix thus slightly improving the $E'_{(60^oC)}$ values of REX-PLA/SiO_2-E and REX-PLA/SiO_2-A.

Referring at *figure 7.24 (a)* at 120 °C, it was observed that $E'_{(120^oC)}$ values of REX-PLA were approximately 36% higher compared to REX-PLA/nano-SiO_2 samples. However, the $E'_{(120^oC)}$ increase does not reach a critical value that can modify the softening temperature (heat distortion temperature, HDT) of all of the investigated samples. As has been elucidated in the DMTA analysis of REX-PLA/o-MMT composites (*c.f. Chapter 6; section 6.2.7*), HDT is a useful measure of the relative service temperature for a polymer when used in load-bearing parts. Typically, *E'* values at approximately 1.5 GPa has a particular physical significance since it usually coincides with the HDT of PLA. from *table 7.10*, it can be seen that temperature at *E'* at 1.5 GPa of all REX-PLA/nano-SiO_2 composites were similar independent of the type of nano-SiO_2. Even though evidences SiO_2-polymer tethering in REX-PLA/SiO_2-A have been presented and discussed in *section 7.1.4* and *section 7.2.2.* respectively, these modifications were still insufficient to modifies the thermomechanical properties of the REX-PLA/SiO_2-A specifically HDT parameter.

According to *table 7.10,* the temperatures that correspond to tan δ and/or *E"* peaks (referred to as T_g), remained fairly insusceptible within the statistical error to both the topological changes and possible SiO_2-polymer tethering brought about by SamfE and surface modified nano-SiO_2 in the modified PLA matrix. These results seem to be consistent with the previous DSC data (*c.f. table 7.5*). However, the tan δ peaks of REX-PLA and REX-PLA/SiO_2-

A were relatively higher than the other samples suggesting an improvement in the damping properties. This could be attributed to the increase in MW (*c.f. table 7.2*) coupled with the formation of non-uniform branched structures in the modified PLA matrix and formation of SiO_2-polymer tethering for REX-PLA/SiO_2-A might have decrease the rate of segmental relaxation over time, thus leading to a remaining larger molecular mobility after being aged for 1 week thus improved damping properties.

7.2.8. Effect of nano-SiO_2 addition on mechanical properties of modified PLA composites.

Representative engineering stress–strain curves of REX-PLA and REX-PLA/nano-SiO_2 composites are compared in *figure 7.25*, while important mechanical parameters obtained from these tests are summarized in *table 7.11*. The general observation that can be surmised is that all of the investigated samples displayed ductile behaviours but without any appreciable cold drawing. All specimens exhibit an almost linear stress-strain relationship nearing to its yield point *i.e.* local maximum in the engineering stress. As it approaches the yield point, the engineering stress start to taper off to a stable state before the engineering stress starts to monotonically decrease beyond the yield point. However, the formation of crazes prevented necking which results in brittle fracture.

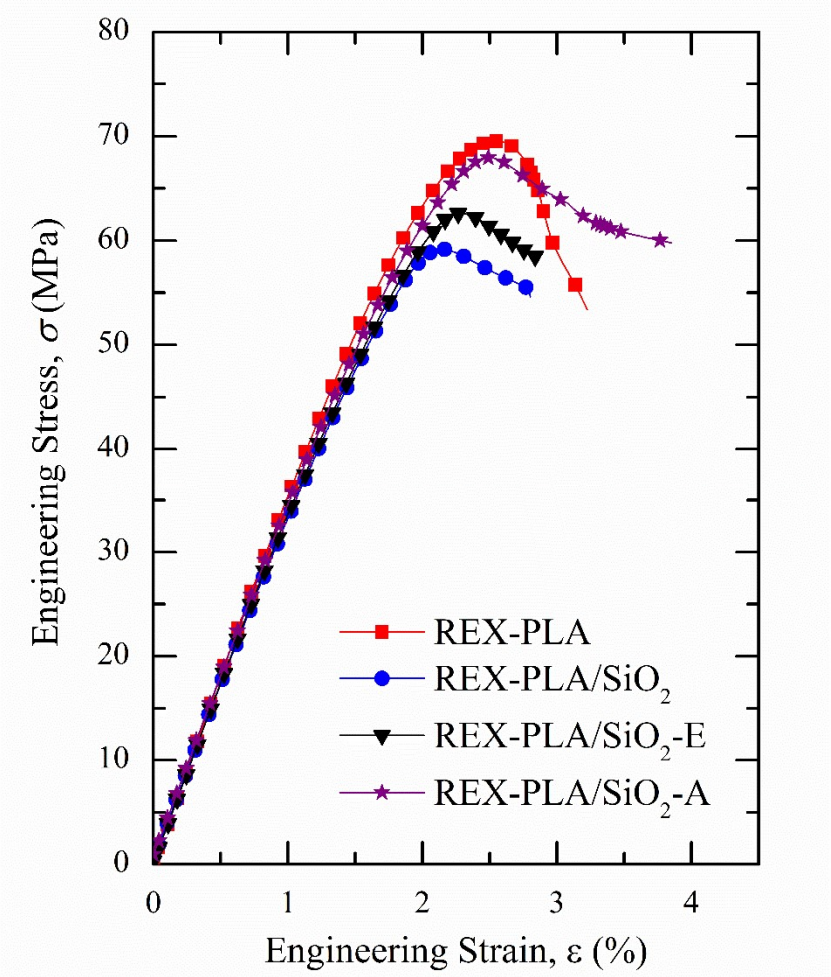

Figure 7.25. *Typical tensile engineering stress-strain curves at 10 mm.min^{-1}.*

Table 7.11. *Uniaxial tensile parameters at 10 mm.min^{-1}.*

Sample nomenclature	E (GPa)	σ_y (MPa)	ε_y (%)	ε_b (%)
REX-PLA	3.5 ±0.1	68 ±3	2.54 ±0.04	3.2 ±0.2
REX-PLA/SiO_2	3.4 ±0.1	60 ±1	2.16 ±0.04	2.7 ±0.1
REX-PLA/SiO_2-E	3.5 ±0.1	63 ±1	2.28 ±0.04	2.9 ±0.1
REX-PLA/SiO_2-A	3.4 ±0.1	66 ±2	2.47 ±0.02	3.8 ±0.4

The general trend that stands out in this table is that addition of SiO_2 and SiO_2-E leads to decrease in σ_y, ε_y and ε_b when compared to REX-PLA. However, E remain relative similar to REX-PLA within the experimental error. The decrease of σ_y and ε_y in REX-PLA/SiO_2 and REX-PLA/SiO_2-E could be probably be attributed stronger particle-particle interactions of SiO_2 and SiO_2-E than the particle-polymer interactions as evidenced in the morphological analysis in the preceding section (*c.f. section 7.2.3*).

In the case of REX-PLA/SiO_2-A, addition of SiO_2-A sees 19% increment of ε_b while exhibiting almost similar E, σ_y and ε_y to REX-PLA when the standard deviations are taken into account. A visual inspection of all the investigated samples were performed post-mechanical test and its light macrophotographs and micrographs are displayed in *figure 7.26*. It was found that both REX-PLA/SiO_2 and REX-PLA/SiO_2-E displayed a relatively straight fractured plane with minimal crazes in the fractured zone. Additionally, REX-PLA/SiO_2-A samples exhibited plastic tearing in the fracture plane.

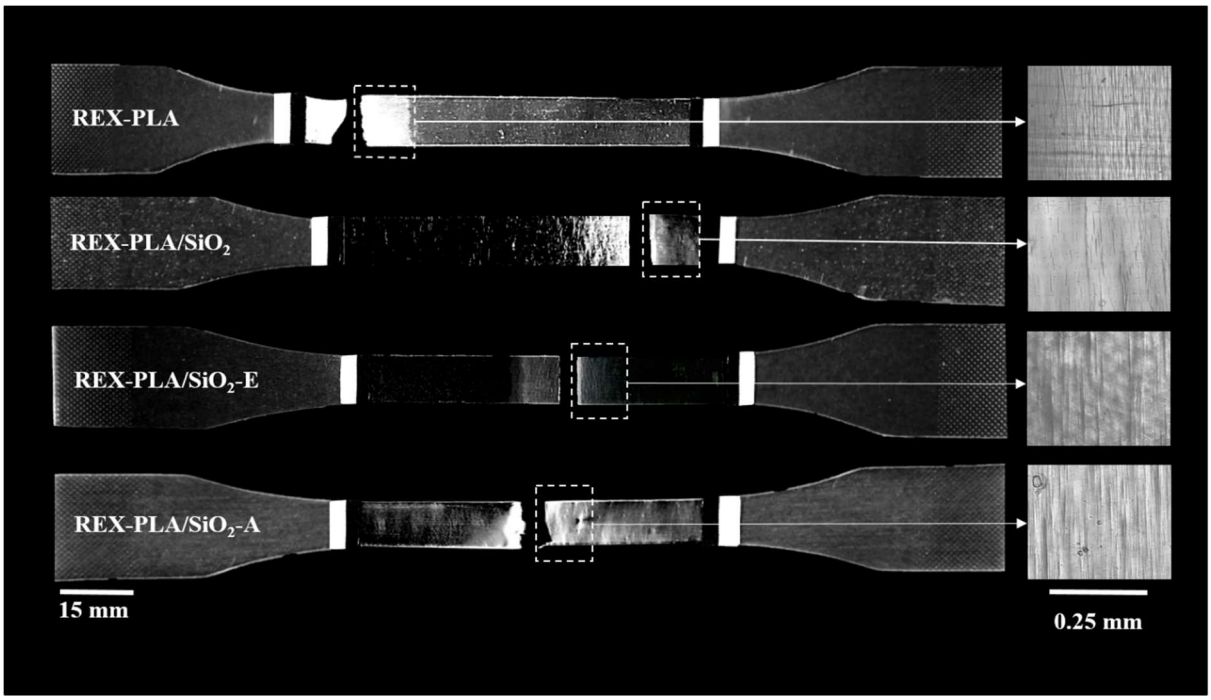

Figure 7.26. *Light macrophotographs of PLA and REX-PLA/nano-SiO_2 composites specimens post-testing at 10 mm.min^{-1}. Micrographs taken were from the fractured part of each sample.*

Mechanical reinforcement has always been linked to good interfacial interaction between the polymer and filler as well as the homogenous dispersion of the filler. Higher crystallinity may also result in a harder but also more brittle material. However, referring to *table 7.5 (c.f. section 7.2.4)* it was observed that X_c of all the investigated materials were roughly around 1-3% which renders REX-PLA and REX-PLA/nano-SiO_2 composites sheets investigated to be amorphous. This may have ruled out the effect of crystallinity on the mechanical properties of REX-PLA/nano-SiO_2 composites sheets.

Looking at *figure 7.25*, it is observed that the brittle fracture without necking of REX-PLA/SiO_2 and REX-PLA/SiO_2-E may be explained by the poor to moderate SiO_2-polymer interaction in addition to poor nano-SiO_2 dispersion as evidenced in particles dispersion analysis (*i.e. figure 7.12*). However, addition of SiO_2-A seems to impart slight improvement in ductility (ε_b) while preserving E, σ_y and ε_y properties. The ε_b increase observed in REX-PLA/SiO_2-A could attest to higher SiO_2-polymer interfacial interactions as evidenced in the SEM micrographs in *figure 7.12* (*c.f. section 7.2.3)*.

Detailed inspections of *figure 7.26* revealed that REX-PLA samples exhibits larger stress-whitened zone within the gauge section compared to REX-PLA/SiO_2-A. However, REX-PLA/SiO_2-A samples shows comparatively higher number of crazes than REX-PLA. In contrast, REX-PLA/SiO_2 and REX-PLA/SiO_2-E specimens displayed only long plane crazes confined only around the fractured zone.

When the fracture regions were observed in detail using micrographs, REX-PLA displayed a high proportion of short crazes, which is thinner and well-defined. As has been reported by Cailloux et al. (2014), the irregularities in the molecular pattern brought about by formation of non-uniform branching structures coupled with a higher entangling knots density could have dissuaded formation of long crazing planes and instead perpetuated the formation of shorter crazes under uniaxial load.

On the other hand, REX-PLA/SiO_2 displayed scattered short crazes while REX-PLA/SiO_2-E has sparsely distributed long crazes when compared to REX-PLA. These observations could have been the outcome of the presence of agglomerates in REX-PLA/SiO_2 and REX-PLA/SiO_2-E. The addition of SiO_2 and SiO_2-E seems to negatively impacted the mechanical properties of its respective REX-PLA/nano-SiO_2 composites. The existence of agglomerates due to poor nano-SiO_2 distribution acts as stress concentrators to initiate formal crack. This ultimately became a hindrance in accommodating formation of high density long crazes under loading.

In contrast, REX-PLA/SiO_2-A has a dense proportion of long crazes upon detailed inspection of the fracture region. Good interfacial interactions due to SiO_2-polymer tethering and improved dispersion of SiO_2-A particle ultimately could have contributed to the slight improvement in ductility of REX-PLA/SiO_2-A. The presence of large number of finely dispersed particle could lead to an increase in formation of small crazes. The stresses can be effectively transferred from the polymer matrix and absorbed by the more efficiently dispersed and tethered SiO2-A particles under tensile stress. This help facilitates highly confined plastic yielding within the crazes that led to a slight increase in ε_b for REX-PLA/SiO_2-A.

7.2.9. Effect of nano-SiO_2 addition on fracture behaviour of modified PLA composites.

Similar to REX-PLA/o-MMT nanocomposites, the influence of the SAmfE and nano-SiO_2 presence on de-aged fracture behaviours of PLA and REX-PLA/nano-SiO_2 composites films with a nominal thickness of 0.6 mm were also investigated using the Post-Yielding Fracture Mechanics. Investigation of micromechanism of deformation of all of the investigated samples was performed using Scanning Electron Microscopy (SEM). The fracture behaviour

of all the samples was evaluated using Deeply Double Edge-Notched Tension (DDENT) specimens. Under uniaxial loading, a large plastic deformation was observed at both crack tips; suggesting the applicability of the *post-yielding fracture mechanisms* through *the Essential Work of Fracture* (EWF) concept. Similar to the fracture behaviour discussion of PLA and modified PLA composites with o-MMT (*c.f. section 6.2.9, Chapter 6)*, EWF experiment results will first be validated prior to the influence of nano-SiO_2 modifications on the fracture behaviour analysis of modified PLA composites.

a) Validation of the Essential Work of Fracture methodology

Figure 7.27 shows the load-displacement curves for REX-PLA and REX-PLA/nano-SiO_2 composites, respectively. Observations on the load-displacement graphs have indicated that the traces were self-similar in terms of the load increases corresponding to the ligament size whilst retaining the resemblance of the overall shape of the stress–strain curve. Therefore, these curves fulfil one of the main prerequisite of the validity of the EWF methodology. This self-similarity trend assures that the cracks propagate under similar conditions, independent of ligament length (l). After maximum load has been exceeded in the graph, the load decline considerably in all graphs which is attributed to the full ligament yielding of the samples.

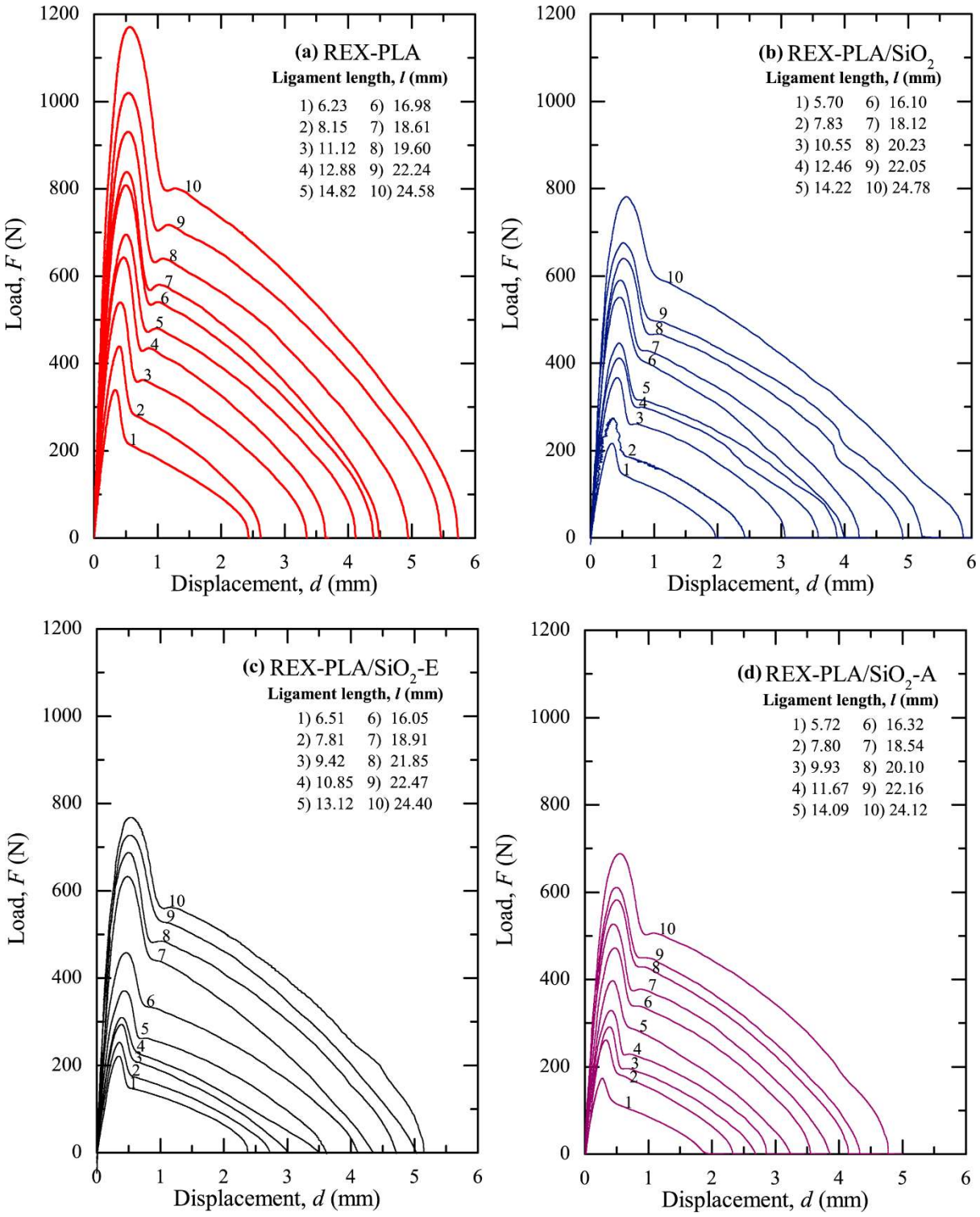

Figure 7.27. *Comparison of the load vs. displacement curves at different ligament length of (a)REX-PLA, (b)REX-PLA/SiO₂, (c)REX-PLA/SiO₂-E and (d)REX-PLA/SiO₂-A composites at 1 mm.min^{-1}.*

An additional validity check on the full ligament yielding prior to final fracture is performed. *Figure 7.28* displays typical engineering stress (σ) vs. normalized displacement (d_N) curves obtained from the EWF tests for de-aged REX-PLA and REX-PLA/nano-SiO_2 composites samples. Digital Image Correlation (DIC) analysis was used to determine the strain field encompassing the ligament length as similarly performed by Gamez-Perez et al. (2011b) and Cailloux et al (2014). From *figure 7.28,* it was observed that the yielding process was initiated prior to reaching the maximum load in all of the investigated samples. Due to co-linear notches introduced on the DDENT specimen prior to testing, it is reasonable to assume that that yielding happened from both sides of specimen due to its considerably higher stress concentration points. Whilst, the crack propagation onset was detected at the point indicated by the arrows as shown in *figure 7.28*. This results should meet the crucial requirement of the full length ligament yielding prior to final fracture (Duan et al., 2006; Karger-Kocsis and Czigány, 2000; Martinez et al., 2009).

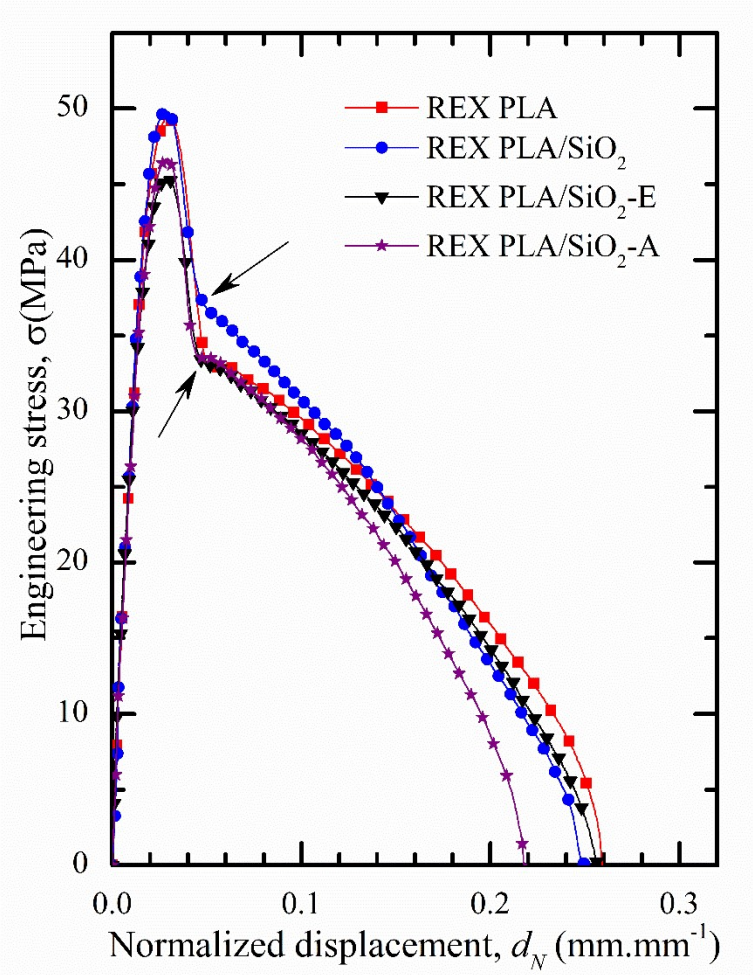

Figure 7.28. *Engineering stress versus normalized displacement (by l of 16 mm) curves for REX-PLA and REX-PLA/nano-SiO₂ composites samples tested at 1mm.min⁻¹.*

In order to ensure that the EWF measurements were performed in a uniform stress state, the results were verified using *equation 6.9* (*c.f. chapter 6, section 6.2.9a)* (Clutton, 2001). *Figure 7.29* displayed the maximum stress vs *l* for REX-PLA and REX-PLA/nano-SiO_2 composites. Regardless of the type of nano-SiO_2, it was observed that σ_{max} values are inversely proportional to *l*. It is also observed that σ_{max} values recorded were between the 1.1-0.9 σ_m limits within analyzed range of *l*. This infers that all the EWF experiments were conducted under uniform stress state or pure plane stress as proposed by Clutton (2001).

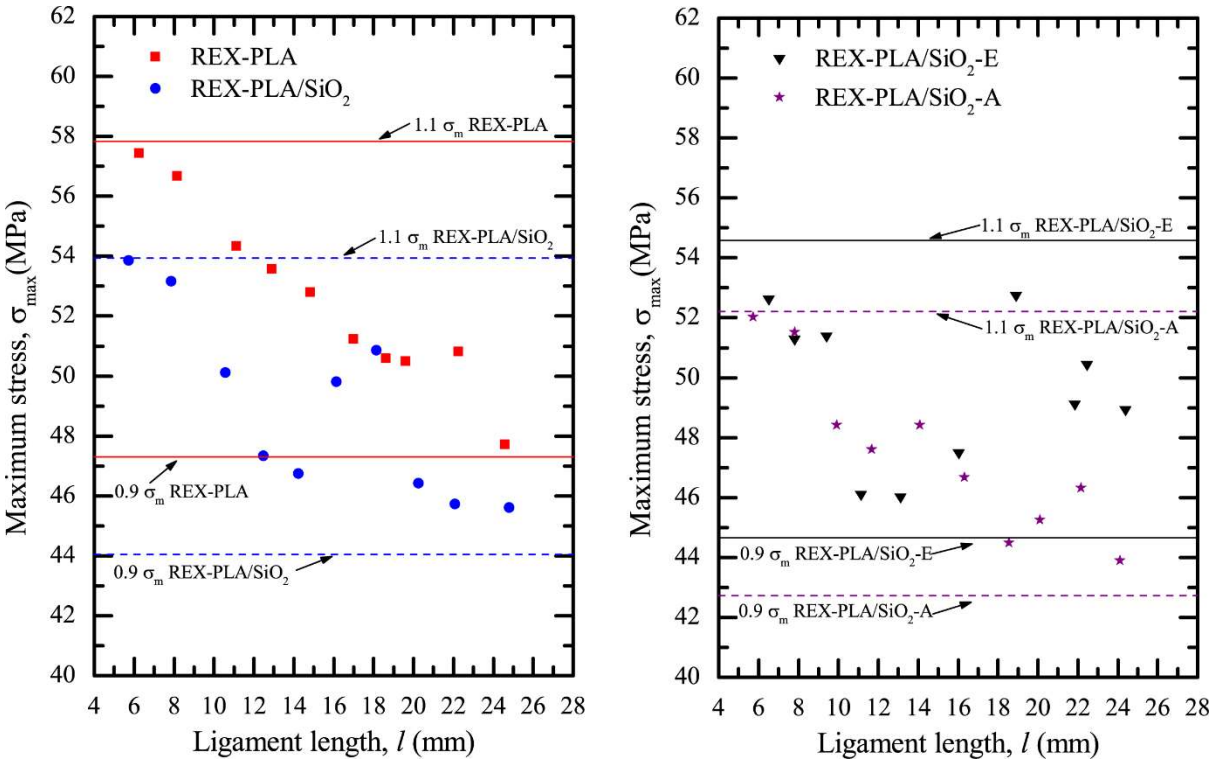

Figure 7.29. *The specific total work of fracture, w_f, as a function of the ligament length, l of de-aged PLA and modified PLA composites with nano-SiO_2. The linear dependence of w_f on l proves that all the EWF experiments were conducted under uniform stress state.*

Figure 7.30 represents specific total work of fracture, w_f, against ligament length, l. The linear dependence of w_f versus l is another proof to substantiate that all the EWF experiments were carried out under uniform stress state, as has been similarly discussed by Karger-Kocsis et al. (1998) and Karger-Kocsis and Moskala (2000).

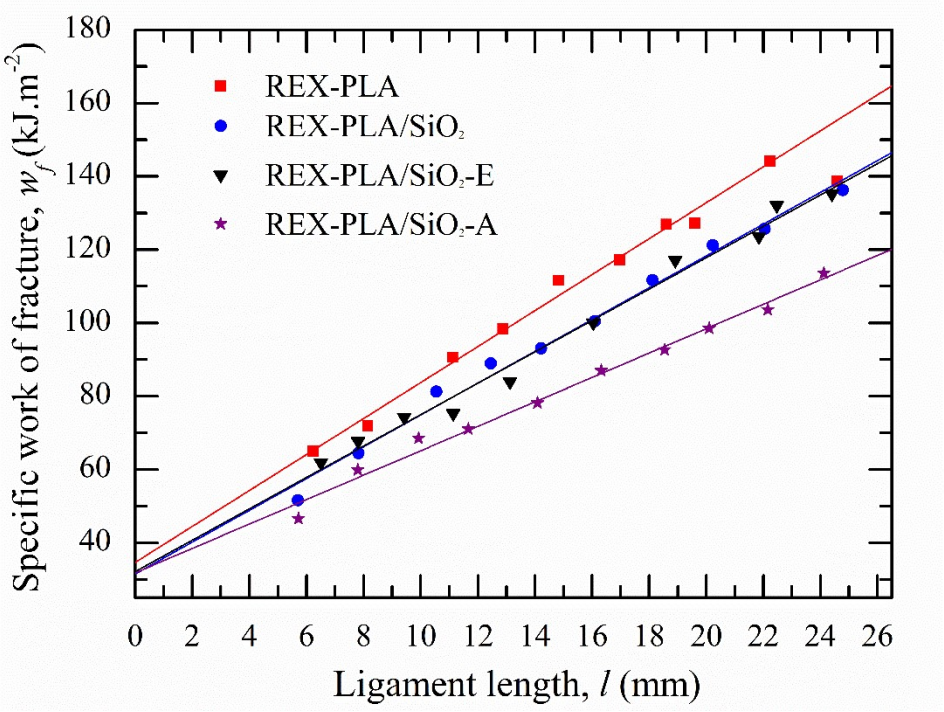

Figure 7.30. *Specific work of fracture as a function of the ligament length for de-aged REX-PLA and REX-PLA/nano-SiO$_2$ composite samples.*

b) Fracture parameters

Taking into account that all prerequisites have been fulfilled, *equation 6.10* (*c.f. chapter 6, section 6.2.9a)* was used for the EWF analysis. All the EWF parameters were analyzed and results are listed in *table 7.12* based from *figure 7.22*.

Table 7.12. *Influence of nano-SiO$_2$ incorporation in modified PLA matrix on the EWF parameters.*

Sample Nomenclature	w_e (kJ.m^{-2})	βw_p (MJ.m^{-3})	β (10^{-2})	w_p (MJ.m^{-3})	R_2 (w_f *vs.* l)
REX-PLA	34 ±2	4.9 ±0.2	6.1 ±0.5	80.3 ±0.2	0.996
REX-PLA/SiO$_2$	31 ±3	4.3 ±0.2	7.7 ±0.8	56.4 ±0.1	0.989
REX-PLA/SiO$_2$-E	32 ±2	3.3 ±0.1	5.8 ±0.9	57.2 ±0.1	0.988
REX-PLA/SiO$_2$-A	32 ±2	3.3 ±0.1	5.6 ±0.3	60.0 ±0.1	0.988

Independent of nano-SiO_2 type, it was observed w_e value of REX-PLA/nano-SiO_2 composite were similar to REX-PLA within the experimental errors. Even though there is slight reduction of work required for the onset of crack propagation; associated to the essential term (w_e), the surface modification or dispersion state of nano-SiO_2 particles does not significantly modifies the w_e value. Comparable w_e values for de-aged PLA sheets with a nominal thickness of 1 mm was reported in EWF analysis of PLA and REX-PLA/o-MMT nanocomposites (*c.f. section 6.2.9 (b), chapter 6*). This seem to be consistent with other publications which states that that the specific essential work of fracture is a material constant which remains independent of specimen geometry and MW under plane stress condition. (Cailloux et al., 2014; Hashemi, 1997; Karger-Kocsis and Moskala, 1997; Martinez et al., 2009; Wu and Mai, 1996).

Specific plastic work of dissipation term (βw_p) of REX-PLA appeared to be considerably higher compared to REX-PLA/nano-SiO_2 samples. Nonetheless, the reduction in βw_p values with the addition of nano-SiO_2 observed must be skeptically viewed due to the higher thickness of REX-PLA samples ($t_{REX\text{-}PLA} \approx 1.0$ mm vs $t_{REX\text{-}PLA/nano\text{-}SiO2} \approx 0.6$ mm). The higher thickness could have consumed larger work to induce plastic deformations hence leading to higher βw_p values. However, the distinction between presence of non-modified and surface modified nano-SiO_2 in REX-PLA can be observed in terms of reduction of the βw_p term. It is observed that βw_p value for REX-PLA/SiO_2 is higher comparing to nanocomposites with surface modified nano-SiO_2. Crack initiation of REX-PLA/SiO_2 also seems to require higher fracture energy and happened at higher stresses, resulting in higher fracture toughness. It is postulated that ductile deformation of REX-PLA/SiO_2 will be higher compared to REX-PLA/SiO_2-E and REX-PLA/SiO_2-A since the poor particle–polymer interactions in REX-

PLA/SiO_2 have resulted poor SiO_2 dispersion and formation of agglomerates which have been evidenced in the TEM micrographs in the morphological analysis of REX-PLA/nano-SiO_2 composites (*c.f. Figure 7.12; section 7.2.3*). However, an analysis of the plastic term, βw_p is needed to validates these assumptions.

On the other hand, βw_p values appeared to decrease with addition of surface modified nano-SiO_2. It has been evidenced in the TEM micrographs in the morphological analysis of REX-PLA/nano-SiO_2 composites (*c.f. Figure 7.12; section 7.2.3*) that both epoxy and amino functionalization of SiO_2 decreases the number of agglomerates formed and improves the dispersion of functionalized silica particle. From *table 7.12,* it can be seen that βw_p value decrease in REX-PLA/SiO_2-E and REX-PLA/SiO_2-A samples are quite similar. The more finely dispersed surface modified nano-SiO_2 can be attributed to the lower plastic energy being dissipated outside the fracture process zone. The restriction of the ductile deformation caused by physical constraint due to SiO_2-polymer tethering can also leads to lower βw_p values. This trend will be further elucidated in the analysis of βw_p below.

To evaluate further the influence of nano-SiO_2 addition on the specific non-essential work (w_p), a detailed analysis of the βw_p term was performed. After testing, a visual examination performed indicates that the plastic zone formed in all of the test specimens featured a parabolic shaped geometry. As has been explained in EWF analysis in the previous chapter (*c.f. Chapter 6; section 6.2.9*), the height of the surrounding OPDZ, h of each ligament length, l, were summed up. The shape parameter, β was obtained from the best linear regression of a set of values represented in a graph plotting h versus l values and using *equation 6.11*(*c.f. section 6.2.9 (b), chapter 6*).

Considering the data computed for REX-PLA/nano-SiO_2 composites from *table 7.12*, presence of SiO_2-E decreases β value markedly (≈ 25%) while w_p (*i.e.* the plastic work dissipated per unit volume) increases slightly (≈ 2%) for REX-PLA/SiO_2-E compared to REX-PLA/SiO_2. In the case of REX-PLA/SiO_2-A, β value decreases markedly (≈ 27%) while w_p increased (≈ 6%) over REX-PLA/SiO_2. It can be suggested that presence of SiO_2 augmented the outer plastic zone of REX-PLA/SiO_2 (higher values of β) which concomitantly compensates the reduction of w_p due to poor filler-polymer interactions.

In contrast, β values of both REX-PLA/SiO_2-E and REX-PLA/SiO_2-A decreased with the introduction of surface-modified nano-SiO_2 which indicates that a significant decrease in the volume of deformed material surrounding the ligament length. However, both w_p values obtained were higher indicating that there is greater energy that was dissipated during plastic deformation process surrounding the plane of crack propagation for both REX-PLA/SiO_2-E and REX-PLA/SiO_2-A compared to REX-PLA/SiO_2.

In order to support these findings, the necking distance of REX-PLA and REX-PLA/nano-SiO_2 composites were measured from *figure 7.28.* The necking distance of all of the investigated samples were measured from the maximum load of each sample until onset of the crack propagation is reach (which is indicated by arrows in *figure 7.28)* while the computed value is tabulated in *table 7.13.*

Table 7.13. *Influence of nano-SiO_2 incorporation on the necking of REX-PLA and REX-PLA/nano-SiO_2 composites samples (l = 16 mm) tested at 1mm.min^{-1}.*

Sample Nomenclature	Necking, .10^{-3}(mm)
REX-PLA	2.3
REX-PLA/SiO_2	2.0
REX-PLA/SiO_2-E	1.9
REX-PLA/SiO_2-A	1.8

From *table 7.13.* it was observed that REX-PLA experience the longest necking. Introduction of SiO_2 have decreases the necking of REX-PLA/SiO_2. This in a way validates the initial conjecture that formation of plastic zone of REX-PLA/SiO_2 should be higher than both REX-PLA/SiO_2-E and REX-PLA/SiO_2-A due to the poor particle-polymer interactions of SiO_2. On the other hand, both REX-PLA/SiO_2-E and REX-PLA/SiO_2-A displayed the shortest necking. This trend is agrees with the analysis of βw_p term in which the value of β decrease as seen in *table 7.12.*

The above trends could be explained considering the observation made by Michler and Baltá-Calleja (2012) who have suggested that composites with smaller particles would exhibit a larger reduction in the amount of deformable matrix because, at any given nominal filler content, the total interfacial area between fillers and polymer is larger for smaller filler particles. Presence of surface modified nano-SiO_2 particles also promotes a stress transfer effect. This trait is demonstrated in the decrease in the size of the outer plastic zone, demonstrated in lower values of β, which compensates the increase of w_p. It is also noted that plastic deformation of localized ligaments between the nano-SiO_2 particles within the matrix following particles-matrix decohesion and voiding can also contribute to enhancement of w_p value.

Even though the agglomerates were detected in the TEM micrographs of REX-PLA/SiO_2-E and REX-PLA/SiO_2-A were of similar size as REX-PLA/SiO_2 ones (*c.f. Figure 7.12; section 7.2.3*), simultaneously a more homogeneous and finely dispersed surface modified nano-SiO_2 distribution in REX-PLA/SiO_2-E and REX-PLA/SiO_2-A were also observed. Thus, it is assumed that a higher mechanical work was generated to produce plastic deformation especially during decohesion of surface modified nano-SiO_2 particles from REX-PLA matrix which releases the local triaxiality. With these assumptions, the specific non-essential work, w_p of REX-PLA/SiO_2-E and REX-PLA/SiO_2-A would have increased compared to REX-PLA/SiO_2 at the detriment of the formation of plastic zone, which is reflected in lower values of β.

The morphology of the fractured surfaces was evaluated using SEM after fracture experiments. *Figure 7.31* shows the macrophotographs taken from the usual plastic zone of the broken DDENT specimens and the SEM images of the corresponding fractured surfaces ahead of the crack tip.

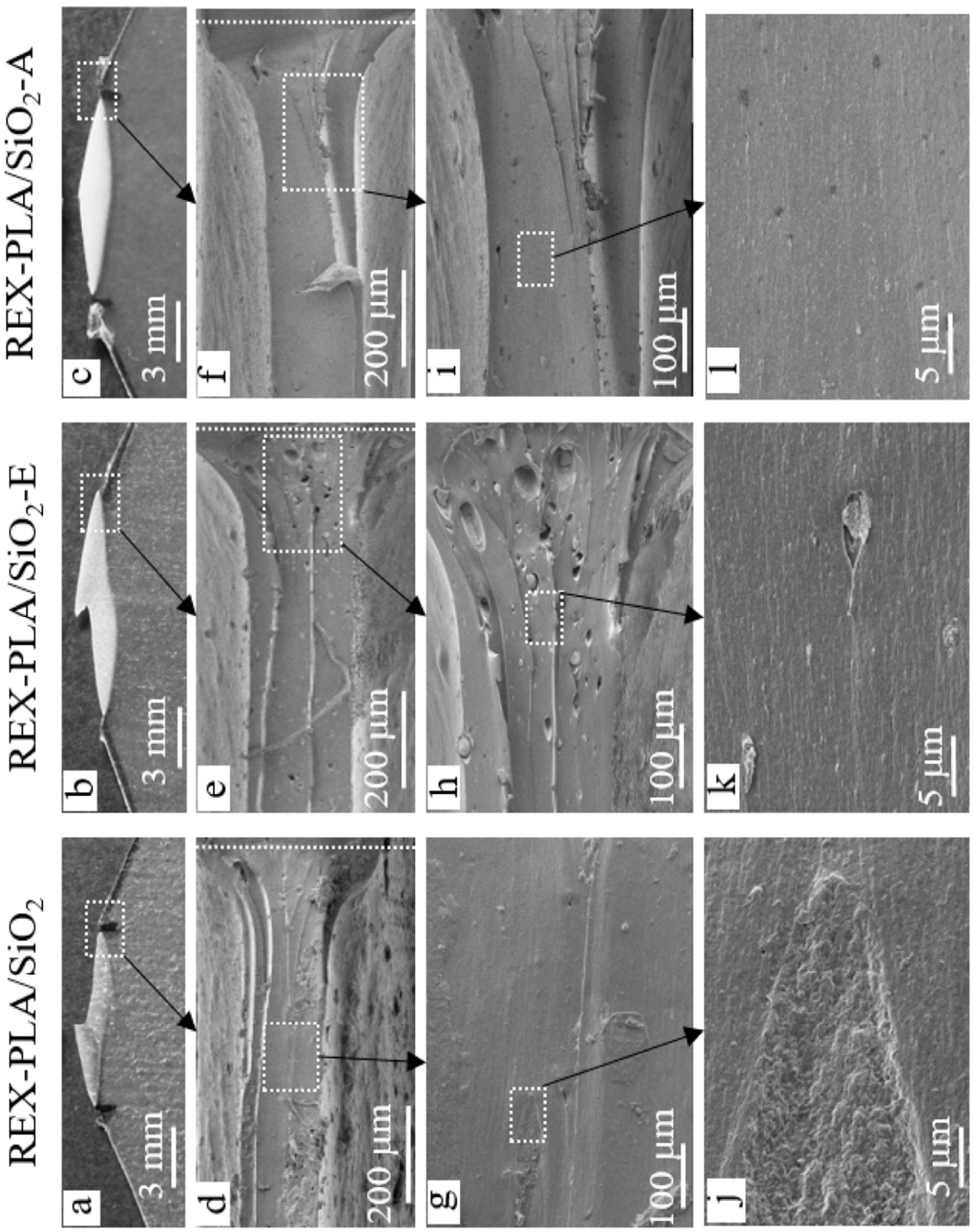

Figure 7.31. *Macrophotographs were taken from the plastic zone of the broken DDENT samples at l=16 mm tested at 1 mm.min^{-1}. SEM micrographs (d -.f: 70X, g -.f: 200X, j - l: 5000X) of REX-PLA/nano-SiO_2 composites were taken from the fractured surface ahead of the crack tip (white dashed rectangle). The white dashed line indicates the initial crack tip.*

From *figure 7.31(d)*, fracture surfaces of REX-PLA/SiO_2 samples revealed relatively smooth surface coupled with formation of ridges parallel to the crack propagation direction. The ridges can be attributed to plastic flow coupled with formation of voids and dimples just ahead of the crack tip. The formation of the dimples is accompanied by the creation of new fracture surfaces, and thus much fracture energy is likely dissipated. The dimple when viewed at higher magnifications as shown in *figure 7.31(g) and (j)*, shows that of a rough surface having formation of hackles emanating radially. This could be attributed to the decohesion of SiO_2 agglomerates from REX-PLA matrix.

The fractured surfaces of REX-PLA/SiO_2-E on the other hand displayed a relatively smooth fracture surface with formation of fibrils and cavities mostly ahead of the crack tip. It is observed that the diameter of the cavities was considerably larger than a single SiO_2-E particle and were mostly present just ahead of the crack tip. Bearing in mind the agglomerates that can be observed in the TEM micrographs of REX-PLA/SiO_2-E (*c.f. Figure 7.12; section 7.2.3*), these cavities could attributed to the decohesion of the aforementioned agglomerates that are poorly bonded to the modified PLA matrix. When the smooth fracture surface was observed at higher magnifications as shown in *figure 7.31(h) and (k)*, most of the SiO_2-E particle were still attached to REX-PLA matrix. This phenomenon implies that the particle–matrix interfacial adhesion is indeed strong. This is probably because SiO_2-E nanoparticles were surface-modified with epoxy groups which may react with REX-PLA matrix and yield strong interfacial adhesion.

In contrast to REX-PLA/SiO_2-E, the fracture surface of REX-PLA/SiO_2-A were distinguished by a relatively smooth area accompanied by small voids together with formation of several ridges also parallel to the crack propagation direction. When the smooth fracture surface of REX-PLA/SiO_2-A were observed at higher magnifications as shown in *figure 7.31(i) and (l)*, diameter of the voids detected on the fracture surface were relatively small and scattered across the fracture surface implying higher and finer SiO_2-A particle distribution. It shows that the fracture surface particle debonding occur at particle–matrix interface. Once axial loading was applied and small voids were propagated rapidly. However, the voids growth and coalescence are also governed by the resistance of the particle-matrix interface. It is hypothesize that SiO_2-polymer tethering behave as a "phase adhesive" at some level and impede the generation of larger plastic deformation hence slightly decreasing βw_p values as observed in *table 7.8* due to the restricting effects.

7.3 Summary

Initial investigation using torque as function of mixing time in an internal mixer reveal that steady increase of torque up to 21 minutes of mixing time were observed for REX-PLA/SiO_2. The observed trends could be due to higher mechanical shearing attributable to diminution of the SiO_2 aggregates into smaller particles during the latter part of mixing. In contrast, REX-PLA/SiO_2-E torque trace gradually decreases over time. The trend could be due to very limited interactions between epoxy functional end group in SiO_2-E towards the epoxy groups in REX-PLA. However, the addition of SiO_2-A seemed to increased the melt stability of REX-PLA/SiO_2-A blends in terms of stability of torque over prolonged mixing time. Nevertheless, the torque observed were still lower when compared to REX-PLA. The slight

increase in reactivity could be attributed to SAmfE being grafted onto the SiO_2-A through the -C-N linkage formation.

FT-IR measurements of REX-PLA/nano-SiO_2 composites revealed that grafting reactions occurred between the epoxy groups of SAmfE with either epoxy or amino functionalities. Intrinsic viscosities, [η] of REX-PLA/SiO_2-E and REX-PLA/SiO_2-A were marginally higher than REX-PLA/SiO_2. SiO_2-polymer tethering reactions due to addition of surface modified nano-SiO_2 may have contributed to this outcome.

The complex viscosity, $|\eta^*(\omega)|$ of REX-PLA/SiO_2 were the highest compared to the other investigated formulations. Cole-Cole plot of REX-PLA/SiO_2 showcase two arcs that represents two relaxation mechanisms as a result of formation of a network structure arising from particle-particle interactions due to hydrogen bonding between silanol groups. On the other hand, SiO_2-E decrease the complex viscosity of REX-PLA/SiO_2-E. Cole-Cole plot of REX-PLA/SiO_2-E also revealed an appearance of a second arc indicating which could be interpreted as presence of aggregates. In contrast, REX-PLA/SiO_2-A yielded similar rheological behaviour as REX-PLA. Cole-Cole plot of REX-PLA/SiO_2-A does not reveal a second relaxation mechanisms. This trend could indicate favourable interaction between amino group from SiO_2-A and epoxy group from SAmfE may have contributed to a more homogenous SiO_2-A dispersion.

TEM analyses revealed that surface modification of nano-SiO_2 achieved higher and finer particle dispersion. SEM micrographs revealed cohesive interactions between surface modified nano-SiO_2 and REX-PLA matrix.

The isothermal crystallization characterization analysis of REX-PLA/SiO_2 display 24% decrease in apparent activation energy values indicating enhanced crystallization rates during isothermal crystallization process. SiO_2 imparts nucleation effects and facilitates crystal growth rate in REX-PLA/SiO_2. However, nucleation effects of both surface-modified SiO_2 nanoparticles were limited due to possible SiO_2-polymer tethering reactions confining or restricting the molecular ability of polymer matrix to crystallize.

Tensile properties remained similar between REX-PLA and REX-PLA/nano-SiO_2 composites. Uniaxial tensile test failed to demonstrate any significant differences in tensile properties between non-modified and surface modified nano-SiO_2 filled REX-PLA composites.

In the case of REX-PLA/nano-SiO_2 composites, w_e values remained unchanged irrespective of nano-SiO_2 filler type. REX-PLA/SiO_2 displayed superior βw_p compared to REX-PLA/SiO_2-E and REX-PLA/SiO_2-A. An analysis of βw_p revealed that presence of SiO_2 augmented the outer plastic zone of REX-PLA/SiO_2 attributed to agglomerates. Surface-modified nano-SiO_2 increases w_p values indicating higher energy were dissipated during plastic deformation.

Chapter 8. Conclusions

8.1. Conclusions

PLA and REX-PLA nanocomposites were prepared using reactive extrusion process, adding either using o-MMT or different kinds of amorphous silicon dioxide (nano-SiO_2). Under the processing conditions used, the obtained results lead to the following conclusions. For the sake of brevity and clarity, the general conclusions have been divided in five parts. For each part, an accompanying comparison between REX-PLA/o-MMT nanocomposites and REX-PLA/nano-SiO_2 composites will be made.

Physico-chemical characterizations

In the case of REX-PLA/o-MMT nanocomposites, conventional chromatographic SEC-DRI analysis revealed addition of SAmfE yielded a significant increase in the molecular weight of REX-PLA samples. The molecular weight spectra changed significantly and a shoulder appeared in the high molecular weight tails. o-MMT addition made no significant difference in the molecular weight of PLA-C and REX-PLA-C. The narrow monomodal molecular weight spectras attained were similar to PLA. FT-IR measurements between o-MMT and SAmfE revealed that a relatively fast chemical grafting reactions between the epoxy groups of SAmfE and the -OH functionalities of o-MMT took place. SAXS profiles and TEM morphologies revealed relatively homogeneous o-MMT distribution with partial intercalation was achieved in REX-PLA-C.

In the case of REX-PLA/nano-SiO_2 composites, intrinsic viscosities measurements of REX-PLA/SiO_2-E and REX-PLA/SiO_2-A were higher than REX-PLA/SiO_2. SiO_2-polymer tethering reactions due to addition of surface modified nano-SiO_2 may have contributed to this outcome. However, FT-IR measurements of REX-PLA/nano-SiO_2 composites revealed that minimal to very limited grafting reactions between the epoxy groups of SAmfE with either epoxy or amino functionalities. TEM analyses revealed that surface modification of nano-SiO_2 achieved higher and finer particle dispersion. SEM micrographs revealed cohesive interactions between surface modified nano-SiO_2 and REX-PLA matrix**.**

Comparing between o-MMT and nano-SiO_2, the molecular weight of REX-PLA/nano-SiO_2 composites were higher than REX-PLA/o-MMT nanocomposites. Premature reactions of SAmfE agent being grafted onto the o-MMT surface through the -C-O-C- linkage formation may have limit the further possible reaction between PLA and SAmfE.

Rheological behaviour

Rheological measurements showed that the addition of SAmfE broadened the melt response time and increased the melt elasticity of REX-PLA. On the other hand, the complex viscosity of PLA-C was lower than PLA while viscosity enhancement of REX-PLA-C were marginal. However, REX-PLA-C displayed thermorheologically complex behaviour which validates the presence of clay-PLA tethering reactions.

In the case of REX-PLA/nano-SiO_2 composites, the complex viscosity of REX-PLA/SiO_2 were the highest compared to the other investigated formulations. Cole-Cole plot of REX-PLA/SiO_2 showcase two arcs that represents two relaxation mechanisms as a result of

formation of a network structure arising from particle-particle interactions due to hydrogen bonding between silanol groups,

Viscosity of REX-PLA/nano-SiO_2 composites were higher than REX-PLA/o-MMT nanocomposites. This is primarily attributed to premature reactions between o-MMT and PLA observed in REX-PLA-C limiting further formation of branched architecture.

Thermal behaviour

The results of this study showed that the thermal properties were not significantly modified with the addition of o-MMT. However, presence of the o-MMT nanoparticle act as nucleating agent and facilitates crystal growth rate of the polymer matrix in PLA-C. Combination of clay-polymer tethering coupled with topological modifications in REX-PLA-C negated the nucleation enhancement imparted by o-MMT presence.

Similarly, SiO_2 imparts nucleation effects and facilitates crystal growth rate in REX-PLA/SiO_2. However, nucleation effects of both surface-modified SiO_2 nanoparticles were limited due to possible SiO_2-polymer tethering reactions confining or restricting the molecular ability of polymer matrix to crystallize.

Comparing to o-MMT, fumed silica is a better nucleating agent due its smaller particle and higher surface area of SiO_2 particles inducing higher number of nuclei point leading to faster and higher crystallization rate of PLA.

Mechanical behaviour

The tensile properties of PLA-C and REX-PLA-C samples were remained statistically similar to its neat homologues. However, o-MMT modifies the deformation mechanisms observed in PLA-C and REX-PLA-C as evidenced by the appearance of a stress-whitening zones appearing along the gauge length attributed to the matrix-particle debonding and the consequent cavities growth.

Tensile properties remained similar between REX-PLA and REX-PLA/nano-SiO_2 composites. Uniaxial tensile test failed to demonstrate any significant differences in tensile properties between non-modified and surface modified nano-SiO_2 filled REX-PLA composites.

Independent of the type of fillers, all of the investigated samples exhibit ductile behaviours but without any appreciable cold drawing after being aged for 1 week at room temperature. However, the formation of crazes prevented necking which results in brittle fracture.

Fracture behaviour

The essential work of fracture (EWF) approach confirmed the enhancement of the fracture toughness of REX-PLA/o-MMT nanocomposites. O-MMT addition elicit 21 and 22% improvements on the specific essential work of fracture parameter (w_e) observed in both PLA-C and REX-PLA-C, respectively. However, the specific plastic work of dissipation (βw_p) of REX-PLA-C did not see any improvement compared to PLA-C.

In the case of REX-PLA/nano-SiO_2 composites, w_e values remained unchanged irrespective of nano-SiO_2 filler type. βw_p analysis revealed that agglomerates presence augmented the outer plastic zone of REX-PLA/SiO_2. Surface-modified nano-SiO_2 increases w_p values indicating higher energy were dissipated during plastic deformation.

Compared to REX-PLA/nano-SiO_2 composites, results indicate that the presence of o-MMT enhances the fracture toughness of REX-PLA matrix. On the other hand, the higher and finer dispersion of surface modified nano-SiO_2 did not translate into significant improvement in fracture parameters.

8.2. Outlook

The following topics are recommended for future research:

The following five technical development areas provide opportunities to increase the utility of PLA-based resins:

(1) Exploring the possibilities of using thermoplastic copolyester elastomer (TPCE) as a toughening agent for improving the impact strength of PLA. TPCE is a synthetic rubber consisting of hard polyester crystallites dispersed in a soft, flexible matrix. Because of this twin-phase composition, these materials possess the elasticity of rubber but also can be moulded and remoulded like plastic. Hytrel® supplied by Dupont® is a thermoplastic copolyester of polyether glycol and polybutylene terephthalate that could be an attractive choice in order to explore new fields of “long term” applications for PLA polymer that is both tough and strong.

(2) Preparation of binary bioblends consisting of REX-PLA with other types of commercial polymers (*i.e.* PBAT, PA) in order to explore new "long term" applications for PLA polymer. Melt blending PLA with other suitable polymers in the presence of a reactive monomer will form a graft copolymer at the interphase, decreases the interfacial tension of the immiscible polymer components and promotes interfacial adhesion. Finer phase morphology developed in the blends facilitates stress transfer between the two phases thereby improving the properties of the blends.

(3) Addition of suitable nucleating agents to enhance crystallization rates in the PLA binary bioblends could be used to attain desired crystallinity for durable applications. Some nucleating agents that can be explored are talc, carbon nanotubes, titanium dioxide, metal salts of phenylphosphonic acid, multiamide and hydrazide compounds, barium sulfate, calcium carbonate and N,N'- ethylene bis-stearamide (EBS). These have been known to impart PLA with enhanced crystallization abilities. However, the long term durability and hydrolysis stabilization of PLA binary bioblends using these additives needs to be investigated.

(4) Preparation of PLA binary bioblends composites using ethylene methyl acrylate-glycidyl methacrylate (EMAGMA) which is commercial chain extender with similar multifunctional epoxy groups like SAmfE. Effect of adding this chain extender to the binary bioblends could be explored to investigate if it promotes compatibilization and reduce interfacial tension which can result in good improvement in mechanical and thermal properties.

(5) Preparation of PLA based biocomposites with biochar or biocarbon will be an interesting future investigation. Biochar is a carbonaceous material obtained from sustainable sources. Several papers have reported promising results. However, there still remain some considerable disadvantages (such as inferior mechanical strength, thickness swell, and rotting) which restrict their proper utilization in wider markets. Addition of the right additives would be able to circumvent these issues.

Chapter 9. Appendix

9.1 Loss Modulus from rheological analysis of PLA and REX-PLA composites.

The loss modulus functions of PLA and modified PLA composites with o-MMT were investigated to verify the presence of clay -PLA tethering within all the investigated samples. Thus, *figure 9.2* shows the loss modulus curve for PLA, REX-PLA, PLA-C and REX-PLA-C samples.

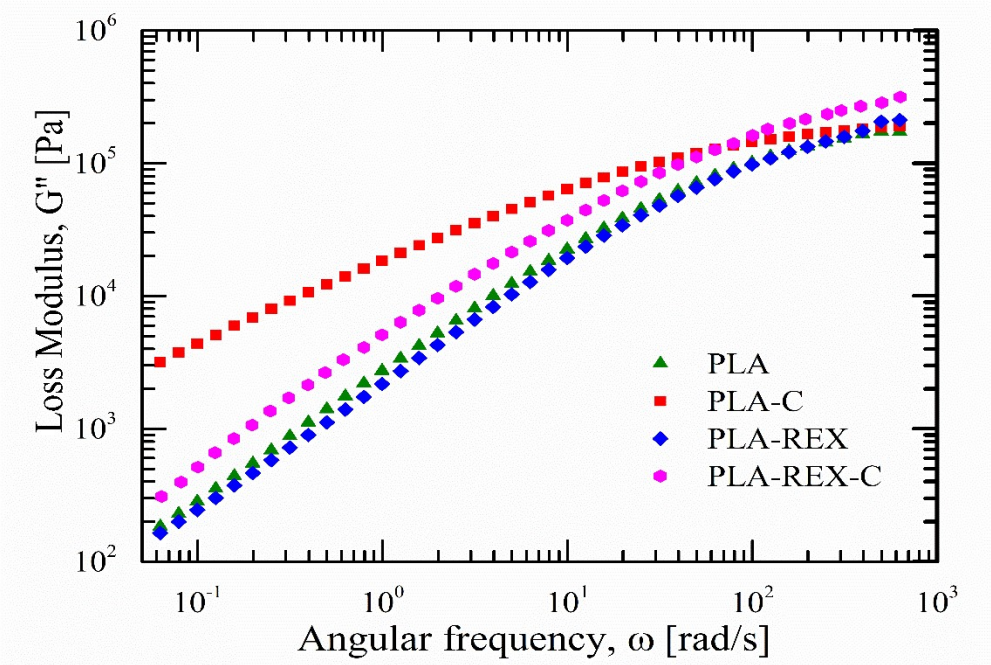

Figure 9.1. *Effect of the addition of o-MMT on the loss modulus versus angular frequencies of PLA and modified PLA composites at a reference temperature of 180 ºC.*

From the figure, it can be generalized that all loss modulus values of all samples converges at high angular frequency (between 10^2 and 10^3 rad.s^{-1}). At this high shearing level, chain orientation (disentanglement) and thermal energy dissipation could be responsible for

these similar rheological behaviour. These factors are very influential for the processability of the samples because typical extrusion shear rate lies in the range of 100 up to 500 s^{-1}.

However at lower ω region (< 10^0 rad.s^{-1}), $G''(\omega)$ of PLA-C starts to monotonically increased with decreasing ω. The theoretical double logarithmic slope of $G''(\omega)$ of PLA-C also were reduced from 1 to 0.8. The loss moduli increase could be due to reptation mode of the polymer chains in PLA-C were being impeded. A possible explanation for this result could be from presence of o-MMT that induced geometric constraints due to probable particle–particle and/or particle–polymer interactions that may have obstructed molecular relaxation of the polymer matrix.

The loss modulus functions of REX-PLA and REX-PLA/SiO_2 nanocomposites were investigated to verify the presence of SiO_2-PLA tethering within all the investigated samples. Thus, *figure 9.2* shows the loss modulus curve for PLA, REX-PLA, REX-PLA/SiO_2, REX-PLA/SiO_2-E and REX-PLA/SiO_2-A samples.

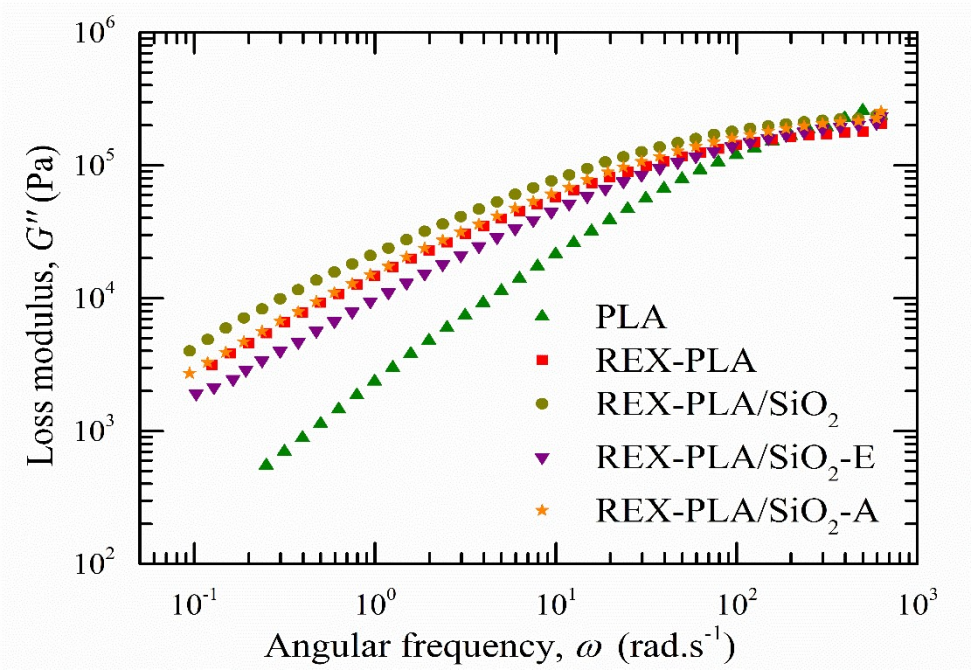

Figure 9.2. *Effect of the addition nano-SiO_2 on the loss modulus versus angular frequencies of modified PLA composites at a reference temperature of 180 ºC.*

Similar to *figure 9.1,* it can be generalized that all loss modulus values of all samples in *figure 9.2* converges at high angular frequency (between 10^2 and 10^3 rad.s^{-1}).

However at lower ω region (< 10^0 rad.s^{-1}), *G''*(*ω*) all of the investigated samples starts to monotonically decreased with decreasing ω. It was observed that the theoretical double logarithmic slope of *G'(ω)* of PLA is 1. However, the theoretical double logarithmic slope of *G'(ω)* of all the other samples were reduced to 0.7. This is chiefly due to introduction sparsely branched structure in the modified PLA matrix.

9.2 Loss modulus, E" from thermomechanical spectrum of PLA and REX-PLA composites.

DMTA analysis was performed using a single cantilever bending mode to evaluate the effects of the topological changes due to o-MMT presence on the dynamic mechanical properties of "as-received" PLA and modified PLA composites sheets. The "as-received" analyzed samples have been subjected to 1 week of physical aging at room temperature to mimic the common industrial conditioning of these prepared sheets. The thermomechanical spectrum of PLA and modified PLA composites with o-MMT sheets which were recorded from 30 to 110 ºC are depicted in *figure 9.3,* in the form of loss modulus, *E'*.

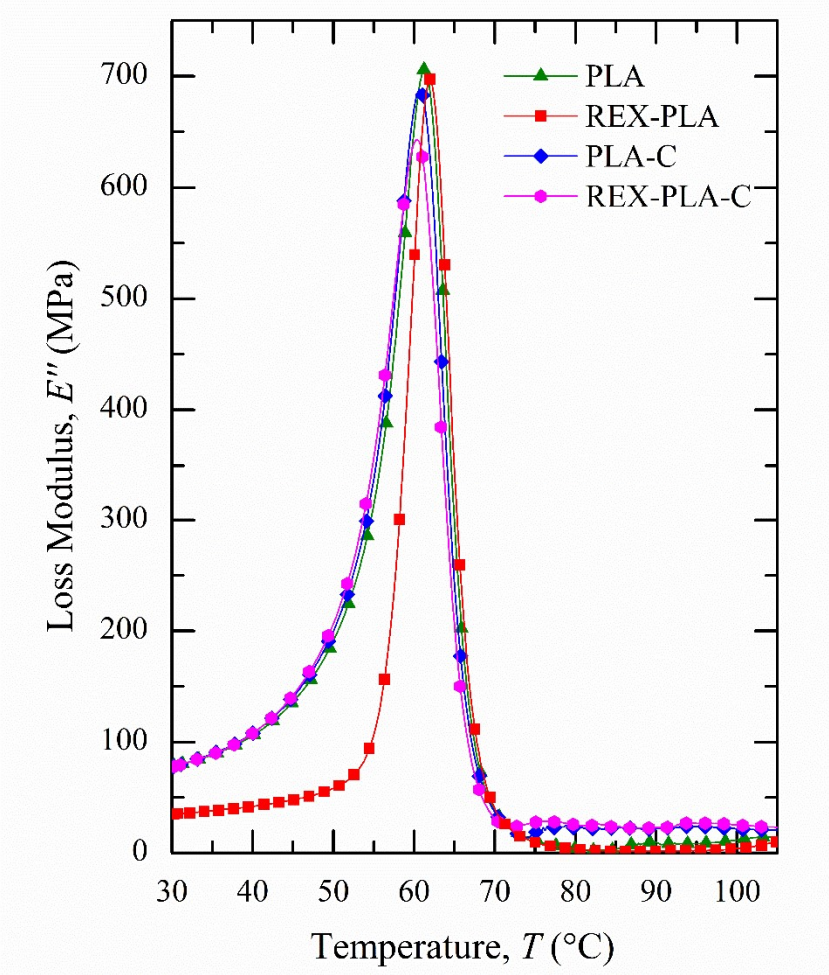

Figure 9.3. *Loss modulus traces of PLA and modified PLA composites with o-MMT tested at 2 °C.min^{-1}.*

Similarly, DMTA analysis undertaken to evaluate the effects of the topological changes due tonano-SiO_2 presence on the dynamic mechanical properties of "as-received" modified PLA composites sheets. The "as-received" analyzed samples have been subjected to 1 week of physical aging at room temperature to mimic the common industrial conditioning of these prepared sheets. The thermomechanical spectrum of modified PLA composites with SiO_2 sheets which were recorded from 30 to 120 ºC are depicted in *figure 9.4,* in the form of loss modulus, *E'*.

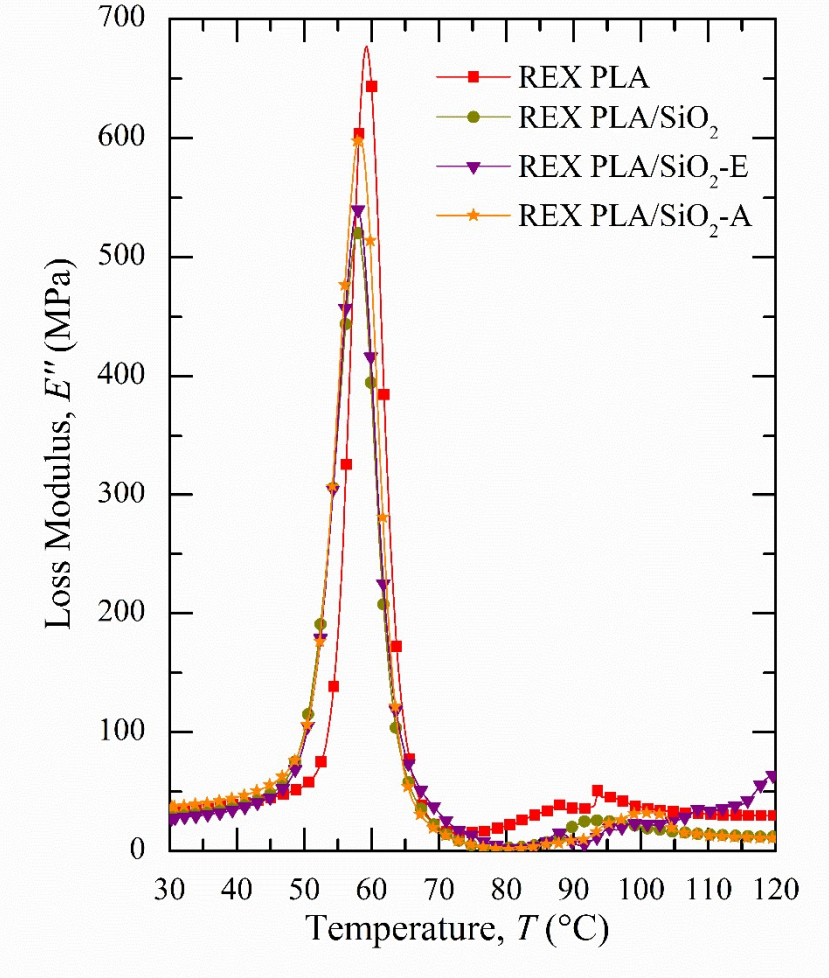

Figure 9.4 *Loss modulus traces of modified PLA composites with nano-SiO_2 tested at 2 °C.min^{-1}.*

References

Publications resulted from this PhD. Thesis

i. Cailloux J, **Hakim RN,** Santana OO, Bou JJ, Abt T, Sánchez-Soto M, Carrasco F, Maspoch ML. Reactive extrusion: A useful process to manufacture structurally modified PLA/o-MMT composites. Composites Part A: Applied Science and Manufacturing. 88, 2016, pp. 106-115.

ii. **Hakim RN,** Cailloux J, Santana OO, Bou JJ, Sánchez-Soto M, Odent J, Raquez JM, Dubois P, Carrasco F, Maspoch ML. PLA/SiO2 composites: Influence of the filler modifications on the morphology, crystallization behavior, and mechanical properties. Journal of Applied Polymer Science 2017; 134: 45367-n/a.

Conference paper resulted from this PhD. Thesis

i. "Characterization Of PD,L-LA/O-MMT Composites Manufactured By One-Step Reactive Extrusion Calendering Process" " by **Hakim RN,** Cailloux J, Santana OO, Bou JJ, Sánchez-Soto M, Franco-Urquiza E, Maspoch ML. "XIII Congreso Nacional de Materiales (CNMAT2014)"

Other references

Abe H, Kikkawa Y, Iwata T, Aoki H, Akehata T, Doi Y. *Microscopic visualization on crystalline morphologies of thin films for poly[(R)-3-hydroxybutyric acid] and its copolymer*. Polymer 2000; 41: 867-874.

Ábrányi Á, Százdi L, Pukánszky B, Vancsó GJ. *Formation and Detection of Clay Network Structure in Poly(propylene)/Layered Silicate Nanocomposites*. Macromolecular Rapid Communications. 27. WILEY-VCH Verlag, 2006, pp. 132-135.

Abt T, Sánchez-Soto M, Martínez de Ilarduya A. *Toughening of in situ polymerized cyclic butylene terephthalate by chain extension with a bifunctional epoxy resin*. European Polymer Journal 2012; 48: 163-171.

Ahmed J, Varshney SK. *Polylactides—Chemistry, Properties and Green Packaging Technology: A Review*. International Journal of Food Properties 2011; 14: 37-58.

Ahmed J, Varshney SK, Auras R. *Rheological and Thermal Properties of Polylactide/Silicate Nanocomposites Films*. Journal of Food Science 2010; 75: N17-N24.

Ajioka M, Enomoto K, Suzuki K, Yamaguchi A. *The basic properties of poly(lactic acid) produced by the direct condensation polymerization of lactic acid*. Journal of environmental polymer degradation. 3, 1995, pp. 225-234.

Akcora P, Liu H, Kumar SK, Moll J, Li Y, Benicewicz BC, Schadler LS, Acehan D, Panagiotopoulos AZ, Pryamitsyn V, Ganesan V, Ilavsky J, Thiyagarajan P, Colby RH, Douglas JF. *Anisotropic self-assembly of spherical polymer-grafted nanoparticles*. Nature Materials 2009; 8: 354-359.

Al-Itry R, Lamnawar K, Maazouz A. *Improvement of thermal stability, rheological and mechanical properties of PLA, PBAT and their blends by reactive extrusion with functionalized epoxy*. Polymer Degradation and Stability 2012; 97: 1898-1914.

Al-Itry R, Lamnawar K, Maazouz A. *Reactive extrusion of PLA, PBAT with a multi-functional epoxide: Physico-chemical and rheological properties*. European Polymer Journal 2014; 58: 90-102.

Alamri H, Low IM. *Effect of water absorption on the mechanical properties of nanoclay filled recycled cellulose fibre reinforced epoxy hybrid nanocomposites*. Composites Part A: Applied Science and Manufacturing 2013; 44: 23-31.

Alexandre M, Dubois P. *Polymer-layered silicate nanocomposites: preparation, properties and uses of a new class of materials*. Materials Science and Engineering: R: Reports 2000; 28: 1-63.

Alexy P, Bugaj P, Feranc J, Pavlačková M, Tomanová K, Benovič F, Plavec R, Mihalovič M, Botošová M. *Blends based on PLA and PHB with improved processing and mechanical properties*. Chem. Listy 2011; 105: s241-s244.

Anderson TL. *Fracture Mechanics: Fundamentals and Applications, Third Edition*: Taylor & Francis, 2005.

Antsiferova Y, Sotnikova N, Parfenyuk E. *Different Effects of the Immunomodulatory Drug GMDP Immobilized onto Aminopropyl Modified and Unmodified Mesoporous Silica Nanoparticles upon Peritoneal Macrophages of Women with Endometriosis*. BioMed Research International 2013; 2013: 10.

Aou K, Hsu SL, Kleiner LW, Tang F-W. *Roles of Conformational and Configurational Defects on the Physical Aging of Amorphous Poly(lactic acid)*. The Journal of Physical Chemistry B 2007; 111: 12322-12327.

Aranda P, Ruiz-Hitzky E. *Poly(ethylene oxide)-silicate intercalation materials*. Chemistry of Materials 1992; 4: 1395-1403.

Argon AS, Hsia KJ, Parks DM. *Growth of Cracks By Intergranular Cavitation in Creep*. In: Argon AS, editor. Topics in Fracture and Fatigue. Springer New York, New York, NY, 1992, pp. 235-270.

Argyo C, Weiss V, Bräuchle C, Bein T. *Multifunctional Mesoporous Silica Nanoparticles as a Universal Platform for Drug Delivery*. Chemistry of Materials 2014; 26: 435-451.

Arroyo OH, Huneault MA, Favis BD, Bureau MN. *Processing and properties of PLA/thermoplastic starch/montmorillonite nanocomposites*. Polymer Composites 2010; 31: 114-127.

Associations of Plastic Manufacturers. *An analysis of European plastics production, demand and waste data*. 28th August 2017. Retrieved from http://www.plasticseurope.org/documents/document/20161014113313-plastics_the_facts_2016_final_version.pdf.

Auras R, Harte B, Selke S. *An Overview of Polylactides as Packaging Materials*. Macromolecular Bioscience 2004; 4: 835-864.

Auras R, Lim L-T, Selke SEM, Tsuji H. *Index*. Poly(Lactic Acid). John Wiley & Sons, Inc., 2010, pp. 487-499.

Avrami M. *Kinetics of Phase Change. I General Theory*. The Journal of Chemical Physics 1939; 7: 1103-1112.

Babu RP, O'Connor K, Seeram R. *Current progress on bio-based polymers and their future trends*. Progress in Biomaterials 2013; 2: 8.

Balazs AC, Singh C, Zhulina E, Lyatskaya Y. *Modeling the Phase Behavior of Polymer/Clay Nanocomposites*. Accounts of Chemical Research 1999; 32: 651-657.

Bansal A, Yang H, Li C, Cho K, Benicewicz BC, Kumar SK, Schadler LS. *Quantitative equivalence between polymer nanocomposites and thin polymer films*. Nat Mater 2005; 4: 693-698.

Baratian S, Hall ES, Lin JS, Xu R, Runt J. *Crystallization and Solid-State Structure of Random Polylactide Copolymers: Poly(l-lactide-co-d-lactide)s*. Macromolecules 2001; 34: 4857-4864.

Barnes HA. *Chapter 1 - Introduction*. In: Barnes HA, Hutton JF, Walters K, editors. Rheology Series. 3. Elsevier, 1989, pp. 1-10.

BASF Corporation. *Joncryl ADR-4300 Technical Data Sheets*. Joncryl ADR-4300, 2006.

Basilissi L, Di Silvestro G, Farina H, Ortenzi MA. *Synthesis and characterization of PLA nanocomposites containing nanosilica modified with different organosilanes II: Effect of the organosilanes on the properties of nanocomposites: Thermal characterization*. Journal of Applied Polymer Science. 128. Wiley Subscription Services, Inc., A Wiley Company, 2013a, pp. 3057-3063.

Basilissi L, Silvestro GD, Farina H, Ortenzi MA. *Synthesis and characterization of PLA nanocomposites containing nanosilica modified with different organosilanes I. Effect of the organosilanes on the properties of nanocomposites: Macromolecular, morphological, and rheologic characterization*. Journal of Applied Polymer Science. 128. Wiley Subscription Services, Inc., A Wiley Company, 2013b, pp. 1575-1582.

Basu S, Mahajan DK, Van der Giessen E. *Micromechanics of the growth of a craze fibril in glassy polymers*. Polymer 2005; 46: 7504-7518.

Beall GW, Powell CE. *Fundamentals of Polymer-Clay Nanocomposites*. Cambridge, United Kingdom: Cambridge University Press, 2011.

Bellamy MK. *Using FTIR-ATR Spectroscopy to teach the Internal Standard Method*. Journal of Chemical Education 2010; 87: 1399-1401.

Bergaya F, Jaber M, Lambert J-F. *Clays and Clay Minerals as Layered Nanofillers for (Bio)Polymers*. London, United Kingdom: Springer-Verlag, 2012.

Bergna HE, Roberts WO. *Colloidal Silica: Fundamentals and Applications*. Boca Raton, Florida: CRC Press 2005a.

Bergna HE, Roberts WO. *Colloidal Silica: Fundamentals and Applications*. Vol 131: CRC Press 2005b.

Bharadwaj RK, Mehrabi AR, Hamilton C, Trujillo C, Murga M, Fan R, Chavira A, Thompson AK. *Structure–property relationships in cross-linked polyester–clay nanocomposites*. Polymer 2002; 43: 3699-3705.

Bigg DM. *Polylactide copolymers: Effect of copolymer ratio and end capping on their properties*. Advances in Polymer Technology 2005; 24: 69-82.

Bikiaris DN, Karayannidis GP. *Chain extension of polyesters PET and PBT with two new diimidodiepoxides. II*. Journal of Polymer Science Part A: Polymer Chemistry 1996; 34: 1337-1342.

Bioplastics Information. *Companies producing PLA around the world*. April 14 2017. Retrieved from http://bioplasticsinfo.com/polylactic-acid/companies-concerned/.

Blaker J, Lee K-Y, Bismarck A. *Hierarchical Composites Made Entirely from Renewable Resources*. Vol 5, 2011.

Bocchini S, Fukushima K, Blasio AD, Fina A, Frache A, Geobaldo F. *Polylactic Acid and Polylactic Acid-Based Nanocomposite Photooxidation*. Biomacromolecules 2010; 11: 2919-2926.

Bogush GH, Tracy MA, Zukoski CF. *Preparation of monodisperse silica particles: Control of size and mass fraction*. Journal of Non-Crystalline Solids 1988; 104: 95-106.

Bordes P, Hablot E, Pollet E, Avérous L. *Effect of clay organomodifiers on degradation of polyhydroxyalkanoates*. Polymer Degradation and Stability 2009; 94: 789-796.

Bouaziz A, Jaziri M, Dalmas F, Massardier V. *Nanocomposites of silica reinforced polypropylene: Correlation between morphology and properties*. Polymer Engineering & Science 2014; 54: 2187-2196.

Bower DI. *Morphology and motion*. In: Bower DI, editor. An Introduction to Polymer Physics. Cambridge University Press, Cambridge, 2002, pp. 117-161.

Buckser S, Tung LH. *The Crystallization Rate of Low Pressure Polyethylene*. The Journal of Physical Chemistry 1959; 63: 763-765.

Bureau MN, Perrin-Sarazin F, Ton-That MT. *Polyolefin nanocomposites: Essential work of fracture analysis*. Polymer Engineering & Science 2004; 44: 1142-1151.

Cabot Corporation. *Cab-O-Sil Fumed Silica in Polyester Resins*. 13th September 2017. Retrieved from http://www.cabotcorp.com/solutions/products-plus/fumed-metal-oxides/hydrophilic.

Cailloux J. *Modified Poly(lactic acid) sheets manufactured by One-Step Reactive Extrusion-Calendering: Thermal, Rheological, Mechanical and Fracture Behaviours* Materials Science and Engineering Ph.D. Thesis. Universidad Politécnica de Cataluña, Barcelona, 2015.

Cailloux J, Santana OO, Franco-Urquiza E, Bou JJ, Carrasco F, Gamez-Perez J, Maspoch ML. *Sheets of branched poly(lactic acid) obtained by one step reactive extrusion calendering process: Melt rheology analysis*. Express Polymer Letters 2013; 7: 304-318.

Cailloux J, Santana OO, Franco-Urquiza E, Bou JJ, Carrasco F, Maspoch ML. *Sheets of branched poly(lactic acid) obtained by one-step reactive extrusion–calendering process: physical aging and fracture behavior*. Journal of Materials Science. Springer US, 2014, pp. 1-15.

Cailloux J, Santana OO, Maspoch ML, Bou JJ, Carrasco F. *Using viscoelastic properties to quantitatively estimate the amount of modified poly(lactic acid) chains through reactive extrusion*. Journal of Rheology. 59, 2015, pp. 1191-1227.

Calmon-Decriaud A, Bellon-Maurel V, Silvestre F. *Standard Methods for Testing the Aerobic Biodegradation of Polymeric Materials. Review and Perspectives*. In: Bellon-Maurel V, Calmon-Decriaud A, Chandrasekhar V, Hadjichristidis N, Mays JW, Pispas S, et al., editors. Blockcopolymers - Polyelectrolytes - Biodegradation. Springer Berlin Heidelberg, Berlin, Heidelberg, 1998, pp. 207-226.

Carrasco F, Gamez-Perez J, Santana OO, Maspoch ML. *Processing of poly(lactic acid)/organomontmorillonite nanocomposites: Microstructure, thermal stability and kinetics of the thermal decomposition*. Chemical Engineering Journal 2011a; 178: 451-460.

Carrasco F, Gámez-Pérez J, Santana OO, Maspoch ML. *Processing of poly(lactic acid)/organomontmorillonite nanocomposites: Microstructure, thermal stability and kinetics of the thermal decomposition*. Chemical Engineering Journal 2011b; 178: 451-460.

Carrasco F, Perez-Maqueda LA, Santana OO, Maspoch ML. *Enhanced general analytical equation for the kinetics of the thermal degradation of poly(lactic acid)/montmorillonite nanocomposites driven by random scission*. Polymer Degradation and Stability 2014; 101: 52-59.

Carrasco F, Santana O, Cailloux J, Maspoch ML. *Kinetics of the thermal degradation of poly(lactic acid) obtained by reactive extrusion: Influence of the addition of montmorillonite nanoparticles*. Polymer Testing 2015; 48: 69-81.

Cassagnau P. *Melt rheology of organoclay and fumed silica nanocomposites*. Polymer. 49, 2008, pp. 2183-2196.

Castiello S, Coltelli M-B, Conzatti L, Bronco S. *Comparative study about preparation of poly(lactide)/Organophilic montmorillonites nanocomposites through melt blending or ring opening polymerization methods*. Journal of Applied Polymer Science 2012; 125: 413-428.

Chang JHL, Rahman MR, Hamdan S. *Physical, Mechanical, and Thermal Analysis of Polylactic Acid/Fumed Silica/Clay (1.28E) Nanocomposites*. International Journal of Polymer Science 2015; 2015.

Cheaburu-Yilmaz CN, Yilmaz O, Cornelia. V. *Eco-Friendly Chitosan-Based Nanocomposites: Chemistry and Applications*. Vol 74. New Delhi, India: Springer, 2015.

Chen H, Wu J. *Understanding the Underlying Physics of the Essential Work of Fracture on the Molecular Level*. Macromolecules 2007; 40: 4322-4326.

Cheng JJ, Polak MA, Penlidis A. *Influence of micromolecular structure on environmental stress cracking resistance of high density polyethylene*. Tunnelling and Underground Space Technology 2011; 26: 582-593.

Chow W, Leu Y, Ishak ZM. *Poly(lactic acid) nanocomposites with improved impact and thermal properties*. Journal of Composite Materials 2014; 48: 155-163.

Chow WS, Lok SK. *Thermal properties of poly(lactic acid)/organo-montmorillonite nanocomposites*. Journal of Thermal Analysis and Calorimetry 2009; 95: 627-632.

Chu M-J, Wu T-M. *Isothermal Crystallization Kinetics of Poly(Lactic Acid)/ Montmorillonite Nanocomposites*. In: Gdoutos EE, editor. Experimental Analysis of Nano and Engineering Materials and Structures: Proceedings of the 13th International Conference on Experimental Mechanics, Alexandroupolis, Greece, July 1–6, 2007. Springer Netherlands, Dordrecht, 2007, pp. 827-828.

Clutton E. *Essential work of fracture*. European Structural Integrity Society 2001; 28: 177-195.

Coiai S, Cicogna F, de Santi A, Amaro LP, Spiniello R, Signori F, Fiori S, Oberhauser W, Passaglia E. *MMT and LDH organo-modification with surfactants tailored for PLA nanocomposites*. eXPRESS Polymer Letters 2017; 11: 163-175.

Cole KS, Cole RH. *Dispersion and Absorption in Dielectrics I. Alternating Current Characteristics*. The Journal of Chemical Physics 1941; 9: 341-351.

Collins RL. *Nuclear spin resonance line width measurements of polyethylene*. Journal of Polymer Science 1958; 27: 67-73.

Corre YM, Duchet J, Reignier J, Maazouz A. *Melt strengthening of poly (lactic acid) through reactive extrusion with epoxy-functionalized chains*. Rheologica Acta 2011a; 50: 613-629.

Corre YM, Maazouz A, Duchet J, Reignier J. *Batch foaming of chain extended PLA with supercritical CO2: Influence of the rheological properties and the process parameters on the cellular structure*. Journal of Supercritical Fluids 2011b; 58: 177-188.

Davachi SM, Kaffashi B. *Polylactic Acid in Medicine*. Polymer-Plastics Technology and Engineering 2015; 54: 944-967.

Day M, Nawaby A, Liao X. *A DSC Study of the crystalization Behaviour of Polylactic acid and its nanocomposites*. Journal of Thermal Analysis and Calorimetry 2006; 86: 623-629.

Dealy JM, Larson RG. *Linear Viscoelasticity : Fundamentals*. Structure and Rheology of Molten Polymers. Carl Hanser Verlag GmbH & Co. KG, 2006, pp. 91-130.

Di Lorenzo ML. *Crystallization behavior of poly(l-lactic acid)*. European Polymer Journal 2005; 41: 569-575.

Di Lorenzo ML. *Calorimetric analysis of the multiple melting behavior of poly(L-lactic acid)*. Journal of Applied Polymer Science 2006; 100: 3145-3151.

Dong W, Zou B, Yan Y, Ma P, Chen M. *Effect of Chain-Extenders on the Properties and Hydrolytic Degradation Behavior of the Poly(lactide)/ Poly(butylene adipate-co-terephthalate) Blends*. International Journal of Molecular Sciences. 14, 2013, pp. 20189.

Dorgan JR, Lehermeier H, Mang M. *Thermal and Rheological Properties of Commercial-Grade Poly(Lactic Acid)s*. Journal of Polymers and the Environment 2000; 8: 1-9.

Dorgan JR, Williams JS, Lewis DN. *Melt rheology of poly(lactic acid): Entanglement and chain architecture effects*. Journal of Rheology 1999; 43: 1141-1155.

Dorigato A, Sebastiani M, Pegoretti A, Fambri L. *Effect of Silica Nanoparticles on the Mechanical Performances of Poly(Lactic Acid)*. Journal of environmental polymer degradation 2012; 20: 713-725.

Drumright RE, Gruber PR, Henton DE. *Polylactic Acid Technology*. Advanced Materials 2000; 12: 1841-1846.

Duan K, Hu X, Stachowiak G. *Modified essential work of fracture model for polymer fracture*. Composites Science and Technology 2006; 66: 3172-3178.

Duan RX, Guo K, He YN, Chen JZ, Niu MJ, Wang LX, Li XF. *Research on Maleic Anhydride Improving the Interfacial Compatibility of PLLA and OMMT by Grafting Method*. Advances in Printing and Packaging Technologies 2013; 262: 567-571.

Eksteen R, Pardue K. *Modified Silica-Based Packing Materials for Size Exclusion Chromatography*. Handbook Of Size Exclusion Chromatography And Related Techniques. CRC Press, 2003.

Elsawy MA, Kim K-H, Park J-W, Deep A. *Hydrolytic degradation of polylactic acid (PLA) and its composites*. Renewable and Sustainable Energy Reviews 2017; 79: 1346-1352.

Endres HJ, Siebert-Raths A. *Introduction*. In: Endres HJ, Siebert-Raths A, editors. Engineering Biopolymers: Markets, Manufacturing, Properties and Applications. Hanser, Munich, 2011, pp. 1-17.

European Bioplastics e.V. *What are bioplastics?* 27th August 2017. Retrieved from http://www.european-bioplastics.org/bioplastics/.

Evans UR. *The laws of expanding circles and spheres in relation to the lateral growth of surface films and the grain-size of metals*. Transactions of the Faraday Society 1945; 41: 365-374.

Evonik Industries GmbH. *Technical Overview: AEROSIL® - Fumed Silica*. 16 June 2016. Retrieved from https://www.aerosil.com/sites/lists/RE/DocumentsSI/Technical-Overview-AEROSIL-Fumed-Silica-EN.pdf.

Farah S, Anderson DG, Langer R. *Physical and mechanical properties of PLA, and their functions in widespread applications — A comprehensive review*. Advanced Drug Delivery Reviews 2016; 107: 367-392.

Filippi S, Paci M, Polacco G, Dintcheva NT, Magagnini P. *On the interlayer spacing collapse of Cloisite® 30B organoclay*. Polymer Degradation and Stability 2011; 96: 823-832.

Fischer EW. *Notizen: Stufen- und spiralförmiges Kristallwachstum bei Hochpolymeren*. Zeitschrift für Naturforschung A 1957; 12: 753.

Flörke OW, Graetsch HA, Brunk F, Benda L, Paschen S, Bergna HE, Roberts WO, Welsh WA, Libanati C, Ettlinger M, Kerner D, Maier M, Meon W, Schmoll R, Gies H, Schiffmann D. *Silica*. Ullmann's Encyclopedia of Industrial Chemistry. Wiley-VCH Verlag GmbH & Co. KGaA, 2000.

Flory PJ. *Principles of Polymer Chemistry*. Vol 119. Ithaca, New York: Cornell Univ. Press,, 1954.

Flory PJ. *On the Morphology of the Crystalline State in Polymers*. Journal of the American Chemical Society 1962; 84: 2857-2867.

Fornes TD, Paul DR. *Modeling properties of nylon 6/clay nanocomposites using composite theories*. Polymer 2003; 44: 4993-5013.

Fried J. *Polymer Science and Technology*: Pearson Education, 2003.

Fukushima K, Tabuani D, Abbate C, Arena M, Rizzarelli P. *Preparation, characterization and biodegradation of biopolymer nanocomposites based on fumed silica*. European Polymer Journal 2011; 47: 139-152.

Gaborieau M, Castignolles P. *Size-exclusion chromatography (SEC) of branched polymers and polysaccharides*. Analytical and Bioanalytical Chemistry 2011; 399: 1413-1423.

Gamez-Perez J, Nascimento L, Bou JJ, Franco-Urquiza E, Santana OO, Carrasco F, Ll. Maspoch M. *Influence of crystallinity on the fracture toughness of poly(lactic acid)/montmorillonite nanocomposites prepared by twin-screw extrusion*. Journal of Applied Polymer Science 2011a; 120: 896-905.

Gamez-Perez J, Velazquez-Infante JC, Franco-Urquiza E, Pages P, Carrasco F., Santana OO, Maspoch ML. *Fracture behavior of quenched poly(lactic acid)*. Express Polymer Letters 2011b; 5: 82–91.

Garlotta D. *A Literature Review of Poly(Lactic Acid)*. Journal of environmental polymer degradation 2001; 9: 63-84.

Gaspar-Cunha A, Covas JA, Vergnes B, Berzin F. *Reactive extrusion - Optimization of representative processes* Nova Science Pub Inc, 2011.

Ghaffar T, Irshad M, Anwar Z, Aqil T, Zulifqar Z, Tariq A, Kamran M, Ehsan N, Mehmood S. *Recent trends in lactic acid biotechnology: A brief review on production to purification*. Journal of Radiation Research and Applied Sciences 2014; 7: 222-229.

Giannelis EP. *Polymer Layered Silicate Nanocomposites*. Advanced Materials 1996; 8: 29-35.

Giannelis EP. *Polymer-layered silicate nanocomposites: Synthesis, properties and applications*. Applied Organometallic Chemistry 1998; 12: 675-680.

Gong J, Tian N, Wen X, Chen X, Liu J, Jiang Z, Mijowska E, Tang T. *Synergistic effect of fumed silica with Ni2O3 on improving flame retardancy of poly(lactic acid)*. Polymer Degradation and Stability 2014; 104: 18-27.

Green DL, Mewis J. *Connecting the Wetting and Rheological Behaviors of Poly(dimethylsiloxane)-Grafted Silica Spheres in Poly(dimethylsiloxane) Melts*. Langmuir 2006; 22: 9546-9553.

Grijpma DW, Penning JP, Pennings AJ. *Chain entanglement, mechanical properties and drawability of poly(lactide)*. Colloid and Polymer Science 1994; 272: 1068-1081.

Groot W, van Krieken J, Sliekersl O, de Vos S. *Production and Purification of Lactic Acid and Lactide*. Poly(Lactic Acid). John Wiley & Sons, Inc., 2010, pp. 1-18.

Gupta AP, Kumar V. *New emerging trends in synthetic biodegradable polymers – Polylactide: A critique*. European Polymer Journal 2007; 43: 4053-4074.

Gupta MC, Deshmukh VG. *Thermal oxidative degradation of poly-lactic acid*. Colloid and Polymer Science. 260, 1982, pp. 514-517.

Hahm W-G, Myung H-S, Im SS. *Preparation and properties ofin situ polymerized poly(ethylene terephthalate)/fumed silica nanocomposites*. Macromolecular Research 2004; 12: 85-93.

Haldorai Y, Shim J-J. *Manufacturing Polymer Nanocomposites*. Rheology and Processing of Polymer Nanocomposites. John Wiley & Sons, Inc., 2016, pp. 29-67.

Halperin BI, Feng S, Sen PN. *Differences between Lattice and Continuum Percolation Transport Exponents*. Physical Review Letters 1985; 54: 2391-2394.

Han CD. *Rheology and Processing of Polymeric Materials*: Oxford University Press, 2007.

Hashemi S. *Work of fracture of PBT/PC blend: Effect of specimen size, geometry, and rate of testing*. Polymer Engineering & Science 1997; 37: 912-921.

Havriliak S, Negami S. *A complex plane analysis of α-dispersions in some polymer systems*. Journal of Polymer Science Part C: Polymer Symposia. 14. Wiley Subscription Services, Inc., A Wiley Company, 1966, pp. 99-117.

Hemlata, Maiti SN. *Nonisothermal crystallization kinetics of PA6 and PA6/SEBS-g-MA blends*. Journal of Polymer Research 2012; 19: 9926.

Hendrick E, Frey M. *Increasing Surface Hydrophilicity in Poly(Lactic Acid) Electrospun Fibers by Addition of PLA-b-PEG Co-Polymers*. Journal of Engineered Fibers and Fabrics 2014; 9: 153-164.

Henton DE, Gruber P, Lunt J, Randall J. *Polylactic Acid Technology*. Natural Fibers, Biopolymers, and Biocomposites. CRC press, 2005, pp. 527–570.

Hernández-Morales V, Nava R, Acosta-Silva YJ, Macías-Sánchez SA, Pérez-Bueno JJ, Pawelec B. *Adsorption of lead (II) on SBA-15 mesoporous molecular sieve functionalized with –NH2 groups*. Microporous and Mesoporous Materials 2012; 160: 133-142.

Hiemenz PC, Lodge T. *Polymer chemistry*. Boca Raton: CRC Press, 2007.

Hoffman JD, Davis GT, Lauritzen JI. *The Rate of Crystallization of Linear Polymers with Chain Folding*. In: Hannay NB, editor. Treatise on Solid State Chemistry: Volume 3 Crystalline and Noncrystalline Solids. Springer US, Boston, MA, 1976, pp. 497-614.

Huang S-M, Hwang J-J, Liu H-J, Lin L-H. *Crystallization behavior of poly(L-lactic acid)/montmorillonite nanocomposites*. Journal of Applied Polymer Science 2010; 117: 434-442.

Hule RA, Pochan DJ. *Polymer Nanocomposites for Biomedical Applications*. MRS Bulletin 2007; 32: 354-358.

Hutchinson JM. *Physical aging of polymers*. Progress in Polymer Science 1995; 20: 703-760.

Hutchinson JM. *Relaxation processes and physical aging*. In: Haward RN, Young RJ, editors. The Physics of Glassy Polymers. Springer Netherlands, Dordrecht, 1997, pp. 85-153.

Iannace S, Nicolais L. *Isothermal crystallization and chain mobility of poly(L-lactide)*. Journal of Applied Polymer Science 1997; 64: 911-919.

Ikada Y, Tsuji H. *Biodegradable polyesters for medical and ecological applications*. Macromolecular Rapid Communications 2000; 21: 117-132.

Inkinen S, Hakkarainen M, Albertsson A-C, Södergård A. *From Lactic Acid to Poly(lactic acid) (PLA): Characterization and Analysis of PLA and Its Precursors*. Biomacromolecules. 12. American Chemical Society, 2011, pp. 523-532.

Jalalvandi E, Majid RA, Ghanbari T, Ilbeygi H. *Effects of montmorillonite (MMT) on morphological, tensile, physical barrier properties and biodegradability of polylactic acid/starch/MMT nanocomposites*. Journal of Thermoplastic Composite Materials 2015; 28: 496-509.

Jamshidi K, Hyon SH, Ikada Y. *Thermal characterization of polylactides*. Polymer 1988; 29: 2229-2234.

Jancar J, Douglas JF, Starr FW, Kumar SK, Cassagnau P, Lesser AJ, Sternstein SS, Buehler MJ. *Current issues in research on structure–property relationships in polymer nanocomposites*. Polymer 2010; 51: 3321-3343.

Japon S, Boogh L, Leterrier Y, Månson JAE. *Reactive processing of poly(ethylene terephthalate) modified with multifunctional epoxy-based additives*. Polymer 2000; 41: 5809-5818.

Jiang L, Zhang J, Wolcott MP. *Comparison of polylactide/nano-sized calcium carbonate and polylactide/montmorillonite composites: Reinforcing effects and toughening mechanisms*. Polymer 2007; 48: 7632-7644.

Johansson C. *Bioplastics*. In: Olabisi O, Adewale K, editors. Handbook of Thermoplastics, Second Edition. CRC Press, Boca Raton, 2016, pp. 865-876.

Kang J, Li J, Chen S, Peng H, Wang B, Cao Y, Li H, Chen J, Gai J, Yang F, Xiang M. *Investigation of the crystallization behavior of isotactic polypropylene polymerized with*

different Ziegler-Natta catalysts. Journal of Applied Polymer Science 2013; 129: 2663-2670.

Karger-Kocsis J, Czigány T. *Strain rate dependence of the work of fracture response of an amorphous poly(ethylene-naphthalate) (PEN) film*. Polymer Engineering & Science 2000; 40: 1809-1815.

Karger-Kocsis J, Czigány T, Moskala EJ. *Deformation rate dependence of the essential and non-essential work of fracture parameters in an amorphous copolyester*. Polymer 1998; 39: 3939-3944.

Karger-Kocsis J, Khumalo VM, Bárány T, Mészáros L, Pegoretti A. *On the toughness of thermoplastic polymer nanocomposites as assessed by the essential work of fracture (EWF) approach*. Composite Interfaces 2013; 20: 395-404.

Karger-Kocsis J, Moskala EJ. *Relationships between molecular and plane-stress essential work of fracture parameters in amorphous copolyesters*. Polymer Bulletin 1997; 39: 503-510.

Karger-Kocsis J, Moskala EJ. *Molecular dependence of the essential and non-essential work of fracture of amorphous films of poly(ethylene-2,6-naphthalate) (PEN)*. Polymer 2000; 41: 6301-6310.

Keller A. *A note on single crystals in polymers: Evidence for a folded chain configuration*. The Philosophical Magazine: A Journal of Theoretical Experimental and Applied Physics 1957; 2: 1171-1175.

Keller A. *Polymer crystals*. Reports on Progress in Physics 1968; 31: 623.

Khan MJ, Al-Juhani AA, Ul-Hamid A, Shawabkeh R, Hussein IA. *Effect of chemical modification of oil fly ash and compatibilization on the rheological and morphological properties of low-density polyethylene composites*. Journal of Applied Polymer Science 2011; 122: 2486-2496.

Khankrua R, Pivsa-Art S, Hiroyuki H, Suttiruengwong S. *Thermal and Mechanical Properties of Biodegradable Polyester/Silica Nanocomposites*. Energy Procedia 2013; 34: 705-713.

Kim GM, Michler GH. *Micromechanical deformation processes in toughened and particle filled semicrystalline polymers: Part 2. model representation for micromechanical deformation processes*. Polymer 1998; 39: 5699-5703.

Kim SH, Ahn SH, Hirai T. *Crystallization kinetics and nucleation activity of silica nanoparticle-filled poly(ethylene 2,6-naphthalate)*. Polymer 2003; 44: 5625-5634.

Kloepfer-Geschichte H. *Technical bulletin: Fine particles. from Degussa AG*. 11, 2006.

Knežević NŽ, Trewyn BG, Lin VSY. *Light- and pH-Responsive Release of Doxorubicin from a Mesoporous Silica-Based Nanocarrier*. Chemistry – A European Journal 2011; 17: 3338-3342.

Kolstad JJ. *Crystallization kinetics of poly(L-lactide-co-meso-lactide)*. Journal of Applied Polymer Science 1996; 62: 1079-1091.

Kopinke FD, Remmler M, Mackenzie K, Möder M, Wachsen O. *Thermal decomposition of biodegradable polyesters—II. Poly(lactic acid)*. Polymer Degradation and Stability 1996; 53: 329-342.

Korhonen H, Helminen A, Seppälä JV. *Synthesis of polylactides in the presence of co-initiators with different numbers of hydroxyl groups*. Polymer 2001; 42: 7541-7549.

Korobko AP, Krasheninnikov SV, Levakova IV, Drozd SN, Chvalun SN, Nikolaev VV, Shcherbina MA, Cherdyntseva SV. *Effect of the chemical grafting of epoxy resin onto organomodified montmorillonite on the structure and heat resistance of an epoxy nanocomposite*. Polymer Science Series A 2011; 53: 75-84.

Kosinski LE, Caruthers JM. *Rheological properties of poly(dimethylsiloxane) filled with fumed silica: II. Stress relaxation and stress growth*. Journal of Non-Newtonian Fluid Mechanics 1985; 17: 69-89.

Kramschuster A, Gong S, Turng L-S, Li T, Li T. *Injection-Molded Solid and Microcellular Polylactide and Polylactide Nanocomposites*. Journal of Biobased Materials and Bioenergy 2007; 1: 37-45.

Krishnamoorti R, Vaia RA, Giannelis EP. *Structure and Dynamics of Polymer-Layered Silicate Nanocomposites*. Chemistry of Materials 1996; 8: 1728-1734.

Kumar AP, Depan D, Singh Tomer N, Singh RP. *Nanoscale particles for polymer degradation and stabilization—Trends and future perspectives*. Progress in Polymer Science 2009; 34: 479-515.

Kumar R, Yakabu MK, Anandjiwala RD. *Effect of montmorillonite clay on flax fabric reinforced poly lactic acid composites with amphiphilic additives*. Composites Part A: Applied Science and Manufacturing 2010; 41: 1620-1627.

La Rosa AD. *4 - Life cycle assessment of biopolymers*. Biopolymers and Biotech Admixtures for Eco-Efficient Construction Materials. Woodhead Publishing, 2016, pp. 57-78.

Lai S-M, Hsieh Y-T. *Preparation and Properties of Polylactic Acid (PLA)/Silica Nanocomposites*. Journal of Macromolecular Science, Part B. 55. Taylor & Francis, 2016, pp. 211-228.

Le Bolay N, Lamure A, Gallego Leis N, Subhani A. *How to combine a hydrophobic matrix and a hydrophilic filler without adding a compatibilizer – Co-grinding enhances use properties of Renewable PLA–starch composites*. Chemical Engineering and Processing: Process Intensification 2012; 56: 1-9.

LeBaron PC, Wang Z, Pinnavaia TJ. *Polymer-layered silicate nanocomposites: an overview*. Applied Clay Science 1999; 15: 11-29.

Lee JH, Park TG, Park HS, Lee DS, Lee YK, Yoon SC, Nam J-D. *Thermal and mechanical characteristics of poly(l-lactic acid) nanocomposite scaffold*. Biomaterials 2003; 24: 2773-2778.

Lee S-H, Wang S, Teramoto Y. *Isothermal crystallization behavior of hybrid biocomposite consisting of regenerated cellulose fiber, clay, and poly(lactic acid)*. Journal of Applied Polymer Science 2008; 108: 870-875.

Lehmann B, Karger-Kocsis J. *Isothermal and non-isothermal crystallisation kinetics of pCBT and PBT*. Journal of Thermal Analysis and Calorimetry. 95, 2009, pp. 221-227.

Lewitus D, McCarthy S, Ophir A, Kenig S. *The Effect of Nanoclays on the Properties of PLLA-modified Polymers Part 1: Mechanical and Thermal Properties*. Journal of environmental polymer degradation 2006; 14: 171-177.

Li M, Hu D, Wang Y, Shen C. *Nonisothermal crystallization kinetics of poly(lactic acid) formulations comprising talc with poly(ethylene glycol)*. Polymer Engineering & Science 2010; 50: 2298-2305.

Li X, Yin J, Yu Z, Yan S, Lu X, Wang Y, Cao B, Chen X. *Isothermal crystallization behavior of poly(L-lactic acid)/organo-montmorillonite nanocomposites*. Polymer Composites 2009; 30: 1338-1344.

Liao R, Yang B, Yu W, Zhou C. *Isothermal cold crystallization kinetics of polylactide/nucleating agents*. Journal of Applied Polymer Science 2007; 104: 310-317.

Lim L-T, Cink K, Vanyo T. *Processing of Poly(Lactic Acid)*. Poly(Lactic Acid). John Wiley & Sons, Inc., 2010, pp. 189-215.

Lim LT, Auras R, Rubino M. *Processing technologies for poly(lactic acid)*. Progress in Polymer Science 2008; 33: 820-852.

Lipik VT, Widjaja LK, Liow SS, Abadie MJM, Venkatraman SS. *Effects of transesterification and degradation on properties and structure of polycaprolactone–polylactide copolymers*. Polymer Degradation and Stability 2010; 95: 2596-2602.

Liu JJ, Zhou KQ, Wen PY, Wang BB, Hu Y, Gui Z. *The influence of multiple modified MMT on the thermal and fire behavior of poly (lactic acid) nanocomposites*. Polymers for Advanced Technologies 2015; 26: 626-634.

Liu JY, Lou LJ, Yu W, Liao RG, Li RM, Zhou CX. *Long chain branching polylactide: Structures and properties*. Polymer 2010; 51: 5186-5197.

Liu R, Luo S, Cao J, Peng Y. *Characterization of organo-montmorillonite (OMMT) modified wood flour and properties of its composites with poly(lactic acid)*. Composites Part A: Applied Science and Manufacturing 2013; 51: 33-42.

Lohse DJ, Milner ST, Fetters LJ, Xenidou M, Hadjichristidis N, Mendelson RA, García-Franco CA, Lyon MK. *Well-Defined, Model Long Chain Branched Polyethylene. 2. Melt Rheological Behavior*. Macromolecules 2002; 35: 3066-3075.

Lorenzo AT, Arnal ML, Albuerne J, Müller AJ. *DSC isothermal polymer crystallization kinetics measurements and the use of the Avrami equation to fit the data: Guidelines to avoid common problems*. Polymer Testing. 26, 2007, pp. 222-231.

Lu H, Nutt S. *Restricted Relaxation in Polymer Nanocomposites near the Glass Transition*. Macromolecules 2003; 36: 4010-4016.

Lv H, Song S, Sun S, Ren L, Zhang H. *Enhanced properties of poly(lactic acid) with silica nanoparticles*. Polymers for Advanced Technologies 2016; 27: 1156-1163.

MacDonald WA, McLenaghan ADW, McLean G, Richards RW, King SM. *A neutron scattering investigation of the transesterification of a main-chain aromatic polyester*. Macromolecules 1991; 24: 6164-6167.

Mackay ME, Tuteja A, Duxbury PM, Hawker CJ, Van Horn B, Guan Z, Chen G, Krishnan RS. *General Strategies for Nanoparticle Dispersion*. Science 2006; 311: 1740-1743.

Maiti P, Yamada K, Okamoto M, Ueda K, Okamoto K. *New Polylactide/Layered Silicate Nanocomposites: Role of Organoclays*. Chemistry of Materials 2002; 14: 4654-4661.

Majer J. *Secondary crystallization of a Ziegler type polyethylene*. Collect. Czech. Chem. Commun. 1960; 25: 2454-2456.

Majesté J-C. *Rheology and Processing of Polymer Nanocomposites: Theory, Practice, and New Challenges*. Rheology and Processing of Polymer Nanocomposites. John Wiley & Sons, Inc., 2016, pp. 69-134.

Malkin AY, Beghishev VP, Keapin IA, Bolgov SA. *General treatment of polymer crystallization kinetics—Part 1. A new macrokinetic equation and its experimental verification*. Polymer Engineering & Science 1984; 24: 1396-1401.

Mark JE. *Some Novel Polymeric Nanocomposites*. Accounts of Chemical Research 2006; 39: 881-888.

Martinez AB, Gamez-Perez J, Sanchez-Soto M, Velasco JI, Santana OO, Ll Maspoch M. *The Essential Work of Fracture (EWF) method – Analyzing the Post-Yielding Fracture Mechanics of polymers*. Engineering Failure Analysis 2009; 16: 2604-2617.

Masaki K, Kamini NR, Ikeda H, Iefuji H. *Cutinase-Like Enzyme from the Yeast Cryptococcus sp. Strain S-2 Hydrolyzes Polylactic Acid and Other Biodegradable Plastics*. Applied and Environmental Microbiology 2005; 71: 7548-7550.

Maspoch ML, Ferrer D, Gordillo A, Santana OO, Martinez AB. *Effect of the specimen dimensions and the test speed on the fracture toughness of iPP by the essential work of fracture (EWF) method*. Journal of Applied Polymer Science 1999; 73: 177-187.

Maspoch ML, Franco-Urquiza E, Gamez-Perez J, Santana OO, Sánchez-Soto M. *Fracture behaviour of poly[ethylene–(vinyl alcohol)]/organo-clay composites*. Polymer International 2009; 58: 648-655.

Maspoch ML, Santana OO, Cailloux J, Franco-Urquiza E, Rodriguez C, Belzunce J, Martínez AB. *Ductile-brittle transition behaviour of PLA/o-MMT films during the physical aging process*. Express Polymer Letters. 9, 2015, pp. 185-195.

Mehta R, Kumar V, Bhunia H, Upadhyay SN. *Synthesis of Poly(Lactic Acid): A Review*. Journal of Macromolecular Science, Part C 2005; 45: 325-349.

Menczel JD, Judovits L, Prime RB, Bair HE, Reading M, Swier S. *Differential Scanning Calorimetry (DSC)*. Thermal Analysis of Polymers. John Wiley & Sons, Inc., 2008, pp. 7-239.

Meng Q, Heuzey M-C, Carreau PJ. *Control of thermal degradation of polylactide/clay nanocomposites during melt processing by chain extension reaction*. Polymer Degradation and Stability 2012; 97: 2010-2020.

Michler GH, Baltá-Calleja FJ. *Composites*. Nano- and Micromechanics of Polymers. Hanser, 2012, pp. 369-414.

Mihai M, Huneault MA, Favis BD. *Rheology and Extrusion Foaming of Chain-Branched Poly(lactic acid)*. Polymer Engineering and Science 2010; 50: 629-642.

Miyata T, Masuko T. *Crystallization behaviour of poly(l-lactide)*. Polymer 1998; 39: 5515-5521.

Mohanty AK, Misra M, Drzal LT. *Natural Fibers, Biopolymers, and Biocomposites*, 2005

Müller AJ, Michell RM, Lorenzo AT. *Isothermal Crystallization Kinetics of Polymers*. Polymer Morphology. John Wiley & Sons, Inc, 2016, pp. 181-203.

Murariu M, Dechief A-L, Ramy-Ratiarison R, Paint Y, Raquez J-M, Dubois P. *Recent advances in production of poly(lactic acid) (PLA) nanocomposites: a versatile method to tune crystallization properties of PLA*. Nanocomposites 2015; 1: 71-82.

Murray HH. *Chapter 2 Structure and Composition of the Clay Minerals and their Physical and Chemical Properties*. In: Murray HH, editor. Developments in Clay Science. 2. Elsevier, 2006, pp. 7-31.

Murray KA, Killion JA, Major I, Geever LM. *Thermal Degradation of Bio-nanocomposites*. In: Visakh PM, Arao Y, editors. Thermal Degradation of Polymer Blends, Composites and Nanocomposites. 1. Springer International Publishing, Heidelberg, 2015.

Najafi CN. *Development of Polylactide-Clay Nanocomposites for Food Packaging Applications*.Maîtrise ès Sciences Appliquées Thesis, Ecole Polytechnique de Montréal, Montréal. 2011.

Najafi N, Heuzey MC, Carreau PJ. *Polylactide (PLA)-clay nanocomposites prepared by melt compounding in the presence of a chain extender*. Composites Science and Technology 2012a; 72: 608-615.

Najafi N, Heuzey MC, Carreau PJ. *Crystallization behavior and morphology of polylactide and PLA/clay nanocomposites in the presence of chain extenders*. Polymer Engineering & Science. 53. Wiley Subscription Services, Inc., A Wiley Company, 2013, pp. 1053-1064.

Najafi N, Heuzey MC, Carreau PJ, Wood-Adams PM. *Control of thermal degradation of polylactide (PLA)-clay nanocomposites using chain extenders*. Polymer Degradation and Stability 2012b; 97: 554-565.

Nam JY, Sinha Ray S, Okamoto M. *Crystallization Behavior and Morphology of Biodegradable Polylactide/Layered Silicate Nanocomposite*. Macromolecules 2003; 36: 7126-7131.

Nandi S, Bose S, Mitra S, Ghosh AK. *Dynamic rheology and morphology of HDPE-fumed silica composites: Effect of interface modification*. Polymer Engineering & Science 2013; 53: 644-650.

NatureWorks LLC. *Sheet Extrusion Processing Guide*. NatureWorks LLC, Minnetonka, MN, 2005.

NatureWorks LLC. *Crystallizing and Drying Ingeo™ Biopolymer.* NatureWorks LLC, Minnetonka, MN, 2007.

Neppalli R, Causin V, Marega C, Modesti M, Adhikari R, Scholtyssek S, Ray SS, Marigo A. *The effect of different clays on the structure, morphology and degradation behavior of poly(lactic acid)*. Applied Clay Science 2014; 87: 278-284.

Nieddu E, Mazzucco L, Gentile P, Benko T, Balbo V, Mandrile R, Ciardelli G. *Preparation and biodegradation of clay composites of PLA*. Reactive and Functional Polymers 2009; 69: 371-379.

Nishida H, Mori T, Hoshihara S, Fan Y, Shirai Y, Endo T. *Effect of tin on poly(l-lactic acid) pyrolysis*. Polymer Degradation and Stability 2003; 81: 515-523.

Nofar M, Zhu W, Park CB, Randall J. *Crystallization Kinetics of Linear and Long-Chain-Branched Polylactide*. Industrial & Engineering Chemistry Research 2011; 50: 13789-13798.

Ogata N, Jimenez G, Kawai H, Ogihara T. *Structure and thermal/mechanical properties of poly(l-lactide)-clay blend*. Journal of Polymer Science Part B: Polymer Physics 1997; 35: 389-396.

Ojijo V, Ray SS. *Super toughened biodegradable polylactide blends with non-linear copolymer interfacial architecture obtained via facile in-situ reactive compatibilization*. Polymer 2015; 80: 1-17.

Okamoto M. *Polylactide/Clay Nano-Biocomposites*. In: Avérous L, Pollet E, editors. Environmental Silicate Nano-Biocomposites. Springer London, London, 2012, pp. 77-118.

Olewnik E, Richert J. *Effect of the compatibilizing agent on the structure, mechanical and thermal properties of polylactide filled with modified and unmodified montmorillonite*. Polymer Composites 2014; 35: 1330-1337.

Ortenzi MA, Basilissi L, Farina H, Di Silvestro G, Piergiovanni L, Mascheroni E. *Evaluation of crystallinity and gas barrier properties of films obtained from PLA nanocomposites synthesized via "in situ" polymerization of l-lactide with silane-modified nanosilica and montmorillonite*. European Polymer Journal 2015; 66: 478-491.

Ouyang P, Kang Y-q, Yin G-f, Huang Z-b, Yao Y-d, Liao X-m. *Fabrication of hydrophilic paclitaxel-loaded PLA-PEG-PLA microparticles via SEDS process*. Frontiers of Materials Science in China 2009; 3: 15-24.

Pan P, Kai W, Zhu B, Dong T, Inoue Y. *Polymorphous Crystallization and Multiple Melting Behavior of Poly(l-lactide): Molecular Weight Dependence*. Macromolecules 2007; 40: 6898-6905.

Pan P, Zhu B, Dong T, Yazawa K, Shimizu T, Tansho M, Inoue Y. *Conformational and microstructural characteristics of poly(L-lactide) during glass transition and physical aging*. The Journal of Chemical Physics 2008; 129: 184902.

Papageorgiou GZ, Achilias DS, Bikiaris DN, Karayannidis GP. *Isothermal and non-isothermal crystallization kinetics of branched and partially crosslinked PET*. Journal of Thermal Analysis and Calorimetry 2006; 84: 85-89.

Papageorgiou GZ, Achilias DS, Nanaki S, Beslikas T, Bikiaris D. *PLA nanocomposites: Effect of filler type on non-isothermal crystallization*. Thermochimica Acta 2010; 511: 129-139.

Patil R, Reneker DH. *Molecular folds in polyethylene observed by atomic force microscopy*. Polymer 1994; 35: 1909-1914.

Pattanayak A, Jana SC. *Synthesis of thermoplastic polyurethane nanocomposites of reactive nanoclay by bulk polymerization methods*. Polymer 2005; 46: 3275-3288.

Paul DR, Robeson LM. *Polymer nanotechnology: Nanocomposites*. Polymer 2008; 49: 3187-3204.

Paul M-A, Alexandre M, Degée P, Henrist C, Rulmont A, Dubois P. *New nanocomposite materials based on plasticized poly(l-lactide) and organo-modified montmorillonites: thermal and morphological study*. Polymer 2003; 44: 443-450.

Pavlidou S, Papaspyrides CD. *A review on polymer–layered silicate nanocomposites*. Progress in Polymer Science 2008; 33: 1119-1198.

Pawar RP, Tekale SU, Shisodia SU, Totre JT, Dombb AJ. *Biomedical Applications of Poly(Lactic Acid)*. Recent Patents on Regenerative Medicine 2014; 4: 40-51.

Perego G, Cella GD. *Mechanical Properties*. Poly(Lactic Acid). John Wiley & Sons, Inc., 2010, pp. 141-153.

Picard E, Espuche E, Fulchiron R. *Effect of an organo-modified montmorillonite on PLA crystallization and gas barrier properties*. Applied Clay Science 2011; 53: 58-65.

Pilić BM, Radusin TI, Ristić IS, Silvestre C, Lazić VL, Baloš SS, Duraccio D. *Hydrophobic silica nanoparticles as reinforcing filler for poly (lactic acid) polymer matrix*. Hemijska Industrija 2015: Article In Press.

Pluta M. *Melt compounding of polylactide/organoclay: Structure and properties of nanocomposites*. Journal of Polymer Science Part B: Polymer Physics 2006; 44: 3392-3405.

Pluta M, Paul M-A, Alexandre M, Dubois P. *Plasticized polylactide/clay nanocomposites. I. The role of filler content and its surface organo-modification on the physico-chemical properties*. Journal of Polymer Science Part B: Polymer Physics 2006; 44: 299-311.

Poole CF, Schuette SA. *Chapter 4 - THE COLUMN IN LIQUID CHROMATOGRAPHY*. Contemporary Practice of Chromatography. Elsevier, Amsterdam, 1984, pp. 213-351.

Pretsch E, Buhlmann P, Affolter C, Herrera A, Martinez R. *Determinación estructural de compuestos orgánicos*. Barcelona: Springer-Verlag Iberica, 2001.

Pretsch E, Bühlmann P, Badertscher M. *IR Spectroscopy*. Structure Determination of Organic Compounds. Springer Berlin Heidelberg, 2009.

Prieto A. *To be, or not to be biodegradable… that is the question for the bio-based plastics*. Microbial Biotechnology 2016; 9: 652-657.

Raquez J-M, Narayan R, Dubois P. *Recent Advances in Reactive Extrusion Processing of Biodegradable Polymer-Based Compositions*. Macromolecular Materials and Engineering 2008; 293: 447-470.

Rasal RM, Hirt DE. *Toughness decrease of PLA-PHBHHx blend films upon surface-confined photopolymerization*. Journal of Biomedical Materials Research Part A 2009; 88A: 1079-1086.

Rasal RM, Janorkar AV, Hirt DE. *Poly(lactic acid) modifications*. Progress in Polymer Science. 35, 2010, pp. 338-356.

Ray S, Easteal AJ. *Advances in Polymer-Filler Composites: Macro to Nano*. Materials and Manufacturing Processes 2007; 22: 741-749.

Redl A, Morel MH, Bonicel J, Guilbert S, Vergnes B. *Rheological properties of gluten plasticized with glycerol: dependence on temperature, glycerol content and mixing conditions*. Rheologica Acta 1999; 38: 311-320.

Ren J. *Lactic Acid*. Biodegradable Poly(Lactic Acid): Synthesis, Modification, Processing and Applications. Springer Berlin Heidelberg, Berlin, Heidelberg, 2010a, pp. 4-14.

Ren J. *Synthesis and Manufacture of PLA*. Biodegradable Poly(Lactic Acid): Synthesis, Modification, Processing and Applications. Springer Berlin Heidelberg, Berlin, Heidelberg, 2010b, pp. 15-37.

Rizzarelli P, Carroccio S. *Role of Mass Spectrometry in the Elucidation of Thermal Degradation Mechanisms in Polymeric Materials*. Reactions and Mechanisms in Thermal Analysis of Advanced Materials. John Wiley & Sons, Inc., 2015, pp. 221-258.

Run M, Wang Y, Yao C, Zhao H. *Isothermal-crystallization kinetics and melting behavior of crystalline/crystalline blends of poly(trimethylene terephthalate) and poly(ethylene 2,6-naphthalate)*. Journal of Applied Polymer Science 2007; 103: 3316-3325.

Rybnik´ř F. *Mechanism of secondary crystallization in polymers*. Journal of Polymer Science Part A: General Papers 1963; 1: 2031-2038.

Sabatini V, Farina H, Basilissi L, Di Silvestro G, Ortenzi MA. *The Use of Epoxy Silanes on Montmorillonite: An Effective Way to Improve Thermal and Rheological Properties of PLA/MMT Nanocomposites Obtained via "In Situ" Polymerization*. Journal of Nanomaterials 2015.

Saeidlou S, Huneault MA, Li H, Park CB. *Poly(lactic acid) crystallization*. Progress in Polymer Science 2012; 37: 1657-1677.

Saiter A, Delpouve N, Dargent E, Oberhauser W, Conzatti L, Cicogna F, Passaglia E. *Probing the chain segment mobility at the interface of semi-crystalline polylactide/clay nanocomposites*. European Polymer Journal 2016; 78: 274-289.

Saito T, Okamoto M, Hiroi R, Yamamoto M, Shiroi T. *Poly(p-phenylenesulfide)-based nano-composite formation: Delamination of organically modified layered filler via solid-state processing*. Polymer 2007; 48: 4143-4151.

Santana OO, Rodríguez C, Belzunce J, Gámez-Pérez J, Carrasco F, Maspoch ML. *Fracture behaviour of de-aged poly(lactic acid) assessed by essential work of fracture and J-Integral methods*. Polymer Testing 2010; 29: 984-990.

Scaffaro R, Botta L. *Chapter 12 - Degradation Behavior of Nanocomposite Polymer Blends*. Nanostructured Polymer Blends. William Andrew Publishing, Oxford, 2014, pp. 423-447.

Schaefer DW, Justice RS. *How Nano Are Nanocomposites?* Macromolecules 2007; 40: 8501-8517.

Schindler A, Harper D. *Polylactide. II. Viscosity–molecular weight relationships and unperturbed chain dimensions*. Journal of Polymer Science: Polymer Chemistry Edition. 17. John Wiley & Sons, Inc., 1979, pp. 2593-2599.

Shechter L, Wynstra J, Kurkjy RP. *Glycidyl Ether Reactions with Amines*. Industrial & Engineering Chemistry 1956; 48: 94-97.

Shen L, Haufe J, *Product Overview and Market Projection of Emerging Bio-based Plastics. PRO-BIP 2009, Final Report, Report Commissioned by European Polysaccharide Network of Excellence (EPNOE) and European Bioplastics.*, Universiteit Utrecht, The Netherlands,,2009.

Shen Y, Vishnyakov A, Tomassone M. *Molecular Dynamics Studies on the Dispersion of Silica Nanoparticles in Polyethylene Melt Using a Coarse-Grained Model*, 2008.

Sheng N, Boyce MC, Parks DM, Rutledge GC, Abes JI, Cohen RE. *Multiscale micromechanical modeling of polymer/clay nanocomposites and the effective clay particle*. Polymer 2004; 45: 487-506.

Shenoy AV. *Basic rheological concepts*. Rheology of Filled Polymer Systems. Springer Netherlands, Dordrecht, 1999, pp. 54-111.

Shi H, Lan T, Pinnavaia TJ. *Interfacial Effects on the Reinforcement Properties of Polymer−Organoclay Nanocomposites*. Chemistry of Materials 1996; 8: 1584-1587.

Shimao M. *Biodegradation of plastics*. Current Opinion in Biotechnology 2001; 12: 242-247.

Sin LT, Rahmat Abdul R, Rahman Wan AWA. *2 - Overview of Poly(lactic Acid) A2 - Ebnesajjad, Sina*. Handbook of Biopolymers and Biodegradable Plastics. William Andrew Publishing, Boston, 2013a, pp. 11-54.

Sin LT, Rahmat AR, Rahman WAWA. *3 - Thermal Properties of Poly(lactic Acid)*. Polylactic Acid. William Andrew Publishing, Oxford, 2013b, pp. 109-141.

Singh S, Ray SS. *Polylactide Based Nanostructured Biomaterials and Their Applications*. Journal of Nanoscience and Nanotechnology 2007; 7: 2596-2615.

Sinha Ray S. *1 - Introduction to environmentally friendly polymer nanocomposites*. Environmentally Friendly Polymer Nanocomposites. Woodhead Publishing, 2013a, pp. 3-24.

Sinha Ray S. *2 - Thermodynamics, Molecular Modeling, and Kinetics of Nanocomposite Formation*. Clay-Containing Polymer Nanocomposites. Elsevier, Amsterdam, 2013b, pp. 25-37.

Sinha Ray S. *3 - Structure and Morphology Characterization Techniques*. Clay-Containing Polymer Nanocomposites. Elsevier, Amsterdam, 2013c, pp. 39-66.

Sinha Ray S, Bousmina M. *Biodegradable polymers and their layered silicate nanocomposites: In greening the 21st century materials world*. Progress in Materials Science 2005; 50: 962-1079.

Sinha Ray S, Okamoto M. *New Polylactide/Layered Silicate Nanocomposites, 6a Melt Rheology and Foam Processing*. Macromolecular Materials and Engineering 2003a; 288: 936-944.

Sinha Ray S, Okamoto M. *Polymer/layered silicate nanocomposites: a review from preparation to processing*. Progress in Polymer Science 2003b; 28: 1539-1641.

Sinha Ray S, Yamada K, Okamoto M, Ogami A, Ueda K. *New Polylactide/Layered Silicate Nanocomposites. 3. High-Performance Biodegradable Materials*. Chemistry of Materials 2003a; 15: 1456-1465.

Sinha Ray S, Yamada K, Okamoto M, Ueda K. *New polylactide-layered silicate nanocomposites. 2. Concurrent improvements of material properties, biodegradability and melt rheology*. Polymer 2003b; 44: 857-866.

Slowing II, Trewyn BG, Giri S, Lin VSY. *Mesoporous Silica Nanoparticles for Drug Delivery and Biosensing Applications*. Advanced Functional Materials 2007; 17: 1225-1236.

Södergård A, Inkinen S. *Production, Chemistry and Properties of Polylactides*. Biopolymers – New Materials for Sustainable Films and Coatings. John Wiley & Sons, Ltd, 2011, pp. 43-63.

Södergård A, Stolt M. *Properties of lactic acid based polymers and their correlation with composition*. Progress in Polymer Science 2002; 27: 1123-1163.

Sokolowska D, Dziob D, Gorska U, Kieltyka B, Moscicki JK. *Electric conductivity percolation in naturally dehydrating, lightly wetted, hydrophilic fumed silica powder*. Physical Review E 2013; 87: 062404.

Southern Clay Products. *Technical Data Sheets*. Cloisite 30B, 2005.

Stöber W, Fink A, Bohn E. *Controlled growth of monodisperse silica spheres in the micron size range*. Journal of Colloid and Interface Science 1968; 26: 62-69.

Storks KH. *An Electron Diffraction Examination of Some Linear High Polymers*. Journal of the American Chemical Society 1938; 60: 1753-1761.

Supaphol P, Spruiell JE. *Application of the Avrami, Tobin, Malkin, and Simultaneous Avrami Macrokinetic Models to Isothermal Crystallization of Syndiotactic Polypropylenes*. Journal of Macromolecular Science, Part B 2000; 39: 257-277.

Taubner V, Shishoo R. *Influence of processing parameters on the degradation of poly(L-lactide) during extrusion*. Journal of Applied Polymer Science 2001; 79: 2128-2135.

Tesoro G. *Textbook of polymer science, 3rd ed., Fred W. Billmeyer, Jr.* Journal of Polymer Science: Polymer Letters Edition. 22. John Wiley & Sons, Inc., 1984, pp. 208-213.

Thellen C, Orroth C, Froio D, Ziegler D, Lucciarini J, Farrell R, D'Souza NA, Ratto JA. *Influence of montmorillonite layered silicate on plasticized poly(l-lactide) blown films*. Polymer 2005; 46: 11716-11727.

Till PH. *The growth of single crystals of linear polyethylene*. Journal of Polymer Science 1957; 24: 301-306.

Tjong SC. *Chapter 10 - Synthesis and Structure-Property Characteristics of Clay-Polymer Nanocomposites*. Nanocrystalline Materials. Elsevier Science Ltd, Oxford, 2006, pp. 311-348.

Tobin MC. *Theory of phase transition kinetics with growth site impingement. I. Homogeneous nucleation*. Journal of Polymer Science: Polymer Physics Edition 1974; 12: 399-406.

Todorov LV, Viana JC. *Characterization of PET nanocomposites produced by different melt-based production methods*. Journal of Applied Polymer Science 2007; 106: 1659-1669.

Tsuji H. *Poly(lactide) Stereocomplexes: Formation, Structure, Properties, Degradation, and Applications*. Macromolecular Bioscience 2005; 5: 569-597.

Tsuji H. *Hydrolytic Degradation*. Poly(Lactic Acid). John Wiley & Sons, Inc., 2010, pp. 343-381.

Tsuji H, Ikada Y. *Crystallization from the melt of poly(lactide)s with different optical purities and their blends*. Macromolecular Chemistry and Physics 1996; 197: 3483-3499.

Uhrlandt S. *Kirk-Othmer Encyclopedia of Chemical Technology, Volume 22*. Vol 22. Hoboken, New Jersey: American Chemical Society, 2006.

Ulrich GD, Rieh JW. *Aggregation and growth of submicron oxide particles in flames*. Journal of Colloid and Interface Science 1982; 87: 257-265.

Vaia RA, Giannelis EP. *Polymer Nanocomposites: Status and Opportunities*. MRS Bulletin 2001; 26: 394-401.

van Gurp M, Palmen J. *Time-temperature superposition method for polymeric blends*. Rheology Bulletin 1998; 67: 5-8.

Van Krevelen DW, Te Nijenhuis K. *Chapter 2 - Typology of Polymers*. Properties of Polymers (Fourth Edition). Elsevier, Amsterdam, 2009, pp. 7-47.

van Ruymbeke E, Stéphenne V, Daoust D, Godard P, Keunings R, Bailly C. *A sensitive method to detect very low levels of long chain branching from the molar mass distribution and linear viscoelastic response*. Journal of Rheology 2005; 49: 1503-1520.

Vansant EF, Van Der Voort P, Vrancken KC. *Chapter 1 Silica: preparation and properties*. In: E.F. Vansant PVDV, Vrancken KC, editors. Studies in Surface Science and Catalysis. Volume 93. Elsevier, 1995, pp. 3-30.

Vasanthan N, Ly H, Ghosh S. *Impact of Nanoclay on Isothermal Cold Crystallization Kinetics and Polymorphism of Poly(l-Lactic Acid) Nanocomposites*. The Journal of Physical Chemistry B 2011; 115: 9556-9563.

Vink ETH, Rábago KR, Glassner DA, Gruber PR. *Applications of life cycle assessment to NatureWorks™ polylactide (PLA) production*. Polymer Degradation and Stability 2003; 80: 403-419.

Vivero-Escoto JL, Huxford-Phillips RC, Lin W. *Silica-based nanoprobes for biomedical imaging and theranostic applications*. Chemical Society Reviews 2012; 41: 2673-2685.

Vladimirov LV, Artemenko SA, Ivanov VV, Zelenetskii AN, Oleinik EF, Salamatina OB. *Mechanism of reactions between epoxy compounds and amines*. Polymer Science U.S.S.R. 1980; 22: 254-261.

Wachsen O, Platkowski K, Reichert KH. *Thermal degradation of poly-l-lactide—studies on kinetics, modelling and melt stabilisation*. Polymer Degradation and Stability 1997; 57: 87-94.

Wang D-Y, Gohs U, Kang N-J, Leuteritz A, Boldt R, Wagenknecht U, Heinrich G. *Method for Simultaneously Improving the Thermal Stability and Mechanical Properties of Poly(lactic acid): Effect of High-Energy Electrons on the Morphological, Mechanical, and Thermal Properties of PLA/MMT Nanocomposites*. Langmuir 2012; 28: 12601-12608.

Wang H, Fang M, Shi T, Zhai L, Tang C. *Preparation of porous poly(lactic acid)/Sio2 hybrid microspheres*. Journal of Applied Polymer Science. 102. Wiley Subscription Services, Inc., A Wiley Company, 2006, pp. 679-683.

Wang H, Qiu Z. *Crystallization kinetics and morphology of biodegradable poly(l-lactic acid)/graphene oxide nanocomposites: Influences of graphene oxide loading and crystallization temperature*. Thermochimica Acta 2012; 527: 40-46.

Wang H, Zhang Y, Tian M, Zhai L, Wei Z, Shi T. *Preparation and degradability of poly(lactic acid)–poly(ethylene glycol)–poly(lactic acid)/SiO2 hybrid material*. Journal of Applied Polymer Science 2008a; 110: 3985-3989.

Wang Y, Steinhoff B, Brinkmann C, Alig I. *In-line monitoring of the thermal degradation of poly(l-lactic acid) during melt extrusion by UV–vis spectroscopy*. Polymer 2008b; 49: 1257-1265.

Wen X, Lin Y, Han C, Zhang K, Ran X, Li Y, Dong L. *Thermomechanical and optical properties of biodegradable poly(L-lactide)/silica nanocomposites by melt compounding*. Journal of Applied Polymer Science 2009; 114: 3379-3388.

Wen X, Zhang K, Wang Y, Han L, Han C, Zhang H, Chen S, Dong L. *Study of the thermal stabilization mechanism of biodegradable poly(L-lactide)/silica nanocomposites*. Polymer International. 60. John Wiley & Sons, Ltd., 2011, pp. 202-210.

Winey KI, Vaia RA. *Polymer Nanocomposites*. MRS Bulletin 2007; 32: 314-322.

Wood-Adams P, Costeux S. *Thermorheological Behavior of Polyethylene: Effects of Microstructure and Long Chain Branching*. Macromolecules 2001; 34: 6281-6290.

Wool RP. *15 - NANOCLAY BIOCOMPOSITES*. Bio-Based Polymers and Composites. Academic Press, Burlington, 2005, pp. 523-550.

Wu D, Wu L, Wu L, Xu B, Zhang Y, Zhang M. *Comparison Between Isothermal Cold and Melt Crystallization of Polylactide/Clay Nanocomposites*. Journal of Nanoscience and Nanotechnology 2008; 8: 1658-1668.

Wu J, Mai Y-W. *The essential fracture work concept for toughness measurement of ductile polymers*. Polymer Engineering & Science. 36. Wiley Subscription Services, Inc., A Wiley Company, 1996, pp. 2275-2288.

Wu X, Yuan J, Yu Y, Wang Y. *Preparation and characterization of polylactide/montmorillonite nanocomposites*. Journal of Wuhan University of Technology-Mater. Sci. Ed. 2009; 24: 562-565.

Xanthos M. *Reactive extrusion: principles and practice*. Hanser Publishers(Germany), 1992 1992: 304.

Xiao L, Wang B, Yang G, Gauthier M. *Poly(Lactic Acid)-Based Biomaterials: Synthesis, Modification and Applications*. In: Dhanjoo NG, editor. Biomedical Science, Engineering and Technology. InTech, Rijeka, Croatia, 2012, pp. 247-282.

Xie X-L, Liu Q-X, Li RK-Y, Zhou X-P, Zhang Q-X, Yu Z-Z, Mai Y-W. *Rheological and mechanical properties of PVC/CaCO3 nanocomposites prepared by in situ polymerization*. Polymer 2004; 45: 6665-6673.

Xiong Z, Dai X, Na H, Tang Z, Zhang R, Zhu J. *A toughened PLA/Nanosilica composite obtained in the presence of epoxidized soybean oil*. Journal of Applied Polymer Science 2015; 132: n/a-n/a.

Xu Y-j, Song Y-h, Zheng Q. *Effects of nanosilica on crystallization and thermal ageing behaviors of polyethylene terephthalate*. Chinese Journal of Polymer Science 2015; 33: 697-708.

Yan S, Yin J, Yang J, Chen X. *Structural characteristics and thermal properties of plasticized poly(l-lactide)-silica nanocomposites synthesized by sol–gel method*. Materials Letters 2007a; 61: 2683-2686.

Yan S, Yin J, Yang Y, Dai Z, Ma J, Chen X. *Surface-grafted silica linked with l-lactic acid oligomer: A novel nanofiller to improve the performance of biodegradable poly(l-lactide)*. Polymer 2007b; 48: 1688-1694.

Yoshida O, Okamoto M. *Direct Melt Intercalation of Polylactide Chains into Nano-Galleries: Interlayer Expansion and Nano-Composite Structure*. Macromolecular Rapid Communications 2006; 27: 751-757.

Zaarei D, Sarabi AA, Sharif F, Kassiriha SM. *Structure, properties and corrosion resistivity of polymeric nanocomposite coatings based on layered silicates*. Journal of Coatings Technology and Research 2008; 5: 241-249.

Zachmann VHG, Stuart HA. *Melting and crystallization phenomena in macromolecular substances. IV. Main and postcrystallization of terylene from the glassy state*. Die Makromolekulare Chemie 1960; 41: 131-147.

Zanetti M, Lomakin S, Camino G. *Polymer layered silicate nanocomposites*. Macromolecular Materials and Engineering 2000; 279: 1-9.

Zhang J, Lou J, Ilias S, Krishnamachari P, Yan J. *Thermal properties of poly(lactic acid) fumed silica nanocomposites: Experiments and molecular dynamics simulations*. Polymer 2008a; 49: 2381-2386.

Zhang MQ, Rong MZ, Friedrich K. *20 - Wear resisting polymer nanocomposites: preparation and properties*. Polymer Nanocomposites. Woodhead Publishing, 2006, pp. 540-577.

Zhang MQ, Rong MZ, Guo QB, Luo Y. *Chapter 6 – Sliding wear performance of epoxy-based nanocomposites*. Tribology of Polymeric Nanocomposites (Second Edition). Butterworth-Heinemann, Oxford, 2013, pp. 163-203.

Zhang X, Wu W, Wang J, Tian X. *Direct synthesis and characterization of highly ordered functional mesoporous silica thin films with high amino-groups content*. Applied Surface Science 2008b; 254: 2893-2899.

Zhang X, Wyss U, Pichora D, Goosen MA. *An investigation of the synthesis and thermal stability of poly(dl-lactide)*. Polymer Bulletin 1992; 27: 623-629.

Zhen W, Wang W. *Structure, properties and rheological behavior of thermoplastic poly(lactic acid)/quaternary fulvic acid-intercalated saponite nanocomposites*. Polymer Bulletin 2016; 73: 1015-1035.

Zhu A, Diao H, Rong Q, Cai A. *Preparation and properties of polylactide–silica nanocomposites*. Journal of Applied Polymer Science. 116. Wiley Subscription Services, Inc., A Wiley Company, 2010, pp. 2866-2873.

Zhuravlev LT. *The surface chemistry of amorphous silica. Zhuravlev model*. Colloids and Surfaces A: Physicochemical and Engineering Aspects 2000; 173: 1-38.

Zou G-X, Zhang X, Zhao C-X, Li J. *The crystalline and mechanical properties of PLA/layered silicate degradable composites*. Polymer Science Series A 2012; 54: 393-400.

Zou H, Wu S, Shen J. *Polymer/Silica Nanocomposites: Preparation, Characterization, Properties, and Applications*. Chemical Reviews 2008; 108: 3893-3957.